# Nondestructive Evaluation of Asphalt Pavement Joints Using LWD and MASW Tests

by

Antonin du Tertre

A thesis

presented to the University of Waterloo

in fulfillment of the

thesis requirement for the degree of

Master of Applied Science

in

Civil Engineering

Waterloo, Ontario, Canada, 2010

I hereby declare that I am the sole author of this thesis. This is a true copy of the thesis, including any required final revisions, as accepted by my examiners.

I understand that my thesis may be made electronically available to the public.

# ABSTRACT

Longitudinal joints are one of the critical factors that cause premature pavement failure. Poor-quality joints are characterized by a low density and high permeability; which generates surface distresses such as ravelling or longitudinal cracking. Density has been traditionally considered as the primary performance indicator of joint construction. Density measurements consist of taking cores in the field and determining their density in the laboratory. Although this technique provides the most accurate measure of joint density, it is destructive and time consuming. Nuclear and non-nuclear gauges have been used to evaluate the condition of longitudinal joint non-destructively, but did not show good correlation with core density tests. Consequently, agencies are searching for other non-destructive testing (NDT) options for longitudinal joints evaluation.

NDT methods have significantly advanced for the evaluation of pavement structural capacity during the past decade. These methods are based either on deflection or wave velocity measurements. The light weight deflectometer (LWD) is increasingly being used in quality control/quality assurance to provide a rapid determination of the surface modulus. Corresponding backcalculation programs are able to determine the moduli of the different pavement layers; these moduli are input parameters for mechanistic-empirical pavement design. In addition, ultrasonic wave-based methods have been studied for pavement condition evaluation but not developed to the point of practical implementation. The multi-channel analysis of surface waves (MASW) consists of using ultrasonic transducers to measure surface wave velocities in pavements and invert for the moduli of the different layers.

In this study, both LWD and MASW were used in the laboratory and in the field to assess the condition of longitudinal joints. LWD tests were performed in the field at different distances from the centreline in order to identify variations of the surface modulus. MASW measurements were conducted across the joint to evaluate its effect on wave velocities, frequency content and attenuation parameters. Improved signal processing techniques were used to analyze the data, such as Fourier Transform, windowing, or discrete wavelet transform. Dispersion curves were computed to determine surface wave velocities and identify the nature of the wave modes propagating through the asphalt pavement. Parameters such as peak-to-peak amplitude or the area of the frequency spectrum were used to compute attenuation curves. A self calibrating technique, called Fourier transmission coefficient (FTC), was used to assess the condition of longitudinal joints while eliminating the variability introduced by the source, receivers and coupling system.

A critical component of this project consisted of preparing an asphalt slab with a joint in the middle that would be used for testing in the laboratory. The compaction method was calibrated by preparing fourteen asphalt samples. An exponential correlation was determined between the air void content and the compaction effort applied to the mixture. Using this relationship, an asphalt slab was prepared in two stages to create a joint of medium quality. Nuclear density measurements were performed at different locations on the slab and showed a good agreement with the predicted density gradient across the joint.

MASW tests were performed on the asphalt slabs using different coupling systems and receivers. The FTC coefficients showed good consistency from one configuration to another. This result indicates that the undesired variability due to the receivers and the coupling system was reduced by the FTC technique. Therefore, the coefficients were representative of the hot mix asphalt (HMA) condition. A comparison of theoretical and experimental dispersion curves indicated that mainly Lamb waves were generated in the asphalt layer. This new result is in contradiction with the common assumption that the response is governed by surface waves. This result is of critical importance for the analysis of the data since MASW tests have been focusing on the analysis of Rayleigh waves.

Deflection measurements in the field with the LWD showed that the surface modulus was mostly affected by the base and subgrade moduli, and could not be used to evaluate the condition of the surface course that contains the longitudinal joints. The LWDmod software should be used to differentiate the pavement layers and backcalculate the modulus of the asphalt layer. Testing should be performed using different plate sizes and dropping heights in order to generate different stress levels at the pavement surface and optimize the accuracy of the backcalculation.

Finally, master curves were computed using a predictive equation based on mix design specifications. Moduli measured at different frequencies of excitation with the two NDT techniques were shifted to a design frequency of 25 Hz. Design moduli measured in the field and in the laboratory with the seismic method were in good agreement (less than 0.2% difference). Moreover, a relatively good agreement was found between the moduli measured with the LWD and the MASW method after shifting to the design frequency.

In conclusion, LWD and MASW measurements were representative of HMA condition. However, the condition assessment of medium to good quality joints requires better control of the critical parameters, such as the measurement depth for the LWD, or the frequency content generated by the ultrasonic source and the coupling between the receivers and the asphalt surface for the MASW method.

# ACKNOWLEDGEMENTS

# TABLE OF CONTENTS

# LIST OF TABLES

# LIST OF FIGURES

# CHAPTER 1.  INTRODUCTION

## 1.1.  Background

Asphalt pavements are usually constructed one lane at a time, resulting in the creation of longitudinal joints at the interface between the lanes. The quality of these joints is critical for the performance of the asphalt pavements. Poor-quality joints are generally characterized by low density and high permeability which cause premature pavement failure with surface distresses (ravelling and longitudinal cracking). Therefore, some agency specifications require joint density to be not less than two percent below the specified mat density (Estakhri et al. 2001).

Conventional longitudinal cold joint construction methods often result in weak joint structures. The outer edge of the first paved lane is not confined and spreads outward in response to the roller pressure, which results in a lower density than the interior portion of the mat. Prior to the construction of the second lane, the first lane had time to cool down (cold lane). The unconfined edge of the cold lane achieves little or no additional compaction during the placement of the second (hot) lane. On the contrary, the outer edge of the hot lane is confined by the cold lane and could reach higher densities than the mat. Nevertheless, poor compaction can also appear at the confined edge if an insufficient amount of hot mix is placed at the joint. These areas of low density and high air voids allow air and water to penetrate into the pavement structure at the joint location, which causes further deterioration. For example, 60 percent of joints require routing and sealing within 5 years in Northern Ontario (Marks et al. 2009).

Several techniques have been used to produce better quality joints, including echelon paving, reheated joints with joint heaters, or warm mix asphalt (WMA) (Uzarowski et al. 2009). Actually, most of the research has been dedicated to the development of methods used to construct good quality joints rather than methods used to evaluate their condition. Density has been used as the primary performance indicator of joint construction. In general, density measurements consist of taking cores in the field and determining their density in the laboratory using methods such as saturated surface dry specimens or vacuum sealing. Although these techniques provide accurate measurements of joint density, they are destructive and time consuming.

Nuclear and non-nuclear density gauges have been used to evaluate the condition of longitudinal joints non-destructively. Problems with the seating of these gauges have been met when testing

joints. Many density gauge measurements across longitudinal joints are actually collected at the location immediately next to the joint (Williams et al. 2009). In 1997, the Ministry of Transportation of Ontario (MTO) conducted different trials to estimate the benefits of specified longitudinal joint construction techniques (Marks et al. 2009). Both nuclear and core density tests were performed at the joints. The results showed that these measurements did not correlate well ($R^2$ values less than 0.4). Consequently, agencies are searching for other non-destructive (NDT) options for longitudinal joint evaluation.

NDT methods have been commonly used in the past decade to evaluate the structural capacity of asphalt pavements. These methods are based either on deflection or wave velocity measurements. The falling weight deflectometer (FWD) has been widely used to determine the stiffness of pavement structures. It measures the deflection of a pavement subjected to an impact loading. Corresponding backcalculation programs are able to determine the moduli of the different pavement layers, which are input parameters for mechanistic-empirical pavement design. The portable version of the FWD, the light weight deflectometer (LWD), has been increasingly used for QA/QC testing of compacted unbound materials, and several studies have been performed regarding its potential use for asphalt pavement evaluation (Ryden and Mooney 2009, Steinert et al. 2005). Although the surface modulus determined with this device is not an absolute measure of the HMA modulus, but rather a weighted mean modulus of the entire pavement structure and the subgrade (Ullidtz 1987), the LWD can be used to compare the stiffness of different pavement sections.

Wave propagation methods such as ultrasonic pulse velocity (UPV), impact echo (IE), spectral analysis of surface waves (SASW), and multi-channel analysis of surface waves (MASW) have been studied for pavement condition evaluation but not developed to the point of practical implementation. Surface wave based methods are suitable for in-situ testing of pavements since they require access to only one surface of the tested object. These techniques have been integrated in pavement evaluation devices such as the seismic pavement analyzer (SPA) (Nazarian et al. 1993). Jiang (2007) used surface waves with an equal spacing configuration for the evaluation of longitudinal joints. The test was sensitive enough to differentiate between levels of joint quality that were defined as good, fair, or poor.

Asphalt is a visco-elastic material with a dynamic modulus that varies with temperature and frequency. Ultrasonic methods measure high frequency moduli. On the other hand, deflection

devices determine elastic moduli at frequencies similar to the one generated by traffic loads on highways (approximately 25 Hz). Master curves have been developed to model the frequency dependant behaviour of asphalt concrete and compare elastic moduli measured under different temperature and frequency conditions (Barnes and Trottier 2009).

## 1.2. Research Objectives

The primary objective of this research is to determine if LWD and MASW can be used as complementary methods to measure the quality of longitudinal joints. Within the primary objective, the first objective is to investigate the capability of these techniques to detect actual changes in pavement condition across longitudinal joints. The second objective is to determine if the methods provide the necessary level of discrimination to properly rank joints of varying quality.

## 1.3. Research Methodology

The methodology employed to achieve the research objectives can be summarized as follows:

- Study the theory of wave propagation in a medium and understand the relation between wave characteristics and material properties. Review the different signal processing techniques used to analyze the data collected during wave based testing.
- Understand the response of pavements to static and dynamic loadings, which is used to calculate pavement moduli from deflection measurements.
- Review the NDT methods used for material characterization and pavement evaluation. Analyze the limitations and advantages of each technique, and develop an improved method based on the complementary use of deflection and ultrasonic measurements.
- Study the frequency-dependant behaviour of asphalt mixtures and understand how master curves can be used to compare moduli measured at difference loading frequencies.
- Develop a new compaction method for the preparation of asphalt slabs in the laboratory. Calibrate the compaction procedure through the preparation of small asphalt samples and determine a regression model between the air void content and the compaction effort applied to the mixture.
- Prepare an asphalt slab with a joint of medium quality. Perform density measurements on the jointed slab in order to see if the compaction procedure used in the laboratory is able to reproduce typical density gradients observed across longitudinal joints in the field.
- Conduct LWD and MASW tests on asphalt slabs in the laboratory and on actual pavements in the field.

- Determine the effect of longitudinal joints on the surface modulus measured in the field with the LWD. Evaluate the effectiveness of the LWDmod software in backcalculating the modulus of the asphalt layer.
- Identify the effect of material properties (pavement density, elastic modulus) on the characteristics of the waves recorded with the MASW method (velocities, attenuation coefficients).
- Evaluate the variability introduced in the measurements by the different components of the MASW method (source, receivers, coupling system). Develop a testing procedure that provides a quick and reliable measure of the joint quality in the field.
- Compute master curves for the HMA mixes tested in this research. Compare the asphalt moduli measured at different frequencies with the LWD and MASW methods in the field.

## 1.4. Thesis Organization

Chapter 2 begins with an overview of the theory of wave propagation. The characteristics of body, surface and plate waves are discussed. Phenomena related to wave propagation such as reflection, refraction, mode conversion, wave interference and wave attenuation are explained. Then, the response of pavement structures to plate loading tests is studied. The theory of a linear elastic half space and a layered media are described.

Chapter 3 provides a review of the signal processing techniques used to analyze the data collected during non-destructive tests. The analysis is performed in both time and frequency domains. Wave velocities are determined from time signals. The frequency content is calculated through the Fourier Transform. Other transformations such as the short time Fourier Transform and wavelet transform are used to investigate the variation of signal characteristics with respect to both time and frequency.

Chapter 4 presents different non-destructive techniques used for the structural evaluation of pavement structures. Deflection methods include static, vibratory and impulse methods. Ultrasonic methods use either body waves (UPV, IE) or surface waves (SASW and MASW). Wave attenuation is evaluated by the Fourier transmission coefficient (FTC) or the wavelet transmission coefficient (WTC).

Chapter 5 describes the temperature and frequency dependant behaviour of asphalt mixtures. The time-temperature superposition principle used to develop dynamic modulus master curves is explained.

Chapter 6 starts with a description of the experimental program followed in this research. The different steps that lead to the fabrication of asphalt slabs with joints in the middle are presented. Particular attention is given to the description of the compaction procedure, which was calibrated in the laboratory to ensure that the desired densities were achieved. The experimental setups used in this research for LWD and MASW testing are described at the end of the chapter.

Chapter 7 begins with a description of the MASW tests performed in the laboratory on the fabricated asphalt slabs. Different processing techniques are used to determine if the propagation of surface waves is affected by the presence of a joint. The analysis of LWD and MASW field data collected at two different sites is presented.

Finally, the conclusions and recommendations of this work are summarized in Chapter 8.

# CHAPTER 2. THEORETICAL BACKGROUND

## 2.1. Introduction

The techniques used in this study to assess the condition of longitudinal joints are based on the measurement of wave characteristics or pavement deflection. This chapter starts, in Section 2.2, with an overview of the theory of wave propagation that is used to understand the results obtained from ultrasonic testing. A description of the methods used to calculate the pavement response to plate loading tests is provided in Section 2.3.

## 2.2. Theory of Wave Propagation

When a deformation is created in a medium, particles start to oscillate at the excited point: a mechanical wave is generated. The elasticity of the medium acts as a restoring force: each oscillating particle tends to return to its equilibrium position, while neighbourhood particles start to oscillate. Combined with inertia of the particles, this elasticity leads to the propagation of the wave. The maximum distance reached by the particles from their equilibrium position is defined as the amplitude of the wave. Other properties of a wave are wavelength ($\lambda$), frequency (f) and velocity (V) which are related through the equation:

$$V = \lambda \times f \tag{2-1}$$

A wave can be also characterized by its time period and wave number, which are defined by:

$$T = 1/f$$
$$k = 2\pi/\lambda \tag{2-2}$$

### 2.2.1. Modes of Propagation

Wave propagation can be characterized by oscillatory patterns, which are called wave modes. Three wave modes are often used in ultrasonic inspections: body waves, surface waves and plate waves. Body waves propagate in the radial direction outward from the source. Surface and plate waves appear at surfaces and interfaces.

#### 2.2.1.1. Body Waves

Body waves can be compression or shear waves. Compression waves, also called longitudinal waves, travel with particle vibrations parallel to the direction of propagation, as illustrated in

Figure 2-1. They can travel through any type of material (solid, liquid and gas). In solids, these waves are the fastest among other modes, thus they are also called primary waves (P-waves).

Shear waves, also called transverse waves, propagate with particle vibrations perpendicular to the direction of propagation (Figure 2-1). Shear waves appear only in solids, because fluids do not support shear stresses. They are also known as secondary waves (S-waves) because they travel at a lower speed than P-waves. In opposition to P-wave, the volume of an element does not change during the propagation of S-waves, thus the volumetric strain is equal to zero.

Wave velocity will refer to group velocity which is the speed of energy and information propagation. As it will be demonstrated in this section, wave velocity can be used to determine material properties, such as stiffness, elasticity or density. In an isotropic infinite elastic solid, Newton's second law leads to the equation of motion, with indicial notation (Wasley 1973):

$$\rho \frac{\partial^2 u_i}{\partial t^2} = \frac{\partial \sigma_{i,j}}{\partial x_j} \qquad \left( i, j \in [1;3]^2 \right) \tag{2-3}$$

where $x(x_1, x_2, x_3)$ is a Cartesian coordinate system, $u(u_1, u_2, u_3)$ is the displacement, $\rho$ is the density and $\sigma_{i,j}$ are the stress components.

According to Hook's law, stresses can be expressed as a linear combination of strains:

$$\sigma_{i,j} = \lambda \cdot \Delta \cdot \delta_{i,j} + 2 \cdot \mu \cdot \varepsilon_{i,j} \tag{2-4}$$

where $\varepsilon_{i,j}$ are the strain components, $\lambda$ is the Lamé's elastic constant, $\mu$ is the shear modulus, $\Delta = \varepsilon_{i,i}$ is the volumetric strain, and $\delta_{i,j}$ the Kronecker's symbol which is equal to 1 if $i = j$, and 0 otherwise.

The strain is related to the displacement through the following equations:

$$\varepsilon_{i,j} = \frac{1}{2}\left( \frac{\partial u_i}{\partial x_j} + \frac{\partial u_j}{\partial x_i} \right) \tag{2-5}$$

By substituting equations ( 2-4 ) and ( 2-5 ) into equation ( 2-3 ), the wave equation becomes:

$$\rho \frac{\partial^2 u_i}{\partial t^2} = (\lambda + \mu)\frac{\partial \Delta}{\partial x_i} + \mu \frac{\partial^2 u_i}{\partial x_j \partial x_j} \tag{2-6}$$

Wasley (1973) splits up the displacements into two parts: a longitudinal part having zero rotation and a transverse part having zero dilatation. If the dilatation is zero, which corresponds to S-waves, the equation becomes:

$$\rho \frac{\partial^2 u_i}{\partial t^2} = \mu \frac{\partial^2 u_i}{\partial x_j \partial x_j} \qquad (2\text{-}7)$$

which is the equation of a wave travelling with the velocity:

$$V_S = \sqrt{\frac{\mu}{\rho}} \qquad (2\text{-}8)$$

In the case of a longitudinal part having zero rotation, which correspond to P-waves, the displacement is derivable from a scalar potential function and the equation ( 2-6 ) becomes:

$$\rho \frac{\partial^2 u_i}{\partial t^2} = (\lambda + 2 \cdot \mu) \frac{\partial^2 u_i}{\partial x_j \partial x_j} \qquad (2\text{-}9)$$

which is the equation of a wave travelling with the velocity:

$$V_P = \sqrt{\frac{\lambda + 2 \cdot \mu}{\rho}} = \sqrt{\frac{M}{\rho}} \qquad (2\text{-}10)$$

where M is the constraint modulus.

These expressions of $V_P$ and $V_S$ confirm that P-waves travel at a higher speed than S-waves. Shear and constraint modulus are defined in terms of Young's modulus E and Poisson's ratio $\upsilon$ as:

$$\mu = \frac{E}{2(1 + \upsilon)} \qquad (2\text{-}11)$$

$$M = \frac{(1 - \upsilon)E}{(1 + \upsilon)(1 - 2 \cdot \upsilon)} \qquad (2\text{-}12)$$

The Poisson's ratio $\upsilon$ is defined by:

$$\upsilon = -\frac{\varepsilon_{transverse}}{\varepsilon_{longitudinal}} \qquad (2\text{-}13)$$

where $\varepsilon_{transverse}$ and $\varepsilon_{longitudinal}$ are respectively the transverse and longitudinal strains of a material being stretched.

In conclusion, P-wave and S-wave velocities are functions of material properties such as elastic modulus, density or Poisson's ratio. This is why their measurement is very useful for ultrasonic testing. For example, using equations ( 2-8 ), ( 2-10 ), ( 2-11 ) and ( 2-12 ), the Poisson's ratio can be obtained from the body wave velocities:

$$\upsilon = \frac{2(V_S / V_P)^2 - 1}{2((V_S / V_P)^2 - 1)} \qquad (2\text{-}14)$$

2.2.1.2.    Surface Waves

A surface wave is a mechanical wave that propagates along the interface between different media. There are two major surface waves: Rayleigh and Love waves. Rayleigh waves (R-waves), first discovered by Rayleigh (Rayleigh 1885), travel with surface particles moving in an ellipse which major axis is perpendicular to the direction of propagation, as illustrated in Figure 2-2. R-wave ground penetration is approximately equal to one wavelength. For material characterization, a penetration depth of approximately one third of the wavelength is effective.

Love waves propagate with particles moving in the plane of the surface, perpendicularly to the direction of propagation (Figure 2-2). They were first studied by A.E.H Love (Love 1911). However, they are not considered in ultrasonic testing because they have an upper frequency limit of a few thousand hertz.

Surface waves are confined to the surface, thus their attenuation is considerably less than that of body waves. This point will be developed at the end of this chapter.

The R-wave velocity ($V_R$) is constant in a homogeneous half-space. A good approximation is given by the following equation (Achenbach 1973):

$$V_R = \frac{0.862 + 1.14\upsilon}{1 + \upsilon} V_S \qquad (\,2\text{-}15\,)$$

As the Poisson's ratio $\upsilon$ varies form 0 to 0.5, the R-wave velocity increases from $0.862 \times V_S$ to $0.955 \times V_S$. For practical purposes, it can be expressed approximately as (Blitz and Simpson 1996):

$$V_R = 0.9 \cdot V_S \qquad (\,2\text{-}16\,)$$

Therefore, surface wave velocity is smaller than body wave velocity. We can draw an interesting conclusion for seismic applications: with higher velocity and lower amplitude than S-waves and surface waves, P-waves can be used as earthquake warning.

In a layered medium, $V_R$ depends not only on the material properties, but also on the frequency of excitation. High frequencies propagate at a velocity determined by the material properties of shallow layers, whereas low frequencies propagate at a velocity affected by the characteristic of deeper layers (Figure 2-3). Two different velocities have to be considered: the group velocity, characterizing the energy propagation, and the phase velocity. They are defined by the following equations:

$$V_{gr} = \frac{d\omega}{dk} \qquad\qquad (\,2\text{-}17\,)$$

$$V_{ph} = \frac{\omega}{k} \qquad\qquad (\,2\text{-}18\,)$$

where $\omega = 2\pi f$ is the circular frequency, and $k$ is the wave number.

The group velocity is always constant. In a homogeneous material, the phase velocity is also constant, equal to the group velocity; whereas, in an inhomogeneous medium, the phase velocity varies with frequency. This phenomenon, called dispersion, is used to determine the properties of layered systems, such as elastic modulus or layer thickness.


2.2.1.3.    Plate Waves

In a slab having a thickness of the order of the wavelength or so, surface waves interact with boundaries and generate plate or Lamb waves. According to Lamb (Lamb 1917), who first studied this phenomenon, the particle motion lies in the plane defined by the plate normal and the direction of wave propagation. Lamb waves can propagate in a number of modes, either symmetric or anti-symmetric, as illustrated by Figure 2-4.

The velocity of Lamb waves varies with frequency, and each mode has its own dispersion curve. Figure 2-5 shows an example of dispersion curves of Lamb wave modes for a typical HMA plate, assumed to be homogeneous and isotropic. The calculation was performed in MathCAD, using a program developed by Yanjun Yang at the University of Waterloo (Yang 2009). Three parameters are given for the calculation: P-wave velocity $V_P = 3500$ m/s, R-wave velocity $V_R = 1700$ m/s, and half the plate thickness $h = 45$ mm. Both symmetric and anti-symmetric fundamental modes (S0, A0) and higher modes (S1, A1, S2, A2…) are presented in the figure.

At frequencies high enough to have wavelengths smaller than the thickness of the plate, waves does not interact with the inferior boundary. Thus, they propagate in the same way as in a homogeneous half-space, characterized by a constant R-wave velocity. That is why Lamb wave modes tend toward a constant velocity at high frequencies, which is a good approximation of the Rayleigh wave velocity. In Figure 2-5, it is noticed that the fundamental modes A0 and S0 converge to $V_R$ at frequencies larger than 36 kHz, or wavelengths shorter than 47 mm which is close to half the plate thickness.

11

The Lamb wave propagation can be described by the Rayleigh-Lamb frequency equation (Graff 1975):

$$\frac{\tan(\beta \cdot b)}{\tan(\alpha \cdot b)} + \left(\frac{4 \cdot \alpha \cdot \beta \cdot k^2}{\left(k^2 - \beta^2\right)^2}\right)^{\pm 1} = 0 \qquad \begin{array}{l} +1 = \text{symmetric} \\ -1 = \text{anti-symmetric} \end{array} \qquad (\,2\text{-}19\,)$$

where $\alpha$ and $\beta$ are defined by:

$$\alpha^2 = \frac{\omega^2}{V_P^{\,2}} - k^2, \ \beta^2 = \frac{\omega^2}{V_S^{\,2}} - k^2 \qquad (\,2\text{-}20\,)$$

and $k = \omega/V_{ph}$ is the wave number, $V_{ph}$ is the phase velocity of Lamb waves, $\omega$ is the angular frequency, b is half the thickness of the plate, $V_P$ and $V_S$ are the P and S-wave velocities.

## 2.2.2. Physical Phenomena of Wave Propagation

In a layered or inhomogeneous medium, additional phenomena affect the wave propagation such as reflection, mode conversion and interference. These phenomena, which are not considered in theoretical models, have to be understood so that their impact on test results can be minimized.

### 2.2.2.1. Acoustic Impedance

The acoustic impedance (Z) of a material is defined as the product of its density ($\rho$) and acoustic velocity (V) (Achenbach 1973).

$$Z = \rho \cdot V \qquad (\,2\text{-}21\,)$$

This impedance, which is an acoustic characterization of the material, is very useful to explain phenomena such as reflection and transmission. Table 2-1 lists typical acoustic impedance values for various construction materials.

### 2.2.2.2. Reflection and Transmission

When an oblique incident wave passes through an interface between two materials, reflected and transmitted (refracted) waves are produced (Figure 2-6). These phenomena appear when there is an impedance mismatch between the two materials on each side of the boundary. If we consider two media with impedances $Z_1$ and $Z_2$, the fraction of the incident wave intensity that is reflected is given by the following equation (Blitz and Simpson 1996):

$$R = \left(\frac{Z_2 - Z_1}{Z_2 + Z_1}\right)^2 \qquad (\,2\text{-}22\,)$$

The greater the impedance mismatch, the greater the percentage of energy that will be reflected at the interface. Since energy is conserved, the transmission coefficient is calculated by subtracting the reflection coefficient from unity:

$$T = 1 - R = \frac{4 \cdot Z_1 \cdot Z_2}{(Z_1 + Z_2)^2}$$

( 2-23 )

According to Snell's law, incident and reflection angles ($\theta_i$ and $\theta_r$) are identical for the same type of wave. The refraction angle ($\theta_t$) is related to the incident angle through the equation:

$$\frac{\sin\theta_i}{V_1} = \frac{\sin\theta_t}{V_2}$$

( 2-24 )

where $V_1$ is the velocity of the medium in which the incident wave is travelling, and $V_2$ is the velocity of the medium in which the refracted wave is propagating.

### 2.2.2.3.    Mode Conversion

Mode conversion, which occurs when an oblique wave encounters an interface between materials of different acoustic impedances, is the transformation of one wave mode into another. For example, when a longitudinal wave hits an interface and one or both of the material supports a shear stress, a particle movement appears in the transverse direction and a shear wave is produced (Figure 2-7). Velocities and angles of the waves follow the Snell's law:

$$\frac{\sin\theta_1}{V_{L_1}} = \frac{\sin\theta_2}{V_{L_2}} = \frac{\sin\theta_3}{V_{S_1}} = \frac{\sin\theta_4}{V_{S_2}}$$

( 2-25 )

where $V_L$ is a longitudinal wave velocity, $V_S$ is a shear wave velocity and $\theta_1$, $\theta_2$, $\theta_3$ and $\theta_4$ are the incident, reflection and refraction angles indicated in Figure 2-7.

As P-waves are faster than S-waves, $\theta_1 > \theta_3$ and $\theta_2 > \theta_4$. This phenomenon, enabling different wave modes to propagate in different directions, can cause imprecision in NDT measurements. A solution to avoid this uncertainty consists of increasing the angle of incidence (Blitz and Simpson 1996). Consider two media: 1 is a fluid and 2 a solid, with $V_{L1}$ being inferior to both $V_{L2}$ and $V_{S2}$. According to equation ( 2-25 ): $\theta_2 > \theta_4 > \theta_1$. Thus, there is a critical value of $\theta_1$ at which $\theta_2$ is equal to 90°. As illustrated in Figure 2-8, for angles of incidence greater than this critical angle, only shear waves enter medium 2. If $\theta_1$ is further increased, no waves are transmitted to medium 2, and only P-waves are reflected.

2.2.2.4.    Interference

Interference is the addition of two or more waves that result in a new wave pattern. When waves are travelling along the same path, they superimpose on each other. The amplitude of particle displacement at any point of the interaction is the sum of the amplitudes of the two individual waves.

This phenomenon is illustrated in Figure 2-9, which shows two sinusoidal signals generated at the same point, with the same frequency. If they are in phase, the amplitude is doubled. This phenomenon is called constructive interference. If they are out of phase, the signals combine to cancel each other out, and the interference is destructive. When the origins of the two interacting waves are not the same, it is harder to picture the wave interaction, but the principle is the same. Interference between different wave modes can cause uncertainty in signal analysis.

## 2.2.3.    Wave Attenuation

When a wave travels through a medium, its intensity diminishes with distance. The decay rate of the wave, called attenuation, depends on the material properties. Therefore, its evaluation can be used for material characterization. Three phenomena are responsible for wave attenuation. First, reflection, refraction, and mode conversion deviate the energy from the original wave beam. Then, absorption converts part of the wave energy into heat. Finally, the wavefront spread leads to energy loss.

2.2.3.1.    Geometric Attenuation

In idealized materials, signal amplitude is only reduced by the spreading of the wave. When a wave propagates away from the source, its energy is conserved and spread out over an increasing area. Thus the wave amplitude decreases, which is called geometric attenuation. The geometric attenuation of body waves propagating in an infinite elastic body is proportional to $1/r$ because their wavefront is a sphere. For surface waves, it is proportional to $1/\sqrt{r}$ because they propagate in a cylinder confined to the surface of the medium. The general equation of geometric attenuation is (Nasseri-Moghaddam 2006):

$$\frac{A_2}{A_1} = \left( \frac{R_2}{R_1} \right)^{-\beta} \tag{2-26}$$

where $A_1$ and $A_2$ are the amplitude at the distance $R_1$ and $R_2$ from the source, and $\beta$ is the geometric attenuation coefficient which depends on the wavefront shape. For example, this coefficient is equal to 0.5 for surface waves.

2.2.3.2.    Material Attenuation

This type of attenuation is composed of scattering and absorption. Absorption is the result of particle vibration which causes friction. The wave energy is converted into heat. Low frequencies generate slower oscillations than high frequencies, thus they are less attenuated and penetrate deeper in a material.

Scattering is the reflection of the wave in directions other than its original direction of propagation. It appears in inhomogeneous materials containing grains with dimension comparable to the wavelength. At each grain boundaries, there is a change in impedance which results to the wave reflection and refraction in random directions. The scattered energy is lost from the incident beam which results in attenuation.

The decrease in amplitude caused by material attenuation is (Nasseri-Moghaddam 2006):

$$\frac{A_2}{A_1} = e^{-\alpha(R_2 - R_1)} \qquad ( 2\text{-}27 )$$

where $A_1$ and $A_2$ are the amplitude at the distance $R_1$ and $R_2$ from the source and $\alpha$ is the attenuation coefficient of the wave travelling in the z-direction. This coefficient depends on material properties and the frequency.

Finally, the combination of both geometrical and material attenuations leads to the equation:

$$\frac{A_2}{A_1} = \left(\frac{R_2}{R_1}\right)^{-\beta} e^{-\alpha(R_2 - R_1)} \qquad ( 2\text{-}28 )$$

Attenuation can be also characterized by the damping ratio, which is defined as the amplitude attenuation per cycle.

$$\xi = \frac{1}{\Delta\varphi} \ln\left(\frac{A_i}{A_{i+n}}\right) \qquad ( 2\text{-}29 )$$

where $A_i$ is the maximum amplitude for the cycle of oscillation i, and $\Delta\varphi$ is the phase shift between the two measurements. An example of damping ratio calculation is provided in Figure 2-10.

**2.2.4.    Flaw Detection**

Ultrasonic testing consists of analyzing signals propagating in a medium. To detect a flaw, an appropriate wavelength has to be selected. If the inspector wants to have a good chance to detect

a discontinuity, the wavelength of the signal sent throughout the medium should be less than double the size of the discontinuity. The ability to detect a flaw is characterized by two terms:

- The sensibility, which corresponds to the technique's ability to detect small flaws
- The resolution, which is the ability to distinguish discontinuities that are close together.

Thus, the higher the frequency of the signal, the better are the sensitivity and resolution of an ultrasonic testing method. Nevertheless, increasing the frequency can have adverse effects. The scattering from large grain structure and small imperfections within a material increases with frequency. Therefore, material attenuation increases and the penetration of the wave is reduced. The maximum depth at which flaws can be detected is also reduced.

Consequently, selecting an optimal frequency for ultrasonic testing requires a balance between the favourable and unfavourable effects described previously.

## 2.3. Pavement Response and Plate Loading Tests

Calculating the pavement response consists of determining the stresses, strains or deflections in the pavement structure caused by wheel loading. The most widespread theory used for this calculation is the theory of elasticity. The simplest version of this theory is based on two parameters: the Young's modulus E and the Poisson's ratio $\upsilon$. According to Hook's law, the Young's modulus is a constant. In the simple case of the elastic theory, the Poisson's ratio is also a constant. When applying the elastic theory, one must remember that neither of these parameters is constant in real pavement materials. They depend on factors such as temperature, moisture content, stress conditions and frequency of loading (Ullidtz 1987). The moduli of pavement materials such as asphalt or subgrade soils are complex numbers; and whenever the term "elastic modulus" will be used in this thesis, it will refer to the absolute value of the complex modulus.

This section starts describing the response of pavements to static loads. The cases of a linear elastic semi-infinite space and a layered system are explained. Some deviations from the classical theory are presented. Finally, the response of pavements to dynamic loading is briefly studied, in order to identify the difference with static loading conditions.

### 2.3.1. Linear Elastic Half-Space

In 1885, Boussinesq determined equations to calculate the stresses, strains and deflections of a homogeneous, isotropic, linear elastic half-space under a point load (Boussinesq 1885). In the

case of load distributed over a certain area, the stresses, strains and displacements can be obtained by integration from the point load solution.

### 2.3.1.1. Uniformly Distributed Circular Load

At the centreline of a load uniformly distributed over a circular area, the integration can be carried out analytically. The equations for the vertical stress ($\sigma_z$) and the vertical displacement ($d_z$) reduce respectively to (Ullidtz 1987; Craig 1997):

$$\sigma_z = \sigma_0 \left[ 1 - \left( \frac{1}{1 + (a/z)^2} \right)^{3/2} \right] \qquad (\,2\text{-}30\,)$$

$$d_z = (1 + \upsilon) \sigma_0 \frac{a}{E} \left( \sqrt{\frac{1}{1 + (z/a)^2}} + (1 - 2\upsilon) \left( \sqrt{1 + \left( \frac{z}{a} \right)^2} - \frac{z}{a} \right) \right) \qquad (\,2\text{-}31\,)$$

where z is the depth below the surface, $\sigma_0$ is the normal stress on the surface, a is the radius of the loaded area, E is the Young's modulus and $\upsilon$ is the Poisson's ratio.

The variation with depth of the vertical stress and deflection at the centreline of a uniformly distributed circular load are presented in Figure 2-11 and Figure 2-12.

### 2.3.1.2. Rigid Circular Plate Loading

If the loading plate is rigid, the surface displacement will be the same across the area of the plate. The contact pressure ($\sigma_0(r)$) under the rigid area is not uniform, and may be expressed by (Ullidtz 1987):

$$\sigma_0(r) = \frac{1}{2} \sigma_0 \frac{a}{\sqrt{a^2 - r^2}} \qquad (\,2\text{-}32\,)$$

where $\sigma_0$ is the mean value of the stress, a is the plate radius and r is the distance from the centre of the plate.

The variation of the stress under the plate with distance from the centre is shown in Figure 2-13. Infinite stresses are observed at the edges of the plate. For this loading condition, the following equations are obtained:

$$\sigma_z = \frac{1}{2} \sigma_0 \frac{1 + 3(z/a)^2}{\left( 1 + (z/a)^2 \right)^2} \qquad (\,2\text{-}33\,)$$

$$d_z = (1 + \upsilon) \sigma_0 \frac{a}{2E} \left( (1 - \upsilon) \left( \pi - 2 \cdot \arctan\left( \frac{z}{a} \right) \right) + \frac{z/a}{1 + (z/a)^2} \right) \qquad (\,2\text{-}34\,)$$

17

where z is the depth below the surface, $\sigma_0$ is the mean value of the stress on the surface, a is the radius of the loaded area, E is the Young's modulus and $\upsilon$ is the Poisson's ratio.

The vertical stress and deflection at the centreline of a rigid circular plate are given in Figure 2-11 and Figure 2-12.

### 2.3.1.3.    Surface Modulus

At the surface of the half-space, equations ( 2-31 ) and ( 2-34 ) reduces to (Steinert et al. 2005):

$$d_0 = \frac{f \cdot (1 - \upsilon^2) \cdot \sigma_0 \cdot a}{E_0} \qquad\qquad (\,2\text{-}35\,)$$

where $d_0$ is the centre deflection, $\sigma_0$ is the mean value of the stress on the surface, a is the radius of the loaded area, $E_0$ is the Young's modulus, $\upsilon$ is the Poisson's ratio and f is a factor that depends on the stress distribution:

- Uniform:    f = 2
- Rigid plate: f = π/2

This equation can be used to determine the elastic modulus ($E_0$) of the semi-infinite space at the centre of the loaded area. Since $E_0$ is calculated from the deflection measured at the surface of the half-space, it is termed the surface modulus. As mentioned in the introduction, asphalt pavements are not purely elastic. Therefore, the surface modulus of a pavement structure, defined by the previous equation, is not the elastic modulus of the pavement, but rather the equivalent Young's modulus of the structure, assuming the medium is elastic. Ullidtz (1987) proposed the following definition of the surface modulus: it "is the "weighted mean modulus" of the half space calculated from the surface deflection using Boussinesq's equations".

Unfortunately, the uniform and rigid plate distributions are never found on actual soils. When assuming a parabolic distribution, the stress distribution factors are 8/3 and 4/3 for granular and cohesive materials respectively. The shape of the stress distributions are shown in Figure 2-14. Consequently, if both the stress distribution and the Poisson's ratio of the material are unknown, the factor $f(1\text{-}\upsilon^2)$ varies from 1 to 8/3. In order to avoid the imprecision due to an unknown stress distribution, one must measure the deflection at different distances from the centre of the load. According to Ullidtz (1987), for distances larger than twice the radius of the plate, the distributed load can be treated as a point load. In this case, the surface modulus E(r) is obtained from Boussinesq equations (Steinert et al. 2005):

$$E(r) = \frac{(1-\upsilon^2) \cdot P}{\pi \cdot r \cdot d_0(r)}$$

( 2-36 )

where P is the impact force, $\upsilon$ is the Poisson's ratio, and $d_0(r)$ is the surface deflection at the distance r from the centre of the load.

The uncertainty on the surface modulus is reduced to the term containing the Poisson's ratio, $(1-\upsilon^2)$, which ranges from 0.75 to 1. Moreover, measuring the deflection at different distances from the centre allows checking if the soil is a linear elastic half-space. If the moduli calculated at different distances are not the same, then the soil is either non-linear elastic or composed of several layers.

### 2.3.1.4.    Measurement Depth of Plate Loading Tests

The measurement depth of a plate loading test is defined in this study as the depth where the vertical stress is equal to $0.1 \times \sigma_0$. Equation ( 2-30 ) gives a measurement depth of $3.71 \times a$ for a uniformly distributed circular load, where *a* is the radius of the plate. Equation ( 2-33 ) gives a measurement depth of $3.65 \times a$ for a rigid plate loading.

Some studies used in-ground instrumentation such as earth pressure cells and linear voltage displacement transducers to determine the actual measurement depth in soils. Mooney and Miller (2009) used the theoretical $\sigma_z$ and $\varepsilon_z$ peak distributions that matched measured values to assess the depth of influence. By evaluating the area under the theoretical $\sigma_z$ peak response and using 80% area as the measurement depth criteria, they found measurement depths of $4.0 \times a$ on clay soil and $2.4 \times a$ on sand. The analysis of in situ strain data suggested that measurement depth are approximately $2.0 \times a$ when using a 95% strain cut-off criteria. As LWD measurements give a deformation modulus, it was assumed that the strain-based method was more appropriate to estimate the measurement depth.

### 2.3.2.    Layered Systems

A number of programs have been developed to determine stresses and displacements in a layered system. When using those programs, one must keep in mind that they are not exact, as they are based on simplified assumptions. Pavement materials are neither linear elastic nor homogeneous. The following sections present an approximate method that has the advantage of being very simple, and can easily include non-linear materials. This is very important for pavement evaluation, as many subgrade materials are highly non-linear.

### 2.3.2.1.    Odemark's Method

This method consists of transforming a layered system with different moduli into an equivalent system where all layers have the same modulus, and on which Boussinesq's equations can be used. It is also called the Method of Equivalent Thicknesses (MET). It is based on two transformations, illustrated in Figure 2-15 (Ullidtz 1987):

(a) When calculating the stresses or strains above an interface, the layered system is treated as a half-space with the modulus and Poisson's ratio of the top layer.

(b) When calculating the stresses or strains below an interface, the top layer is transformed to an equivalent layer with the modulus and Poisson's ratio of the bottom layer, and the same stiffness as the original layer.

The stiffness of a layer is defined by:

$$\frac{I \times E}{1 - \upsilon^2} \tag{2-37}$$

where I is the moment of inertia, E the Young's modulus, and $\upsilon$ the Poisson's ratio.

I is proportional to the cube of the layer thickness. Therefore, the stiffness of the top layer remains the same if:

$$\frac{h_e^3 \times E_2}{1 - \upsilon_2^2} = \frac{h_1^3 \times E_1}{1 - \upsilon_1^2}$$

$$h_e = h_1 \left( \frac{E_1}{E_2} \times \frac{1 - \upsilon_2^2}{1 - \upsilon_1^2} \right)^{1/3} \tag{2-38}$$

where $h_1$ is the original thickness of the top layer, $h_e$ is the equivalent thickness, $E_1$ and $E_2$ are the moduli of the top and bottom layer respectively, $\upsilon_1$ and $\upsilon_2$ are the Poisson's ratios of the layers.

### 2.3.2.2.    Correction Factor

The MET is an approximate method. A better agreement with the elastic theory is obtained by applying an adjustment factor to the equivalent thickness. It does not necessarily provide a better agreement with the actual stresses and strains in the pavement. Usually, the Poisson's ratios of all pavement materials are assumed to be the same, and equal to 0.35 (NCHRP 1-37A 2004). In this case, the equivalent thickness is expressed by (Ullidtz 1987):

$$h_e = f \times h_1 \left( \frac{E_1}{E_2} \right)^{1/3} \tag{2-39}$$

where f is the correction factor, $h_1$ is the original thickness of the top layer, $h_e$ is the equivalent thickness, $E_1$ and $E_2$ are the moduli of the top and bottom layer respectively.

This equation can be applied to determine the equivalent thicknesses of multi-layer systems. The equivalent thickness of the upper n-1 layers with respect to the modulus of layer n are calculated using a recursive equation:

$$h_{e,n} = f \times \sum_{i=1}^{n-1} h_i \left( \frac{E_i}{E_n} \right)^{1/3}$$

( 2-40 )

The multi-layer structure is transformed into an equivalent system with a homogeneous modulus equal to the one of the semi-infinite bottom layer. Boussinesq's equations can then be applied to determine the stresses and strains in the equivalent homogeneous system.

### 2.3.3.    Non-linearity

Many subgrade materials are known to be highly non-linear. Asphalt mixes present visco-elasto-plastic properties, as described in Chapter 5. Therefore, the stress-strain response of these materials depends on the stress condition and the stress level. If this phenomenon is neglected, it may result in very large errors when calculating the pavement moduli.

The variation of the modulus with the vertical stress is given by the equation (Ullidtz 1987):

$$E = C \times \left( \frac{\sigma_z}{\sigma'} \right)^n$$

( 2-41 )

where C and n are constants, E is the modulus, $\sigma_z$ is the vertical stress and $\sigma'$ is a reference stress, usually 160 MPa. n is a measure of the non-linearity. It is equal to zero for linear elastic materials, and decreases as the non-linearity becomes more and more pronounced.

According to Ullidtz (1987), the stresses and strains in a non-linear half-space, at the centreline of a circular load, could be calculated using Boussinesq's equations when the modulus is treated as a non-linear function of the principal stress. If the modulus of a non-linear material is expressed by equation ( 2-41 ), a uniformly distributed plate loading test gives a surface modulus ($E_0$) of:

$$E_0 = (1 - 2n) \times C \times \left( \frac{\sigma_0}{\sigma'} \right)^n$$

( 2-42 )

where C and n are constants, $\sigma_0$ is the normal stress at the surface and $\sigma'$ is a reference stress. Odemark's method can be used for a pavement structure having a non-linear subgrade and linear surface layers. The modulus of elasticity of the subgrade must be substituted by the surface modulus ($E_0$) given by the previous equation.

### 2.3.4. Dynamic Loading

Schepers et al. (2009) studied the stresses elicited by time-varying point loads applied onto the surface of an elastic half-space. Isobaric contours were determined for the six stress components at various frequencies corresponding to engineering applications. The objective was to predict the extent of dynamic effects in practical situations in engineering. Pressure bulbs, which are simply contour plots of the stress components with depth, were computed for a nominal S-wave velocity of 100 m/s, which is much lower than the velocity observed in asphalt pavement (values around 1800 m/s were found in this project). The results showed that, at low to moderate frequencies (below 10 Hz), dynamic effects could be neglected. Above this threshold, dynamic effects become important and the stress patterns deviate significantly from the static loading case. Dynamic stresses reach deeper into the soil, which may result in a larger depth of influence for plate loading tests. Also, the stress patterns become more complex because of constructive and destructive interference. According to the authors, the frequency threshold for dynamic effects decreases as the ratio of actual to nominal shear wave velocity decreases. This ratio is approximately 18 for asphalt pavement, thus dynamic effects would appear at much higher frequencies than the threshold of 10 Hz mentioned in the previous paper. As will be demonstrated in Chapter 7, the plate loading tests performed in this research project showed a dominant frequency around 60 Hz. Consequently, dynamic effects were believed to range from negligible to moderate, and it was concluded that a static analysis of the tests should provide reasonable results.

## 2.4. Summary

This chapter describes the different wave modes that propagate in a medium: body waves and surface waves. Wave velocities have been linked to material properties so their measurement can be used for material characterization. Physical phenomena related to wave propagation, such as reflection, refraction, mode conversion and interference are explained so that their impact on experimental result can be recognized. The material and geometric attenuation mechanisms are described.

Then, the pavement response to a static loading is presented. The calculation is explained for a linear elastic half space, and then extended to layered systems. The deviation from the classical theory due to non-linearity is approximated in order to account for the non-linear behaviour of subgrades in pavements. Finally, dynamic effects on generated stress patterns are discussed.
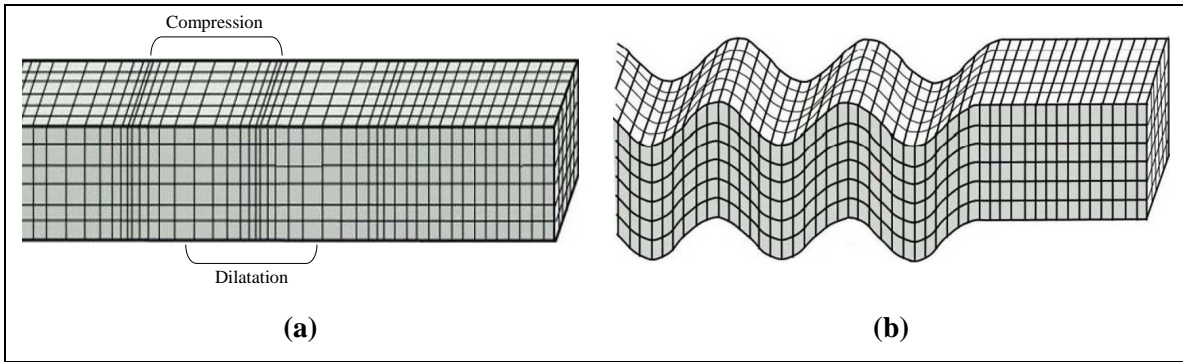
Figure 2-1: Particle motion of (a) P-waves and (b) S-waves

(Yang 2009)
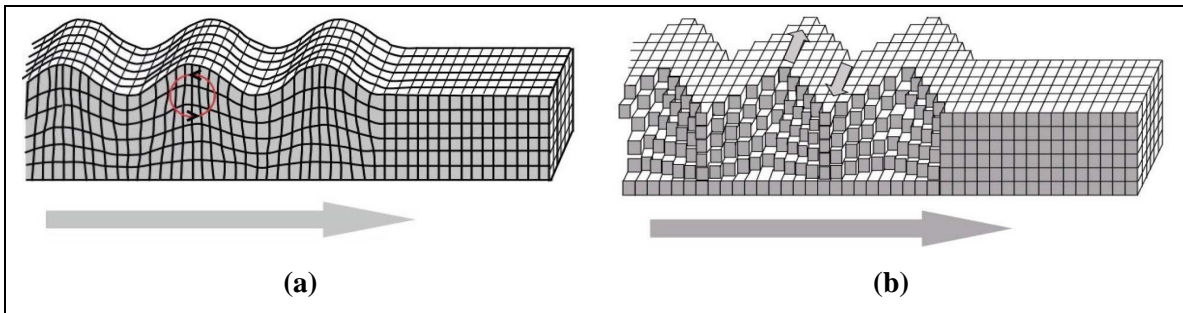


Figure 2-2: Particle motion of (a) Rayleigh waves and (b) Love waves

(Nasseri-Moghaddam 2006)
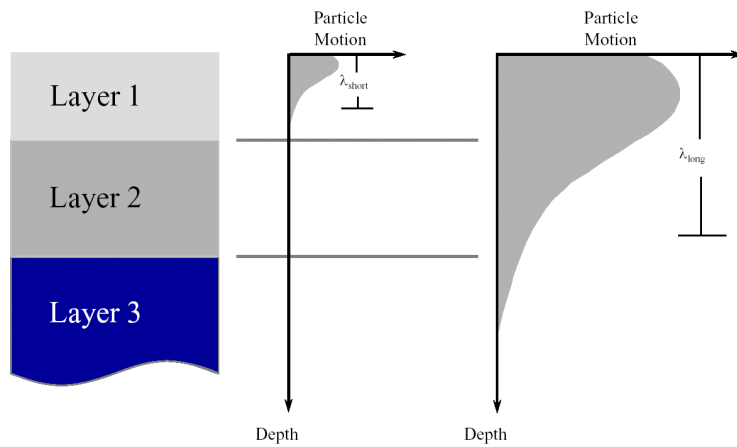


Figure 2-3: Surface waves in a layered medium

(Rix 2000)
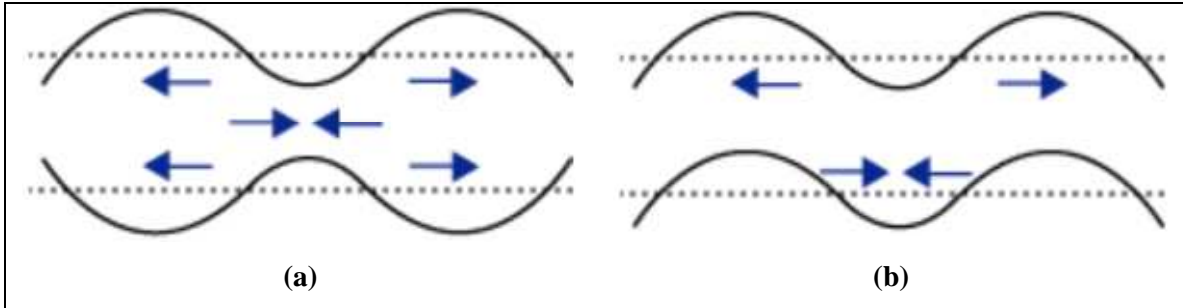
Figure 2-4: (a) Symmetric and (b) anti-symmetric Lamb modes

(NDT Resource Centre 2010)
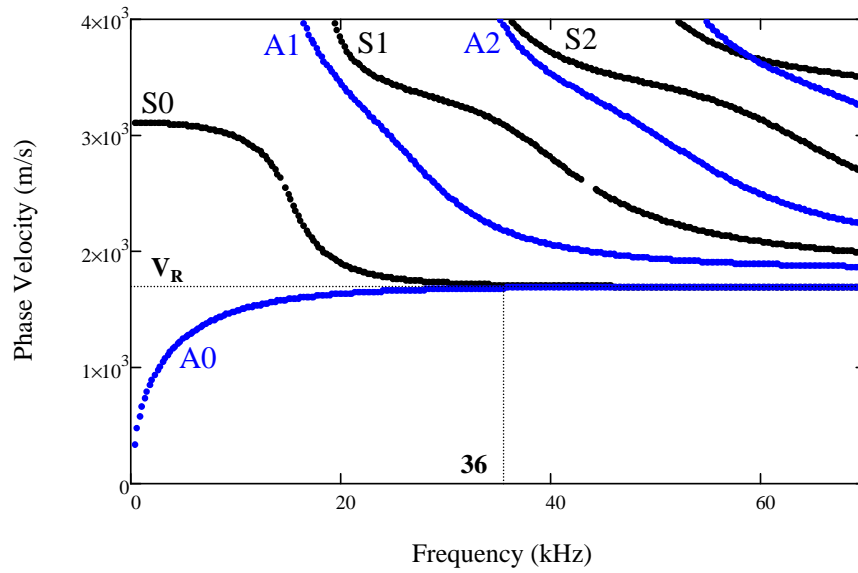


Figure 2-5: Dispersion curves for (a) symmetric and (b) anti-symmetric Lamb modes
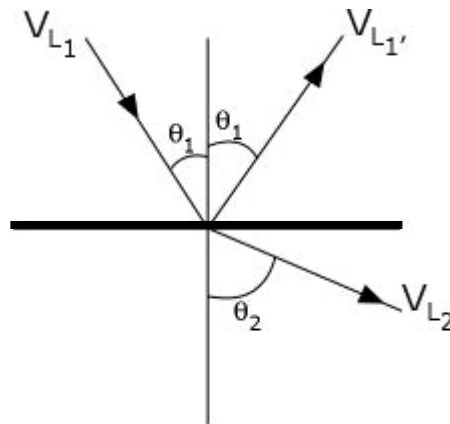


Figure 2-6: Incident, reflected and refracted beams at an interface

(NDT Resource Centre 2010)

24
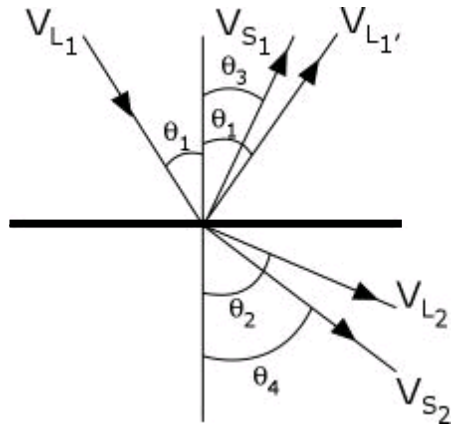
Figure 2-7: Phenomenon of mode conversion

(NDT Resource Centre 2010)
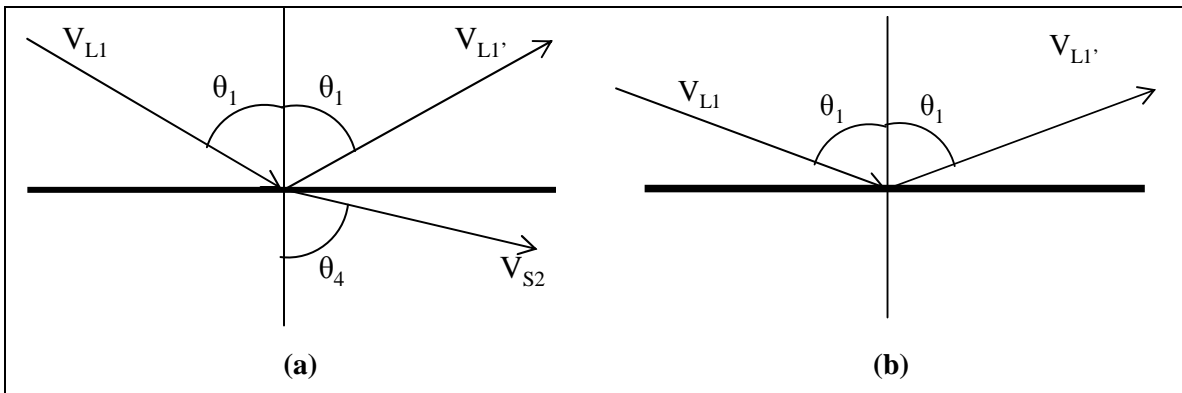


Figure 2-8: Angle of incidence and mode conversion
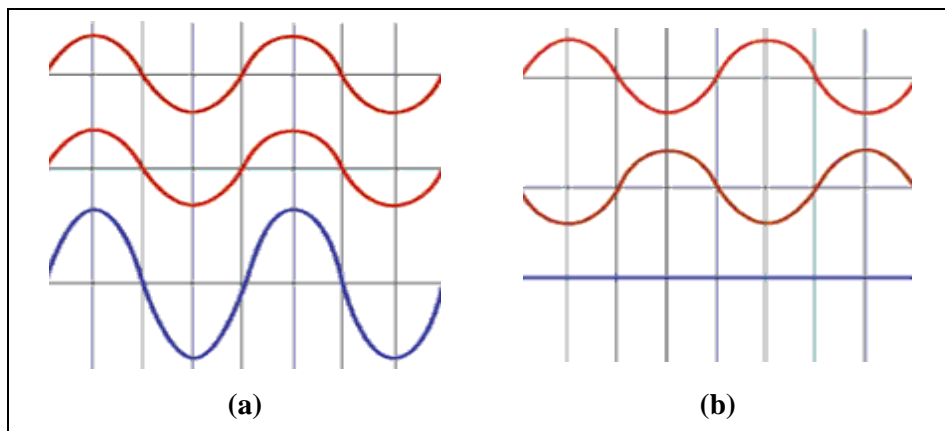


Figure 2-9: Interaction of two sinusoidal signals (a) in phase and (b) out of phase

(NDT Resource Centre 2010)

**Damping Ratio:**

$$\xi = \frac{1}{2\pi} \ln\left(\frac{A_1}{A_2}\right)$$

$A_1$: amplitude of the wave at $t = t_1$

$A_2$: amplitude of the wave at $t = t_2$
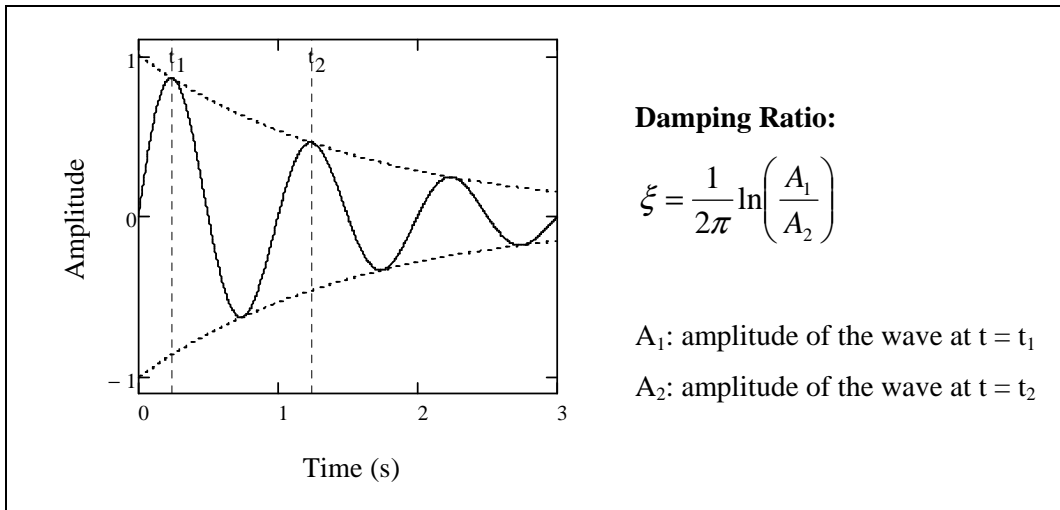
Figure 2-10: Example of material damping ratio calculation
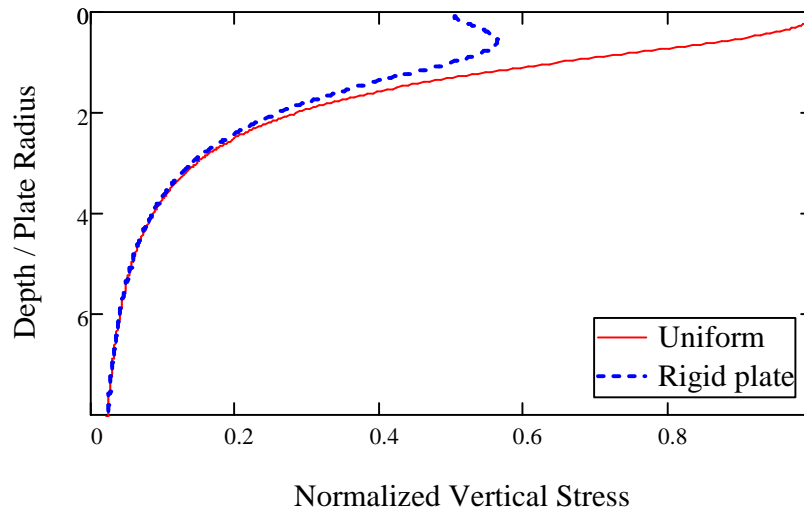


Figure 2-11: Vertical normal stress at the centreline of circular load
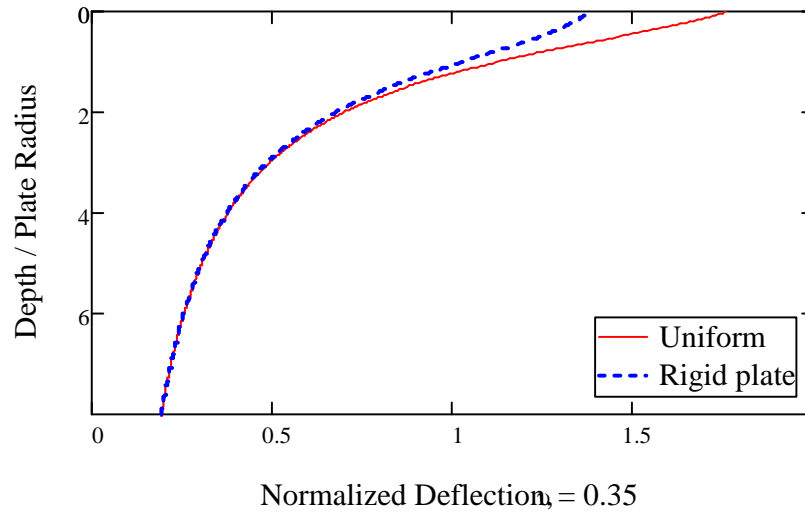
Figure 2-12: Deflection at the centreline of a circular load
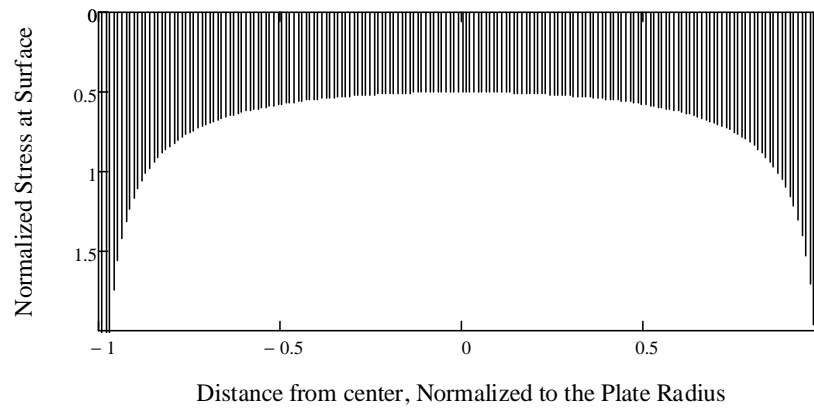


Figure 2-13: Stress distribution under a rigid circular plate
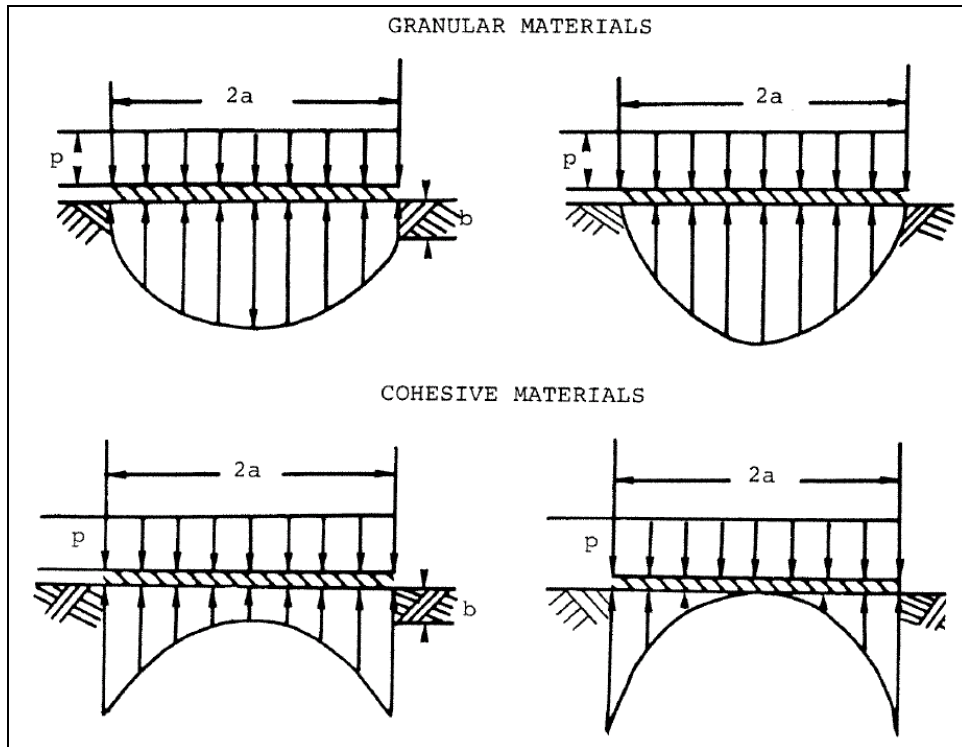
Figure 2-14: Typical stress distributions on granular and cohesive soils

(Ullidtz 1987)
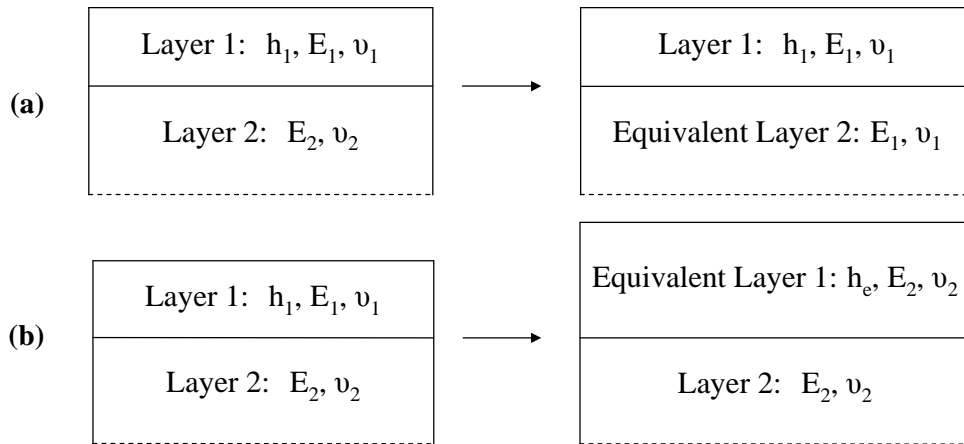


Figure 2-15: Transformations used in the method of equivalent thicknesses

Table 2-1: Acoustic impedance of typical construction materials
(Jiang 2007)

| Material | Acoustic impedance (km/m$^2$s) |
| :---: | :---: |
| Air | $4.1 \times 10^{-1}$ |
| Water | $1.5 \times 10^{6}$ |
| Soil | $(1 \text{ to } 3) \times 10^{6}$ |
| Bitumen | $1 \times 10^{6}$ |
| Asphalt | $5 \times 10^{6}$ |
| Concrete | $(8 \text{ to } 10) \times 10^{6}$ |
| Granite | $(15 \text{ to } 17) \times 10^{6}$ |
| Steel | $4.6 \times 10^{7}$ |

# CHAPTER 3.   SIGNAL PROCESSING TECHNIQUES

## 3.1.  Introduction

Many signal processing techniques are used to analyze the signals measured with nondestructive tests. An observation of these signals in the time domain provides a preliminary assessment of the tested material. As a matter of fact, the variation of the signal amplitude with time gives information such as the first arrival and the following reflections, allowing the calculation of the wave velocities, which are related to the material properties. Nevertheless, much information regarding the frequency content of the signal is not available in the time domain. Several techniques used to perform the frequency analysis and look at the time dependant behaviour of the different frequencies in a signal are described in this chapter.

## 3.2.  Fourier Analysis

If a function repeats periodically with period T, it can be expressed as a sum of sinusoidal terms having circular frequencies $\omega$, $2\omega$ …, where $\omega=2\pi/T$. This is called the decomposition in a Fourier series. If the function is not periodic, it can be expressed as a Fourier integral.

### 3.2.1.   Fourier Series

A periodic function x of period T can be represented by a Fourier series:

$$x(t) = a_0 + \sum_{n=1}^{\infty}\left(a_n\cos(\omega_n t) + b_n\sin(\omega_n t)\right) \tag{3-1}$$

where $\omega_n = n\times 2\pi/T$.

The coefficients of the Fourier series are defined by:

$$a_0 = \frac{1}{T}\int_0^T x(t)dt$$

$$a_n = \frac{2}{T}\int_0^T x(t)\cos(\omega_n t)dt \tag{3-2}$$

$$b_n = \frac{2}{T}\int_0^T x(t)\sin(\omega_n t)dt$$

Euler's formula allows decomposing x into exponential functions with imaginary components:

$$x(t) = \sum_{n=-\infty}^{+\infty} c_n e^{j\omega_n t} \tag{3-3}$$

31

where j is the complex unit.

The $c_n$ coefficients can be calculated directly, or with the previous $a_n$ and $b_n$ coefficients:

$$c_n = \frac{1}{T}\int_0^T x(t)e^{-j\omega_n t}dt \qquad\qquad (3\text{-}4)$$

$$c_n = \frac{a_n + jb_n}{2} \qquad\qquad (3\text{-}5)$$

The frequency content of the periodic function is exposed by plotting the coefficients of the Fourier series versus the frequency. An example spectrum is provided in Figure 3-1.Fourier series can also be used for non-periodic functions, if we are looking at a limited range of the variable. In this case, the limited duration is considered as the period of a periodic function.

### 3.2.2. Fourier Transform

Fourier series are applicable only to periodic functions. However, non-periodic functions can also be decomposed into Fourier components; this process is called a Fourier Transform. If the period T tends to infinity, $\omega_n$ becomes a continuous variable, the coefficient $c_n$ becomes a continuous function of $\omega$, and the summation can be replaced by an integral. The Fourier Transform of a signal x(t) is defined by the following relationship:

$$X(\omega) = \int_{-\infty}^{+\infty} x(t)e^{-j\omega t}dt \qquad\qquad (3\text{-}6)$$

By identifying the similarities between the signal and complex exponential functions, this transformation allows examining the frequency content of a given time signal. It decomposes a non-periodic signal into sinusoidal functions of various frequencies and amplitudes Under suitable conditions, x(t) can be reconstructed from $X(\omega)$ by the inverse Fourier Transform:

$$x(t) = \frac{1}{2\pi}\int_{-\infty}^{+\infty} X(\omega)e^{j\omega t}d\omega \qquad\qquad (3\text{-}7)$$

These representations are all continuous. However, any information stored in computers is discrete. Therefore, it is necessary to define a discrete Fourier Transform to perform the Fourier analysis of discrete time signals.

$$X_k = X(k \times \Delta\omega) = \sum_{n=0}^{N-1} x(n \times \Delta t)e^{-j2\pi\frac{k \times n}{N}}\Delta t \qquad (k = 0, 1\ldots N\text{-}1) \qquad (3\text{-}8)$$

where N is the number of points, k and n are integer counters, $\Delta\omega$ and $\Delta t$ are the circular frequency and time resolutions, related through the equation:

$$\Delta\omega = \frac{2\pi}{N \times \Delta t}$$
( 3-9 )

Using the same notations, the inverse discrete Fourier Transform is defined by:

$$x_n = x(n \times \Delta t) = \frac{1}{2\pi} \sum_{k=0}^{N-1} X(k \times \Delta\omega) e^{-j2\pi\frac{k \times n}{N}} \Delta\omega \qquad (n = 0, 1 \ldots N\text{-}1)$$
( 3-10 )

### 3.2.3. Discretization Effects

As described previously, $X_k$ has values only in the range k = 0, 1…N-1. Moreover, due to the symmetry property of the discrete Fourier Transform, only frequencies up to k = N/2 can be represented. The maximum upper frequency $f_{Nyq}$ is called the Nyquist frequency (Bérubé 2008):

$$f_{Nyq} = \frac{N}{2} \frac{1}{N \times \Delta t} = \frac{1}{2 \times \Delta t}$$
( 3-11 )

Frequencies present in the signal that are higher than the Nyquist frequency cannot be accurately represented. They are seen as lower frequencies. This phenomenon is called aliasing. If the sampling rate is not large enough and the signal contains frequencies higher than the Nyquist frequency, the signal must be filtered in order to remove these high frequencies and obtain an accurate spectrum at lower frequencies.

Usually, the Fourier analysis is performed by looking at the magnitude and the phase of the Fourier Transform. These two real components contain all the information carried by the Fourier Transform. Figure 3-2 presents a typical time signal with the corresponding magnitude and phase of its Fourier Transform.

In addition to providing the frequency spectra of a signal, the Fourier Transform presents many advantages in term of calculation. For example, a derivation in the time domain is equivalent to a multiplication by the term (j×ω) in the frequency domain. Moreover, this transformation is used to define the transfer function of a system, which is the ratio of the Fourier Transform of the output over the one of the input. This transfer function, which carries all the properties of the system, is a very useful tool for material characterization. Nevertheless, this transformation presents one main limit: it doesn't indicate the frequency distribution over time. This information is hidden in the phase, but not revealed by the plot of the magnitude of the spectrum.

## 3.3. Windowing

Windowing consists of selecting a specific section of the time signal by multiplying this signal by a window function. Some of the most commonly used window functions (Rectangular, Hanning, Hamming and Kaiser) are plotted in Figure 3-3. This technique allows the frequency analysis of an isolated portion of a time signal. For example, as illustrated in Figure 3-4, the first arrival of a signal recorded by a transducer can be selected to focus on P-waves analysis.

In addition, windowing is capable to reduce the signal noise, which can have a significant participation in the signal, especially at the beginning and the end of a transient signal. It gradually sets the initial and final values of the signal to zero in order to avoid any leakage when computing the Fourier Transform.

Windowing performed in the frequency domain is referred to as filtering. For example, a band-pass filter is used to remove any low-frequency and high-frequency noise present in the signal.

## 3.4. Short Time Fourier Transform (STFT)

Contrary to the Fourier Transform, the STFT has the advantage to indicate how the frequency content of a signal changes over time. Its calculation process is illustrated in Figure 3-5. The signal x(t) to be transformed is multiplied by a window function w(t). Then, the Fourier Transform of the resulting signal is performed. These two steps are iterated as the window is moved along the time axis. The obtained function is a 2-D function of time and frequency. Mathematically, the STFT is written as (Yang 2009):

$$\text{STFT}\{x(t)\} = X(\tau, \omega) = \int_{-\infty}^{+\infty} x(t) w(t - \tau) e^{-j\omega t} dt \qquad (3-12)$$

where $\tau$ is the time shift used to localize the window function.

The width of the window determines the frequency and time resolutions. This is one of the disadvantages of the STFT: a trade-off has to be made between time and frequency resolutions, which are related through the equation:

$$\Delta f = \frac{1}{N_w \times \Delta t} \qquad (3-13)$$

where $\Delta f$ and $\Delta t$ are the frequency and time resolutions respectively, and $N_w$ is the size of the applied window. Therefore, low frequencies cannot be caught with short windows, whereas short pulses cannot be detected with long windows.

## 3.5. Wavelet Transform (WT)

As explained previously, the Fourier Transform consists of comparing the time signal with selected complex exponentials. In the wavelet transform, the signal is compared with wavelets. These wavelets are scaled and time-shifted copies of a finite-length or fast-decaying oscillating waveform, called a mother wavelet. Like the STFT, the WT is a two parameter transform. It is given by (Yang 2009):

$$WT(a,b) = \frac{1}{\sqrt{|a|}} \int_{-\infty}^{+\infty} x(t) \times \psi * \left( \frac{t-b}{a} \right) dt \qquad (3\text{-}14)$$

where x(t) is the time signal, $\Psi*$ is the window used as the mother wavelet, and the star represents the complex conjugate.

By contracting or stretching the wavelet, the parameter *a* allows looking at different frequency scales. This windowing with a variable size is the main advantage of the WT. Contrary to the STFT, the WT allows to improve frequency and time resolutions simultaneously. The parameter *b* is used to time shift the wavelet.

A common mother wavelet is the Morlet function, defined by:

$$\psi(t) = e^{j2\pi 2_0 t} \times e^{\left( t/\tau \right)^2} \qquad (3\text{-}15)$$

where $f_0$ is the central frequency and $\tau$ the frequency bandwidth.

The discrete form of the wavelet transform is given by:

$$WT_{k,m} = \frac{1}{\sqrt{k}} \sum_{n=0}^{N-1} x_n \times \psi * \left( \frac{n-m}{k} \right) \times \Delta t \qquad (3\text{-}16)$$

where N is the number of point used to digitize the time signal $x_n$, and $\Delta t$ is the time resolution. The counter k defines the frequency scale and m the time shift ($m \times \Delta t$).

An example of a WT using a Morlet function as mother wavelet is shown on Figure 3-6.

The discrete form of the WT is fundamentally different from the discrete WT, which allows decomposing a signal into its wavelet components. Figure 3-7 presents the discrete WT of a signal performed with the WPNDTool program developed by F. Tallavó at the University of Waterloo (Tallavó 2009). The number of levels used for the decomposition depends on the number of points recorded in the time domain.

## 3.6. Summary

This chapter describes the different signal processing techniques used to examine signals in the time and frequency domains. The Fourier Transform allows translating the signal from the time domain to the frequency domain. However, it does not indicate the signal's frequency distribution over time. The Short Time Fourier Transform, based on a time windowing shifted along time, maps a signal into a 2-D function of time and frequency. Finally, the wavelet transform can be considered as an improvement of the STFT as it overcomes the limits in getting both time and frequency high resolutions. These techniques are widely used to obtain the information required for material characterization.
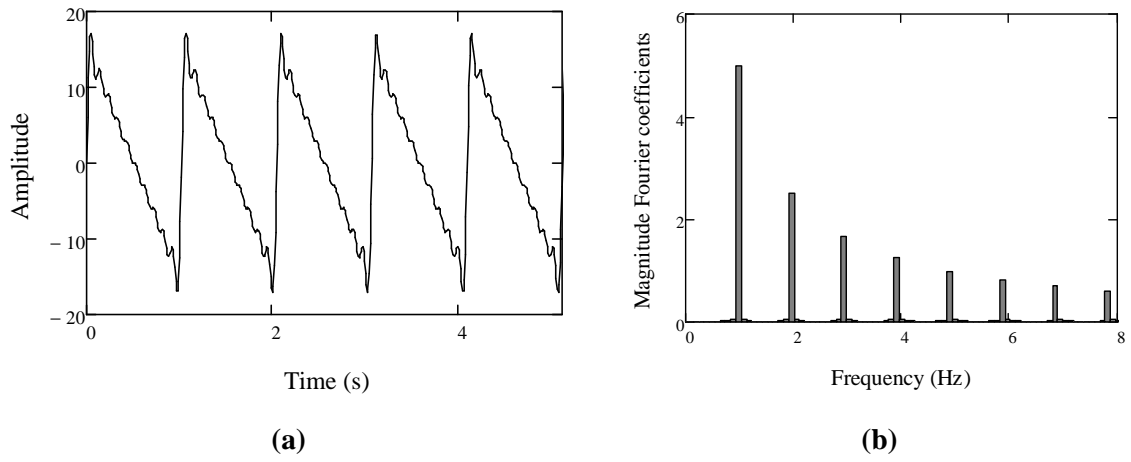
Figure 3-1: (a) Periodic time signal and (b) line spectrum of its Fourier series coefficients
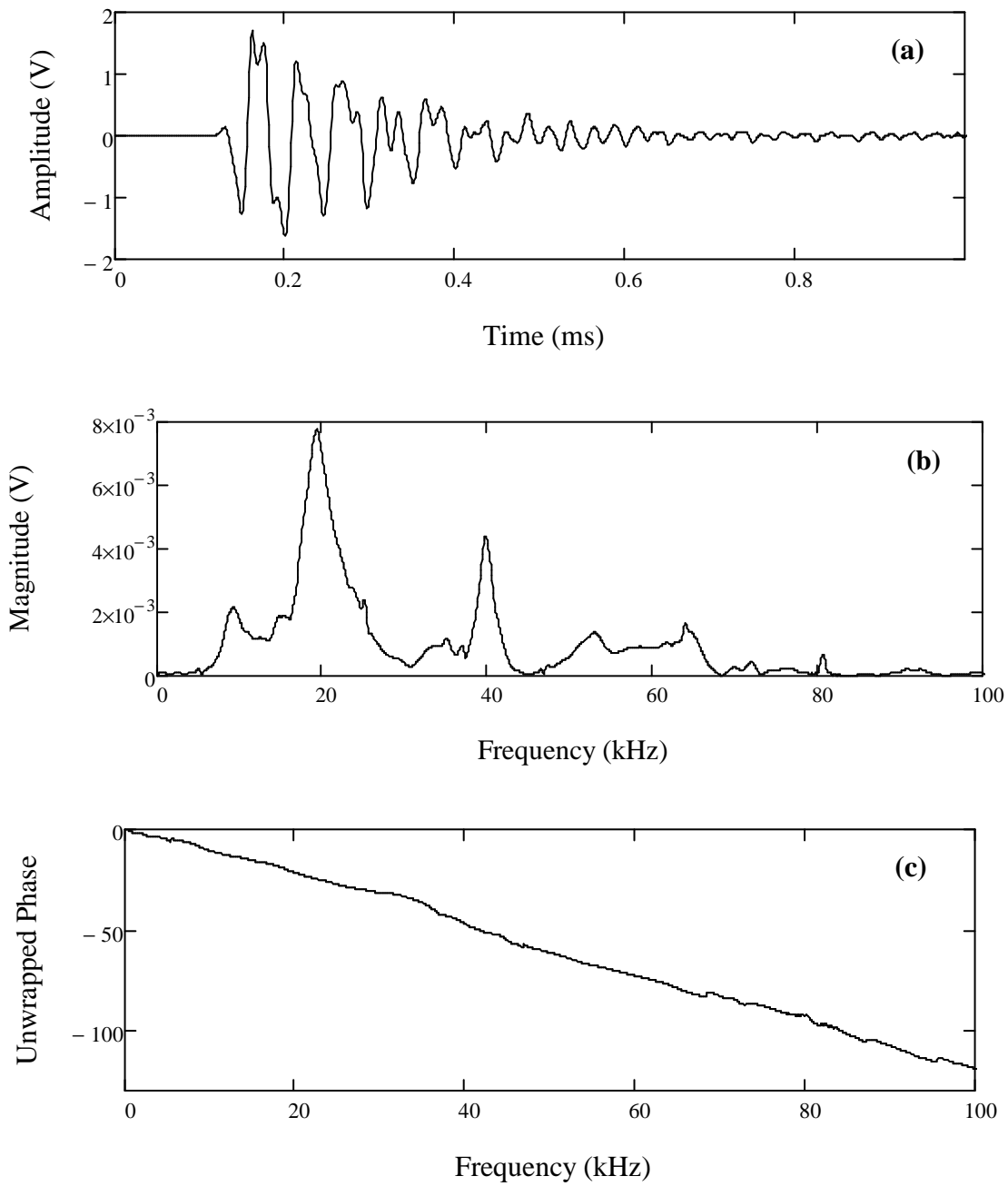
Figure 3-2: (a) Time signal with (b) magnitude and (c) phase of its Fourier Transform

38
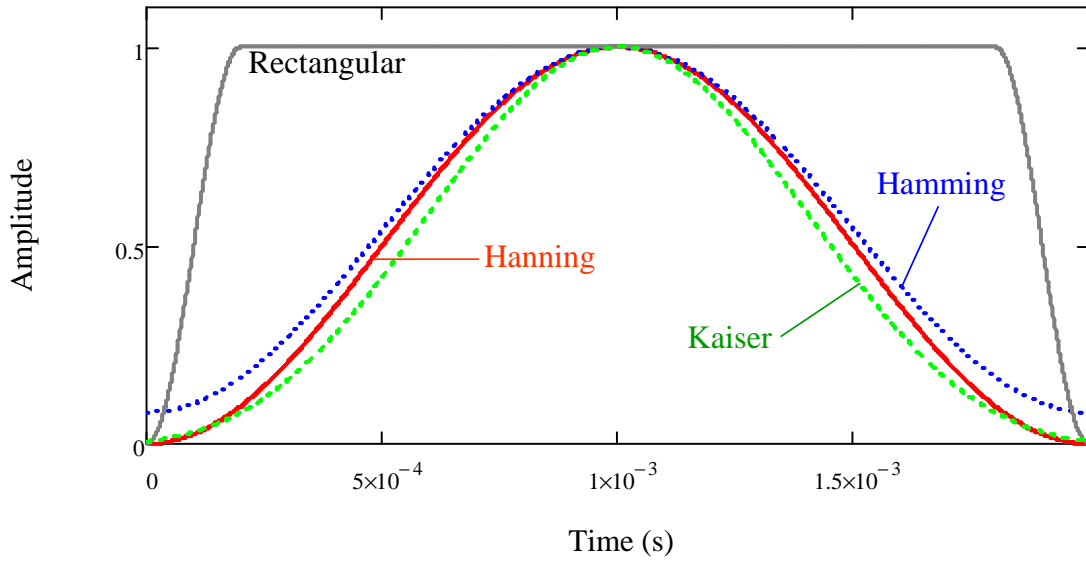
Figure 3-3: Hanning, Hamming, Rectangular and Kaiser ($\beta = 7$) windows
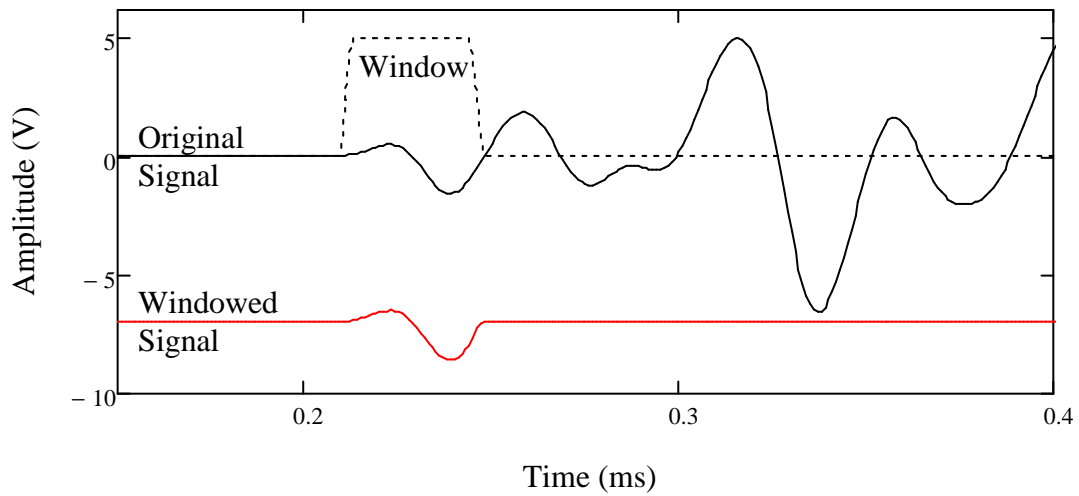


Figure 3-4: Time windowing of the first arrival (P-waves)
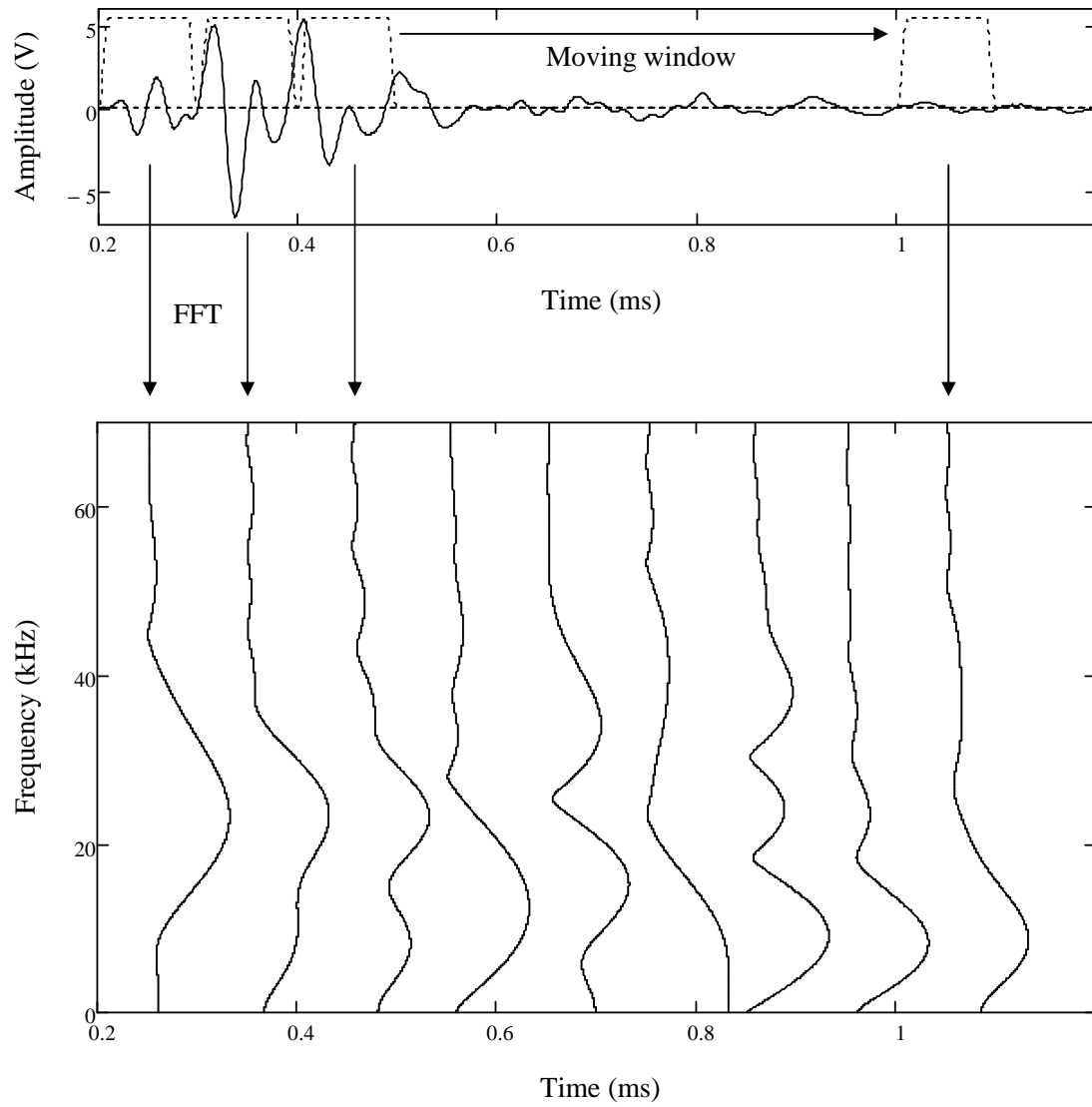
Figure 3-5: The different steps of the STFT calculation

**(a)**

Amplitude (V)

Time (ms)

**(b)**

Magnitude (V)

Shift Time (ms)

**(c)**

Real component

Time (ms)

Parameters of the Morlet wavelet:

$f_0 = 25$ kHz

$\tau = 2.24 \times 10^{-5}$
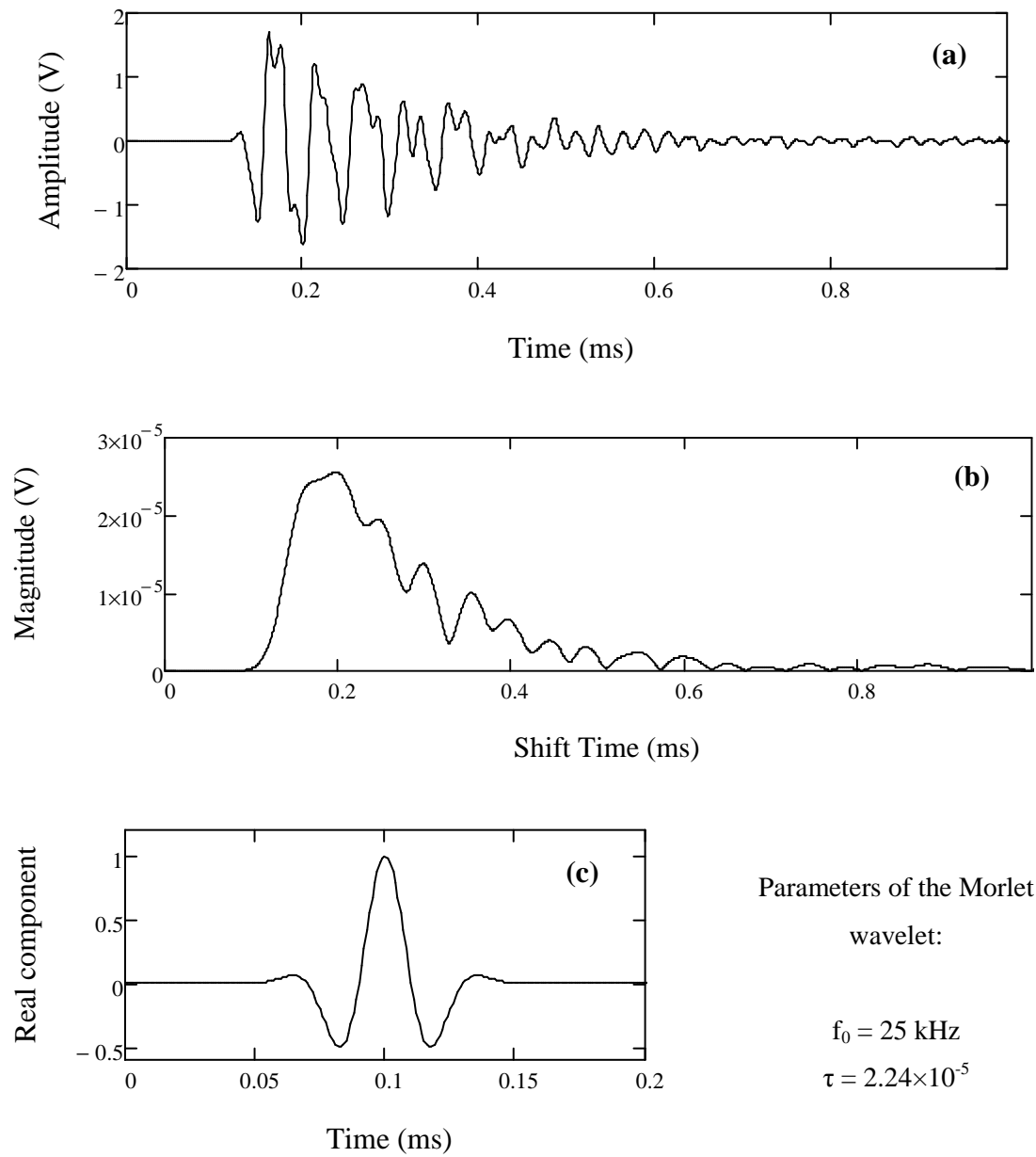
Figure 3-6: (a) Time signal and (b) magnitude of its WT calculated using a (c) Morlet wavelet
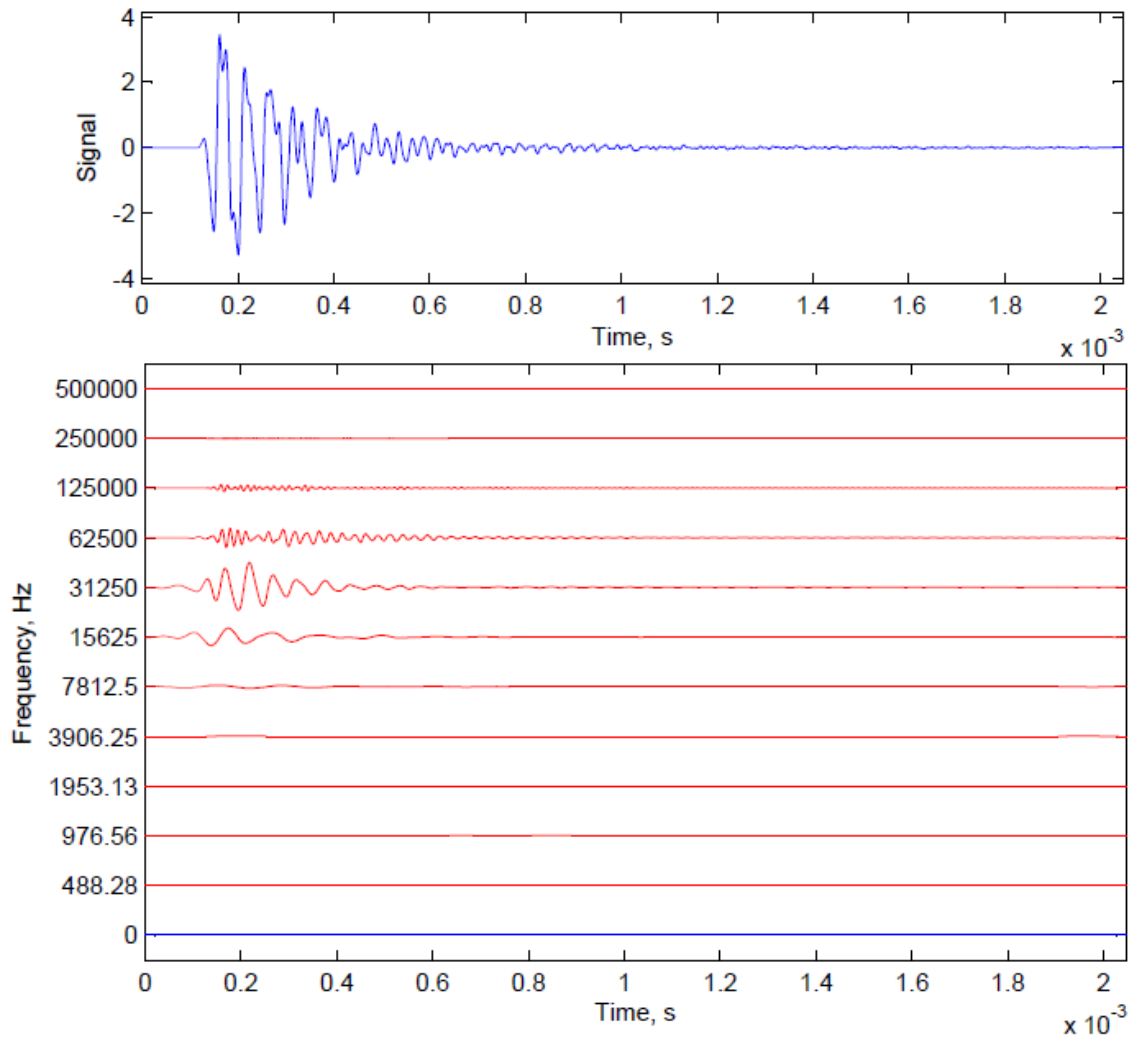
Figure 3-7: Discrete wavelet transform

(Tallavó 2009)

# CHAPTER 4.   NON DESTRUCTIVE TESTING METHODS FOR ASPHALT PAVEMENT EVALUATION

## 4.1.  Introduction

Non-destructive testing (NDT) methods have been commonly used in the past decade to evaluate pavement performance. They efficiently determine the physical properties of the pavement structure such as stiffness which can be related to performance. These techniques are generally preferred over destructive methods as they are less expensive, require less interruption to the traffic, do not damage the pavement, and have the ability to make enough measurements to quantify variability.

The correct determination of the structural condition is very important to the management of a pavement structure. Although it has no direct impact on how the user will rate a pavement, the structural capacity of a pavement must be known to predict its future condition.

The following sections describe the different NDT techniques that are being used for pavement evaluation. Nuclear density gauges are able to measure the compaction of asphalt mixture. Deflection analysis can be used to estimate of the stiffness of the different pavement layers. Since the propagation of seismic waves is affected by the density and the modulus of the medium, ultrasonic methods can be used to measure the density and the stiffness of asphalt pavements.

## 4.2.  Nuclear Density

A schematic of a nuclear density gauge is given in Figure 4-1. The source emits gamma rays, which interact with electrons through absorption, Compton scattering and photoelectric effect (Washington State DOT 2010). Pavement density is measured by counting the number of gamma rays received by a Geiger-Mueller detector, located in the gauge opposite from the handle. Nuclear gauges can be operated in one of two modes:
- Direct transmission: the radiation source fixed at the extremity of a retractable rod is lowered into the asphalt layer through a pre-drilled hole. Since the electrons present in the material tend to scatter gamma rays moving towards the detector, the density is inversely proportional to the detector count.

- Backscatter: the source remains within the gauge, at the same level as the detector. In this case, the interaction with the electrons redirects part of the gamma rays toward the detector and the density is proportional to the detector count.

Measurements with the backscatter modes are significantly affected by the irregularities of the pavement surface, and a better precision is obtained with the direct transmission mode. However, the backscatter mode presents the key advantage to be non-destructive. Moreover, a measurement depth of 88 mm is obtained with the backscatter mode, instead of 150 mm for direct transmission (Humboldt 2010). This is of particular importance for the evaluation of thin asphalt pavements (less than 100 mm thick).

Nuclear density gauges have been commonly used to determine the density of asphalt pavement in a non-destructive manner. They present the advantage of providing much quicker measurements than typical densities obtain from cores. However, questions still remain concerning their reliability. Problems with the seating of the gauge have been met when testing at the joints. Many density gauge measurements across longitudinal joints are actually collected at the location immediately next to the joint (Williams et al. 2009). The Ministry of Transportation of Ontario (MTO) conducted its own trials to estimate the benefits of different longitudinal joint construction techniques (Marks et al. 2009). Both nuclear and core density tests were performed at the joint. Analysis of the results showed poor correlate between the two methods ($R^2 < 0.4$).

## 4.3. Deflection Methods

Currently, any practical non destructive evaluation of pavement structural capacity is based on deflection measurements (Haas et al. 1994). There are three types of deflection devices: static, vibratory and impulse devices.

### 4.3.1. Static Methods

Static methods consist of measuring the deflection under static or slow-moving truck wheel loads. The most extensively used static method is the Benkelman Beam, developed in 1952 at the Western Association of State Highway Organizations (WASHO) Road Test. As illustrated in Figure 4-2, it operates on the lever arm principle. Measurements are made by placing the tip of the beam probe between the dual tires of a loaded truck. The pavement surface rebound is measured by the dial gauge as the truck is moved away from the test point.

It is a simple deflection device, but requires lot of time for testing. When testing on stiff pavements, the support legs may be within the deflected area which would result in inaccurate measurements.

For many years, the Benkelman beam has been the standard. However, it became necessary to develop better methods to adequately represent pavement behaviour under moving wheel loads.

### 4.3.2.    Vibratory Methods

Steady-state vibratory devices measure the deflection of a pavement produced by an oscillating load. The typical force output of a vibratory device is shown in Figure 4-3. It is composed of a static load and a dynamic sinusoidal force. The most common steady state deflection devices are the Dynaflect and the Road Rater.

An illustration of the Dynaflect is given in Figure 4-4. Two counter-eccentric masses rotating at a frequency of 8 Hz are generating the load (Haas et al. 1994). A peak to peak dynamic load of 1,000 lb (450 kg) is applied on the pavement through the two load wheels. Five geophones are installed on the trailer to measure the deflection basin.

The Road Rater is another vibratory device, which is capable of varying the load magnitude and the frequency. The dynamic load is generated hydraulically by raising and lowering a mass. The weight of the trailer is transferred from the travel wheels to the load plate in order to vary the static load. Four geophones are used to measure the deflection of the pavement.

The main advantage of steady state over static deflection equipment is that it can measure a deflection basin, which is used to backcalculate the profile of the pavement structure. However, vibratory devices apply relatively light weights. Therefore, it is more suitable for measurement on thin pavements.

### 4.3.3.    Impulse Methods

Impulse load devices measure the deflection of a pavement generated by a falling mass. These devices are generally called falling weight deflectometers. They are able to produce peak forces corresponding to a moving heavy truck wheel. The heavy weight deflectometer has been designed for airfield evaluation. A portable version has been developed: the light weight deflectometer.

4.3.3.1. Falling Weight Deflectometer (FWD)

Figure 4-5 shows the most commonly used FWD in Europe and North America: the Dynatest 8000 Falling Weight Deflectometer (Ullidtz 1987). In order to simulate a load impulse similar to moving truck wheel loads, a weight is dropped on a loading plate in contact with the road. The weight is hydraulically lifted to predetermined heights, and dropped on a 30 cm or 45 cm diameter loading plate. The resulting impact load has a duration of approximately 30 ms and a peak magnitude up to 120 kN. The deflection basins are measured by seven geophones located at different distances from the loading system. The deflection measurements are used to compute the thickness and stiffness of construction layers including subgrades, base courses and pavements. This device presents several advantages such as a high degree of accuracy and a good repeatability which justify its use for Mechanistic-Empirical design. However, the FWD presents high purchase and operation costs. Therefore, a portable version of this device has been developed: the Light Weight Deflectometer (LWD).

4.3.3.2. Dynatest Light Weight Deflectometer (LWD)

For this research, the Dynatest 3031 LWD, presented in Figure 4-6, has been selected as the primary instrument because of its high level of flexibility. The apparatus and the signal conditioning and recording system follow the requirements specified in (ASTM Standard E 2583-07).

The size of the load plate, the mass of the weight and the drop height can be adjusted to apply a suitable stress to the pavement surface (Dynatest International 2006). Three different plate sizes can be used: 100, 150 and 300 mm diameters. The maximum drop height is 850 mm. Two additional weights can be added to the original one, which results in three available falling masses: 10, 15 and 20 kg. The Dynatest 3031 is able to apply a load up to 15 kN, which corresponds to a peak contact stress of 200 kPa if the 300 mm plate is used. The pulse duration is between 15 ms and 30 ms.

Several sensors are used by the Dynatest 3031. First, a load cell measures the impact force from the falling weight, with a precision of 0.3 N. Then, a geophone located at the centre of the loading plate is used to measure the centre deflection with a precision of 1μm. Two geophones can be added radially outward from the main unit to record the deflection basin. The different sensors are shown in Figure 4-7.

A personal digital assistant (PDA) equipped with the software LWD 3031 is used to record the stress and deflection measured by the sensors. Any calculation performed by the program follows the elastic theory exposed in Section 2.3 for static loading. Equations ( 2-35 ) and ( 2-36 ) are used to calculate the surface moduli at the centre of the loading plate and at distances larger than twice the radius of the plate. Figure 4-8 shows an example of a PDA display after one deflection measurement.

Further analysis can be obtained from the LWD measurements, using the LWDmod Program. This program is able to backcalculate the modulus profile of the pavement. The backcalculation is limited to three layers, and provides:

- The thickness and modulus of the first/asphalt layer ($h_1$, $E_1$)
- The depth to bedrock, and the third/subgrade modulus ($h_3$, $E_3$)

The thickness of the second layer is fixed. Its modulus cannot be backcalculated, and is either regarded as a fixed value or a proportion of $E_1$. As subgrade layers are known to be highly non-linear, the modulus of the third layer is calculated using equation ( 2-41 ).

A screen shot of the backcalculation interface is provided in Figure 4-9. First, structural information must be entered in terms of definitions of layers and seed values. Based on these input values, and the elastic theory equations, the program calculates the expected deflection. Then, it calculates the root mean square (RMS) value of the difference between the calculated and the measured deflections, and changes the properties of the layers in order to minimize the RMS value. The calculation is performed in a selected number of iterations. After all iterations, the results that fit best to all deflection measurements included in the analysis are listed in the "Results" frame.

The estimation of the top layer thickness requires the use of different plate sizes during LWD testing. The bedrock depth can be calculated by the program only if testing was performed with more than one geophone. Finally, it is recommended to measure the deflection with different falling heights. A better interpolation is obtained if different stress levels are applied at the surface of the pavement.

## 4.4. Ultrasonic Methods

Many non-destructive wave-based methods have been studied for the evaluation of pavement structural capacity, but not developed to the point of common implementation. Most of them are

based on the analysis of two types of stress waves: either P-waves or surface waves. P-waves travel at the highest velocity and can be easily identified as the first arrival in a recorded signal. Surface waves energy is dominant along the surface of the medium, which makes them very useful for the evaluation of pavement structures that are accessible only from the surface.

### 4.4.1. Ultrasonic Testing Methods Using Body Waves

Body waves are either P-waves or S-waves. Most reported ultrasonic methods are based on the use of compression waves, as it is the only mode present in the first arrival of any time signal generated by a mechanical impact. According to equation ( 2-16 ), shear wave velocity is very close to Rayleigh wave velocity. Therefore, S-wave arrival is masked by surface waves that carry most of the wave energy.

4.4.1.1.    Ultrasonic Pulse Velocity (UPV)

The UPV is the most popular ultrasonic method for material characterization. It relies on the measurement of body wave velocities through a specimen. Young's modulus of elasticity, Poisson's ratio, acoustic impedance, and other useful properties can be calculated for solid materials with the ultrasonic velocities if the density is known (ASTM Standard E 494-05).

The UPV test setup is presented in Figure 4-10. Two ultrasonic transducers are placed at each extremity of the specimen. One transducer, used as a transmitter, transforms an electrical pulse into a mechanical vibration. The wave propagates through the specimen and reaches the other transducer, used as a receiver, which converts the energy into an electric pulse. An oscilloscope displays the measured signals, which are stored in a computer for further processing. An average of several recordings is computed by the oscilloscope to reduce the noise. An example of a signal recorded by the oscilloscope during a UPV test is given in Figure 4-11. The arrival time of the wave, $\Delta t$, is obtained from this graph. Since the length $\Delta L$ of the specimen is known, the velocity of the wave can be calculated. The transmitter used in this example generates mainly compression waves, thus the calculation gives $V_P = \Delta L/\Delta t$. Similarly, a shear wave transmitter can be used to determine $V_S$. Then, the Young's modulus and the Poisson's ratio are calculated using the equations presented in Section 2.2.

A coupling agent such as vacuum grease should be used to improve the transmission and reception of the waves. Moreover, a constant pressure should be applied to each transducer for a better consistency between different measurements. Jiang, who performed UPV measurements on

HMA specimen in the Non-destructive Laboratory at the University of Waterloo (Jiang 2010), used a load cell to avoid the variation of wave amplitude due to changes in contact pressure.

The calibration of the UPV method consists of measuring the arrival times for different specimens made of the same material but having different lengths. A linear regression is performed to relate the arrival times to the lengths of the specimen. The intercept represents the time delay introduced by the equipment and the coupling condition. Therefore, this intercept must be subtracted from the arrival time obtained from UPV measurements.

Wave attenuation is another property that can be determined by UPV. For this purpose, measurements must be performed on specimens of different lengths. The energy of the wave propagating through the specimens is given by wave characteristics such as peak-to-peak amplitude or frequency spectrum area. In many cases, wave velocities do not provide enough information on the material, and wave attenuation should also be considered for a better analysis. For example, Jiang found low correlation between the compaction of HMA samples and wave velocity, whereas he found good correlation between the level of compaction and wave attenuation parameters (Jiang 2010).

### 4.4.1.2.    Impact Echo (IE)

Impact-Echo is a method that has been developed in the mid 1980s (Sansalone and Carino 1986), and successfully employed to measure the wave velocities and the thickness of concrete plates. It has also been used to locate voids, cracks and other damage in structures. In this method, a mechanical wave is generated into a test object by impact on the free surface. Body waves propagate into the solid spherically outward from the source, and get reflected back and forth between the top surface and internal defects or the bottom surface of the test member, as illustrated in Figure 4-12. A transducer located near the impact point is used to detect the arrivals of these reflected waves. At points close to the impact point, displacements caused by P-waves are more important than the one caused by S-waves. Therefore, the Impact-Echo method is primarily based on P-wave reflections. The frequency of the P-wave arrivals at the receiver is determined by transforming the received time-signal into frequency domain using the Fourier Transform. Any high amplitude peak in the Fourier spectrum could be associated with a reflection event. Knowing the P-wave velocity, the depth D to a reflecting interface can be determined by:

$$D = \frac{V_P}{2f} \qquad\qquad (\,4\text{-}1\,)$$

where $V_P$ is the compression wave velocity and f is the frequency of P-wave reflections between the solid surface and the defect or boundary.

An advantage of the IE method is that it requires the access to only one surface of the tested object. Besides, the use of a relatively low frequency range allows measuring thicknesses up to several meters, but limits the investigation of small voids and micro-cracks.

## 4.4.2. Ultrasonic Testing Methods Using Rayleigh Waves

As explained previously in Section 2.2, surface waves attenuate slower than body waves. Moreover, surface waves resulting from a vertical impact are primarily Rayleigh waves. Miller and Pursey (1954; 1955) showed that for a vertical impact, more than 67% of the energy propagates as R-waves. Therefore, the analysis of R-waves is very important for ultrasonic testing.

### 4.4.2.1. Spectral Analysis of Surface Waves (SASW)

The practical aspects of the SASW method have been presented by Heisey et al. (1982a) and Nazarian et al. (1983). Surface waves are dispersive in a layered medium: their velocity varies with frequency. Based on the experimental dispersion curve, the SASW method is able to determine the shear wave velocity profile of the medium, which is related to its modulus profile. The test setup for SASW is presented in Figure 4-13. A source generates energy over a wide range of frequencies by mean of a mechanical impact on the ground surface. Two receivers are attached to the surface in order to record the waves propagating in the medium. A waveform analyzer is used to record the time signals, which are then transformed into the frequency domain. The phase information is used to obtain the phase difference between the two receivers at each frequency:

$$\Delta\varphi = \text{Phase}(\text{FT}_2) - \text{Phase}(\text{FT}_1) \qquad\qquad (\ 4\text{-}2\ )$$

where $\Delta\varphi$ is the phase difference, $\text{FT}_i$ is the Fourier Transform of the signal recorded by the receiver No. i (i = 1,2), and $\text{Phase}(\text{FT}_i)$ is the unwrapped phase of the Fourier Transform.

In order to avoid any internal phase shift associated with the receivers or the data acquisition system, the test is repeated from the reverse direction: the impact is generated on the other side of the two receivers (Nazarian and Stokoe 1986). Then, the phase velocity, defined as the velocity with which a wave of a specific frequency propagates in a medium, is given by:

$$V_{ph} = \omega \frac{\Delta x}{\Delta \varphi}$$  ( 4-3 )

where $V_{ph}$ is the phase velocity, $\omega$ is the circular frequency, $\Delta x$ is the receiver spacing and $\Delta \varphi$ is the phase difference.

As the range of frequencies generated by a single source is limited, testing should be performed for several source and receiver spacings. Close spacings are used to look at high frequencies and near-surface materials, whereas large spacings sample lower frequencies and deeper materials. Moreover, surface waves become fully formed only beyond a minimum distance from the source. Conversely, the signal-to-noise ratio becomes lower at large distances from the source. These phenomena are respectively called near-field and far-field effects. A common criterion used to select a receiver spacing and a range of wavelengths that minimizes those effects is expressed as (1982a):

$$\frac{\lambda}{3} < \Delta x < 2\lambda$$  ( 4-4 )

where $\lambda$ is the wavelength and $\Delta x$ is the receiver spacing.

The next step consists of converting the experimental dispersion curve into a function of shear wave velocity versus depth. Since the penetration of surface waves depends on their wavelengths, velocities of given frequencies could be assigned to depths using a wavelength criterion. Heisey et al. (1982b) performed SASW on a pavement surface, and found that a depth criterion of one third of the wavelength provided a velocity profile that correlated best with the one obtained from crosshole testing. A more rigorous method involves an inversion process. It is an iterative process in which a theoretical dispersion curve is constructed by assuming a shear wave velocity profile. The experimental and theoretical curves are compared, and the assumed shear wave velocity profile is changed until the two curves match within a reasonable tolerance.

The SASW is part of the seismic pavement analyzer (SPA) that was developed through the Strategic Highway Research Program (SHRP) at the University of Texas, El Paso (Nazarian et al. 1993). It is a trailer mounted wave propagation measurement based device, which has been developed to detect pavement distresses at their early stages, so that problems can be resolved through preventive maintenance. The SPA estimates Young's and shear moduli in the pavement structure from five wave propagation measurements, among which are the Impact-Echo and the SASW methods. An evaluation of this device for pavement monitoring was conducted by testing

a number of flexible and rigid pavements in New Jersey (Gucunski and Maher 2002). This report showed that the SPA is a well designed automated data collection and analysis system for seismic testing of pavements. However, the authors pointed out that the interpretation procedures related to SASW data had significant space for improvement.

The portable seismic pavement analyzer has been recently developed to evaluate the stiffness of a pavement structure (Steyn and Sadzik 2007). This device, presented in Figure 4-14, is mainly aimed at determining the stiffness of the upper-most pavement layers through a spectral analysis of the surface waves recorded by two receivers.

### 4.4.2.2.     Multi-Channel Analysis of Surface Waves (MASW)

The SASW method considers only the fundamental mode of the Rayleigh waves. In general, the contribution of the higher modes of the Rayleigh waves is important in a pavement structure, therefore it is difficult to determine a shear wave velocity profile from the inversion process of the SASW data (Karray and Lefebvre 2009). The different modes can change the apparent dispersion characteristics of the fundamental mode by being misinterpreted as fundamental (Park et al. 1999). The multi-channel analysis of surface waves uses a different signal processing technique that identifies and separates the different modes of the Rayleigh waves. The dispersion curves are obtained for the fundamental mode and higher modes, which results in a better determination of the shear wave velocity profile by the inversion process. One of the objectives of the source and receiver configuration of the SASW is to minimize the contribution of the higher modes. Therefore, several spacings must be tested. This is not the case for the MASW, which results in a faster data collection. Another advantage of the MASW with respect to the conventional SASW is a better noise control.

The MASW test configuration is provided in Figure 4-15. An array of equally spaced receivers is used to record the surface waves propagating in the medium. The data is stored in a computer for future processing.

In this research project, the program SWAN (Russo 2006) has been selected to compute the dispersion curves. This program is able to interpret raw data related to SASW or MASW acquisition through several processing steps. First, the time signals are cleaned by deleting the DC offset and removing any noise. Then, the FK (frequency – wave number) spectrum is computed to view the energy distribution between the different modes of propagation. The

experimental dispersion curve is extracted by selecting the maxima of the FK spectrum. Finally, an inversion process is performed to find a shear wave velocity profile of the ground that is linked to the experimental dispersion curve.

The MASW is also used to look at wave attenuation with distance. The energy carried by the waves is expressed in the time or frequency domain by several indicators such as:

- Peak to peak amplitude in time domain:

$$PTP_i = \max(x_i(t)) - \min(x_i(t)) \qquad (4\text{-}5)$$

where i is a counter indicating the location where the amplitude $x_i(t)$ is recorded.

- Area in frequency domain:

$$Area_i = \sum_j |X_i(f_j)| \qquad (4\text{-}6)$$

where *i* is a counter indicating the location where the spectrum $X_i(f)$ is obtained, and j is another counter for the discrete frequency $f_j$.

### 4.4.2.3.     Fourier Transmission Coefficient (FTC)

The practical measurement of wave attenuation on pavement structures has been restricted because of the variability introduced by the source, the receivers, and the coupling condition (Popovics et al. 1998). The FTC method, based on a self-compensating technique, allows the removal of those unknown characteristics. It has been used for the determination of the depth of surface-breaking cracks in concrete (Yang 2009; Popovics et al. 2000).

As illustrated in Figure 4-16, two receivers separated by a given distance are placed on the surface of a specimen (locations B and C). A force is applied by a source located along the line formed by the receivers, at location A. The generated surface wave propagates through the specimen and is detected by the two sensors. The signal received by the nearest sensor at location B can be expressed in the frequency domain as the product:

$$F_{AB} = S_A d_{AB} R_B \qquad (4\text{-}7)$$

where $S_A$ is the source response term including the coupling effect at location A, $d_{AB}$ is the transfer function of the medium between location A and B, and $R_B$ is the transfer function of the receiver at location B.

Similarly, the signal received at location C is expressed in the frequency domain by:

$$F_{AC} = S_A d_{AB} d_{BC} R_C \qquad (4\text{-}8)$$

The $S_i$ and $R_i$ terms contain variability introduced by the source, receivers, and coupling condition. This variability masks the desired terms: the attenuation response $d_{BC}$ between the two receivers. In order to eliminate this variability and the extraneous $d_{AB}$ term, the source is placed on the other side of the receivers, at location D. The signals received by the two sensors are given in the frequency domain by:

$$F_{DC} = S_D d_{DC} R_C$$
$$F_{DB} = S_D d_{DC} d_{CB} R_B$$

( 4-9 )

Note that the material is assumed globally isotropic and: $d_{BC} = d_{CB}$. A mathematical manipulation of the above equations results in an expression of the Fourier transmission coefficient between location B and C (Popovics et al. 2000):

$$|d_{BC}| = \sqrt{\left|\frac{F_{AC}F_{DB}}{F_{AB}F_{DC}}\right|}$$

( 4-10 )

The transmission coefficient ranges from 0 to 1. A value of 0 indicates a complete attenuation whereas a value of 1 indicates a complete transmission.


The FTC technique presents the advantage that the results are independent of the type of source, receivers, and coupling conditions. The coefficient $d_{BC}$ can be used to estimate the attenuation due to a crack such as the one indicated in Figure 4-16. However, it also includes the geometrical attenuation experienced by the surface waves between locations B and C. Therefore, measurements should be performed on both cracked and crack-free surfaces for comparison in order to determine the attenuation due to the crack only. Moreover, reflected waves from the crack could interfere with the surface waves recorded by the receivers and affect the results.


4.4.2.4.    Wavelet Transmission Coefficient (WTC)

A new WTC method has been developed to overcome the main limitations of the FTC method (Yang 2009). For this purpose, an equal spacing configuration is used. Two piezoelectric transmitters are placed at point A and D, and two accelerometers are placed at point B and C, as illustrated in Figure 4-17. As the four points define a square, a pulse sent from any of the source locations travels the same distance before reaching the receivers. The variability introduced by the source, receivers and coupling condition is eliminated by using the self-compensating technique defined previously in the FTC method. The wavelet transform is applied to the four signals recorded by the two receivers for the two source locations. The parameter $a$ is fixed to the value: $a_0 = 1/(2f_0)$, where $f_0$ is the centre frequency of the measurements. Four time constants $b_1$,

$b_2$, $b_3$ and $b_4$ are obtained by identifying the first peaks of the wavelet transforms. The wavelet transmission coefficient is defined by:

$$WTC = \sqrt{\frac{W_{AC}(a_0, b_2)}{W_{AB}(a_0, b_1)} \frac{W_{DB}(a_0, b_3)}{W_{DC}(a_0, b_4)}} \qquad (\text{ 4-11 })$$

where $W_{ij}(a_0, b_k)$ is the wavelet transform of the signal send by the source i, received at location j, and computed using equation ( 3-14 ).

Contrary to the FTC method, the WTC calculation uses an equal spacing configuration. It allows reducing the effect of wave reflections in the presence of a crack. Besides, the distances traveled by the four waves are the same, and the geometrical attenuation is cancelled in the WTC. Jiang (2008) applied the WTC method to the evaluation of longitudinal joints in asphalt pavements. The results obtained from measurements performed on asphalt slabs compacted in the laboratory showed that the WTC parameter was able to differentiate between good (WTC>0.49), medium (0.32<WTC<0.34), and weak joints (WTC<0.13). Field evaluations of longitudinal joints were performed at the Highway 401 and at the Centre for Pavement And Transportation Technology (CPATT) Test Track located near the University of Waterloo, Ontario. The WTC method was found to clearly identify deteriorated and newly constructed joints, and was sensitive enough to distinguish between the joints constructed using the traditional and the echelon paving method.

## 4.5. Summary

The different NDT techniques used for pavement evaluation are reviewed in this chapter. Nuclear density gauges provide a quick estimation of HMA density, but the accuracy of the readings highly depends on the seating of the gauge, which can be a significant problem when testing at the joints. Among all deflection devices, the falling weight deflectometer presents the highest accuracy and a good repeatability. Its portable version, the light weight deflectometer, has been selected to perform deflection tests in this research project. Many wave-based methods have been developed for the characterisation of materials. As non-destructive evaluation of pavement structures can be performed only from the surface, methods using surface waves are more suitable for this purpose. The MASW is able to backcalculate the stiffness profile of the structure, and the attenuation properties of the surface layers, which can be used for the evaluation of longitudinal joints in asphalt pavements.
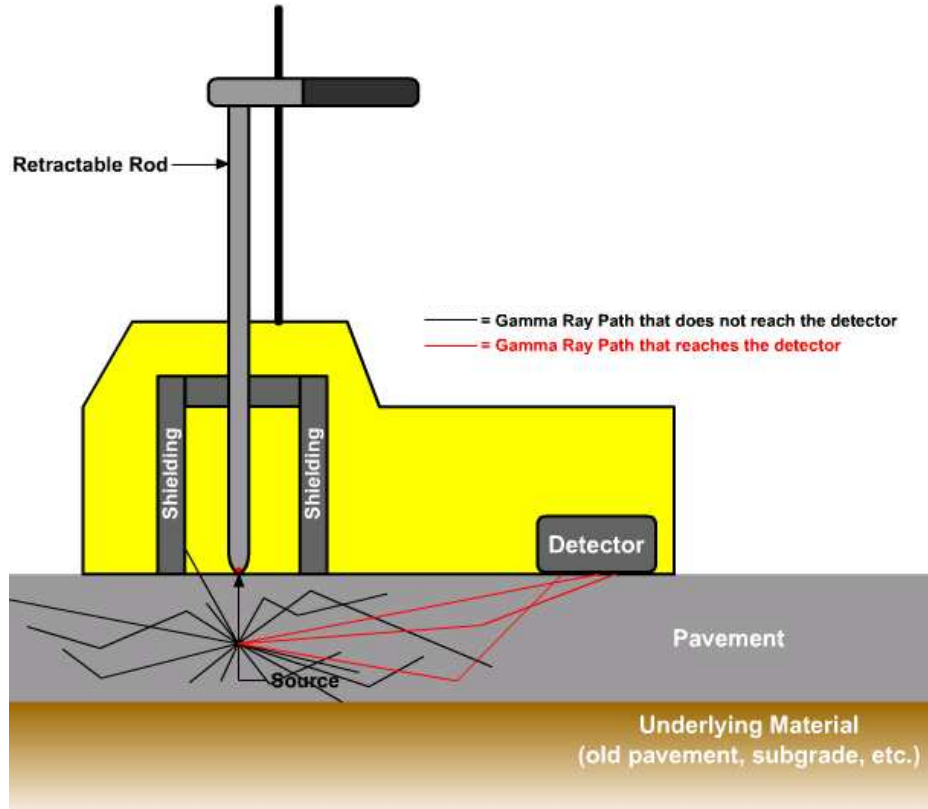
Figure 4-1: Nuclear density gauge, backscatter mode

(Washington State DOT 2010)
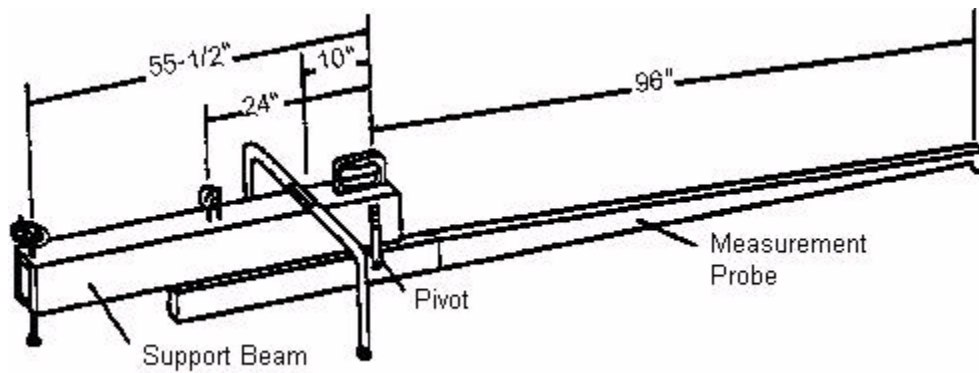


Figure 4-2: Benkelman Beam

(Washington State DOT 2010)
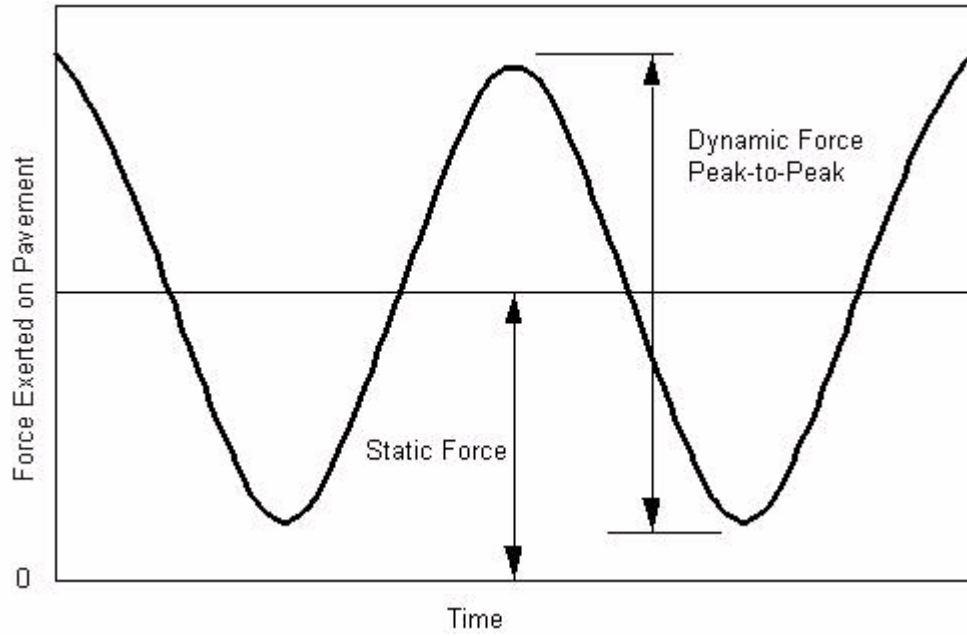
Figure 4-3: Dynamic force output of vibratory devices

(Washington State DOT 2010)



Figure 4-4: Dynaflect in the test position

Figure 4-5: Dynatest FWD in the test position
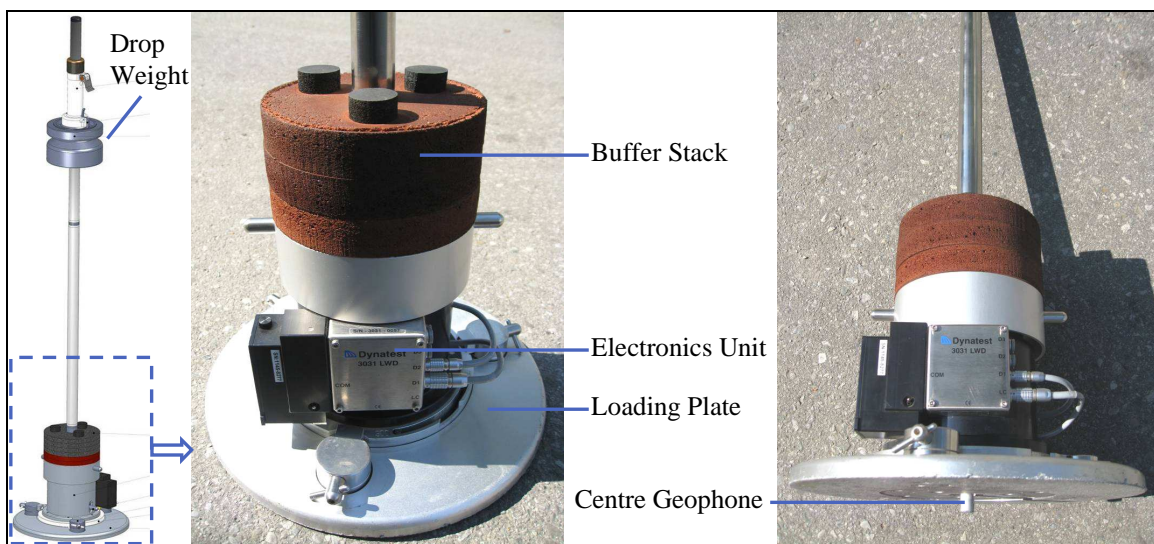


Figure 4-6: CPATT Dynatest 3031 LWD
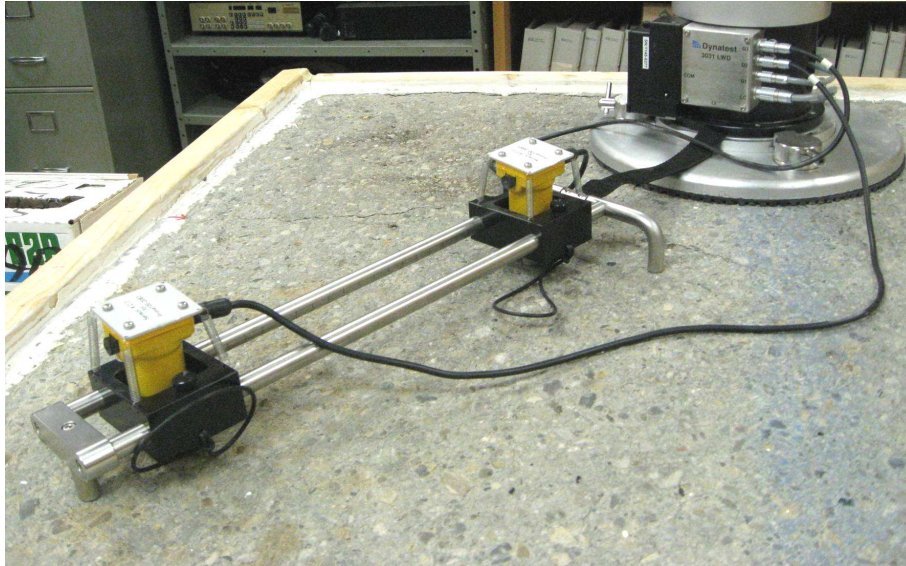
Figure 4-7: Additional geophones for the CPATT LWD
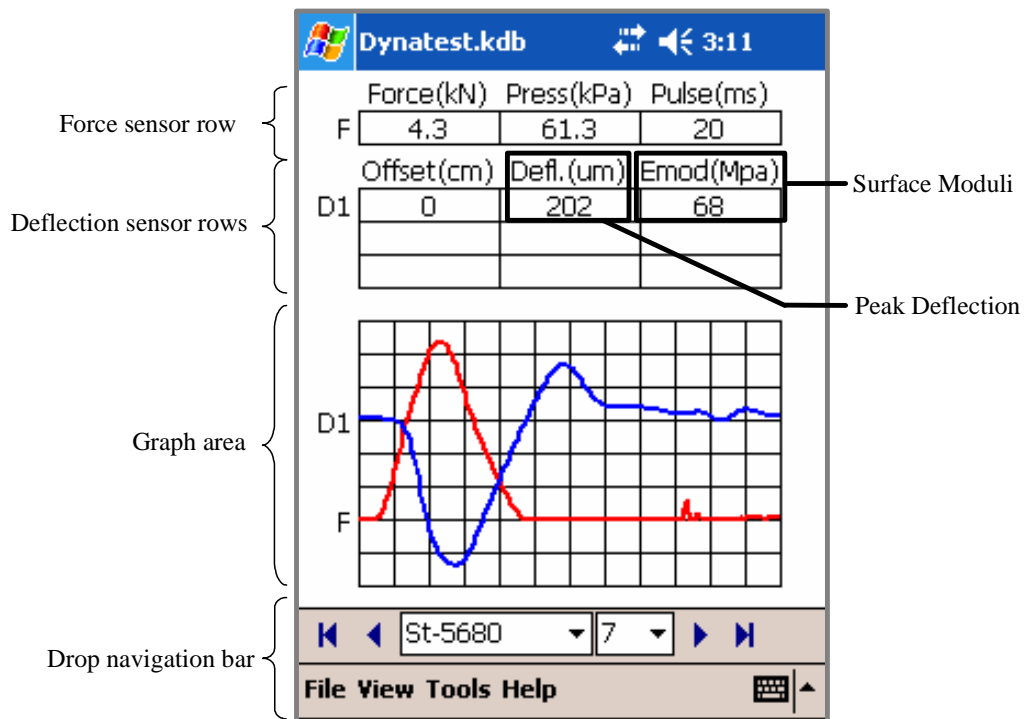


Figure 4-8: Dynatest 3031 LWD – PDA display
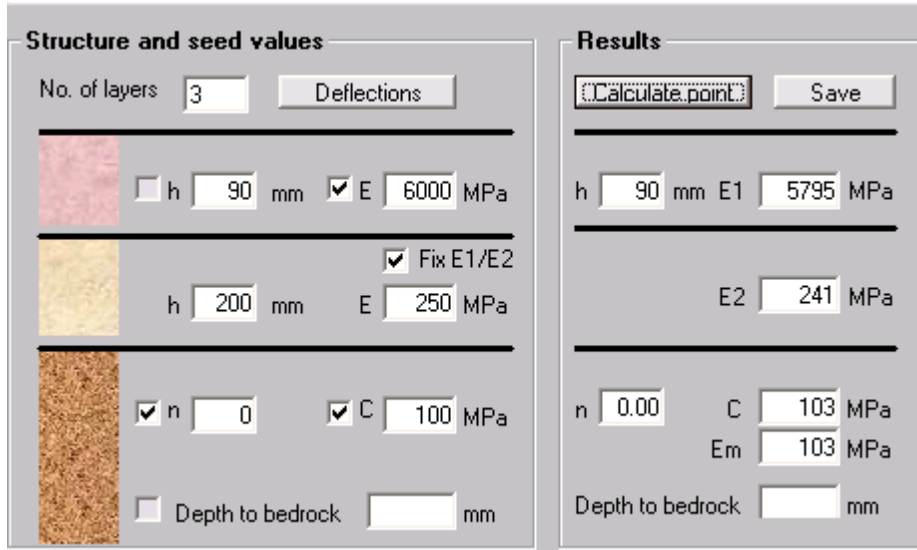
Figure 4-9: LWDmod Program – backcalculation interface
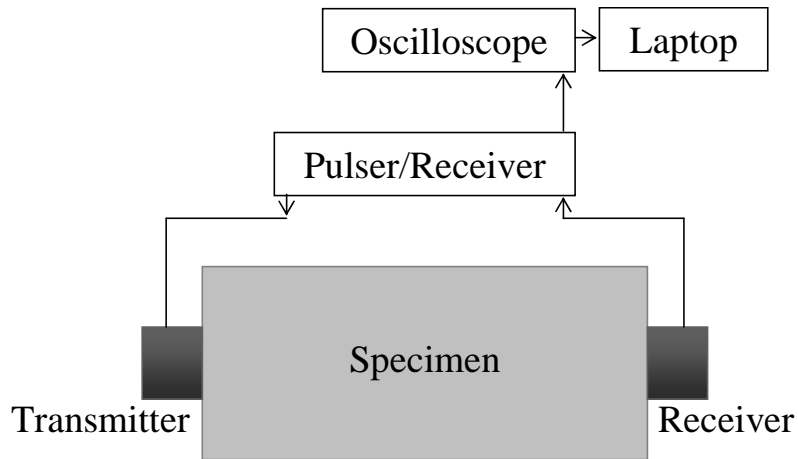


Figure 4-10: UPV test setup
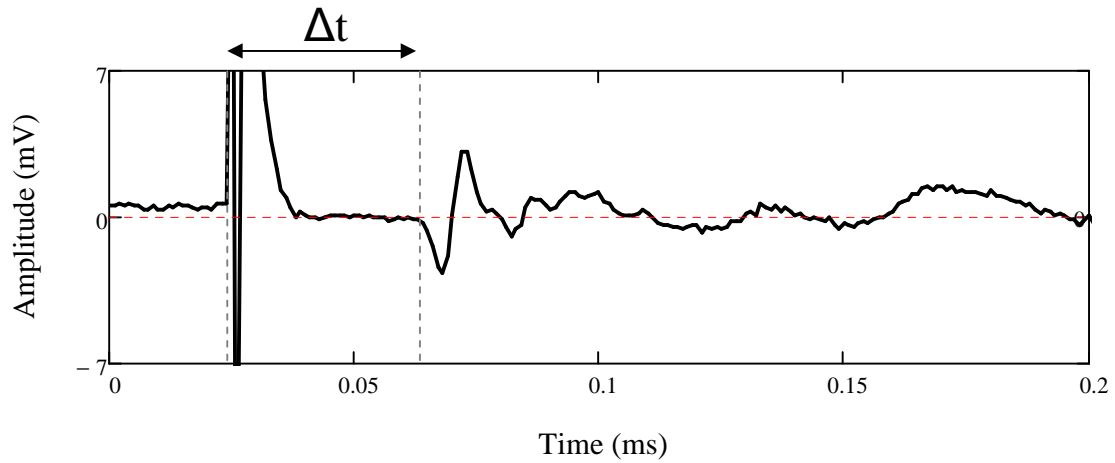
Figure 4-11: Signal recorded during a UPV test
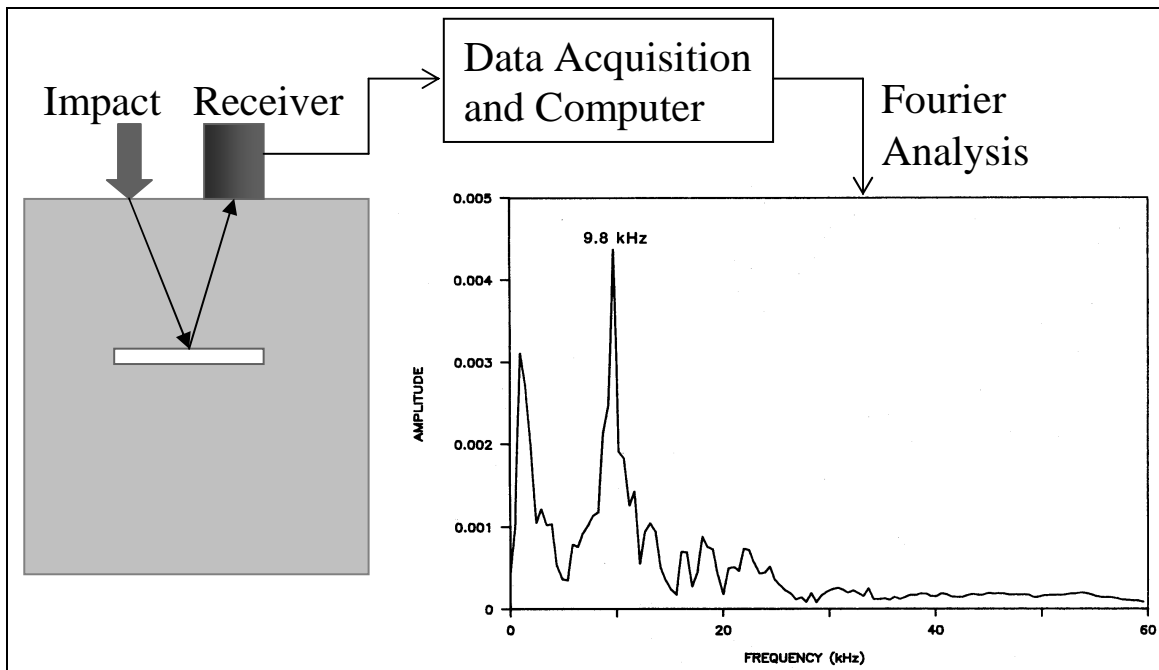


Figure 4-12: Impact-Echo test setup

(Inspired from Sansalone and Carino, 1989)
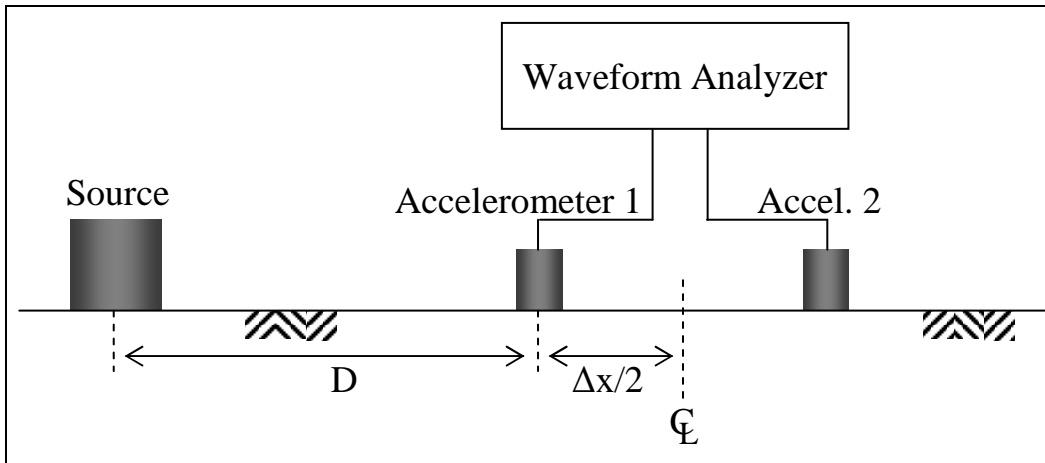
Figure 4-13: SASW test setup



Figure 4-14: Portable seismic pavement analyzer

(Steyn and Sadzik 2007)
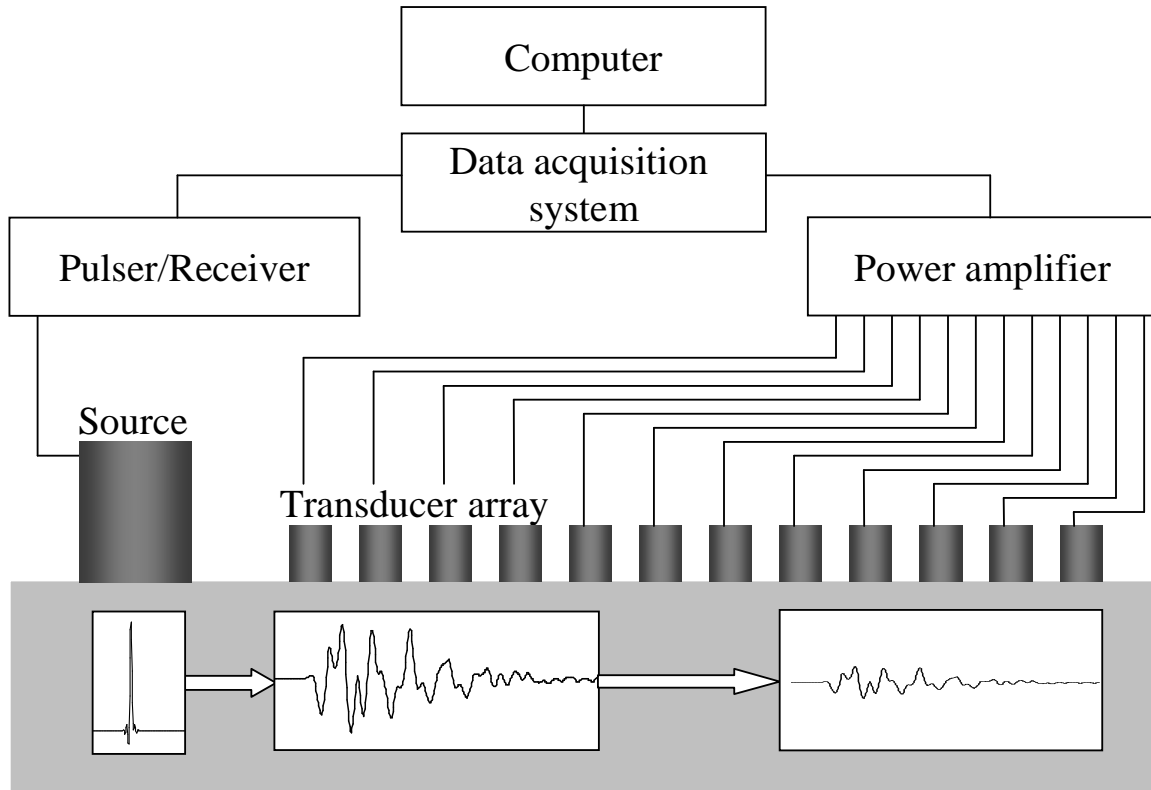
Figure 4-15: MASW test setup
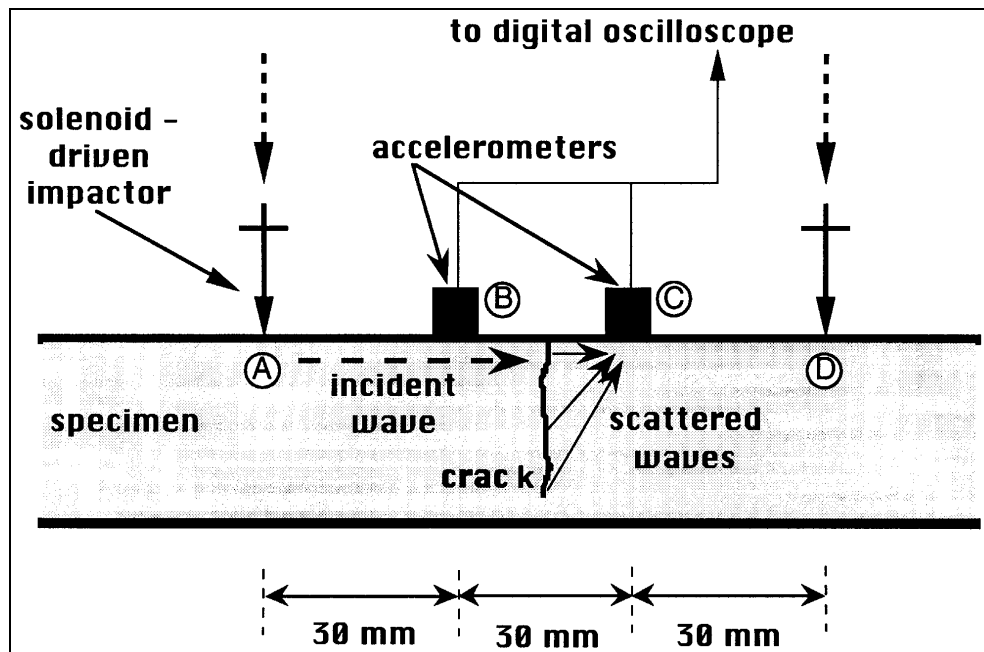

Figure 4-16: FTC configuration

(Popovics et al. 2000)
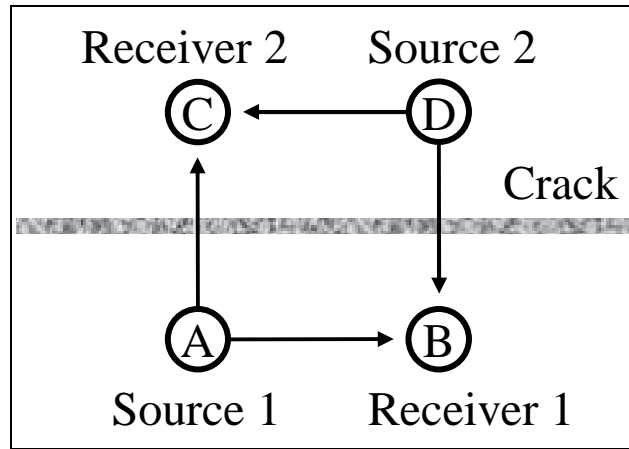
Figure 4-17: WTC test setup for the evaluation of cracks

# CHAPTER 5. VISCO-ELASTIC FREQUENCY-DEPENDANT PROPERTIES OF ASPHALT CONCRETE

## 5.1. Introduction

The strain of a pavement structure under a certain load is determined by the stiffness of its asphalt concrete mixture. As asphalt mixes are composite materials, their mechanical behaviour primarily depends on the viscous properties of the asphalt binder and the volumetric properties of the mixture. Because of this visco-elastic characteristic, the stiffness of a given mixture varies with temperature and frequency.

On one hand, ultrasonic methods used for asphalt pavement evaluation are able to determine high frequency moduli. On the other hand, traffic loads on highways correspond to a frequency of approximately 25 Hz. Therefore, a model describing the frequency dependant behaviour of asphalt concrete needs to be determined in order to compare the measured high frequency moduli with the 25 Hz design value (Barnes and Trottier 2009).

## 5.2. Dynamic Complex Modulus

For visco-elastic materials such as asphalt mixes, the stress-to-strain relationship is defined by a complex stiffness E*, which is the ratio of the stress amplitude σ over the strain amplitude ε. When the load is sinusoidal, with an angular frequency ω, it is expressed as follows:

$$\sigma = \sigma_0 \cdot e^{j\omega t} \tag{5-1}$$

$$\varepsilon = \varepsilon_0 \cdot e^{j(\omega t - \varphi)} \tag{5-2}$$

$$E^* = \frac{\sigma}{\varepsilon} = \frac{\sigma_0}{\varepsilon_0} e^{j\varphi} \tag{5-3}$$

The dynamic modulus is defined as the absolute value of the complex number E*:

$$\left| E^* \right| = \frac{\sigma_0}{\varepsilon_0} \tag{5-4}$$

The phase angle φ characterizes the viscous properties of the material. φ = 0 refers to a pure elastic material (E* is a real number) whereas φ = π/2 corresponds to a pure viscous material (E* is a pure imaginary number).

## 5.3. Time-Temperature Superposition Principle

Tests at different temperatures provide different values of dynamic modulus. The various curves can be shifted with respect to time or frequency at a reference temperature $T_R$ in order to form a single master curve. A reference temperature of 70°C (21.1°C) is commonly used (NCHRP 1-37A 2004).The shifting is performed using a shift factor a(T) which is a function of temperature. The reduced frequency of loading $f_r$ at reference temperature is calculated from the frequency of loading f at desired temperature according to the equation:

$$f_r = f \times a(T) \tag{5-5}$$

At reference temperature, no shifting is required and $a(T_R) = 1$.

The temperature dependency of the material is described by the amount of shifting that is required to form the master curve. Several models have been developed to determine the shift factors. Two functions have been commonly used to model the time-temperature superposition relationship in asphalt binders and mixtures: the Williams-Landel-Ferry (WLF) and Arrhenius equations (Bonaquist and Christensen 2005). In 1955, Williams, Landel and Ferry proposed the following model to calculate the shift factors (Williams et al. 1955):

$$Log[a(T)] = \frac{-C_1(T - T_S)}{C_2 + T - T_S} \tag{5-6}$$

where $T_S$ is a reference temperature, and $C_1$ and $C_2$ are two coefficients. If $T_S$ is chosen about 50°C above the glass transition temperature of the mix, $C_1 = 8.86$ and $C_2 = 101.6$.

The Arrhenius equation is (Medani et al. 2004):

$$Ln[a(T)] = \frac{\Delta H}{R} \left( \frac{1}{T} - \frac{1}{T_R} \right) \tag{5-7}$$

where ΔH is the activation energy (J/mol), R = 8.314 J/(mol·K) is the ideal gas constant, and $T_R$ is the reference temperature (K). If the difference between the temperature to be shifted and the reference temperature $(T-T_R)$ is less or equal to 20°C, the Arrhenius equation gives a better fit than the WLF equation. Otherwise, it is the contrary.

Another model to determine the shift factor, used by Witczak and Bari (2004; 2006), is a second order polynomial relationship between the logarithm of the shift factor and the temperature:

$$Log[a(T)] = aT^2 + bT + c \tag{5-8}$$

66

where T is the temperature of interest (°F), and a, b, c are coefficients of the polynomial.

The mechanistic-empirical pavement design guide (M-EPDG) uses a different equation that accounts for both temperature and asphalt aging (NCHRP 1-37A 2004). This guide uses a hierarchical approach based on three levels. Level 1 involves comprehensive laboratory and field tests. In contrast, level 2 and level 3 require the designer to estimate the most appropriate design input values and are based on little or no testing. In the input level 1, the shift factors are expressed as a function of the binder viscosity:

$$\text{Log}[a(\text{T})] = c\left(\log(\eta) - \log(\eta_{T_R})\right) \tag{5-9}$$

where $\eta$ is the viscosity at the age and temperature of interest (cPoise), $\eta_{TR}$ is the Rolling Thin Film Oven (RTFO) aged viscosity at the reference temperature (cPoise), and c is a constant.

In order to determine the shift factors, a relationship must be established between binder viscosity and temperature. First, binder complex shear modulus (G*) and phase angle (δ) testing are conducted on the asphalt binder over a range of temperature. Then, the binder stiffness data is converted to viscosity for the selected range of temperature:

$$\eta = \frac{G*}{10}\left(\frac{1}{\sin(\delta)}\right)^{4.8628} \tag{5-10}$$

Finally, the ASTM viscosity temperature relationship is determined by linear regression, after log-log transformation of the viscosity data and log transformation of the temperature data:

$$\log\log\eta = A + VTS \times \log T \tag{5-11}$$

where $\eta$ is the viscosity in cPoise, T is the temperature in Rankine at which the viscosity was determined, and A and VTS are regression parameters.

The viscosity of the binder at any time is predicted using the Global Aging System, which is part of the Design Guide software. The aged viscosity can then be used in equation (5-9) to calculate shift factors that account for both temperature and aging effects.

## 5.4. Sigmoidal Model

In general, master curves are mathematically modeled by a sigmoidal function, written as follows:

$$\text{Log}|E*| = \delta + \frac{\alpha}{1 + e^{\beta - \gamma \cdot \log(f_r)}} \tag{5-12}$$

where δ is the minimum modulus value, α is the span of modulus values, β and γ are shape parameters. As illustrated in Figure 5-1, γ represents the steepness of the function and β

determines the horizontal position of the turning point. Thus, in logarithmic scales, $\beta/\gamma$ is the x-value of the turning point, which has a y-value of $\delta+\alpha/2$.

The master curve is constructed by fitting the dynamic modulus test data with a sigmoidal function using a non linear optimization method. Two different methods can be used to determine the Shift factors. On one hand, they can be calculated using one of the equations (5-6), (5-7) or (5-8). On the other hand, they can be determined simultaneously with the coefficients of the sigmoidal function, when performing the non linear regression. The second method is used in the M-EPDG: the coefficient $c$ from equation (5-9) is calculated simultaneously with $\alpha$, $\beta$, $\gamma$ and $\delta$ when fitting the model. Figure 5-2 illustrates this fitting process.

The sigmoidal model is used to model the dynamic modulus data because it captures the physical properties of asphalt mixtures. At cold temperatures, the mixtures stiffness is limited by the binder stiffness. The upper part of the sigmoidal function approaches this maximum stiffness. At high temperatures, the mechanical behaviour is more dominated by the aggregates, and the stiffness approached a minimum equilibrium value. The lower part of the sigmoidal function captures this limiting equilibrium.

## 5.5. E* Predictive Equation.

The master curve can be directly determined from existing predictive models and mixture properties, without requiring any laboratory test data. This is performed at the hierarchical levels 2 and 3 of the M-EPDG. The Witczak dynamic modulus predictive equation is one of the most comprehensive models available. Based on information readily available from material specifications or volumetric design of the mixture, it can predict the mixture stiffness over a range of temperatures, loading rates, and aging conditions (Garcia and Thompson 2007):

$$\log|E^*| = 3.750063 + 0.02932\rho_{200} - 0.001767(\rho_{200})^2 - 0.002841\rho_4 - 0.058097 \cdot V_a$$
$$- 0.802208\frac{V_{beff}}{V_{beff}+V_a} + \frac{3.871977 + 0.0021\rho_4 + 0.003958\rho_{38} - 0.000017(\rho_{38})^2 + 0.00547\rho_{34}}{1 + \exp(-0.603313 - 0.313351 \cdot \log(f) - 0.393532 \cdot \log(\eta))} \quad (5-13)$$

where,

$|E^*|$ = dynamic modulus of mix, psi

$\eta$ = viscosity of binder, $10^6$ Poise

$\rho_{200}$ = % passing the 0.075 mm (#200) sieve

$\rho_4$ = cumulative % retained on the 4.76 (#4) sieve

68

$\rho_{38}$ = cumulative % retained on the 9.5 mm (3/8) in sieve

$\rho_{34}$ = cumulative % retained on the19 mm (3/4) in sieve

$V_a$ = air void, % by volume

$V_{beff}$ = effective binder content, % by volume

According to Bari and Witczak, this relationship does not consider the effect of frequency on the stiffness of the binder (Bari and Witczak 2006). Therefore, they proposed a new revised version of the predictive model using the complex shear modulus $G_b*$ of binder instead of the stiffness obtained from a typical ASTM viscosity temperature relationship:

$$Log|E*| = -0.349 + 0.754|G_b*|^{-0.0052}$$
$$\times \left( \begin{array}{c} 6.65 - 0.032\rho_{200} + 0.0027(\rho_{200})^2 + 0.011\rho_4 - 0.0001(\rho_4)^2 \\ + 0.006\rho_{38} - 0.00014(\rho_{38})^2 - 0.08V_a - 1.06\left( \dfrac{V_{beff}}{V_{beff} + V_a} \right) \end{array} \right)$$
$$+ \frac{2.56 - 0.03V_a + 0.71\left( \dfrac{V_{beff}}{V_{beff} + V_a} \right) + 0.012\rho_{38} - 0.0001(\rho_{38})^2 - 0.01\rho_{34}}{1 + \exp\left( -0.7814 - 0.5785 \cdot \log|G_b*| + 0.8834 \cdot \log\delta_b \right)}$$

(5-14)

where,

|E*| = dynamic modulus of mix, psi

$\rho_{200}$ = % passing #200 sieve

$\rho_4$ = cumulative % retained on #4 sieve

$\rho_{38}$ = cumulative % retained on 3/8 in sieve

$\rho_{34}$ = cumulative % retained on 3/4 in sieve

$V_a$ = air void, % by volume

$V_{beff}$ = effective binder content, % by volume

$|G_b*|$ = dynamic shear modulus of binder, psi

$\delta_b$ = phase angle of binder associated with $|G_b*|$, degree

Due to its similarities to the model currently used in the M-EPDG, this new model could be easily incorporated in a future revision of the pavement design guide. Moreover, with the adoption of the performance grading system, the $G_b*$ data will be more available than the A-VTS data, defined in equation (5-11), which is another motivation for the revised version.

## 5.6. Comparison of Low and High Frequency Measurements

Once the master curve has been determined, using laboratory test data and a fitting method or using a predictive equation and mixture properties, it can be used to shift the high frequency modulus measured with ultrasonic waves down to a low frequency design value. The shifting

process is described in Figure 5-3. The measured high frequency modulus at the temperature of interest is first shifted to the reference temperature. Then, it is multiplied by the ratio of the master curve modulus at low frequency divided by the master curve modulus at the reduced frequency of interest.

Barnes and Trottier performed MASW measurements on asphalt concrete specimens to determine their high frequency moduli (Barnes and Trottier 2009). Using a master curve constructed from dynamic modulus tests to shift the high frequency moduli down to a design frequency of 25 Hz, they found that the MASW results agreed well with the reference modulus.

In a project conducted at the University of Texas, both dynamic modulus and seismic measurements were performed on asphalt specimens (Nazarian et al. 2002). The master curve at reference temperature was found to follow the shifted seismic points quite nicely. It was concluded that the seismic and dynamic moduli of a given material could be readily related through a master curve, and that the quality control of an asphalt concrete layer can be carried out with seismic data.

In this research project, master curves are used to compare high frequency moduli measured with surface waves and low frequency moduli determined with the portable falling weight deflectometer.

## 5.7. Summary

One of the most important properties of hot-mix asphalt affecting the structural capacity of a flexible pavement is its dynamic modulus. Due to the visco-elastic behaviour of asphalt mixes, the modulus changes significantly with temperature, rate of loading, as well as aging. This chapter describes the time-temperature superposition principle that is used to shift moduli to a reference temperature. The shifting process results in a master curve that shows the variation of the modulus with the frequency of loading at the reference temperature. This curve can be used to compare high-frequency moduli measured with seismic methods and low-frequency moduli measured with dynamic modulus testing or deflection devices.
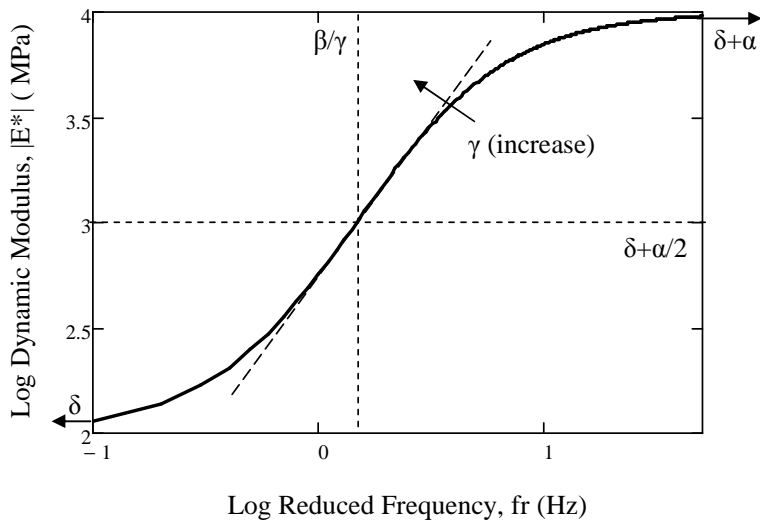
Figure 5-1: Sigmoidal function

$\alpha = 2$

$\beta = 0.5$

$\gamma = 3$

$\delta = 2$
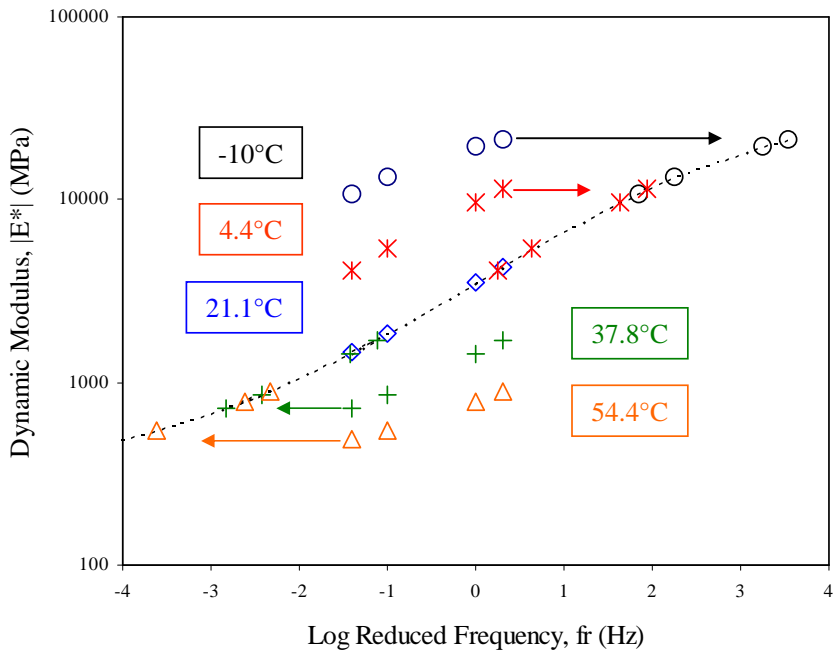


Test performed at:
- 5 temperatures
  (1 symbol each)
- 4 frequencies

Figure 5-2: Fitting the sigmoidal function

71
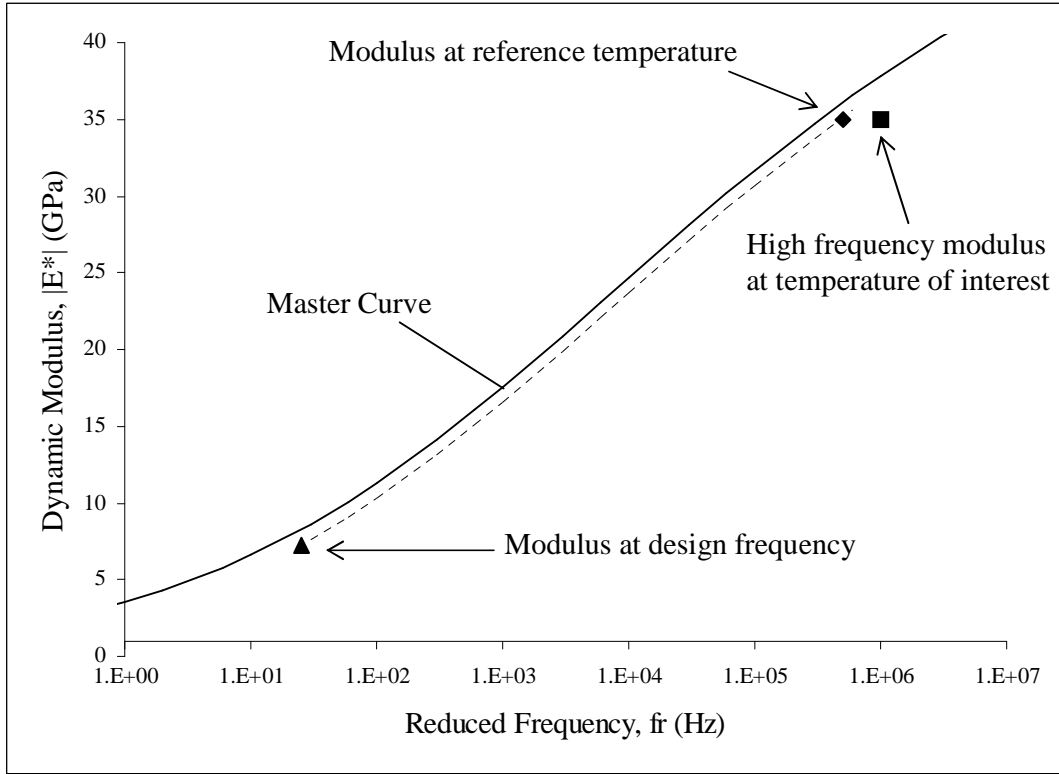
Figure 5-3: Shifting the high frequency modulus to a design frequency

# CHAPTER 6.   EXPERIMENTAL METHODOLOGY, PREPARATION OF ASPHALT SPECIMENS, AND TEST SETUP

## 6.1.  Introduction and Experimental Program

The experimental program presented in Figure 6-1 consisted of two phases: the fabrication of jointed asphalt slabs and the development of the LWD and MASW techniques for longitudinal joint evaluation. The compaction procedure used for the preparation of the slabs was not standard and had to be calibrated. Therefore, asphalt samples were prepared to estimate a relationship between the density and the effort required for compaction. Then, an asphalt slab with a medium quality longitudinal joint was manufactured in the laboratory. The selection of the configurations used for LWD and MASW tests was based on preliminary measurements performed on asphalt samples in the laboratory or on real roads. Then, MASW testing was performed on the jointed asphalt slab to determine if this technique was, first, able to detect the joint, and second, able to discriminate between sections of different qualities. Finally, field tests were conducted at different sites to see if longitudinal joints compacted with the actual equipment used in the field could be detected, and if the testing configuration used in this study was suitable for testing on actual roads with traffic control.

This chapter describes the compaction procedure that was developed for the fabrication of asphalt slabs with joints in the laboratory. Following this, the configuration of the LWD and MASW methods used in this study are presented.

## 6.2.  Fabrication of Pavement Slabs

Several techniques have been commonly used for the compaction of HMA specimens in the laboratory. Three of them are available at the CPATT laboratory at the University of Waterloo:

- Marshall Hammer
- Asphalt Vibratory Compactor
- Superpave Gyratory Compactor

The Superpave Gyratory Compactor produces specimens with densities comparable to the one achieved in actual pavements. However, differences can be observed so it is desirable to test both gyratory prepared samples and field samples. It simulates the kneading action of rollers used in the field. However, this compactor is not suitable for the preparation of large asphalt slabs. The

73

Asphalt Vibratory Compactor presents the same limitations since the available moulds are too small.

Zhiyong Jiang (2007) tried three compaction methods to prepare asphalt slabs in the laboratory as part of his MASc project at the University of Waterloo. The roller compactor was not suitable to achieve the desired compaction level. The use of a vibrating plate compactor was not successful either, as vibrations resulted in the displacement of loose material. The traditional method based on a hand hammer provided better compaction. Consequently, a method similar to the Marshall procedure was developed in this project to compact asphalt slabs with joints in their middle.

### 6.2.1.    Calibration of the Compaction Procedure

The Marshall method was developed by Bruce G. Marshall just before World War II resulting in a procedure that would determine the asphalt content of asphalt mixtures using available laboratory equipment (Roberts et al. 2003). It is a simple, compact and inexpensive method. Despite its limitations to reproduce the compaction performed in the field, the Marshall method is probably the most widely used mix design method in the world. The preparation of Marshall specimens is described in the Ministry of Transportation of Ontario Laboratory Testing Manual (Test Method LS-261 2001). First, the aggregates and the asphalt cement are mixed in a bowl. Then, the mix is poured in a cylindrical mould, and compacted using a hand hammer or a mechanical compactor.

In this research project, a procedure similar to the Marshall method has been developed for the compaction of HMA slabs. Before compacting any slab that require large quantities of material, the method was calibrated by preparing samples in smaller moulds, as explained in the following section. The objective of this preliminary phase was to determine a relationship between the volumetric properties of the asphalt samples and the effort required to compact them.

6.2.1.1.    Method for Preparation of HMA Specimens

For this research project, hot mix collected directly from an asphalt plant was used for the preparation of the specimens. It had the advantage of providing more consistency between different HMA batches, as aggregates and asphalt cement mixing was performed in large quantities. Mixing in the laboratory would result in a higher variability among the batches. The method adopted for the preparation of the specimens was based on the Marshall method for preparation of field samples (Test Method LS-261 2001). Table 6-1 describes the different steps

of the preparation. The compaction was performed with the hand hammer shown in Figure 6-2. A 20.2 kg weight was dropped at a height of 72.8 cm on a steel plate having the same dimensions as the mould. A $20\times20\times10$ cm$^3$ wooden box was used as a mould for the asphalt specimens. Three boxes were built to allow the preparation of several samples at the same time. The compaction was performed in two layers. Each layer was 40 mm thick; as a result the compacted specimens were 80 mm thick, as illustrated in Figure 6-3.

### 6.2.1.2.     HMA Mixes Used for the Fabrication of Slabs

A Hot-Laid 4 (HL 4) mix was used to prepare the first specimens. The objective was to get a first idea of the compaction procedure and the number of blows that are required to reach targeted densities. Before preparing any specimen, the theoretical maximum relative density (TMRD) of the mix was measured according to the test method described in the MTO Laboratory Testing Manual (Test Method LS-264 2001). The TMRD must be known to calculate the weight of material needed for the preparation of a specimen in order to reach the desired density. The results are presented in Table 6-2. Two measurements gave an average TMRD of 2.500, with a range of ±0.003.

More material was required to properly calibrate the compaction procedure, which is to find a relationship between the number of blows and density. For this purpose, a Hot-Laid 3 (HL 3) mix containing 15% of reclaimed asphalt pavement (RAP) was used. It is a dense-graded surface course mix for intermediate volume roads with a maximum aggregate size of 16 mm, which compares to the Superpave mix SP 12.5. It is typically used throughout Ontario on most collector and arterial facilities. Four samples were used to determine the TMRD, as shown in Table 6-2. A TMRD of 2.529 was found, with a standard deviation of 0.002.

Both HL 4 and HL 3 mixes were collected from Steed and Evans Limited. The mix design report is provided in Appendix A for the HL 3 mix.

### 6.2.1.3.     Preparation of HMA Specimens

The objective was to determine the number of blows required to compact specimens at a desired density. First, the number of blows was calculated by comparison with the Marshall compaction method, which has the following features:
   ·    Number of blows: $Nb_M = 75$ per side = 150 total
   ·    Weight of the falling mass: $m_M = 4.536$ kg

- Dropping height: $h_M$ = 457 mm
- Size of the compacted briquette: height: 63.5 mm; diameter: 101.5 mm; volume: $V_M$ = 513.8 cm$^3$

The compaction method developed in this study had the following features:

- Number of blows: Nb
- Weight of the falling mass: m
- Dropping height: h
- Size of the compacted sample: height: 40 mm (for one layer); width: 207 mm; volume: V = 1714 cm$^3$

Theoretically, the same density should be achieved with both methods provided that the same compaction effort is impacted to the specimen. Therefore, the ratio energy over volume should be the same, which results in the following equation:

$$\frac{Nb \cdot m \cdot h}{V} = \frac{Nb_M \cdot m_M \cdot h_M}{V_M} \qquad (6\text{-}1)$$

During the compaction of the specimens, the hammer broke three times and had to be reinforced. Consequently, the theoretical number of blows required to achieve the same density as the Marshall method was calculated for the four versions of the hand hammer. The results are given in Table 6-3.

The first specimens were compacted with a number of blows close to the theoretical value. However, density measurements indicated that the desired density was not achieved. This was probably due to the fact that the compaction could not be performed on both sides of the specimen, and the shape of the mould was different from the one used in the Marshall method. Therefore, more specimens were prepared and the numbers of blows required for their compaction were estimated by interpolation of the results obtained from the previous specimens. Specimens were prepared until the regression model obtained from previous measurements was able to predict future results over a wide range of densities.

6.2.1.4.    Density Measurements and Regression Model

Two methods were used to measure the density of the specimens. First, the standard method of test using saturated surface-dry specimens was adopted (AASHTO T 166-07 2009). The results are shown in Table 6-4. As expected, the air void increased when the number of blows was reduced. However, the increase in air void was not significant for the specimens D1, D2 and D3

which were compacted with only 8, 14 and 24 blows in total. This is due to the limitations of the saturated surface-dry specimens' method which is not well suited for samples that contain open or interconnecting voids. When the air void is high, water trapped inside the specimen can escape and the mass of saturated surface-dry specimens after immersion could be significantly reduced. Consequently, a second standard method of test was used to calculate the density of the specimens with a better accuracy: the automatic vacuum sealing method (AASHTO T 331-08 2009). This time, measurements were performed only on the specimens prepared with the HL 3-R15 mix that would be used for the preparation of the slabs. The results are presented in Table 6-5. In accordance with the previous remarks, air voids were found to be higher than the one obtained with the first method, especially for low compacted specimens.

Before comparing the densities of all the specimens, some corrections should be applied to the results. The specimens did not weigh the same so the number of blows required for compaction had to be divided by the dry mass in order to compare air voids of different specimens. Also, four different versions of the hammer were used for compaction and did not impact the same energy to the specimens. Therefore, the numbers of blows applied with the first three versions had to be multiplied by a correction factor to compare the results with the fourth version. The equivalent number of blows $Nb_{Deq}$ that needs to be applied with hammer D to generate the same energy as $Nb_i$ blows applied with hammer i is given by:

$$Nb_{Deq} = \frac{m_i h_i}{m_D h_D} Nb_i \qquad (6\text{-}2)$$

where i is an index for the hammer version (i = A, B, C or D), and $m_i$ and $h_i$ are respectively the falling weight and dropping height of the hammer i.
Table 6-6 provides the values of the correction factor for the different hammer versions.

Figure 6-4 shows the results after correction for all the specimens prepared in this study. It presents the variation of air void with respect to the number of blows applied per kilogram of mix. Several observations can be made from this graph:

- As noticed before, air voids measured with saturated surface-dry specimens are lower than the ones measured with the automatic vacuum sealing method.
- Two different trends are observed for the air voids measured with the automatic vacuum sealing method: one for the specimens compacted with hammer C, and the other one for the specimens compacted with hammer D.

- The results obtained with the HL 4 mix do not follow any of the two trends obtained with the HL 3 mix.

As a result, only HL 3 specimens compacted with the last version of the hammer were considered for the model. Equation (6-2) was not able to correct the results obtained with different hammers and density measurements with saturated surface-dry specimens were less accurate than the one performed with the automatic vacuum sealing method.

The final regression model between the number of blows and the air void is provided in Figure 6-5. An exponential model was used for the regression, as it provided a higher coefficient of determination than linear, polynomial, and logarithmic models. The following equation was obtained:

$$Nb = 127.4 \times e^{-0.3676 \times AV}$$
$$R^2 = 0.9938$$

(6-3)

where Nb is the number of blows required to compact one kilogram of mix and AV is the air void of the specimen.

### 6.2.2. Fabrication of the Slabs

Two asphalt slabs were cut from the HL 3 section of the CPATT Test Track, Waterloo, Ontario (Tighe et al. 2007). The slabs were cut with a concrete saw, delicately extracted from the road, and transported to the laboratory. Then, they were placed on bedding sand and a wooden frame was built around each slab in order to mitigate the creation of cracks that would appear without confinement. A picture of the two pavement slabs is provided in Figure 6-6. Slab 1 was cut on the right wheel path while Slab 2 was collected near the centreline of the road. These slabs have the advantage to be representative of an actual pavement. However, they do not have a longitudinal joint and could not be used to evaluate the ability of NDT techniques to detect joints.

The preparation of slabs in the laboratory allows constructing a joint of controlled density. Originally, the objective was to build slabs with joints of different quality (poor, medium and good) to see their effect on non destructive measurements. Nevertheless, only one slab could be compacted at this point of the research project. It is recommended that more slabs be prepared for further testing in the future to assess the ability of the LWD and MASW to properly discriminate between levels of joint quality.

A picture of the molding frame that was built to fabricate the slab in the laboratory is given in Figure 6-7. Its internal dimensions were: 80×60×9 cm$^3$. The frame was divided into two equal parts by a wooden beam in order to create a joint. The bottom and the sides of the frame were covered with heat resistant plastic sheets to prevent the mixture from sticking to the frame. The compaction procedure was similar to the one used for the preparation of small specimens that was described in the previous section. The construction of the jointed slab was performed in two layers, as explained in Table 6-7.

The objective of this slab was to determine if the NDT methods were able to detect a joint of poor quality. Wedge joints and tack coats have been used in the field to achieve a better compaction and bonding between the two lanes (Kandhal and Mallick 1996). These techniques were not used for the construction of the jointed slab in order to reduce the quality of the joint. Instead, the divider was kept vertical to obtain a conventional joint. Moreover, the material compacted in the first side was allowed to cool to about 60°C before placing asphalt in the other side, which reduced the bonding between the two sides. This method resulted in the construction of a semi-hot joint. The temperature of the asphalt mix during the compaction of the different layers is provided in Table 6-8.

The next step consisted of defining the desired density of the joint. In the field, joints are characterized by two edges. When the first lane is compacted, there is no confinement at the edge which results in a lower density than the interior portion of the mat. When the adjacent lane is placed, the unconfined edge of the first lane is colder and can not be compacted anymore. On the contrary, the edge of the second lane is confined and could reach higher densities than the mat. Typical density gradients across a longitudinal joint are presented in Figure 6-8. Most agency specifications require joint densities to be no more than two percent less than the mat density (Williams et al. 2009). Estakhri et al. (2001) proposed a comprehensive documentation of several studies of joint densities performed in different states of the US. Density differences between the unconfined edge of the joint and the interior portion of the mat ranged from 1.5% to more than 10%, with an average value around 4.5%. The report also presented data collected on airfield pavements. FAA specifications allow joint densities to be no more than three percent less than the required mat densities. Density data from several airport paving jobs indicated density differences between 1.9% and 4.1%. Based on the previous data, the following air voids were selected for the fabrication of the jointed slab:

- Interior portion of the mat: 7.5%

- Good quality joint: 9.5%
- Medium quality joint: 12.0%
- Poor quality joint: 15.0%

According to equation (6-3), the compaction of the mat requires 8 blows per kilogram of mix, which corresponds to 30 blows for one layer of a small specimen such as the one presented in Figure 6-3 ($20\times20\times4$ cm$^3$). The compaction of a poor quality joint with 15% air voids required only 0.5 blows per kilogram of mix, so 2 blows for one layer of a small specimen. During the preparation of the slab, this number of blows was found to be too small and did not provide a good surface condition as loose material was observed at the edges of the slab. Therefore, it was decided to construct a medium quality joint using 1.5 blows per kilogram of mix, thus 6 blows for one layer of a small specimen.

During the compaction of each layer, the hammer was moved along the slab following the path indicated in Figure 6-9. First, the hammer was placed at the upper left corner of the left side, and moved along line 1 at 10 mm intervals. Then, the hammer was moved along lines 2 and 3. The compaction of the right side started from the upper right corner and followed lines 4, 5, 6 and 7. As explained previously, the desired density required 30 hammer blows for each $20\times20$ cm$^2$ portion of the mat, and 6 blows for each $20\times20$ cm$^2$ portion of the left side of the joint that corresponds to the unconfined edge. Therefore, the following procedure was applied:
- Step 1: apply one blow per location along lines 1 and 3
- Step 2: apply four blows per location along line 2
- Step 3: repeat twice steps 1 and 2
- Step 4: apply one blow per location along lines 4 and 6
- Step 5: apply four blows per location along lines 5 and 7
- Step 6: repeat twice steps 4 and 5

According to the model developed in Section 6.2.1, the expected air void profile of the slab should be as presented in Figure 6-10. The unconfined edge of the joint is simulated by a 10 cm wide stripe of asphalt having an air void of 11.8%, which is 4.3% higher than the mat.

A picture of the compacted slab, termed Slab 3, is given in Figure 6-11. Severe segregation was observed at the corners, which were the least compacted areas of the slab. Moreover, some lighter segregation was observed at the left side of the joint. This is due to the fact that much more energy was applied to the interior portion of each side of the slab and resulted in the creation of loose material at the edges. Figure 6-11 also shows the bottom of the slab which surface condition

appeared to be much better than the top surface. Slight bumps were formed on the bottom surface because of air bubbles trapped between the plastic sheet and the wooden base of the frame. As described in the next chapter, testing was performed on the top and the bottom surfaces of the slab, termed as surface X and surface Y respectively. The idea was to compare MASW measurements on a rough and a smooth surface.

### 6.2.3. Nuclear Density Measurements on the Slabs

The compaction method used to prepare Slab 3 was calibrated with small samples. The mixture is not confined in the same way when preparing large slabs or small samples, which might result in different densities. Nuclear density measurements were performed on Slab 3 to estimate its actual density. Slab 3 was placed on a uniform pavement section in order to avoid any variation related to the density of the underlayer. The main objective was to compare the relative density of the different sections of the slab.

Nuclear density testing requires a good contact between the gauge and the asphalt surface. Any air gap would result in a significant drop in the measured density. Therefore, measurements were conducted on the smooth surface Y of the slab. As it will be explained in the following chapter, aluminum plates were glued across the joint to provide a good coupling between the accelerometers and the asphalt surface. The nuclear gauge was moved along line 1 and line 2 in order to avoid any interaction with the metallic plates, as indicated in Figure 6-10. Measurements were taken at six locations every 10 cm intervals so as to follow the compaction path. Two different orientations of the gauge were used at each location to reduce the variability introduced by the surface irregularities. Five readings were collected for each orientation, and the results are provided in Appendix B.

Figure 6-12 shows the average air void measured at each location, including readings from both lines. The expected air void indicated on the graph was calculated by taking the average of the expected air voids on both sides of the line. The measured density was consistently lower than the expected density, with an average increase of 1.7% air void. Equation (6-3) over predicted the density, which was due to the fact that the mixture was less confined in the slab than in the squared samples. Another reason might be that the wooden base used for the preparation of the slab was not very stiff, resulting in less compaction effort than expected.

A good agreement was observed between the trends of the expected and measured density curves, indicating that a lower density was achieved at the unconfined edge of the joint. Nevertheless, an important variability was noticed in the data. The air void showed an average standard deviation of 1.8%.

Another factor must be taken into consideration when analysing the data. The surface of the density gauge in contact with the asphalt was 30 cm long, and measurements taken at each location were affected by the adjoining sections. The previous analysis was based on the assumption that the measurements were mostly affected by the 10 cm wide asphalt section located below the centre of the gauge.

In conclusion, the results indicated that the compaction procedure used in this study was able to reproduce the horizontal density profile of a longitudinal joint. However, this conclusion should be confirmed by taking cores from the slab and measuring densities with the automatic vacuum sealing method.

Density measurements were also performed on Slab 1 and Slab 2. The following average densities were obtained:

- Slab 1: $\rho = 2352$ kg/m$^3$; $\sigma = 13$ kg/m$^3$
- Slab 2: $\rho = 2381$ kg/m$^3$; $\sigma = 26$ kg/m$^3$
- Slab 3: $\rho = 2251$ kg/m$^3$; $\sigma = 51$ kg/m$^3$

The densities of the slabs extracted from the Test Track were significantly higher than the density of the slab compacted in the laboratory. Consequently, higher densities were achieved in the field with roller compactors than in the laboratory with the hand hammer. The standard deviation was lower for Slab 1 and Slab 2 than for Slab 3 since fewer locations were tested on these slabs.

According to the theoretical maximum density provided in the mix design report for the HL 3 mix used at the Test Track (Appendix C), Slab 1 and 2 are characterized by air voids of 4.9% and 6.0% respectively.

## 6.3. Testing Equipment and Configuration

### 6.3.1.    Portable Falling Weight Deflectometer

The Dynatest LWD 3031 described in Section 4.2 was used to collect the deflection data. In order to get the best results from the analysis with the LWDmod software, testing was performed with:

- ·  Different falling heights
- ·  Different plate sizes (300 mm, 150 mm and 100 mm diameters)

Small plate diameters were used to ensure that the measurements were mostly affected by the top layers of the pavement that contain the joint. An average of six measurements was taken at each testing location. The additional geophones were not calibrated and could not be used.

Figure 6-13 presents the configuration used for testing across the joints. The LWD was placed at three different locations:

- ·  On the centreline
- ·  On the northbound lane, one meter away from the centreline
- ·  On the southbound lane, one meter away from the centreline

The objective was to detect any difference in stiffness across the joint.

### 6.3.2.    Surface Wave Based Method

#### 6.3.2.1.    Testing Equipment

The configuration used in this project for MASW testing is schematically illustrated in Figure 4-13. A 50 kHz ultrasonic transmitter was used to generate surface waves in the pavement. Tallavó et al. (2009) proposed a characterization of this source in a detailed paper. The Fourier spectra of the ultrasonic transmitter excited by a one-cycle sinusoidal pulse showed three main frequencies at 25.4 kHz, 36.6 kHz and 49.8 kHz. The latter is the nominal frequency of the transmitter. Twelve Dytran 3055B3 accelerometers with a 35 kHz resonant frequency and a sensitivity of 500±10 mV/g were used to record the surface waves. The transmitter was driven by a corresponding pulser (Pundit) while the accelerometers were driven by a power supply (Dytran 4123B) that could amplify the signal by a factor of 10 or 100. The LDS Nicolet Genesis was used for the acquisition of the data with a resolution in time of 1μs.

Measurements were taken across longitudinal joints with the transmitter on each side of the receiver array, as illustrated in Figure 6-14. The evaluation of the joint was based on attenuation parameters in the time and frequency domains, as explained in the next chapter.

6.3.2.2.    Coupling System

A critical point in the development of the wave based method was the selection of the coupling system between the pavement surface and the transducers. A good coupling was required between the transmitter and the asphalt to generate a strong wave that could propagate throughout the entire pavement section located under the receiver array. Similarly, proper coupling was needed between the receivers and the surface to record good quality signals. In order to determine the best coupling system, measurements were performed in the laboratory on an asphalt slab with one source and one accelerometer. The source was placed directly on the pavement, either without coupling or with vacuum grease. Different weights were placed on top of the source to apply a vertical pressure. The accelerometer was either placed directly on the asphalt surface or glued on an aluminum plate (15 mm diameter) which was fixed to the asphalt with epoxy. In the first case, the accelerometer was placed with or without vacuum grease while a vertical pressure was applied on its top.

The following results were obtained:

- A good-quality signal is transmitted by the source when coupled directly to the asphalt surface with vacuum grease.
- When a vertical pressure is applied on top of the source, the intensity of the transmitted signal is increased while the frequency content remains the same, as illustrated in Figure 6-15.
- The best measurement is obtained when the accelerometer is glued to an aluminum plate. However, this coupling method is time-consuming because of epoxy curing. A relatively good-quality signal is recorded by the accelerometer when coupled directly on the asphalt surface with vacuum grease. Figure 6-16 shows the differences between the signals acquired when gluing the accelerometer on an aluminum plate or using vacuum grease.
- When a vertical pressure is applied on top of the accelerometer, the intensity of the recorded signal is increased. Nevertheless, the frequency content is modified, as illustrated in Figure 6-17.

Using the previous observations, a first configuration was determined for the MASW tests conducted in July 2009 at the CPATT Test Track. Its characteristics are presented in Figure 6-18:

- The transmitter and the accelerometers are coupled to the asphalt surface with vacuum grease.
- Weights of 5.3 kg and 250 g are applied on top of the transmitter and the receivers respectively.
- A spacing of 40 mm is selected for two consecutive accelerometers.

6.3.2.3.    Design of a Structure to Hold the Receivers

The previous configuration did not require epoxying metallic plates on the asphalt which reduced the testing time. However, each accelerometer had to be placed individually on the pavement with vacuum grease and a weight on its top, which was still time consuming. Besides, the condition of the pavement surface had an important impact on the recorded signals. As a matter of fact, if the surface was very rough, some accelerometers had to be slightly moved from their original position to a flatter area in order to have a better coupling.

Consequently, a structure was design to hold the transducers vertically with a consistent pressure, and make the setup easier and less time consuming. Figure 6-19 provides a picture of the structure. Twelve small PVC pipes are fixed on a PVC plate. Foam cylinders which inside dimensions match the shape of the accelerometers are placed inside the pipes to isolate the receivers from the main structure. The objective was to ensure that any wave propagating through the structure would not be transmitted to the receivers. Finally, a foam stripe with twelve openings was placed on the side of the structure to keep parallel the cables coming out of the transducers.

## 6.4. Summary

The main objectives of the experimental program were described in this chapter. Asphalt samples were prepared in the laboratory to determine a relation between the volumetric properties and the effort required for compaction. Based on this relation, an asphalt slab with a joint in the middle was prepared in the laboratory. Nuclear density measurements showed a good agreement with the expected horizontal density profile of the slab. Finally, this chapter explained the different steps followed in this project to develop both MASW and LWD configurations used for longitudinal joint testing.

| Preparation of asphalt samples to calibrate the compaction procedure | Preliminary wave based measurements on asphalt samples in the laboratory to determine the coupling configuration for MASW testing | Preliminary LWD measurements on asphalt pavements to determine the testing procedure |
| --- | --- | --- |
| Preparation of an asphalt slab with a medium quality joint | | |
| MASW laboratory testing on the jointed asphalt slab | LWD and MASW field testing at the CPATT test track and the city of Hamilton | |

Figure 6-1: Experimental program



Figure 6-2: Hand hammer and mould used for compaction of HMA slab specimens
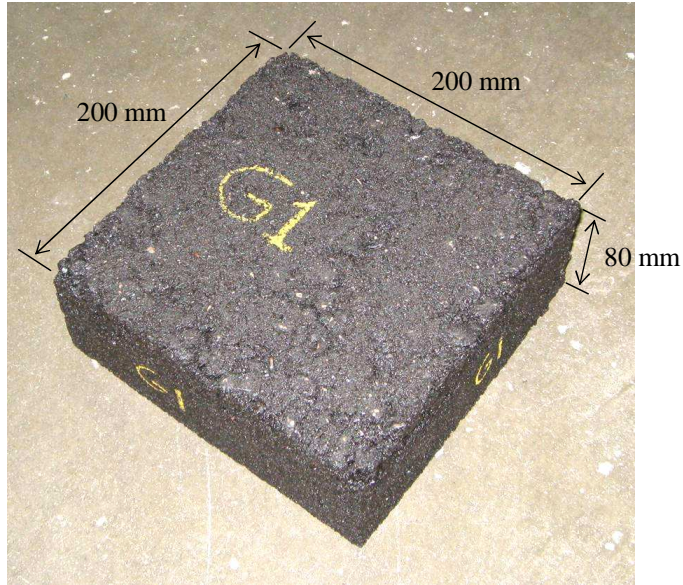
Figure 6-3: Compacted slab specimen
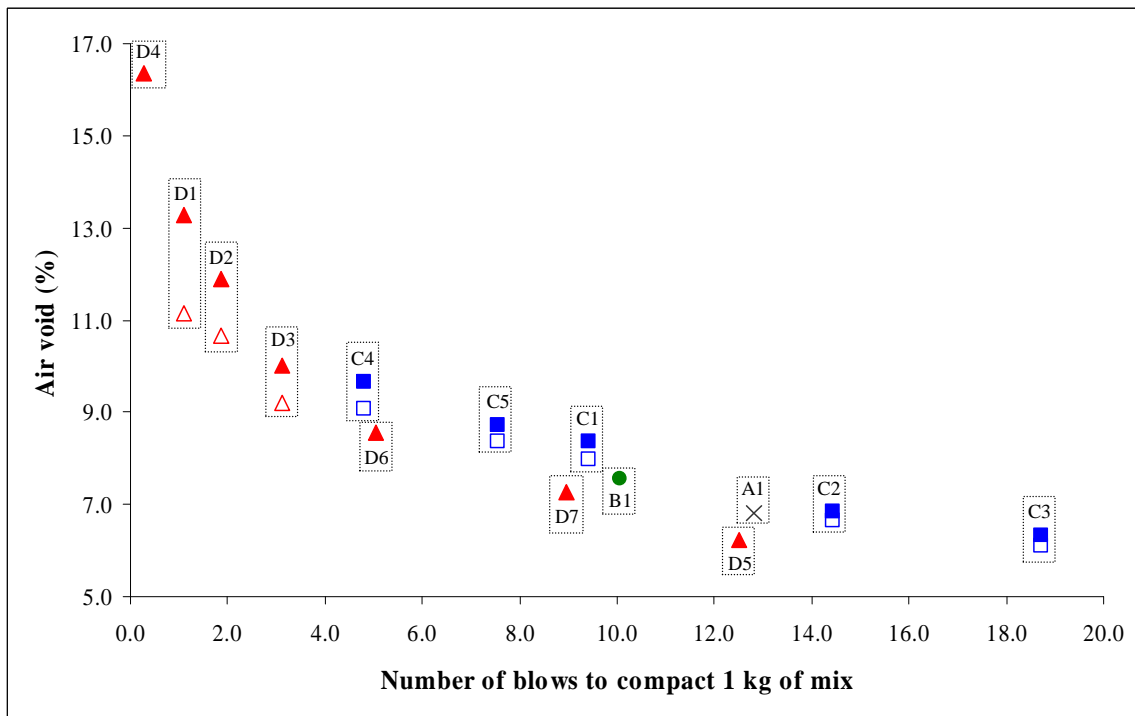


□ BRD 1 - Hammer C - HL3
■ BRD 2 - Hammer C - HL3
△ BRD 1 - Hammer D - HL3
▲ BRD 2 - Hammer D - HL3
✕ BRD 1 - Hammer A - HL4
● BRD 1 - Hammer B - HL4

*BRD 1: Bulk relative density measured with saturated surface-dry specimens*

*BRD 2: Bulk relative density measured with the automatic vacuum sealing method*

Figure 6-4: Air void vs. number of blows per kilogram of mix
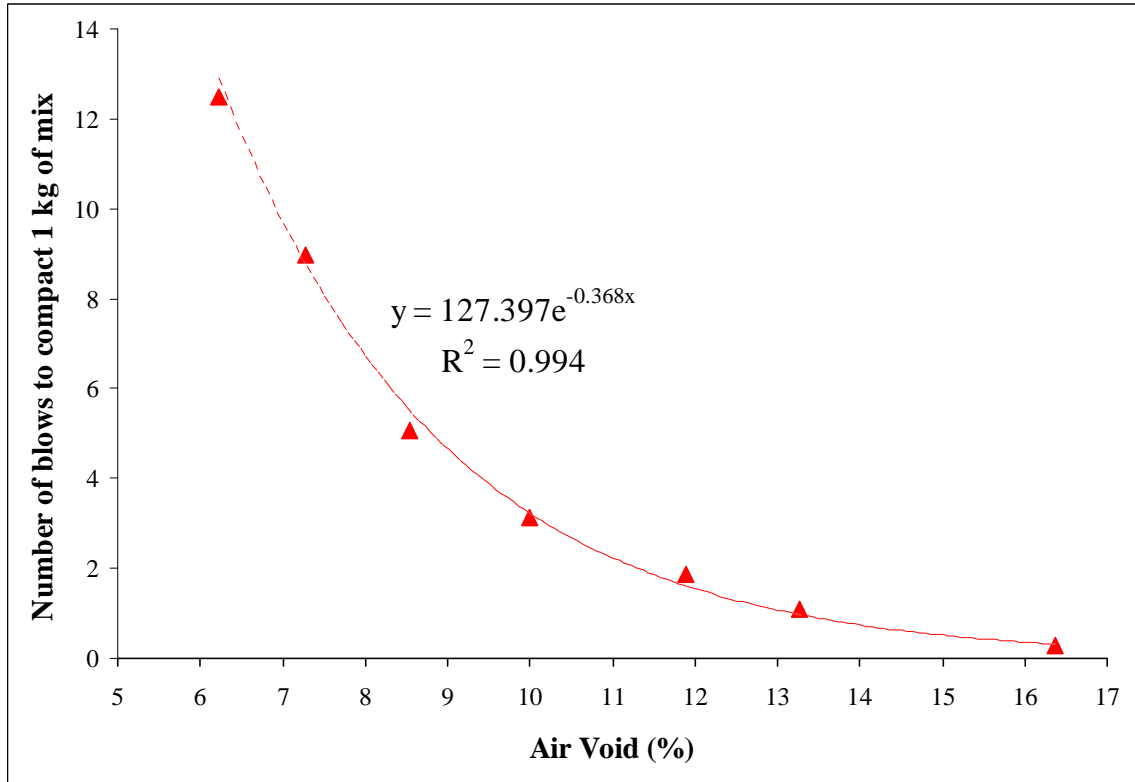
Figure 6-5: Regression model between air void and compaction effort

The equation shown on the chart:

$$y = 127.397e^{-0.368x}$$
$$R^2 = 0.994$$

Chart axis labels: Number of blows to compact 1 kg of mix (y-axis), Air Void (%) (x-axis)



835 mm
700 mm
Slab 2
720 mm
835 mm
Slab 1
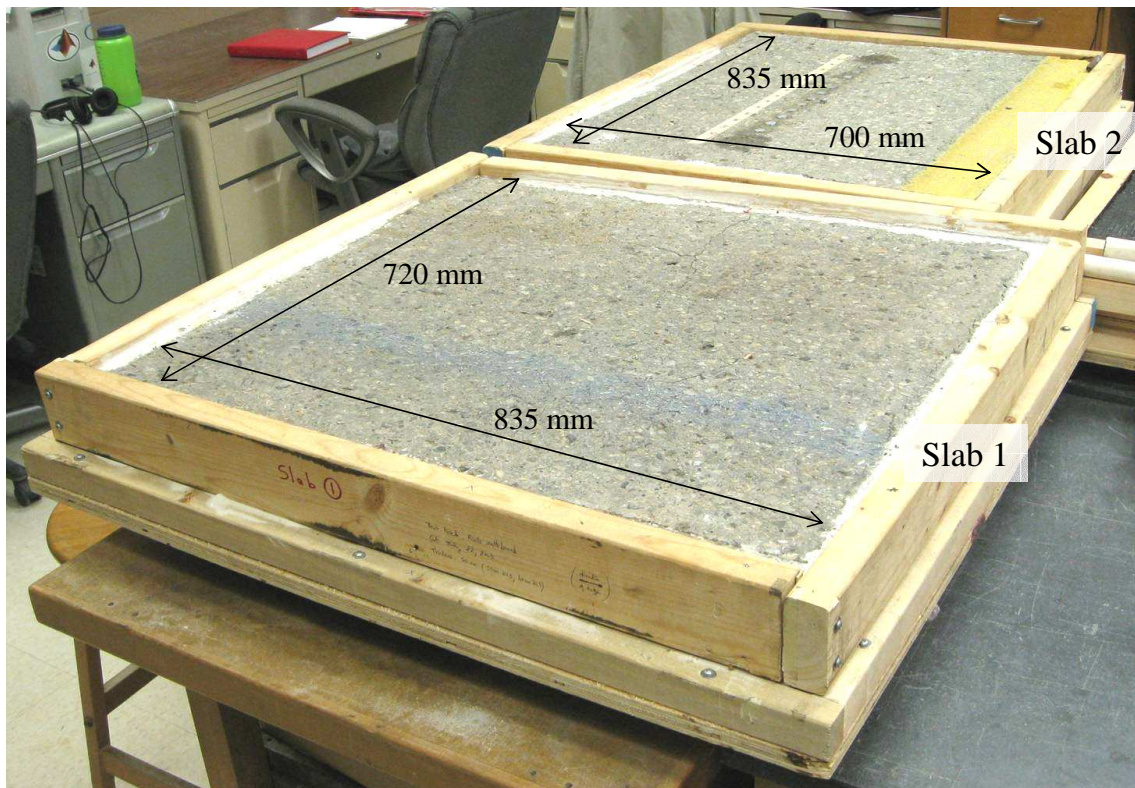
Figure 6-6: Asphalt slabs cut from the CPATT Test Track
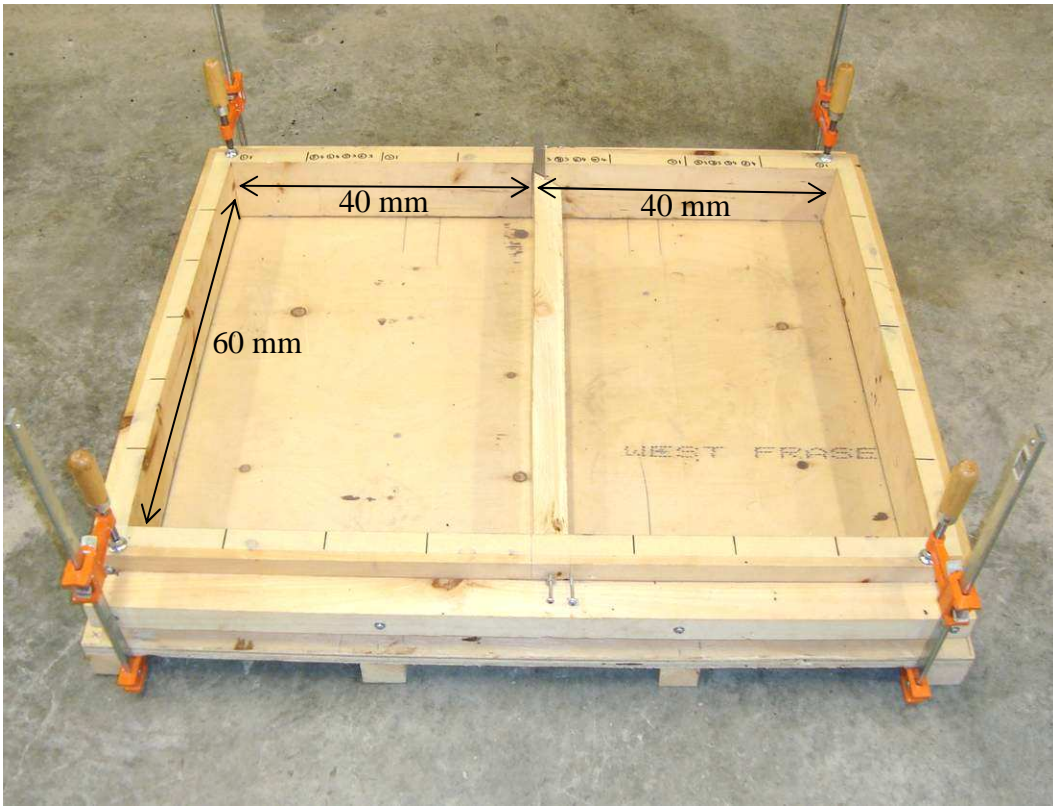
Figure 6-7: Mould for asphalt slab preparation in the laboratory
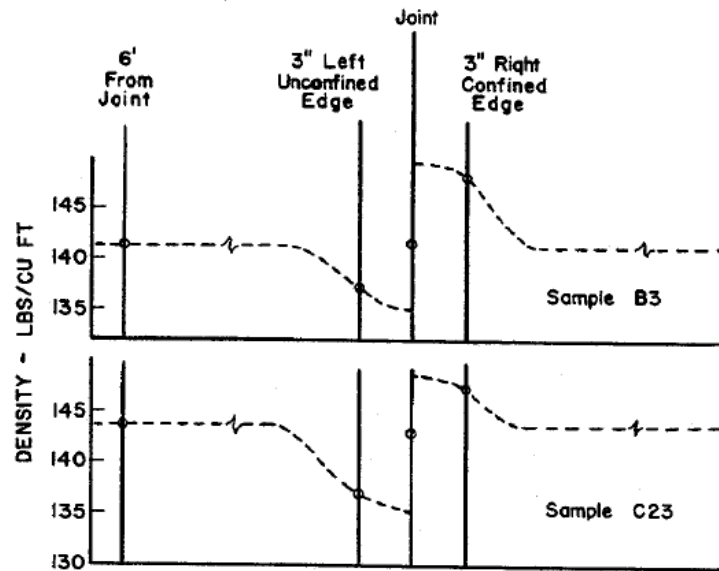


Figure 6-8: Typical density gradients across a joint (inspired from
(Estakhri et al. 2001)
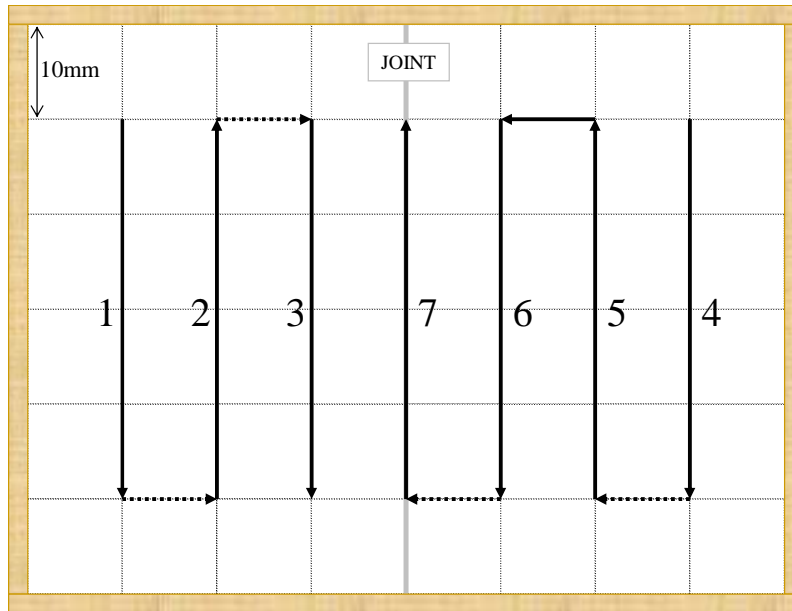
Figure 6-9: Compaction procedure of the slab with the hand hammer
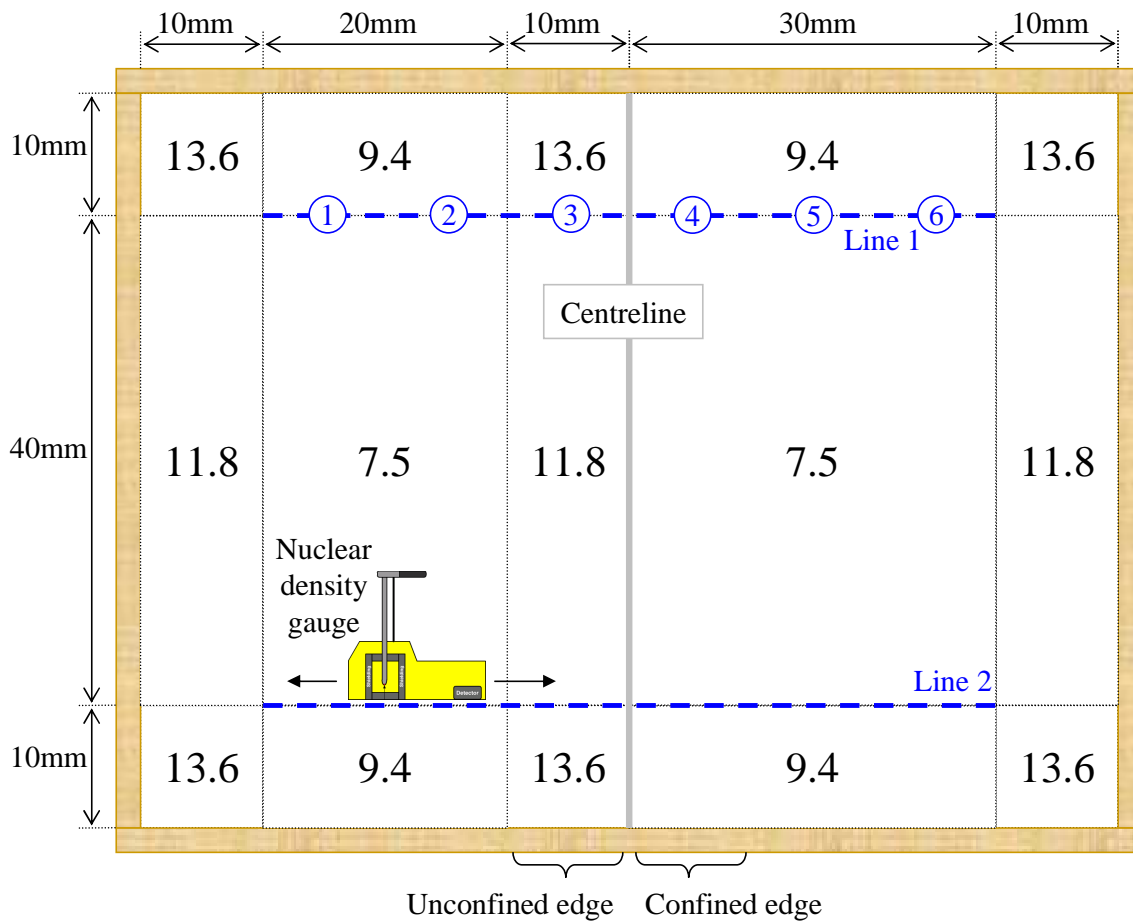


Figure 6-10: Expected air voids (%) of the different parts of the slab
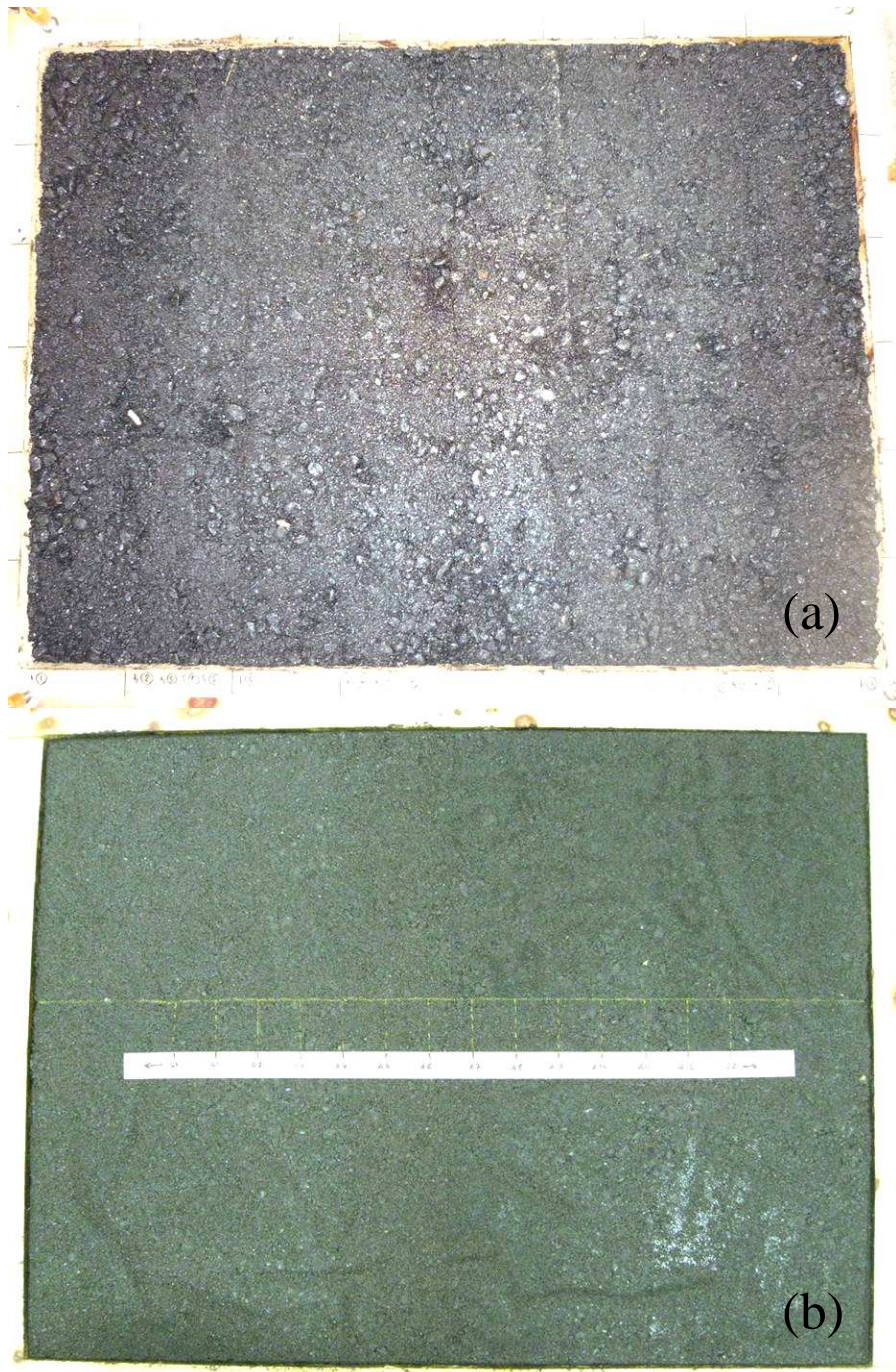
Figure 6-11: (a) Top and (b) Bottom surfaces of the jointed slab prepared in the laboratory
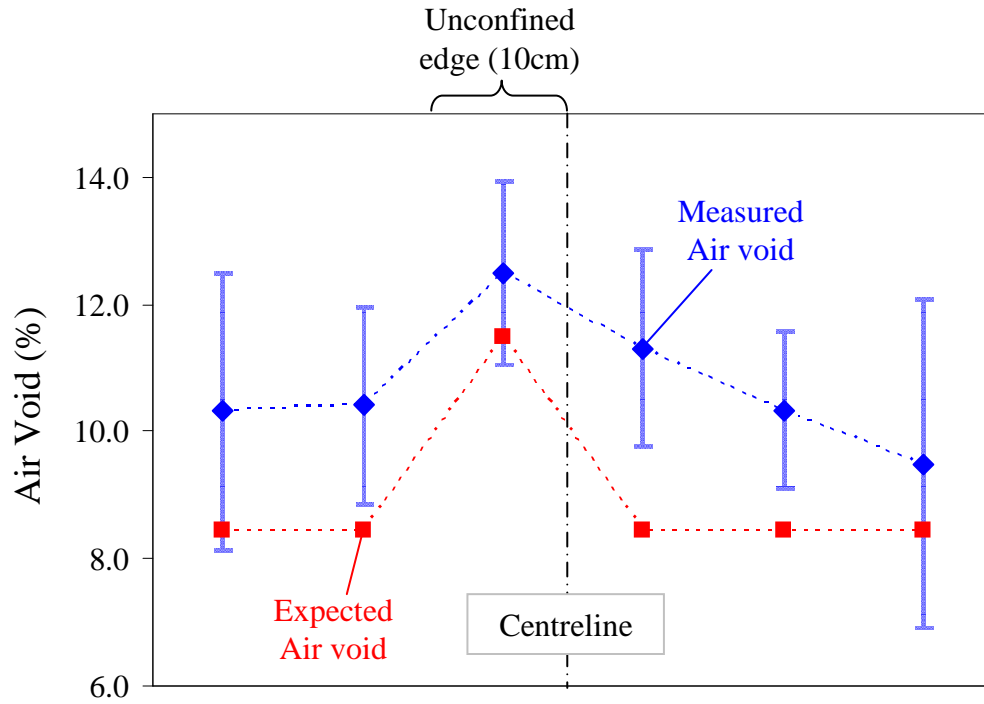
Figure 6-12: Nuclear density measurements on Slab 3
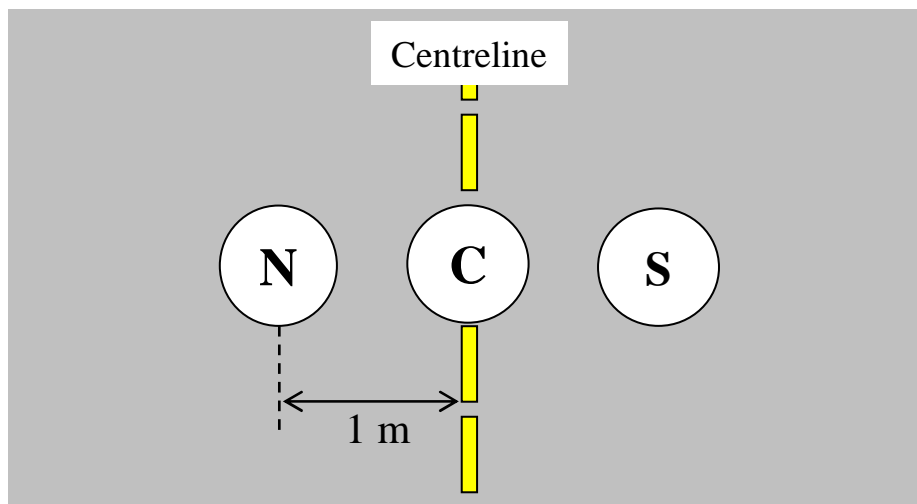


Figure 6-13: Configuration used for deflection measurements across longitudinal joints
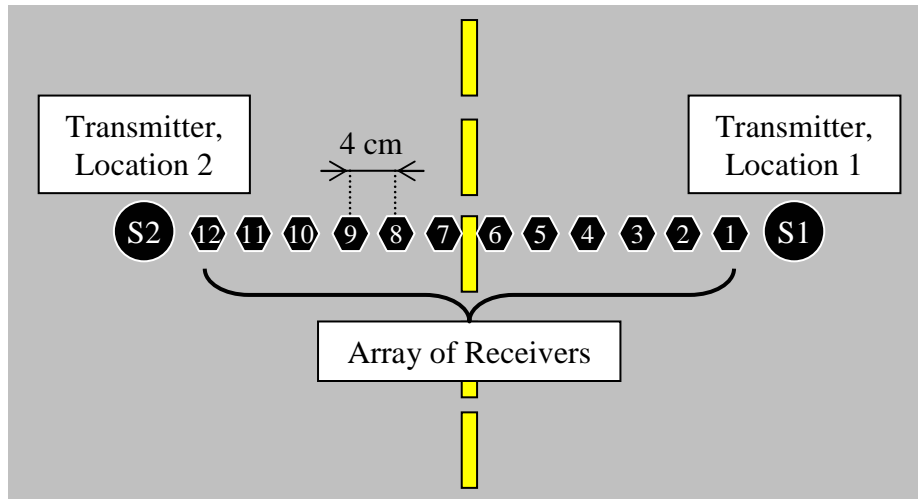
Figure 6-14: Configuration used for MASW testing of longitudinal joints
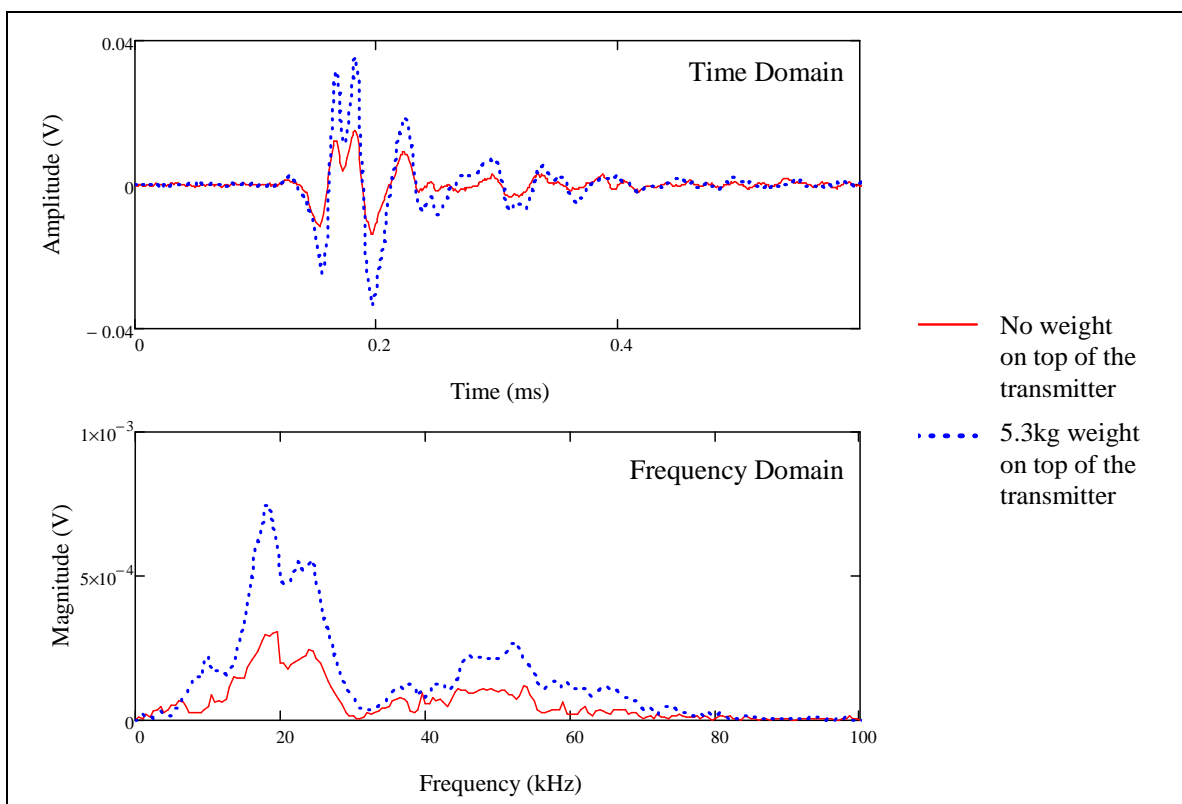


Figure 6-15: Effect of a vertical pressure applied on top of the ultrasonic source
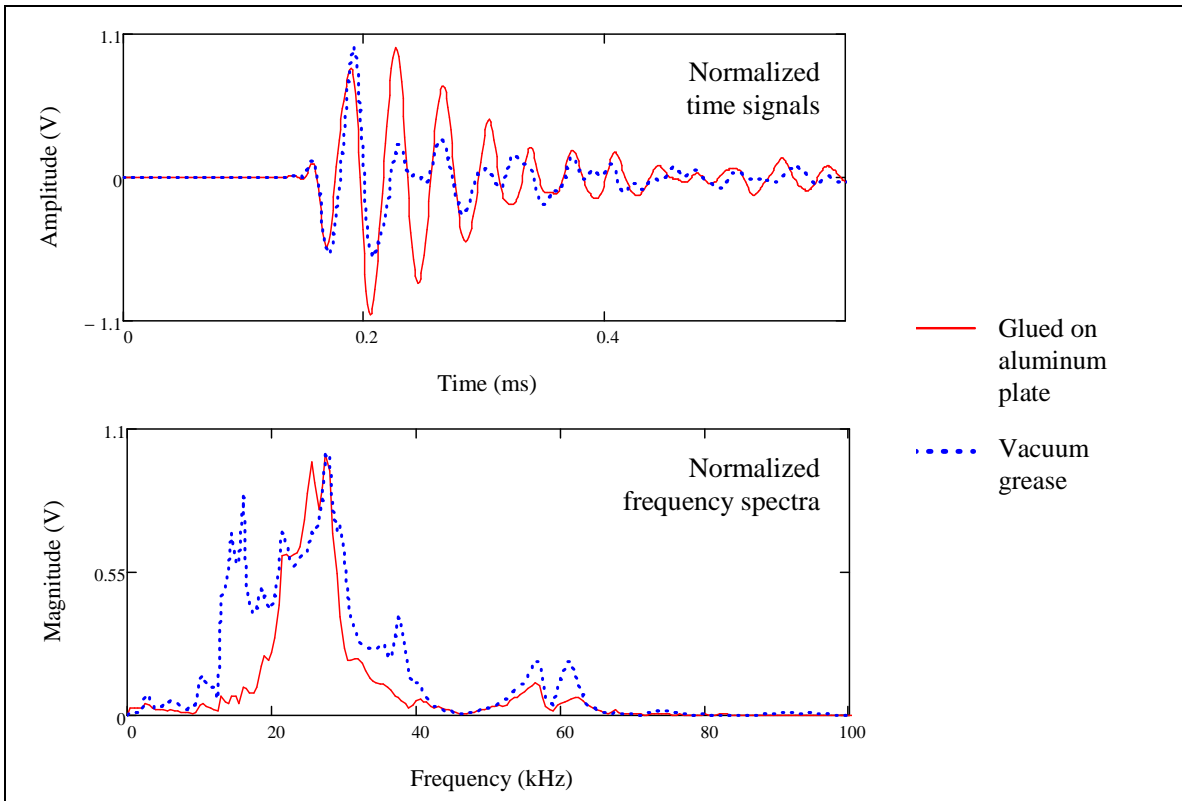
Figure 6-16: Effect of the coupling between the accelerometer and the pavement surface
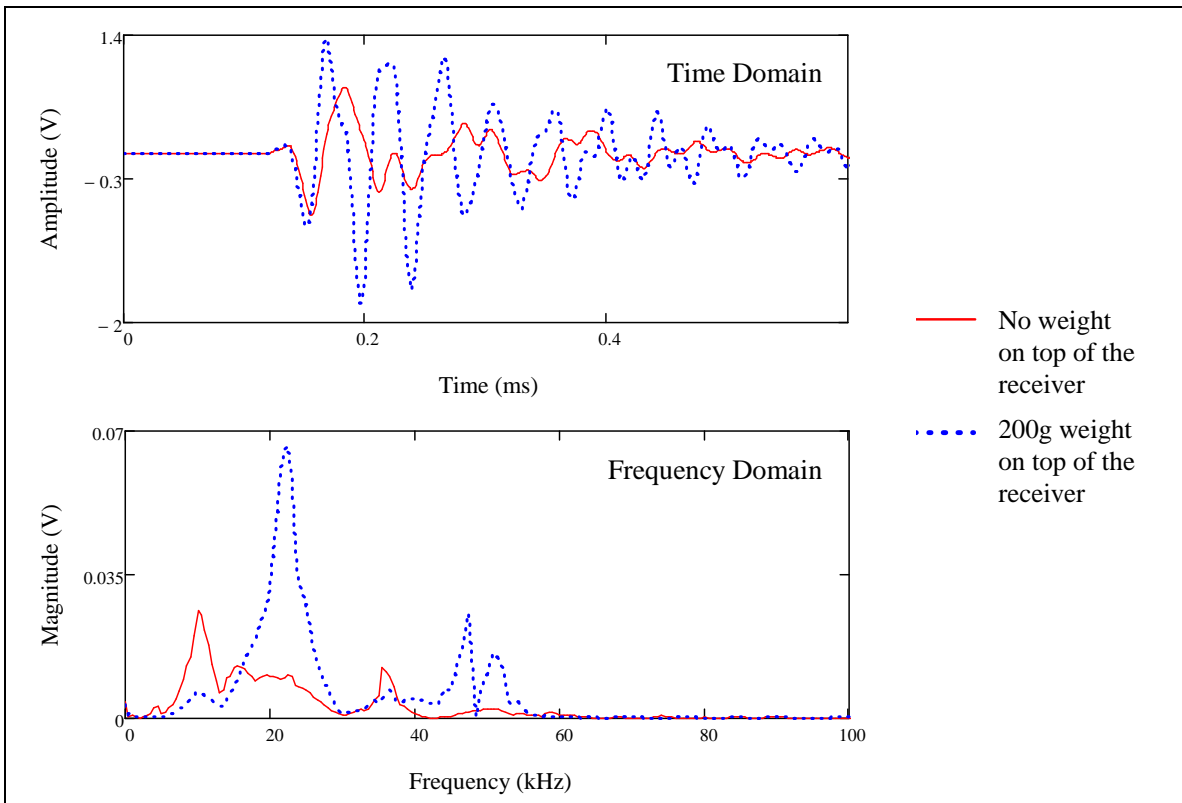


Figure 6-17: Effect of a vertical pressure applied on top of the accelerometer
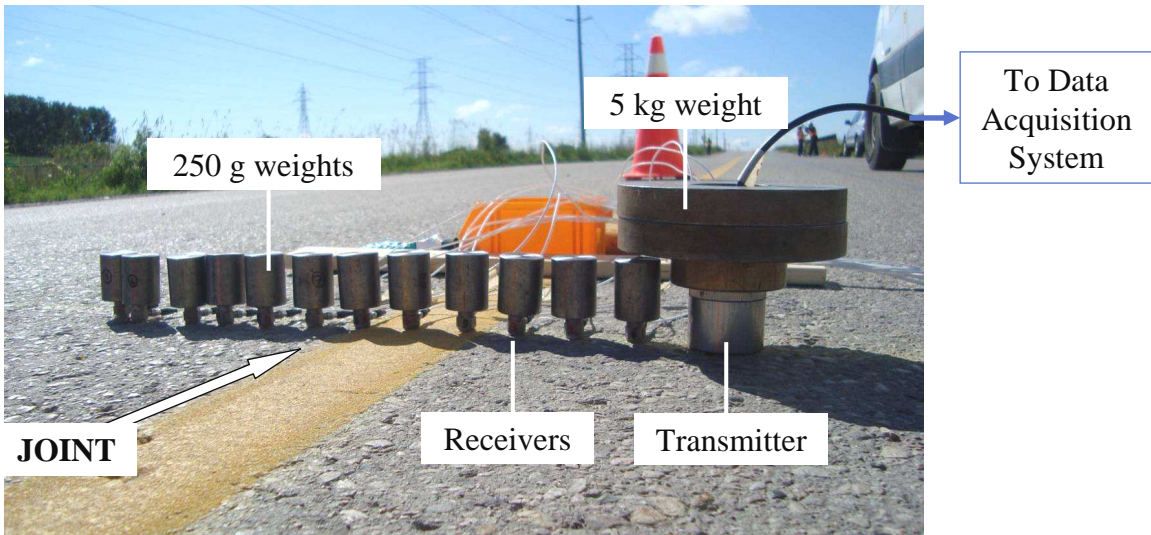
Figure 6-18: MASW setup used for testing at the CPATT Test Track in July 2009
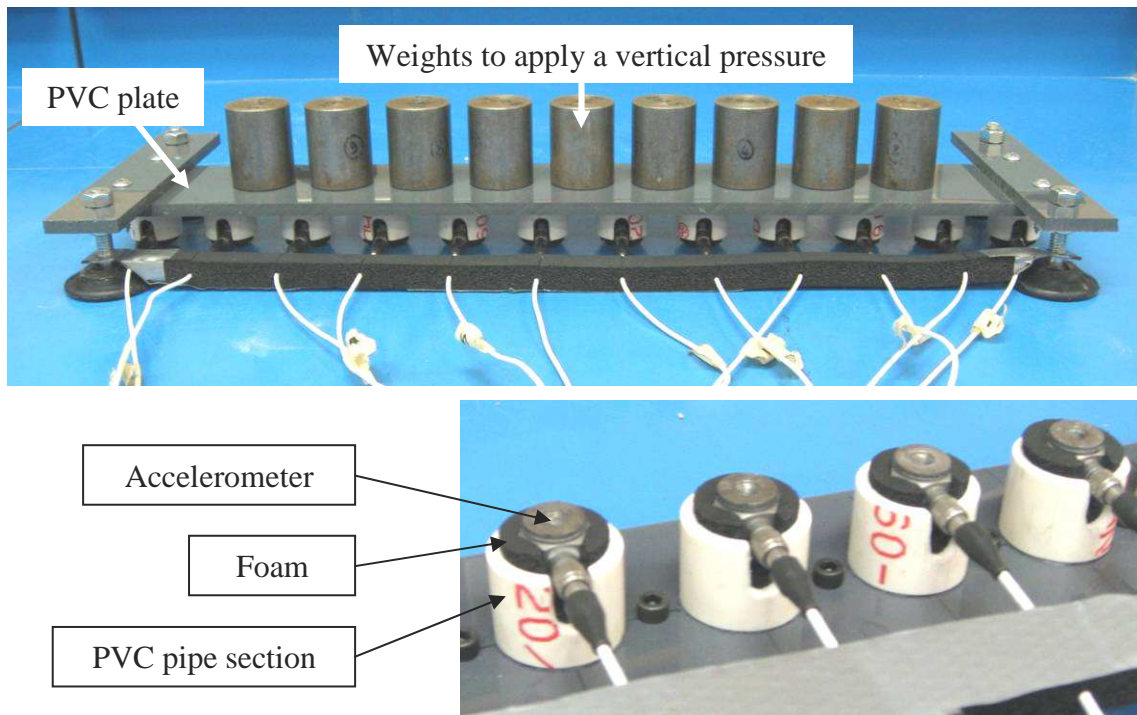


Figure 6-19: Structure used to hold the receivers

Table 6-1: Method of test for preparation of HMA specimens

| 1 | Warm the HMA using a microwave oven to achieve sufficient workability (temperature around 105°C). Heat all metallic tools that will be in contact with the mixture by placing them inside an oven or on a hot plate. |
|---|---|
| 2 | Reduce the sample to testing size by pouring the mixture in a riffle splitter.  |
| 3 | Spread the mixture in a flat pan, and weight it. Remove any extra material with a flat bottom scoop until the proper weight is measured. Prepare two pans with the same weight of material for each specimen.  |
| 4 | Cover the pans with aluminum foil and heat in an oven to a temperature no more than 5°C above the compaction temperature of 138°C. |
| 5 | Place a heat resistant plastic sheet in the mould and slightly spray some 'Pam' on the sides to prevent the sample from adhering to the mould. |
| 6 | Pour the mixture from the first pan in a bowl and mix it with a scoop to ensure it is of uniform composition. Place the HMA in the mould using the scoop and a 100 mm diameter funnel to make sure it is equally spread in the mould.  |

| | | |
|---|---|---|
| 7 | Rod the mixture in the mould with a squared end spatula 80 times, 40 times around the outside, 40 times around the centre. When rodding around the outside, keep the spatula flat against the inside of the mould. When rodding around the centre, do not change direction of the blade. |  |
| 8 | Place the second plastic sheet on top of the mix. | |
| 9 | Place the hammer on top of the mix and compact the specimen by applying a predetermined number of blows. Try to compact the specimen at a rate of $60 \pm 5$ blows per minute. |  |
| 10 | Remove the hammer and the plastic sheet. Take the second pan out of the oven and repeat steps 6 to 9. | |
| 11 | When both layers have been compacted, allow the specimen to cool until warm to touch. Use fans to quicken cooling. | |
| 12 | Unscrew the sides of the mould and remove the specimen. Allow to sit at room temperature for a minimum of one hour before any further testing. | |

Table 6-2: Theoretical maximum relative densities of HL 4 and HL 3-R15 mixes

| Mix | HL4 | | HL3-R15 | | | |
|---|---|---|---|---|---|---|
| Mass of dry specimen in air (g) | 3088.5 | 3232.9 | 3125.8 | 2691.4 | 2885.3 | 2802.7 |
| Mass of Flask + Water (g) | 548.5 | 548.2 | 548.5 | 548.1 | 548.5 | 548.1 |
| Mass of Flask + Water + Sample (g) | 2404.1 | 2487.5 | 2440.0 | 2176.3 | 2292.8 | 2241.6 |
| Water temperature (°C) | 28.6 | 28.3 | 27.4 | 27.3 | 26.5 | 26.3 |
| Correction factor K | 0.99901 | 0.99910 | 0.99936 | 0.99938 | 0.99960 | 0.99966 |
| TMRD | 2.503 | 2.497 | 2.531 | 2.530 | 2.528 | 2.526 |
| **Average TMRD** | **2.500** | | **2.529** | | | |
| Standard deviation | NA | | 0.002 | | | |

Table 6-3: Theoretical number of blows

| **Hammer version** | **A** | **B** | **C** | **D** |
|---|---|---|---|---|
| Falling mass m (kg) | 14 | 16.6 | 18.86 | 20.2 |
| Dropping height (mm) | 700 | 698 | 728 | 728 |
| Theoretical number of blows for one layer | 106 | 90 | 76 | 71 |

Table 6-4: Bulk relative density using saturated surface-dry specimens

| Mix | HL4 | | HL3-R15 | | |
|---|---|---|---|---|---|
| Hammer version | A | B | C | | |
| **Specimen** | **A1** | **B1** | **C1** | **C2** | **C3** |
| Date of compaction | Apr-09 | Oct-09 | Nov-09 | | |
| **Total number of blows for two layers** | **160** | **100** | **80** | **126** | **166** |
| Mass of dry specimen (g) | 8315.6 | 7843 | 7937.9 | 8144.3 | 8285.1 |
| Mass of surface-dry specimen after immersion(g) | 8359.9 | 7897.7 | 8036.5 | 8196.6 | 8321.5 |
| Mass of sample in water (g) | 4785.9 | 4506 | 4627 | 4748.4 | 4834.8 |
| Water temperature (°C) | 19 | 27.8 | 27.55 | 27.5 | 27.4 |
| Correction factor K for temperature | 1.00116 | 0.99924 | 0.99931 | 0.99933 | 0.99936 |
| Bulk relative density at 25°C | 2.329 | 2.311 | 2.327 | 2.360 | 2.375 |
| **Air void (%)** | **6.82** | **7.56** | **7.99** | **6.65** | **6.09** |

| Mix | HL3-R15 | | | | |
|---|---|---|---|---|---|
| Hammer version | C | | D | | |
| **Specimen** | **C4** | **C5** | **D1** | **D2** | **D3** |
| Date of compaction | Dec-09 | | Dec-09 | | |
| **Total number of blows for two layers** | **40** | **64** | **8** | **14** | **24** |
| Mass of dry specimen (g) | 7767.5 | 7910.5 | 7335.1 | 7510.6 | 7685.8 |
| Mass of surface-dry specimen after immersion(g) | 7895.7 | 8018.5 | 7532.8 | 7689.2 | 7821.6 |
| Mass of sample in water (g) | 4516.9 | 4604.4 | 4266.8 | 4363 | 4472.6 |
| Water temperature (°C) | 24.5 | 24.3 | 23.4 | 23.4 | 23.65 |
| Correction factor K for temperature | 1.00013 | 1.00018 | 1.0004 | 1.0004 | 1.00034 |
| Bulk relative density at 25°C | 2.299 | 2.317 | 2.247 | 2.259 | 2.296 |
| **Air void (%)** | **9.07** | **8.35** | **11.14** | **10.66** | **9.21** |

Table 6-5: Bulk relative density using the automatic vacuum sealing method

| Hammer version | C | | | | | D |
|---|---|---|---|---|---|---|
| **Specimen** | **C1** | **C2** | **C3** | **C4** | **C5** | **D1** |
| Date of compaction | Nov-09 | | | Dec-09 | | Dec-09 |
| **Total number of blows for two layers** | **80** | **126** | **166** | **40** | **64** | **8** |
| Mass of dry specimen (g) | 7938.5 | 8148.5 | 8285 | 7772.5 | 7915.5 | 7330.6 |
| Mass of sealed specimen in air (g) | 7996.3 | 8206.6 | 8343.1 | 7830.3 | 7973.2 | 7387.8 |
| Mass of sealed specimen in water (g) | 4478.5 | 4654.4 | 4752.5 | 4337.5 | 4453.3 | 3956.9 |
| Mass of bag (g) | 58.1 | 58.4 | 58.8 | 58.4 | 58.3 | 57.9 |
| Specific gravity of bag | 0.63279 | 0.62798 | 0.6257 | 0.63867 | 0.63422 | 0.64943 |
| Bulk Relative Density at 25°C | 2.317 | 2.355 | 2.369 | 2.284 | 2.308 | 2.193 |
| **Air void (%)** | **8.37** | **6.85** | **6.32** | **9.65** | **8.70** | **13.27** |

| Hammer version | D | | | | | |
|---|---|---|---|---|---|---|
| **Specimen** | **D2** | **D3** | **D4** | **D5** | **D6** | **D7** |
| Date of compaction | Dec-09 | | Jan-10 | | | |
| **Total number of blows for two layers** | **14** | **24** | **2** | **100** | **40** | **72** |
| Mass of dry specimen (g) | 7508.3 | 7689.4 | 7358.7 | 8001.7 | 7910.2 | 8032.2 |
| Mass of sealed specimen in air (g) | 7565.7 | 7746.7 | 7416.6 | 8058.2 | 7968.2 | 8090.4 |
| Mass of sealed specimen in water (g) | 4106.3 | 4278.4 | 3848.3 | 4599.4 | 4456.2 | 4572.5 |
| Mass of bag (g) | 58 | 58.4 | 58.9 | 58.2 | 58.3 | 58.5 |
| Specific gravity of bag | 0.64471 | 0.64103 | 0.65221 | 0.63137 | 0.63437 | 0.63168 |
| Bulk Relative Density at 25°C | 2.228 | 2.276 | 2.115 | 2.375 | 2.313 | 2.345 |
| **Air void (%)** | **11.90** | **10.00** | **16.36** | **6.08** | **8.54** | **7.27** |

Table 6-6: Correction factors for the equivalent number of blows with hammer D

| **Hammer version** | **A** | **B** | **C** | **D** |
|---|---|---|---|---|
| Correction factor for the number of blows | 0.66 | 0.79 | 0.93 | 1 |

Table 6-7: Preparation of the jointed slab in the laboratory

| 1 | Warm the HMA using a microwave oven to achieve sufficient workability (temperature around 105°C). |
|---|---|
| 2 | Place the mixture in four different bowls, weight each of them and remove extra material until the desired weight is reached.<br>Cover the bowls with aluminum foil and heat in an oven to 145°C.  |
| 3 | Mix the material present in one of the bowl with a scoop to ensure it is of uniform composition. Place the HMA in the left side of the mould and rod the mixture with a square end spatula 100 times on the outside and 240 times around the centre.  |
| 4 | Place a plastic sheet at the bottom of the hammer with double sided tape, and start the compaction by applying a predetermined number of blows.  |
| 5 | Once the first layer of the left side is compacted, remove the divider and let the asphalt cool down to 60°C.  |

| 6 | Repeat step 3: mix the HMA present in another bowl; place it in the right side, and rod the mixture. |  |
|---|---|---|
| 7 | Compact the right side with the hammer, and make sure to overlap the left side when compacting the centreline of the slab. |  |
| 8 | Repeat steps 3 to 7 to compact the second layer of the slab. | |

Table 6-8: Asphalt temperature during the preparation of the slab

| Construction Step | Temperature (°C) | | | |
|---|---|---|---|---|
| | Layer 1 | | Layer 2 | |
| | Left (1$^{st}$) Side | Right (2$^{nd}$) Side | Left (1$^{st}$) Side | Right (2$^{nd}$) Side |
| Layer 1, Left | 138-144 | - | - | - |
| Layer 1, Right | ~60 | 138-142 | - | - |
| Layer 2, Left | ~60 | ~80 | 138-150 | - |
| Layer 2, Right | - | ~80 | ~80 | 138-145 |

# CHAPTER 7.   RESULTS

## 7.1.  Introduction

This chapter presents the results obtained from the laboratory and field NDT tests performed in this project. First, ultrasonic measurements were conducted in the laboratory on two different slabs: Slab 2, which was extracted from an actual pavement and did not have a joint; and Slab 3, which was compacted in the laboratory in order to create a joint in its middle. Measurements on these two slabs were compared to identify the effect of the joint on the data. The signal processing techniques developed in this study are detailed in the first section of this chapter.

Then, deflection and ultrasonic data was collected at two field sites: the CPATT Test Track in Waterloo and Garth Street in the City of Hamilton. Slab 2 was taken from the CPATT Test Track, thus an interesting comparison could be made between results obtained in the laboratory and the field. Ultrasonic tests in the City of Hamilton were performed with the MASW structure showed in Figure 6-19, which main objective was to reduce the testing time.

## 7.2.  Laboratory Testing on Asphalt Slabs (Sept. 2009 – June 2010)

Ultrasonic measurements were conducted in the laboratory on a field slab without joint (Slab 2, presented in Figure 6-6) and a jointed slab prepared in the laboratory (Slab 3, showed in Figure 6-11). Slab 2 is representative of actual pavements; thus it was used as a control slab to develop testing and processing techniques that would be employed for the assessment of longitudinal joints. Slab 3 was prepared in the laboratory with a calibrated compaction procedure in order to create a joint at a desired density. Ultrasonic measurements taken on the jointed slab were compared to its horizontal density profile in order to determine if the techniques developed with the control slab were able to detect the joint in Slab 3.

The MASW tests were performed with two different accelerometers and coupling systems. As observed in Section 6.3, the best coupling consisted in gluing the accelerometers on aluminum plates previously fixed to the asphalt with epoxy. However, this method was time consuming and could not be used for field testing. A coupling system combining vacuum grease and a vertical pressure was found to provide relatively good quality measurements and required less time for setup; thus it was selected for field testing. Laboratory measurements were performed with both

coupling systems at the same locations for comparison. Besides, recordings are affected by the transfer function of the receivers. Thus, two different types of accelerometer were used to investigate their impacts on the measurements. Consequently, three configurations were used for testing on the slabs:

*(A)* Accelerometer Dytran 3055B3 (sensitivity: 500 mV/g; resonant frequency: 35 kHz) glued on aluminum plates fixed to the asphalt surface with epoxy.

*(B)* Accelerometer Dytran 3055B3 coupled directly to the pavement with vacuum grease. A vertical pressure is applied by a weight placed on top of the transducers.

*(C)* Accelerometer PCB 352A60 (sensitivity: 9.8 mV/g; resonant frequency: 90 kHz) glued on aluminum plates. Only one PCB accelerometer was available, thus twelve individual measurements had to be taken for each test.

The transmitter was placed on both sides of the receiver array, in accordance with Figure 6-14. Signals were processed in MathCAD. Analysis was performed in the time and frequency domains to calculate wave velocities and attenuation parameters. Dispersion curves were computed with the software SWAN.

## 7.2.1.    Control Slab 2

Slab 2 was cut from an actual pavement and its dimensions are $83 \times 69 \times 9$ cm$^3$. Measurements were performed along the middle line of the control slab with configurations A, B and C, as showed in in Figure 7-1. The objective was to determine the best methods to calculate wave velocities and attenuation parameters that could be used for joint evaluation.

### 7.2.1.1.    Wave Velocities

Time signals were recorded with a sampling rate of 1 MHz over a period of 2 ms. Normalized signals are presented in Figure 7-2 for the three configurations and both source locations. Signals collected with the PCB accelerometer showed lower signal-to-noise ratios because of the low sensitivity of the transducer. P-wave and R-wave arrivals were detected on the graphs, as indicated by the two doted lines for configuration A. Arrival times were plotted with respect to the distance from the source, and linear regressions were performed as illustrated in Figure 7-3. The slopes of the lines are the inverse of the wave velocities. Table 7-1 provides the values of the velocities calculated for the three configurations.

All coefficients of determination were higher than 0.9965, which indicates that the linear regression provided a good estimation of the wave velocities for all configurations. A program was written in MathCAD to detect P-wave arrivals automatically, instead of having to locate them one by one on the time signals. $R^2$ values were found to be smaller than the ones calculated previously, especially for configuration C. This is due to the noise present in the signals. P-waves generate low amplitude displacements and their arrival could be masked by the noise. Therefore, the author preferred to identify the arrivals manually to make sure they are not confused with unexpected high amplitude noise.

The highest $V_P$ was measured with configuration B, and the lowest with configuration C. Configuration B used the best coupling system and high sensitivity accelerometers which resulted in large signal-to-noise ratios. Therefore, P-wave arrivals could be easily identified on the time signals. In configuration A, accelerometers were directly coupled to the asphalt, introducing noise in the signals, especially at large distances from the source. Thus, the very first P-wave arrivals could not be identified on signals recorded far from the source, and the linear regression resulted in a lower $V_P$. In configuration C, the accelerometer was responsible for the noise and P-wave arrivals were even harder to detect.

It was difficult to identify R-wave arrivals because of the interference caused by body waves that propagate faster than surface waves. $V_R$ was estimated by selecting the time corresponding to the maximum absolute amplitude of the first large peak identified as the R-wave arrival. Too much dispersion was observed in the signals recorded by the furthest receivers. Consequently, only the arrival times detected with the ten receivers closest to the source were included in the regression calculations. The resulting average R-wave velocities were quite consistent from one configuration to the other (less than 5 percent differences).

The difference between the velocities obtained with the source at location 1 and location 2 was less than 1.3 percent for configuration A and B. Therefore, there was a good consistency between measurements performed at the two source locations. Due to the noise recorded with the PCB transducer, higher changes in velocities were observed between the measurements performed at the two source locations with configuration C.

Surface wave velocities were also calculated using dispersion curves. At high frequencies, surface waves penetrate only in the slab and the phase velocity is equal to the surface wave velocity of

the asphalt mix. Figure 7-4 shows the dispersion curves computed for configuration A with the source at the two locations. Both curves converged to a constant value at frequencies higher than 20 kHz. $V_R$ was calculated as the average phase velocity between $f_1 = 25$ kHz and $f_2 = 42$ kHz. Similarly, surface wave velocities were computed for the three configurations, as reported in Table 7-2. The calculation provided very close values, less than 1.5 percent different. Moreover, a very good consistency was observed between measurements taken at both source locations. Consequently, the method based on dispersion curves was preferred to the method based on time signals for the calculation of surface wave velocities.

Further observations could be made regarding the dispersion curves. Figure 7-5 presents the curves computed for the three configurations and the source placed at location 2. It was noticed that the three curves were very similar, especially for configuration B and C that used the same coupling system, and converged to a consistent R-wave velocity. An average $V_R$ of 1698 m/s was calculated using the three curves. Theoretically, all wavelengths shorter than the slab thickness (9 cm) should propagate only in the slab, at a phase velocity equal to $V_R$. Those wavelengths correspond to frequencies higher than: $f_{crit} = V_R/\lambda_{crit} = 1698/0.09 = 18.87$ kHz. As indicated on Figure 7-5, $f_{crit}$ is very close to the inflection point at which the curves start converging to $V_R$. This result showed that dispersion curves were able to determine the slab thickness.

A jump of the phase velocity was observed around $f_{jump} = 12.9$ kHz. In order to explain this phenomenon, theoretical dispersion curves of Lamb modes were computed using a program developed by Yang (2009) as part of his doctoral work at the University of Waterloo. It requires three inputs for the calculation of the dispersion curves:

- Half the slab thickness: h = 4.5 cm
- $V_P = 3377$ m/s (average of the P-wave velocities determined with the time signals)
- $V_R = 1698$ m/s

The theoretical dispersion curves of the fundamental symmetric and anti-symmetric Lamb modes are showed on Figure 7-5. A comparison of the experimental and theoretical curves showed that the experimental curve followed the anti-symmetric mode at frequencies below $f_{jump}$ and above $f_{crit}$, while it followed the symmetric mode at frequencies between $f_{jump}$ and $f_{crit}$.

An example of a FK spectrum is given in Figure 7-6 for configuration A. Most of the wave energy was observed at frequencies between 15.5 kHz and 25 kHz, which correspond to Lamb modes. Surface waves propagate at higher frequencies, above 25 kHz. Consequently, mainly

Lamb waves were generated in the slab. When collecting the MASW data, Slab 2 was seating on a 2.5 cm thick layer of sand and a 2 cm thick wooden board. In theory (see Section 2.2), Lamb waves propagate in plates with two free boundary conditions at the top and bottom surfaces. The results obtained in this section showed that the previous statement might be applicable to plates seating on a soft layer like sand. The vertical excitation of a plate should result in the apparition of anti-symmetric modes. However, symmetric modes were observed at frequencies between $f_{jump}$ and $f_{crit}$. This might be due to mode conversion occurring at the vertical edges of the slab. Further work is needed to explain this phenomenon.

### 7.2.1.2. Attenuation Coefficients

As mentioned in Section 2.2, low frequencies are less attenuated than high frequencies. Therefore, the frequency content of the MASW data must be analysed before looking at attenuation parameters. Frequency spectra are presented in Figure 7-7 for the three configurations and both source locations. The calculation involved windowing of the time signals and zero-padding to improve the resolution in frequency. The spectra obtained with configuration A and B were quite similar. Both spectra had two main frequencies around 8 kHz and 19 kHz. A third peak was observed at different frequencies: 50.5 kHz for A and 37 kHz for configuration B. The aluminum plates used in configuration B were probably acting as a low-pass filter. The signals recorded with configuration C contained much lower frequencies because a different type of accelerometer was used to collect the data. The resonant frequency of the PCB accelerometer is very high (90 kHz). On the contrary, the resonance of the Dytran is around 35 kHz. The ultrasonic source generates frequencies around 25.4 kHz, 36.6 kHz and 49.8 kHz. Consequently, the resonance of the PCB did not affect the frequency content of the signals, whereas the Dytran significantly amplified frequencies around 35 kHz.

As a result, the highest attenuation should be observed with configuration A whereas the lowest one should be measured with configuration C.

Two parameters were used to quantify the attenuation of the waves propagating through the slab:
- Peak to peak (PTP) amplitude calculated in the time domain with equation ( 4-5 )
- Spectral area (SA) given by equation ( 4-6 )

Attenuation parameters were computed from both acceleration and displacement traces. Displacements were calculated by integrating twice the acceleration signals using the signal

processing software WPNDTool-box (Tallavó 2009). The double integration consisted of performing twice the following sequence of calculations:

- Computation of discrete wavelet transforms to remove undesired low frequency components. Level 4 to 11 were used to reconstruct the new signals (frequencies between 1.5 kHz and 300 kHz).
- Windowing to remove any noise before the arrival of the waves and at the end of the signals.
- Single integration.

Two theoretical models, based on equation ( 2-28 ), were used to fit the attenuation curves:

- *Model 1:* Only one fitting parameter: $\alpha$, material attenuation coefficient.

  The geometrical attenuation coefficient is fixed to its theoretical value: $\beta = 0.5$.

$$\text{Mod1}(\alpha, n) = \left( \frac{X_n}{X_1} \right)^{-0.5} e^{-\alpha(X_n - X_1)} \tag{7-1}$$

  where $X_n$ is the distance between the $n^{th}$ receiver and the source.

- *Model 2:* Both coefficients $\alpha$ and $\beta$ are changed during the regression.

$$\text{Mod2}(\alpha, \beta, n) = \left( \frac{X_n}{X_1} \right)^{-\beta} e^{-\alpha(X_n - X_1)} \tag{7-2}$$

Model 1 and model 2 were compared to determine if the experimental attenuation curves were able to capture the theoretical value of $\beta$ (0.5 for surface waves).

Non-linear regressions were performed by minimizing the sum of squares of the errors expressed either in linear or logarithmic scale:

- Regression 1: Minimize $\text{SSE1} = \sum_{n=1}^{12} \left[ \text{Mod1}(\alpha, n) - \text{Att}_n \right]^2$

- Regression 2: Minimize $\text{SSE2} = \sum_{n=1}^{12} \left[ \log(\text{Mod1}(\alpha, n)) - \log(\text{Att}_n) \right]^2$

  where $\text{Att}_n$ is an attenuation parameter (PTP or SA) calculated for the $n^{th}$ receiver.

Similar equations are defined for Model 2. Attention must be paid regarding the terminology: the regression in linear scale (regression 1) is a non-linear regression.

Figure 7-8 shows the PTP attenuation curve corresponding to configuration A with the source at location 2. The parameters of models 1 and 2 were determined for both regression types. The two

models obtained with regression 1 were significantly different: almost no geometric attenuation was observed with model 2 (β = 0.03). On the contrary, regression 2 lead to relatively similar curves: β = 0.64 for model 2. Consequently, regression 2 provided more reasonable results with a geometric attenuation coefficient close to the theoretical value for surface waves.

Attenuation coefficients were calculated for all cases: PTP amplitude and SA, acceleration and displacement, model 1 and model 2, regression 1 and regression 2. The results are analysed in the following paragraphs.

The values of the geometric attenuation coefficient β obtained for all regressions with model 2 are presented in Figure 7-9. In accordance with the previous observation, coefficients calculated with regression 2 were closer to 0.5. In most of the cases, regression 1 gave coefficients between 0 and 0.35 while regression 2 lead to coefficients between 0.3 and 0.65. For the same reason, SA provided attenuation curves that were more consistent with the theory than PTP amplitudes. Besides, coefficients computed with displacements were closer to 0.5 than with accelerations. Finally, the best consistency between the values of β for different source locations was observed when fitting the SA of the displacements. Consequently, results that best matched the theory were calculated by fitting the spectral area of the displacements with regression 2.

Regressions diagnostics were performed by calculating coefficients of determination for model 1. Regressions were non-linear, so the $R^2$-value could not be considered as an exact estimation of the percentage of the variation in the data that was accounted for by the model. However, it was believed that $R^2$-values could be used to compare different regressions, and determine which method provided the best fitting of the data. Coefficients of determination were calculated with the following equation, and summarized in Table 7-3.

$$R^2 = \frac{SST - SSE}{SST} \tag{7-3}$$

where SST is the total sum of squares and SSE is the error sum of squares.
Higher $R^2$-values were obtained with spectral areas, displacements, and regression 1. Consistency with the theory was the primary criteria for the selection of the regression method. That is why regression 2 was identified as the best fitting method.

The next step of the analysis consisted of comparing the results obtain with different configurations. As indicated in Figure 7-9, geometric attenuation coefficients of 0.50 and 0.51

were calculated when fitting with model 2 and regression 2 the SA of the displacements measured with configuration B. Those coefficients are closest to the theoretical value. Moreover, coefficients of determination were, in average, highest for configuration B, and lowest for configuration C. For instance, $R^2$-values of 0.99 were calculated when fitting the spectral areas of displacements for configuration B. Figure 7-10 shows the attenuation curves and regression models determined for the three configurations with the best fitting method: regression 2 applied to SA of displacements. The highest attenuation was observed with configuration A whereas the lowest one was measured with configuration C, which is consistent with the observation made at the beginning of this section regarding the frequency spectra.

Material attenuation coefficients were converted to damping ratios for comparison with values available in the literature. Equations ( 2-27 ) and ( 2-29 ) lead to the relation:

$$\xi = \frac{\alpha \times \lambda}{2\pi} = \frac{\alpha \times V_R}{2\pi \times f}$$ ( 7-4 )

Where $\alpha$ is the material attenuation coefficient, $\xi$ is the damping ratio, $\lambda$ is the wavelength, $V_R$ is the surface wave velocity determined with the dispersion curve, and f is the frequency.

The values of damping ratios calculated at the dominant frequency with the best fitting method for the three configurations are given in Table 7-4. The Asphalt Research Consortium performed dynamic modulus tests on a PG64-22 mix to measure its stiffness and internal damping as a function of frequency (Asphalt Research Consortium 2008). Damping ratios between 8% and 8.5% were measured at frequencies between 10 kHz and 100 kHz. Although the dynamic properties of asphalt can significantly change from one mix to the other, those values have the same order of magnitude as the one determined in this study.

Another processing technique was developed to improve the quality of the attenuation curves. In this case, the calculation of the areas in frequency domain only included given bandwidths of frequencies. The areas were calculated using five different bandwidths (2, 4, 7, 10 and 15 kHz) that were moved along the frequency axis. As a result, five attenuation curves were obtained at each frequency, selected as the centre frequency of the bandwidths. Regressions were performed using the same models as previously. Figure 7-11 presents the coefficients of determination calculated for configuration A with two different bandwidths. The $R^2$-value determined previously with the total spectral areas of the displacements is indicated on the graph ($R^2_{total}$). $R^2$-values higher than $R^2_{total}$ were obtained with the new method for frequencies between 48 kHz and 64 kHz. A maximum value of 0.990 was determined with the 7 kHz bandwidth at 57.9 kHz.

7.2.1.3.    Conclusions

The following results were determined from the experiments conducted on Slab 2:

- $V_P$ was calculated by detecting the P-wave arrivals on the time signals. Linear regressions performed between the arrival times and the distances from the source showed very strong correlations ($R^2 > 0.996$).

- The most accurate calculation of $V_R$ was obtained from dispersion curves. $V_R$ was defined as the average of the phase velocities corresponding to frequencies higher than 25 kHz.

- The thickness of the slab could be determined with the dispersion curves.

- A comparison of experimental and theoretical dispersion curves showed that mainly Lamb waves were generated in the slab. A jump from the anti-symmetric to the symmetric fundamental Lamb mode was observed at $f_{jump} = 12.9$ kHz. Surface waves were propagating at frequencies higher than : $f_{crit} = 18.9$ kHz

- Aluminum plates seemed to act as a low-pass filter as higher frequencies were recorded with Configuration A. The resonance of the Dytran accelerometers used in configuration A and B resulted in an amplification of the frequencies around 35 kHz, as opposed to the PCB accelerometer which resonant frequency was outside of the frequency bandwidth generated by the source.

- The spectral area of the displacements provided attenuation curves that best matched the theory ($0.43 < \beta < 0.51$). Regression of these curves resulted in highest $R^2$-values ($R^2 > 0.97$).

- Two regression methods were evaluated: regression 1 (linear scale) resulted in higher $R^2$-values while regression 2 (logarithmic scale) provided more consistency with the theory and was selected as the best fitting method.

- Regression of the attenuation curves measured with configuration B presented values of $\beta$ closest to 0.5, and highest $R^2$-values. This configuration is believed to provide the best quality measurements.

- The highest material attenuation was measured with configuration A, then configuration B, and configuration C.

- Finally, spectral areas were calculated for different bandwidths moved along the frequency axis. For a certain range of frequencies, regressions of the attenuation curves computed with this method provided $R^2$-values significantly higher than the one obtained with the total spectral area.

**7.2.2.    Jointed Slab 3**

Slab 3 was constructed in the laboratory according to the procedure described in Chapter 6 in order to create a joint. Its dimensions are $80 \times 60 \times 8$ cm$^3$. First, experiments were conducted across the joint on the top surface, which showed segregation, especially near the sides and the joint interface. The top surface will be referred to as "surface X". The joint was located between accelerometers 6 and 7, and S1 was on the cold side while S2 was on the hot side. Then, the slab was flipped to the other side, and testing was performed on the former bottom surface, termed as "surface Y", which was very smooth. The transducers were placed at the same locations when testing on surface X and Y. The expected horizontal density profile of the tested section is provided in Figure 7-12.

The main purpose of these experiments was to evaluate the effect of the joints on the results. Secondary objectives were to investigate the influence of the surface condition on the quality of the data, and to compare measurements taken on field Slab 2 and laboratory Slab 3. Data was processed using the techniques that provided the best results from the analysis of the tests performed on Slab 2.

7.2.2.1.    Wave Velocities

P-waves arrivals were identified on the time histories and lead to the P-wave velocities indicated in Table 7-5. Dispersion curves were used to calculate R-wave velocities. In accordance to the results obtained with Slab 2, the lowest $V_P$ was measured with configuration C because of the noise present in the signals. Overall, values of $V_R$ determined with the three configurations were consistent. The following average velocities were obtained for each test location:

- Slab 2: $V_P = 3388$ m/s; $V_R = 1693$ m/s
- Slab 3, surface X: $V_P = 3055$ m/s; $V_R = 1498$ m/s
- Slab 3, surface Y: $V_P = 3247$ m/s; $V_R = 1638$ m/s

Velocities measured at surface Y of Slab 3 were significantly higher than at surface X. The difference in P-wave velocities is related to the surface condition. Good coupling between the transducers and the asphalt was achieved at surface Y, whereas poor coupling was observed at surface X. Thus, accelerometers installed on surface X could not detect the very first P-wave arrival, resulting in a higher $V_P$.

The difference in $V_R$ is harder to explain, as surface waves carry most of the energy and their arrival should be easily identified even if the surface condition is poor. A possible reason could be the difference in density between the two construction layers of Slab 3. Although the bottom layer was allowed to cool down to a temperature of approximately 60°C, it must have achieved additional compaction during the placement of the top layer. The higher density of the bottom layer resulted in higher wave velocities. Furthermore, dissimilar frequency contents might be transmitted to the slab by the source when placed on the two surfaces that provided different coupling conditions. As surface waves are dispersive, such dissimilarity would result in different wave velocities. This phenomenon also explains the relatively large changes between R-wave velocities measured on surface X with the source at location 1 or 2, as illustrated in Table 7-5. Surface Y provided a good coupling between the source and the asphalt, resulting in consistent measurements. On the contrary, the coupling condition at surface X varied significantly from location 1 to location 2, producing sizeable different wave velocities.

Overall, velocities measured on Slab 2 were higher than on Slab 3 (~7% difference). This is due to the fact that higher densities were achieved in the field than in the laboratory, as demonstrated with the nuclear density tests. Moreover, hardening of the asphalt must have occurred in Slab 2 which was extracted from a seven years old road.

The interface of the joint did not have a significant impact on P-wave velocities. As can be seen in Table 7-5, all regressions between P-wave arrivals and distances from the source provided straight lines with $R^2$-values higher than 0.99.

Since relatively consistent velocities were determined with different measurements on each slab, and $V_P$ calculations were associated to very high $R^2$-values, the wave velocities obtained in this study were believed to be close to the true values and could provide a good estimation of Poisson's Ratios. Testing on Slab 2 showed that configuration B gave the most accurate velocity measurements, thus they were used along with equations ( 2-14 ) and ( 2-15 ) to calculate Poisson's ratios:

- Slab 2: Source at location 1: $\upsilon = 0.309$

  location 2: $\upsilon = 0.313$

- Slab 3, surface Y: Source at location 1: $\upsilon = 0.307$

  location 2: $\upsilon = 0.291$

Dispersion curves computed for all measurements on Slab 3 are given in Figure 7-13. A jump from the anti-symmetric to the symmetric fundamental Lamb mode was observed when testing on surface Y but not on surface X. This may be due to the fact that the bottom surface was in good contact with the wooden base when testing on surface X. On the contrary, after flipping over the slab for testing on surface Y, only point contacts were achieved between surface X and the base. This difference in boundary condition could be responsible for the propagation of different Lamb modes in Slab 3.

### 7.2.2.2. Attenuation Coefficients

Attenuation curves were computed by calculating spectral areas of displacements. The best fitting method identified with Slab 2 (regression 2) was applied to the data collected on Slab 3. Resulting attenuation coefficients and damping ratios are presented in Table 7-6. Higher coefficients were measured when testing on surface Y. This is related to the frequency content of the signals recorded by the receivers. As can be seen in the table, the main frequencies of the spectra recorded at surface Y were higher than at surface X, thus they were more attenuated.

Experimental curves and regression models are showed in Figure 7-14. Attenuation curves provided by configuration B and C were very close to the theoretical models, with $R^2$-values higher than 0.97. On the contrary, spectral areas measured with configuration A showed significant variation, with $R^2$-values as low as 0.90. This was due to the coupling system used in configuration A: vacuum grease did not provide as much consistency as aluminum plates. For both configuration B and C, very similar curves were obtained at surface X and Y. Therefore, a good and consistent coupling was achieved between the receivers and the asphalt, and any variation identified in the attenuation curves should be strongly related to the properties of the asphalt mix. However, no clear relation could be established between the density gradients across the joint of the slab indicated in Figure 7-12c and the attenuation curves. The low density area of the unconfined edge and the interface of the joint did not seem to have a significant effect on the attenuation parameters.

### 7.2.2.3. Fourier Transmission Coefficients

The FTC method explained in Section 4.3 was applied to the data collected on the asphalt slabs in order to remove or at least reduce the variability introduced by the source, the receivers and the coupling condition. FTC coefficients were defined for each pair of consecutive accelerometers:

$$FTC_n = \sqrt{\left|\frac{F_{1,n+1}F_{2,n}}{F_{1,n}F_{2,n+1}}\right|} \qquad\qquad ( 7\text{-}5 )$$

where $F_{1,n}$ is the Fourier Transform of the signal sent by the source at location i (i = 1,2) and received by the $n^{th}$ accelerometer (n = 1,…,11).

$FTC_n$ represents the attenuation response of the pavement section located between the $n^{th}$ and $(n+1)^{th}$ receivers. Theoretically, this coefficient is independent of the transducers and the coupling condition, and the only factors having an effect on its value are:

- The geometrical attenuation related to the receiver spacing,
- The material attenuation of the asphalt section,
- Reflections at an interface characterized by a change in acoustic impedance.

The twelve receivers used for MASW testing were equally spaced. Thus, the same geometrical attenuation should be observed between any pair of consecutive receivers. As illustrated in Figure 7-12c, the unconfined edge located between the $4^{th}$ and $7^{th}$ receivers was less compacted. As wave scattering increases with air void, higher material attenuations should be measured between the $4^{th}$ and $7^{th}$ receivers. Moreover, wave reflections should occur at the joint interface between the $6^{th}$ and $7^{th}$ receivers. In conclusion, the only factors that should have an effect on the FTC values measured in this study are the increased material attenuation at the unconfined edge and the wave reflection at the joint interface.

The calculation of $FTC_n$ showed too much variation from one frequency to another. If the magnitude of one of the factors present at the denominator was very low, then the coefficient became very high. In order to reduce this variation, areas in frequency domain were used instead of magnitudes of single frequencies. As the total area of the frequency spectrum of the displacement provided the best attenuation curve, it was used to get a first estimation of the FTC. The resulting coefficients are showed in Figure 7-15a for the measurements on surface Y. The three curves obtained with the different configurations presented comparable trends. Both types of receivers (PCB or Dytran) and both coupling systems (vacuum grease or aluminum plate) provided relatively consistent FTC values. Consequently, the calculation method was able to significantly reduce the variability due to the receivers and the coupling system, and FTC values were representative of the HMA condition.

Theoretical FTC coefficients were calculated using the theoretical attenuation curves presented in Figure 7-14. The resulting theoretical FTC curves are provided for the three configurations in

Figure 7-16. As can be seen, all curves were arched in the same way, which was due to the geometric attenuation. The plain black curve showed at the top part of the graph was determined by removing the material attenuation component from the theoretical FTC. The three theoretical curves appeared to be shifted down from the black curve, and the amount of shifting was only function of the material attenuation coefficients.

Averages of the three experimental and theoretical curves were computed for comparison, as illustrated in Figure 7-17. For the pairs 1-2, 4-5 and 10-11, the experimental FTC was below the theoretical curve, suggesting that these locations had higher material attenuation than the rest of the tested section. The FTC values for the pairs 5-6 and 6-7 showed relatively good pavement condition. These results did not show a good agreement with the expected horizontal density profile of the slab, and could not reveal the presence of the joint between the $6^{th}$ and $7^{th}$ receivers.

This lack of correlation between FTC and estimated pavement condition may be due to the fact that, although comparable trends were observed between the three curves, there was still some disparity among the values determined for each pair of receivers. Standard deviations between the coefficients obtained with the three configurations were calculated for each pair of receivers. As can be seen in Figure 7-15b, the deviation decreased as the pair of receivers moved toward the centre of the array. This was probably due to the near-field and far-field effects that took place at short and large distances from the source, but were not accounted for in FTC calculations. This variability could hide the effect of the joint on the measurements.

Another frequency parameter, similar to the one described at the end of Section 7.2.1, was used to compute FTC coefficients. Areas in frequency domain were calculated for five different bandwidths (2, 4, 7, 10 and 15 kHz) that were moved along the frequency axis. Figure 7-18 provides the five FTC curves obtained for a centre frequency of 20 kHz, which was close to the dominant frequency observed in the Fourier spectra. Again, good correlation was found between the curves corresponding to different configurations. This confirms that the FTC method reduces the variability due to the receivers and the coupling condition. However, FTC values did not show a good agreement with the density gradient of the slab and the presence of an interface between the $6^{th}$ and $7^{th}$ receivers.

7.2.2.4.    Conclusions

The following conclusions were drawn from the measurements performed on Slab 3:

- Velocities measured at surface Y were significantly higher than at surface X. This was due to the roughness of the top surface, resulting in a poor coupling condition between the asphalt and the receivers. Moreover, the bottom layer was more compacted than the top one, thus surface waves were faster when propagating through the bottom layer. Finally, different frequency contents may be generated by the source because of the disparity in coupling condition. These frequencies propagated at different velocities because of the dispersive nature of surface waves.

- Slab 2 was characterized by higher velocities than Slab 3. This result is consistent with the conclusion drawn from nuclear density measurements: high densities were achieved in the field with roller compactors; whereas low densities were obtained in the laboratory, especially at the unconfined edge of the joint present in the middle of Slab 3. Asphalt hardening also contributed in increasing the velocity of Slab 2.

- Similarly to the results observed with Slab 2, dispersion curves showed that Lamb waves were produced in Slab 3. Symmetric modes were recorded only when testing on surface Y. This may be related to the nature of the surface in contact with the wooden base: the smooth bottom surface was in good contact with the entire surface of the base whereas, after flipping over the slab, the rough surface X only provided point contacts with the base.

- Higher attenuation was measured at surface Y than at surface X, which was consistent with the fact that higher frequencies were recorded at surface Y.

- Configuration B and C provided consistent attenuation curves that matched well with the theoretical curves ($R^2 > 0.97$). However, they did not show clear correlations with the horizontal density profile of the slab. No significant effect of the joint could be identified on the attenuation curves.

- FTC coefficients were computed to reduce the undesired variability due to the source, the receivers, and the coupling system. FTC curves showed good consistency from one configuration to another, which means that the coefficients were representative of the HMA condition. Nevertheless, a comparison of the experimental and theoretical FTC curves showed that the estimated density gradient across the joint of Slab 3 did not agree well with the FTC values.

In conclusion, the low density area and the interface of the joint were not clearly identified by the different methods described in this section. The following points indicate the different factors responsible for the limitations of the MASW in detecting the joint, and propose possible improvements to the method:

- As noticed with both Slab 2 and Slab 3, mainly Lamb waves were generated by the source. Density discontinuities may not have a significant effect on the propagation of Lamb modes. This point must be studied for further analysis of the data.

- Higher frequencies should be transmitted to the pavement slab in order to generate surface waves. This requires a better control of the frequency content sent by the source. Ideally, the transmitter should produce a higher frequency bandwidth, with minimum energy below 30 kHz. Moreover, the coupling system used to set the source on the asphalt surface must be improved. Unbonded couplants such as vacuum grease are believed to attenuate high frequencies. An interesting paper addressing those issues was written by Barnes and Trottier (2009).

- The heterogeneous and visco-elastic nature of HMA is responsible for complex phenomena such as wave reflection, mode conversion, and dispersion, introducing unexpected variability in the measurements. Moreover, asphalt presents a difficult coupling surface for both the source and the receivers. The dimension of the surface texture could exceed the size of the transducers and have an effect on the amplitude and quality of the measured signals.

- Finally, NDT results were compared to the density of Slab 3 estimated with equation (6-3). This relationship was calibrated with small specimens, thus it might lead to different densities when compacting larger slabs. Cores should be taken at several locations of the slab in order to check its actual density. The joint might be of better quality than expected, which would agree with the results obtained in this section.

## 7.3. Field Testing at the CPATT Test Track (July 2009)

Field tests combining deflection and seismic measurements were performed in July 2009 at the Centre for Pavement And Transportation Technology (CPATT) Test Track, Waterloo, Ontario. Results were presented at the 89th Transportation Research Board Annual Meeting, and lead to a publication in the Transportation Research Record Journal (Du Tertre, Cascante, and Tighe 2010). Some of the processing techniques have been improved since the publication and revised results are presented in this section of the thesis.

The Test Track was constructed in June 2002 (Tighe et al. 2007). All sections of the road presented the same subgrade, base and binder course Hot-Laid 4 (HL 4) which was a standard municipal mix. As illustrated in Figure 7-19a, four different mixes were used for the surface course, including Hot-Laid 3 (HL 3) for the control sections, polymer-modified asphalt (PMA), stone mastic asphalt (SMA), and Superpave®. The profile of the pavement structure is given in Figure 7-19b.

MASW measurements were performed on two locations of the centreline, at 25 m and 50 m from the beginning of the Test Track. These locations were part of the HL 3-1 section from which the field slabs 1 and 2 were extracted. The material and structural design of this section are typically used throughout Ontario on most collector and arterial facilities. The mix design reports of the HL 4 and HL 3 mixes are provided in Appendix C. LWD tests were performed at the centreline and the right wheel path of the southbound lane. It is notable that the south lane has all the heavy loaded trucks.

### 7.3.1.    Deflection Testing

Two sets of deflection data were collected at the Test Track with the LWD. First, the deflection was measured at the right wheel path of the HL 3-1 and PMA sections of the south lane for comparison with previous data. Second, the deflection was measured at the centreline of the HL 3-1 section, using the configuration presented in Figure 6-13. Six measurements were taken at each location, with maximum weight, dropping height, and plate size. For comparison purposes, all deflections were normalized to a 100 kPa stress level. During the analysis, the points presenting unexpected stress levels (deviation higher than 30%) or unexpected deflection values (deviation higher than 80%) were deleted. Then, an average of the centre deflection was determined for each location.

7.3.1.1.    Testing on the Right Wheel Path

Deflection surveys on the right wheel path of the south lane were performed in 2007 and 2009. Figure 7-20 presents the deflection and surface modulus data collected during the different surveys. Average deflection and modulus values are summarized in Table 7-7. The deflection increased by approximately 10% from 2007 to 2009, which means that the structural capacity of the pavement decreased over time. Even though the surface course was subject to asphalt hardening, this trend is consistent with the deterioration of the whole structure (surface course, base, subbase, subgrade and drainage system). The change in standard deviation between 2007

and 2009 measurements is less than 20% for the HL 3-1 section. However, for the PMA section, 2009 measurements present a standard deviation more than five times higher than 2007 measurements.

In addition to pavement deterioration, seasonal variations and temperature must be considered when analysing the results. In 2007, the data was collected in Spring, whereas 2009 surveys were performed in the beginning of summer. Because of thawing, deflections could be higher in spring than in summer, but more data is required to verify if this is the case. The temperature of the pavement, which was not available for the 2007 survey, should be also included in the analysis. The impact of the temperature can be very significant and deflections should be normalized to a standard temperature of 21ºC.

Finally, in 2007, the deflection was measured with the PFWD Keros Prima 100 whereas in 2009, it was measured with the LWD Dynatest 3031. This difference in apparatus was also likely responsible for the difference in the deflections measured in 2007 and 2009.

7.3.1.2.    Testing on the Centreline

During the survey performed on July 4, 2009, LWD tests were conducted at four locations across the centreline using the configuration described in Figure 6-13. The temperature of the pavement surface varied from 21°C to 27°C. The centre deflections measured at each location are provided in Figure 7-21. The average deflection and modulus for locations C, S and N are presented in Table 7-8. The change in surface modulus between the three locations was less than 7%. If the deflection measured by the PFWD was only affected by the stiffness of the surface course, these results would lead to the conclusion that the joint was in good condition. However, as explained in Section 2.3.1, the measurement depth of the LWD was equal to $3.71 \times a$, where $a$ is the radius of the loading plate. Since the 300 mm diameter plate was used for this survey, the stiffness of sub layers up to 557 mm deep were taken into account in the surface modulus values. Therefore, the PFWD used with the configuration described in this section did not provide sufficient precision to determine the quality of the joint. Moreover, the calculation of the surface modulus was based on the elastic theory which does not consider all the characteristics of a pavement structure. To improve the accuracy of the results:

·    A smaller loading plate should be used in order to have deflection measurements mainly affected by the 90 mm asphalt surface course that contains the joint.

- Geophones should be added radially outward from the centre to measure the deflection basin.
- The weight should be dropped at various heights in order to generate different stress levels that would improve the calculation of the moduli of the different pavement layers with the LWDmod software.
- A higher number of locations must be tested for a better statistical analysis.

### 7.3.2. Seismic Testing

As explained in Section 6.3.2, preliminary experiments were performed in the laboratory to determine a suitable configuration for testing in the field. Figure 6-18 presents the test setup used for seismic measurements at the CPATT Test Track, which was identical to configuration A used for testing on the slabs. Measurements were taken at two locations (A and B) of the HL 3-1 section, with the source placed on both sides of the transducer array. S1 was on the south lane while S2 was on the north lane. The terms A1, A2, B1 and B2 will refer to measurements performed at location A and B with the source on the south and north lane respectively. The data was collected on July 4, 2009; under the same climatic conditions as for the PFWD testing performed at the centreline.

#### 7.3.2.1. Time Domain and Dispersion Curves

Signals recorded by the twelve accelerometers at location A are presented in Figure 7-22. The signals were normalized to their maximum absolute amplitude value for a better visibility. Unfortunately, some signals were saturated. As can be seen on the figure, the largest peaks of the signals recorded by accelerometers 5, 8, 9 and 10 with the source on the north lane were cut. The same saturation problem was noticed on the signal recorded by the 8th receiver with the source on the south lane of location B. This saturation was introduced by the data acquisition system, since the spans selected during the acquisition of those signals were too short.

Arrivals of compression waves (first arrival, low amplitude) and surface waves (second arrival, large amplitude) were identified on the signals. Velocities were calculated by linear regression of arrival times, as explained in Section 7.2. R-wave velocities were also determined with dispersion curves, by taking the average of the phase velocities corresponding to frequencies between 25 and 52 kHz. Table 7-9 summarizes the velocities obtained for location A and B with time signals and dispersion curves. R-wave velocities computed with dispersion curves ($V_{R2}$) were more consistent than with time signals ($V_{R1}$). Moreover, as indicated by the ratio $V_{R2}/V_{R1}$, time signals provided

consistently lower surface wave velocities than dispersion curves. A constant delay might have been introduced when selecting the R-wave arrivals in time domain and dispersion curves were believed to provide the most accurate velocities.

Slab 2 was cut from the same HL 3-1 section of the Test Track. Thus, measurements performed on Slab 2 with configuration A should give comparable results to the field tests presented in this section. The following average velocities were calculated from each test:

- Slab 2: $V_P = 3429$ m/s; $V_R = 1696$ m/s
- Field test: $V_P = 3214$ m/s; $V_R = 1615$ m/s

Measurements on Slab 2 provided higher velocities than the field tests. This could be attributed to the difference in asphalt temperature observed in the field and the laboratory. Field tests were performed under sunny conditions, with temperature up to 27°C; whereas the temperature was maintained to approximately 21°C in the laboratory. As the stiffness of asphalt cement decreases with temperature, the propagation of the waves was slower through the field pavement than the laboratory slab. Moreover, field tests were conducted at the centreline whereas Slab 2 was extracted from the right wheel path of the road. Therefore, Slab 2 should be of higher density than was the field section.

A comparison of Table 7-1 and Table 7-9 revealed that field velocities showed less consistency than Slab 2 velocities. This contrast was particularly important for P-waves: the difference between $V_P$ measured with the source on the south and north lane was less than 1% for Slab 2, whereas it was more than 5% for both field locations. This variation may be accounted for the coupling system. Accelerometers were placed directly on the asphalt surface and often had to be moved from their original position to relatively flat areas in order to achieve good coupling, resulting in slightly modified receiver spacings. This variability was more pronounced in the field since less time was available to ensure proper coupling and spacing were obtained in the field.

Dispersion curves were computed for both test locations, as illustrated in Figure 7-23. All four curves were very similar and converged to an average $V_R$ of 1615 m/s. The wavelength equal to the thickness of the asphalt layer (9 cm) corresponds to the frequency: $f_{crit} = 1615/0.09 = 17.94$ kHz. As noticed on the graph, $f_{crit}$ is very close to the inflection point at which the curves start converging to $V_R$, which shows that the method could be used to estimate the thickness of the surface course. Theoretical dispersion curves of Lamb modes propagating through the asphalt layer were computed with the MathCAD program described in Section 7.2. The average values of

$V_P$ and $V_R$ calculated previously and the thickness of the asphalt layer were used as inputs for the program. The four experimental dispersion curves appeared to match very well with the anti-symmetric Lamb mode. Contrary to the measurements performed on Slab 2, no jump to the symmetric mode was observed. This was probably due to the difference in boundary conditions. First, the asphalt layer of the Test Track was not limited in the horizontal direction and could be considered as an infinite plate. Mode conversion may occur at vertical edges, which would result in the generation of symmetric modes in the slab but not in the field. Moreover, since Lamb waves propagate in plates, they are significantly affected by the boundary condition at the bottom surface. Slab 2 was seated on a thin layer of sand, which was probably softer than the base course of the Test Track. The difference in acoustic impedance between the surface course and the base was less important in the field than it was in the laboratory, resulting in the generation of different modes. Again, more work is required to understand this phenomenon.

In order to evaluate the sensitivity of dispersion curves with respect to the thickness of the asphalt layer, theoretical Lamb wave dispersion curves were computed for two other thicknesses (7 cm and 11 cm). The three theoretical curves are showed in Figure 7-24 along with the average of the four experimental dispersion curves obtained from the field tests. The theoretical curve corresponding to the actual thickness of the surface course (9 cm) best matched the experimental curve, especially at frequencies above $f_{crit}$. Therefore, this method provided an estimation of the thickness of the asphalt layer with a relatively good precision.

7.3.2.2.      Frequency Spectra and Attenuation

Frequency spectra normalized to their maximum magnitude are provided in Figure 7-25. Two main peaks were observed around 20 and 50 kHz, which should correspond to the 25.4 and 49.8 kHz frequencies sent by the source. The 50 kHz spike was observed only in the Fourier spectra of the signals recorded by the first receivers, which was consistent with the fact that high frequencies attenuate faster than low frequencies.

As noticed previously, some time signals were saturated, which significantly changed their peak-to-peak (PTP) amplitude. Since only one or two peaks of those time signals were cut, it only had limited effect on the area in frequency domain. Therefore, spectral areas (SA) were preferred to PTP for the determination of attenuation properties. Furthermore, previous measurements on the slabs showed that displacements provided attenuation curves closer to the theory than accelerations. Consequently, acceleration traces were integrated twice with the software

WPNDTool-box, and SA of displacements were computed to draw experimental attenuation curves, as illustrated in Figure 7-26.

Non-linear regressions were performed for both models and both regression methods described in Section 7.2. As noticed on the figure, the 11th accelerometer recorded unexpectedly higher energy than the 12th when testing at location A with the source on the north lane (case A2). Thus, only receivers 1 to 11 were included in the regression. The same procedure was applied to the attenuation curve corresponding to case B1. In accordance with previous observations, regression 2 provided geometric attenuation coefficients more consistent with the theoretical value (0.5) than regression 1. Figure 7-26 shows the theoretical curves obtained by fitting model 1 to the experimental curve using regression 2. Theoretical and experimental curves were normalized to the maximum value of the theoretical curve.

The material attenuation coefficient determined at location B with the source on the north lane was significantly smaller than it was for the three other cases (A1, A2 and B1). This was due to the fact that signals measured in case B2 had very low amplitudes. The average spectral area was approximately four times lower than it was for the three other cases, which may be attributed to a poor coupling between the source and the asphalt surface at this specific location. Consequently, the noise significantly increased the energy recorded by the far receivers, reducing the apparent attenuation determined for case B2.

Damping ratios were calculated using equation ( 7-4 ). Cases A1, A2 and B1 provided an average value of 10.4%, which was significantly higher than the average damping ratio of 8.0% measured on Slab 2 with configuration A. This was consistent with the previous observations regarding wave velocities. Due to different temperature conditions, the asphalt cement was softer in the field than in the laboratory, resulting in higher damping. Moreover, field tests were performed at the longitudinal joint which was expected to have higher air void than the right wheel path from which Slab 2 was extracted. The lower density of the field section resulted in higher damping.

For the three cases A1, A2 and B1, an important drop in spectral area was observed at the joint interface located between the 6th and 7th accelerometers. However, this reduction in energy could not be directly related to the condition of the joint, since other factors such as the geometric and material attenuations contributed to the attenuation. FTC coefficients were computed to reduce undesired variability components and isolate the attenuation due to the joint. Experimental and

theoretical FTC curves are compared in Figure 7-27. On one hand, location B showed relatively consistent FTC coefficients, indicating that the pavement condition was probably constant across the joint. On the other hand, a significant variability was observed among the FTC values determined at location A. Coefficients determined for the pairs of receivers 6-7 and 7-8 were below the theoretical curve, indicating higher material attenuation near the longitudinal joint. This result suggests that the joint was probably in poor condition. Unexpected low FTC coefficients were also observed for the pairs 2-3 and 3-4. As mentioned in the analysis of Slab 3 test results, FTC values presented more variability at the extremities of the receiver array than near its centre, and the latter observation might not be related only to pavement performance.

In conclusion, the drop in FTC observed near the centreline of location A might be attributed to the low density and the interface of the longitudinal joint; however the quality of the joint could not be determined with enough confidence.

### 7.3.3. Summary of the Results

The following results were determined from the filed tests at the CPATT Test Track:

- A comparison of the deflection data collected in 2007 and 2009 on the right wheel path suggested that there was a slight deterioration of the pavement structure. However, seasonal variations and temperature might have a significant impact on the data.
- Deflection measurements were not only affected by the stiffness of the surface layer but also by the sub structure of the pavement. Therefore, it was difficult to identify the quality of the joint which was confined to the surface course.
- Field measurements at the Test Track provided lower velocities than laboratory tests on Slab 2 (6.3% and 4.8% reduction in $V_P$ and $V_R$ respectively). This difference was probably due to:
  - The higher temperature of the asphalt in the field, resulting in softer material,
  - The lower density of the field section, located across the longitudinal joint.
- Dispersion curves could be used to determine the thickness of the asphalt layer with a relatively good precision ($\pm 1$ cm).
- The symmetric mode did not appear on the dispersion curves measured in the field, which suggests that mode conversion may occur at the edges of the slabs.
- Damping ratios measured in the field were in average 2.4% higher than in the laboratory, which was consistent with the results obtained from wave velocities.

- FTC coefficients suggested that the pavement condition was probably consistent across the longitudinal joint at location B; whereas the joint at location A may be in poor condition.

## 7.4. Field Tests at the City of Hamilton (Nov. 2008 and July 2010)

The CPATT at the University of Waterloo in cooperation with the City of Hamilton, McAsphalt Industries and King Paving Ltd., is currently investigating the use of warm mix technologies to improve longitudinal joint performance (Tighe et al. 2008). Warm Mix Asphalt (WMA) is a new technology which has many proposed advantages compared to traditional Hot Mix Asphalt (HMA). Additives are used to increase the workability of the asphalt mixes at lower temperature, resulting in several constructions and performance benefits such as reduced asphalt aging, reduced tenderness of the mix during compaction, reduced energy consumption and reduced emissions. However, questions still remain regarding the performance of WMA.

A WMA trial section was placed in June 2007 on Garth Street from Stone Church Road to approximately 200 m north of the Lincoln Parkway in Hamilton. The main objective was to investigate if the WMA technology could mitigate longitudinal joint cracking. The HMA Control Section was placed prior to the WMA trial.

Seismic tests were performed in November 2008 on both HMA and WMA sections using the WTC method developed by Jiang (2008). Results were included in a report addressed to the city of Hamilton, and are provided in Appendix D.

Both seismic and deflection tests were conducted in July 21 2010, at four and three locations of the WMA and HMA sections respectively. The structure presented in Figure 6-19 was used to perform MASW tests. Since the testing time was significantly reduced, measurements were taken across the longitudinal joint and across joint-free sections for comparison. The analysis of this data was outside the scope of this thesis.

The traffic control setup involved the closure of one lane, and LWD tests could only be performed on one side of the longitudinal joint. The deflection was measured at the centreline (location C) and one meter apart from the longitudinal joint (location M). Four tests configurations were used in order to generate four different stress levels at the pavement surface, as indicated in Table 7-10. Five good drops were recorded for each configuration, resulting in

twenty readings at each location. Figure 7-28 shows the surface modulus obtained at each location with the four configurations.

The results were relatively consistent from one configuration to another. Overall, the surface modulus measured at the WMA section was higher than at the HMA section, as illustrated in Table 7-11. A difference of 24% was observed between the surface modulus of the two sections. A significantly higher modulus was obtained with the 150 mm plate than the 300 mm plate. This was consistent with the fact that measurements with smaller plate size were affected by shallower and stiffer layers.

Locations 3 and 4 of the WMA section and location 2 of the HMA section showed considerably higher surface modulus at the joint than at location M. This unexpected result might be related to the condition of the base or subgrade underneath the asphalt layer. The surface modulus was slightly lower at the joint than inside the lane for locations 1 and 2 of the WMA section and location 1 and 3 of the HMA section.

## 7.5. Master Curves and Comparison of LWD and MASW Moduli

The objective of this section was to compare the modulus measured with the two NDT techniques at different frequencies of loading. The seismic tests were performed with a 50 kHz source, and dominant frequencies around 8, 19, 36 and 50 kHz were recorded by the receivers. During the field survey at the CPATT Test Track, the MASW array was placed next to the LWD in order to analyze the wave generated by the deflection device. Figure 7-29 shows the time signals and frequency spectra recorded by the twelve receivers. The dominant frequency was around 60 Hz, which was much lower than the frequency content produced by the ultrasonic source. In order to compare the moduli obtained with the two methods, a master curve was used to shift the moduli to a design frequency of 25 Hz, as explained in Section 5.6.

The most accurate method to determine master curves consists of conducting dynamic modulus testing at five temperature (-10, 4.4, 21.1, 37.8 and 54.4°C) and six loading frequencies (0.1, 0.5, 1.0, 5, 10 and 25 Hz), as recommended in (AASHTO TP 62-07 2009). However, 150 mm height cylinders are required for the tests, which could not be obtained from the CPATT Test Track. Another alternative consists of using the E* predictive equation (5-13), as suggested in the input level 3 of the M-EPDG (NCHRP 1-37A 2004). This equation was established with 2750 data

points and provided a $R^2$-value of 0.96. Therefore, it was used in this study to estimate the dynamic modulus of the asphalt mixtures over a range of temperatures and frequencies.

7.5.1.1.    Moduli Measured on Slab 2 and at the CPATT Test Track

As mentioned previously, field tests were performed at the HL 3-1 section of the CPATT Test Track, from which Slab 2 was extracted. The mix design parameters used to compute the master curve of the HL 3-1 section are indicated in Table 7-12 (Tighe et al. 2007). The viscosity was calculated with the ASTM viscosity temperature relationship (5-11). The A and VTS regression parameters were obtained from the AASHTO 2002 Design Guide which recommends typical values for all binder grades. The air void was assumed to be 7%, which is a typical value for this type of pavement. The resulting master curve and shift factors are presented in Figure 7-30.

Seismic measurements provided good estimations of the P-wave and R-wave velocities. Using the equations presented in Section 2.2.1, elastic moduli were determined from $V_P$, $V_R$ and the HMA density, as illustrated in Table 7-13. Measurements on Slab 2 with configuration A, B and C provided an average modulus of 20.06 GPa with a standard deviation of 0.24 GPa. The temperature of the laboratory was assumed to be equal to the reference temperature, thus no shifting was required. However, field tests were performed at an average temperature of 24°C, and the elastic modulus needed to be shifted to a reduced frequency for comparison with the master curve.

The master curve and the average seismic moduli are plotted in Figure 7-31. The MASW results appeared to be higher than the dynamic modulus given by the master curve. This difference was due to the fact that the master curve was established with a predictive equation, without laboratory test, and therefore probably underestimated the dynamic modulus of the asphalt mix. The high frequency seismic measurements could be used to correct the master curve obtained from E* predictive equations. This is of particular interest for in-situ measurement of asphalt dynamic modulus. A few MASW tests combined with a E* predictive equation based on information readily available from material specifications could provide a good estimation of the dynamic modulus over a range of frequency, without requiring destructive testing.

Design moduli were calculated by shifting the seismic values to a design frequency of 25 Hz using the master curve. Although significantly different seismic moduli were obtained for Slab 2 and the field section (9.1% difference), both measurements lead to very similar design moduli

(less than 0.2% difference). This result confirms that the difference in wave velocity and elastic modulus observed between laboratory and field measurements were mainly related to a difference in pavement temperature.

The dominant frequency produced by the LWD was around 60 Hz, corresponding to a reduced frequency of 25.11 Hz since field tests were performed at 24°C. This reduced frequency was very close to the design frequency; hence the LWD should provide modulus values similar to the average seismic design modulus of 6.23 GPa. The software LWDmod was used to estimate the modulus of the asphalt course of the Test Track. The backcalculation involved three layers, as shown in Figure 7-32. Typical base and subgrade moduli and the asphalt seismic design modulus were used as seed values. The results of the analysis are presented in Figure 7-33 for the LWD tests performed with two different plate sizes (150 mm and 300 mm diameter) across the centreline of location A and B of the CPATT Test Track. An average modulus of 6.06 GPa was obtained for the asphalt surface layer, which was very close to the design modulus obtained from seismic measurement. However, this average value was associated to a high standard deviation of 1.07 GPa.

As can be seen in Figure 7-33, deflection testing with the 150 mm diameter plate provided higher surface modulus E0 than the 300 mm diameter plate. As the measurement depth is proportional to the plate radius, measurements with the 150 mm diameter plate were affected by shallower and stiffer pavement layers. The figure also highlights the important effect of the subgrade on the surface modulus. For location 2, the surface modulus followed the same trend as the subgrade modulus, unlike the base and asphalt moduli. Several seed values were tried during the backcalculation process, and the asphalt modulus had to be increased by approximately 2000 MPa in order to obtain a reduction of about 10 MPa for the subgrade modulus. This result confirms that the surface modulus is not or little correlated to the condition of the surface layer that contains the longitudinal joint. A backcalculation process is required to isolate each layer of the pavement structure. Measurements with different plate sizes and dropping heights should be combined at the same testing location in order to optimize the calculation. Only two different stress levels were used for testing at the CPATT Test Track, and the results of the backcalculation were not accurate enough to evaluate the effect of the joint on the stiffness of the asphalt course.

7.5.1.2. Moduli Measured on Laboratory Slab 3

The mix design parameters used to compute the master curve of laboratory Slab 3 are summarized in Table 7-14. Based on the predicted density of the slab, an average air void of 7.5% was selected. A comparison of Table 7-12 and Table 7-14 shows that the two HL 3 mixes used at the Test Track and for the preparation of Slab 3 had very similar characteristics, resulting in the computation of almost identical master curves with the predictive equation.

The seismic modulus measured at the surfaces X and Y of Slab 3 are indicated in Table 7-15. Testing at surface X provided lower modulus than surface Y, which was probably due to the difference in compaction and coupling condition observed at the top and bottom surfaces, as explained in Section 7.2.1. Besides, Slab 3 showed a lower modulus than Slab 2. Asphalt hardening and high densities achieved in the field were probably the main reasons.

Finally, the master curve was used to shift the high frequency seismic moduli to the design frequency, as illustrated in Figure 7-34.

## 7.6. Summary

The results of the different experiments conducted in the laboratory and in the field were presented in this chapter. The analysis of the MASW data involved the calculation of wave velocities, attenuation curves and Fourier transmission coefficients. The centre deflection measured with the PFWD was used to determine the surface modulus of the tested pavement structures. The MASW measurements performed on asphalt slabs are described. Then, results from LWD and MASW tests conducted in the field, on the asphalt section of the CPATT Test Track, and on the HMA and WMA sections of Garth Street in the City of Hamilton, are presented. Finally, pavement moduli measured at different frequencies of loading with the deflection and seismic methods are compared using master curves. The results indicated that the methodology presented in this chapter has potential application for quality control of longitudinal joints in the field, provided improvements are made regarding the test setup and the signal processing techniques.
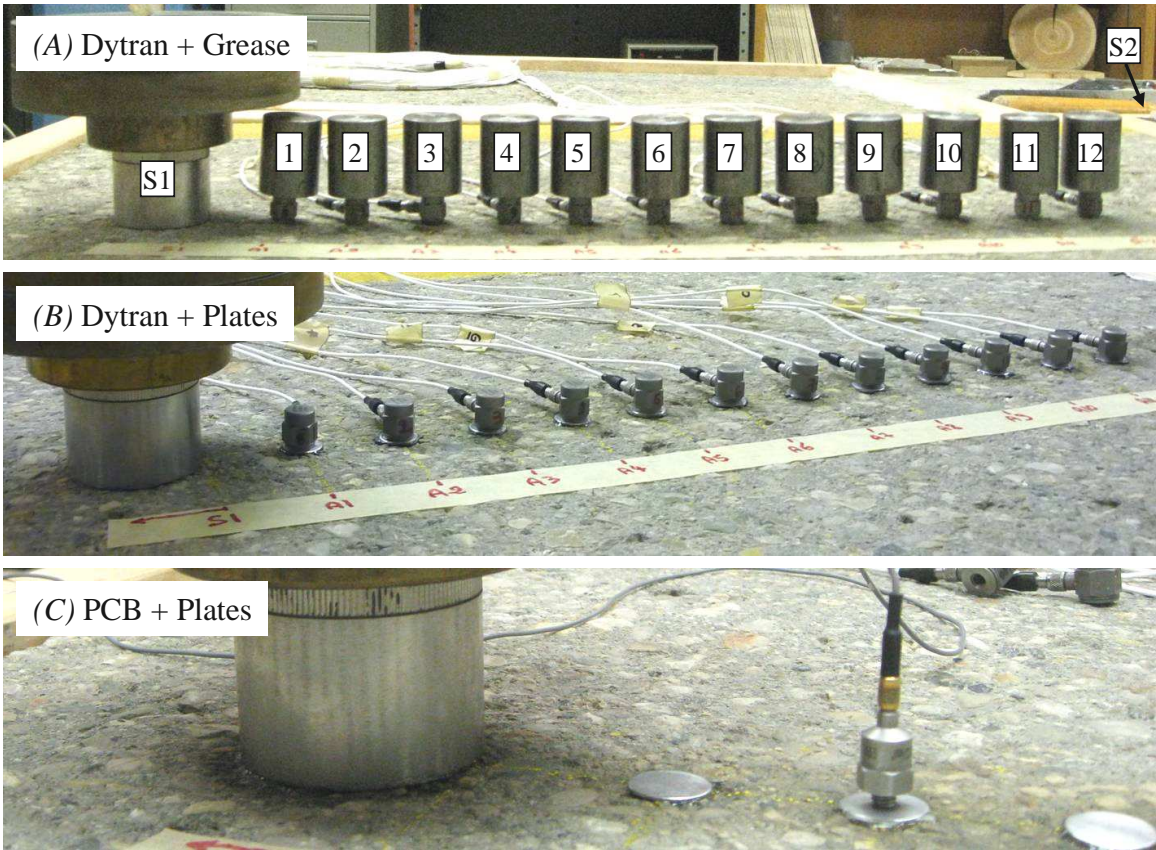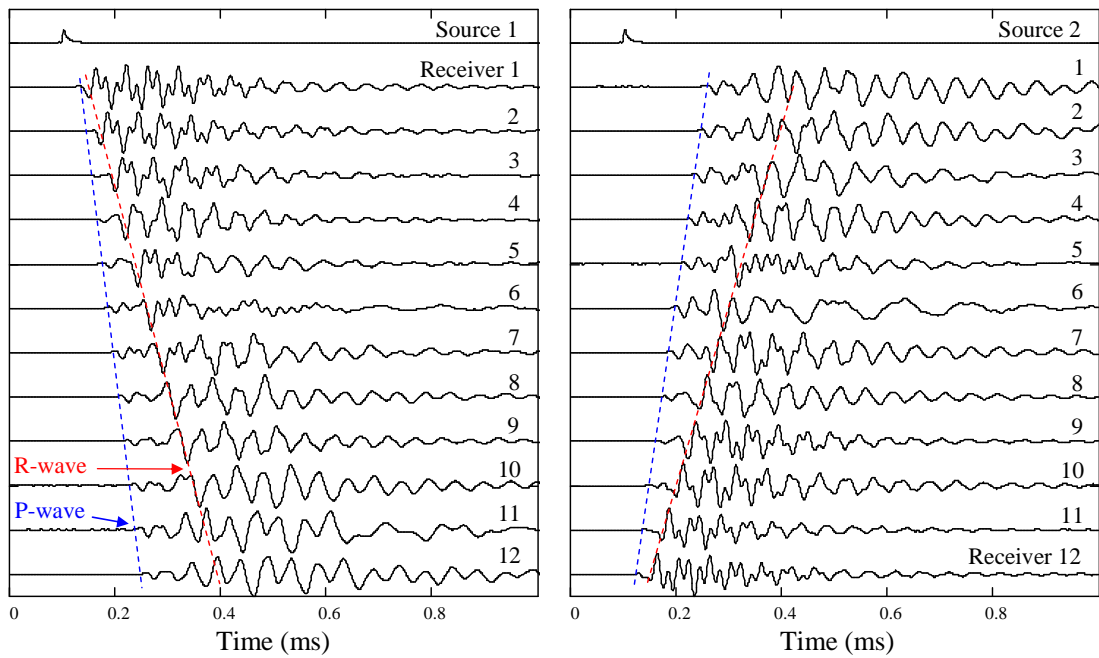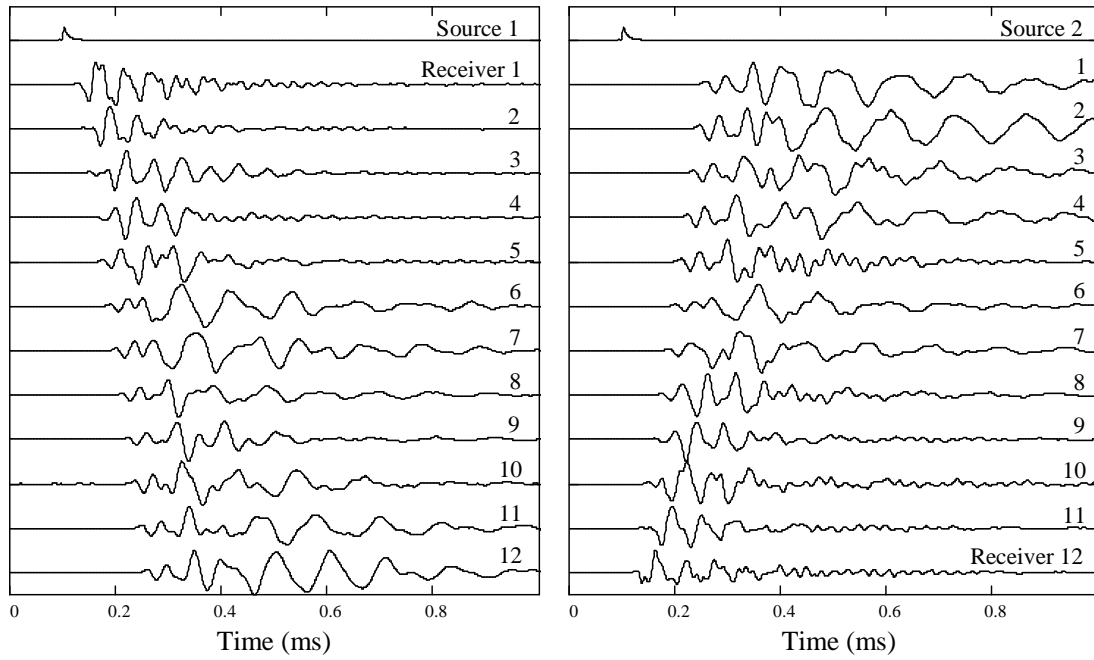
Figure 7-1: MASW setups used for testing on control Slab 2

*(A)* Dytran + Grease

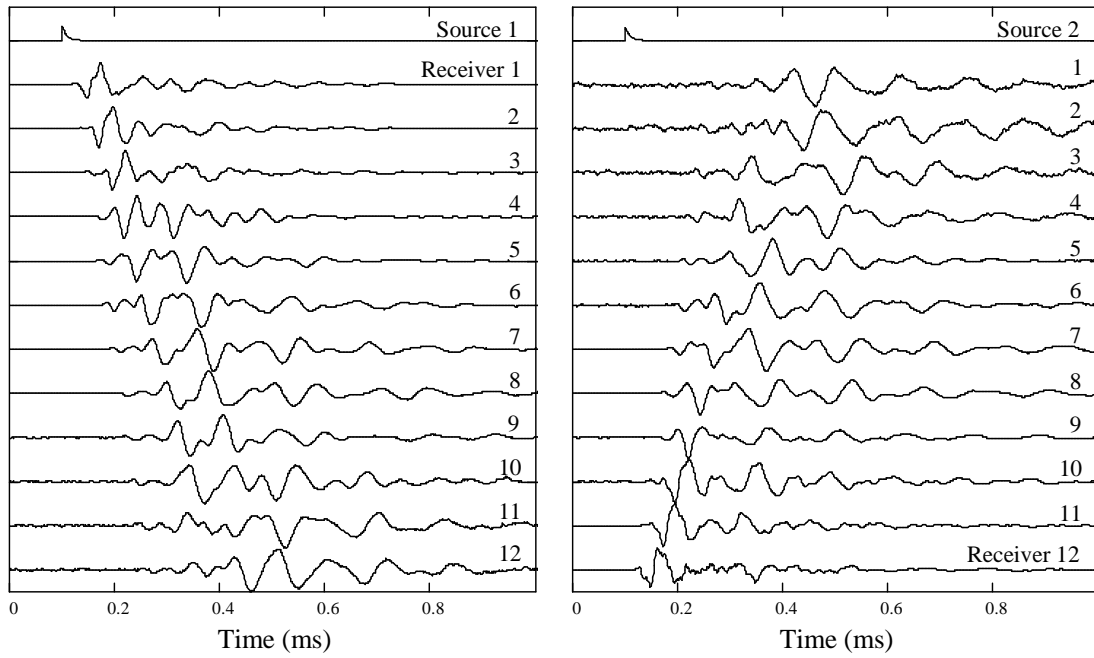*(B)* Dytran + Plates



*(C)* PCB + Plates



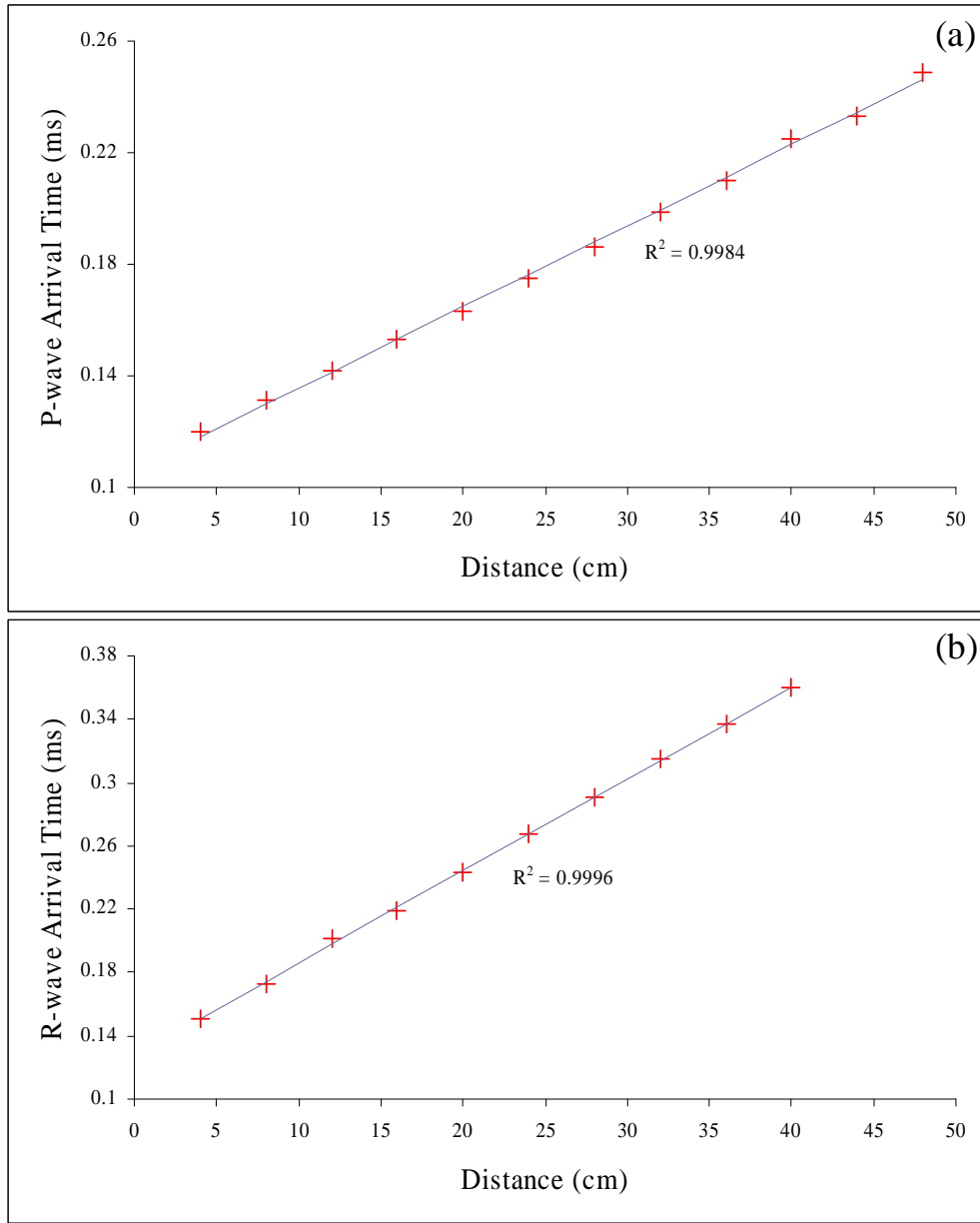Figure 7-2: Normalized time signals recorded with configurations A, B and C (Slab 2)

Figure 7-3: (a) $V_P$ and (b) $V_R$ calculation for configuration A, source at location 1 (Slab 2)
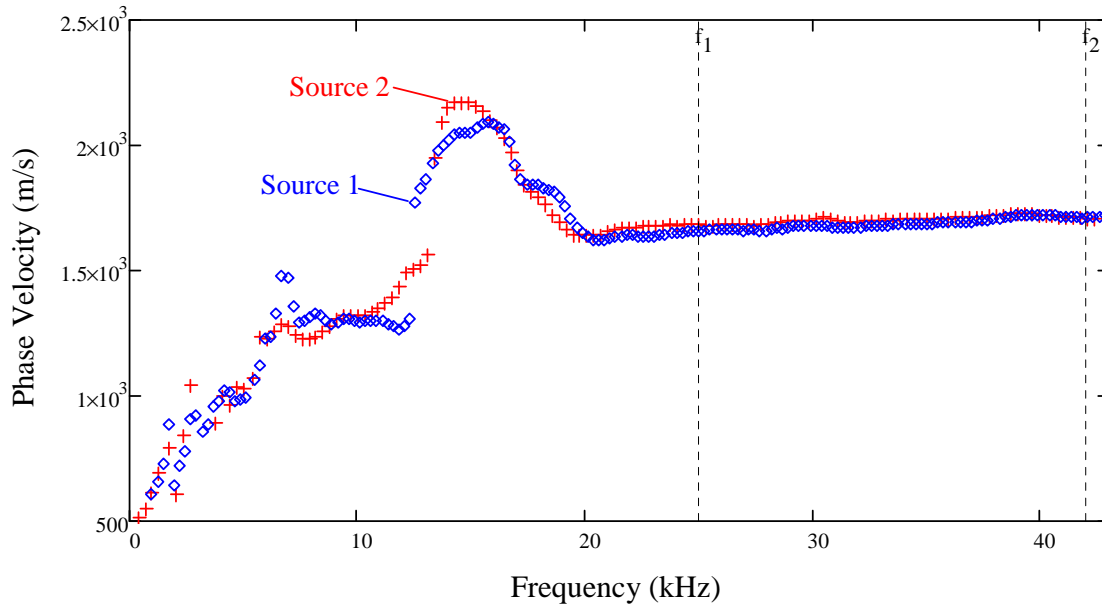
Figure 7-4: Dispersion curves for configuration A, source at locations 1 and 2 (Slab 2)
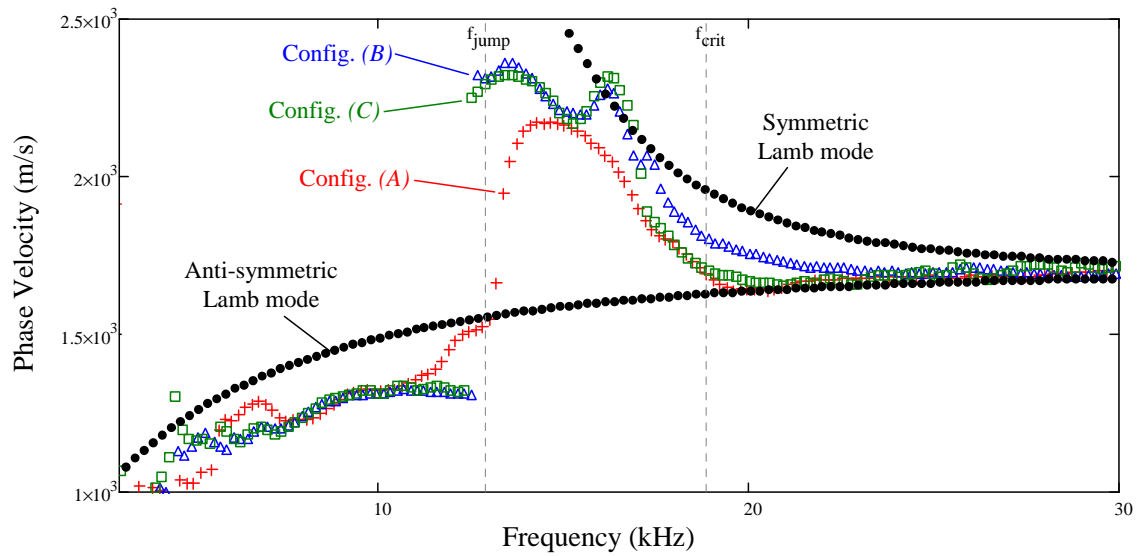


Figure 7-5: Dispersion curves for the three configurations, source at location 2 (Slab 2)
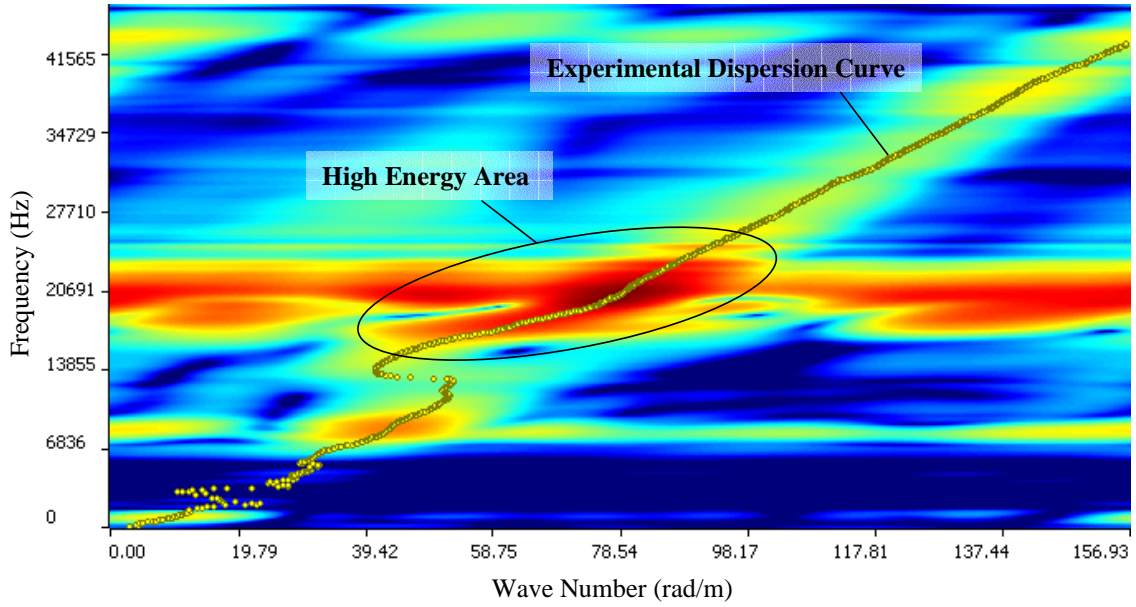
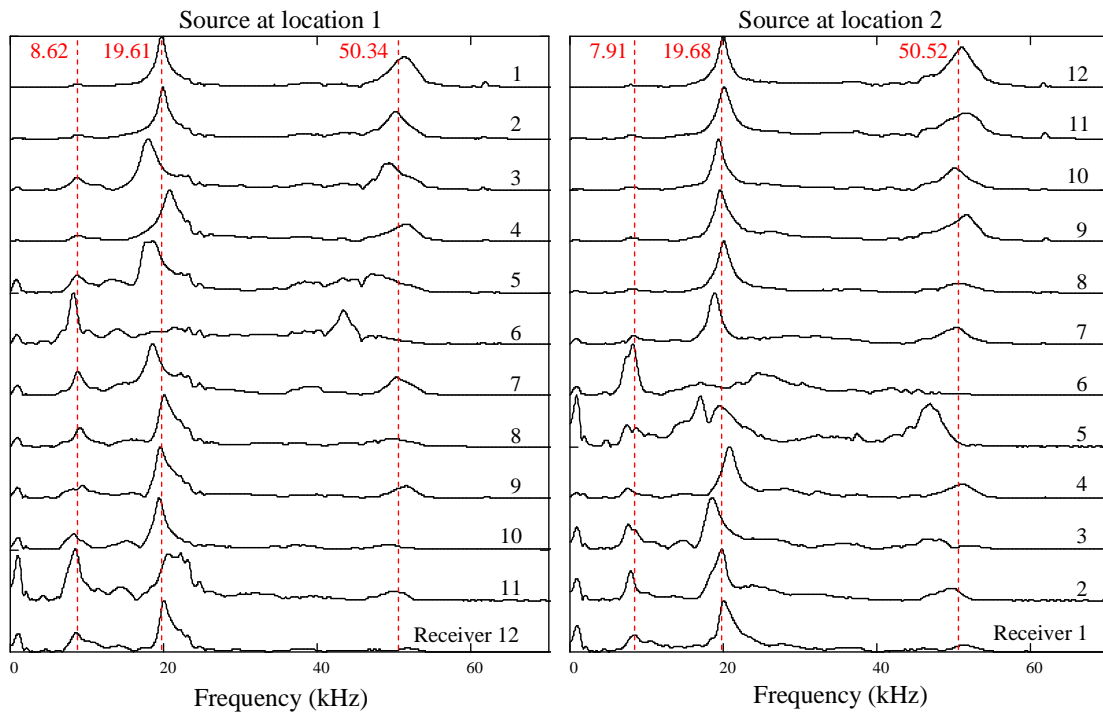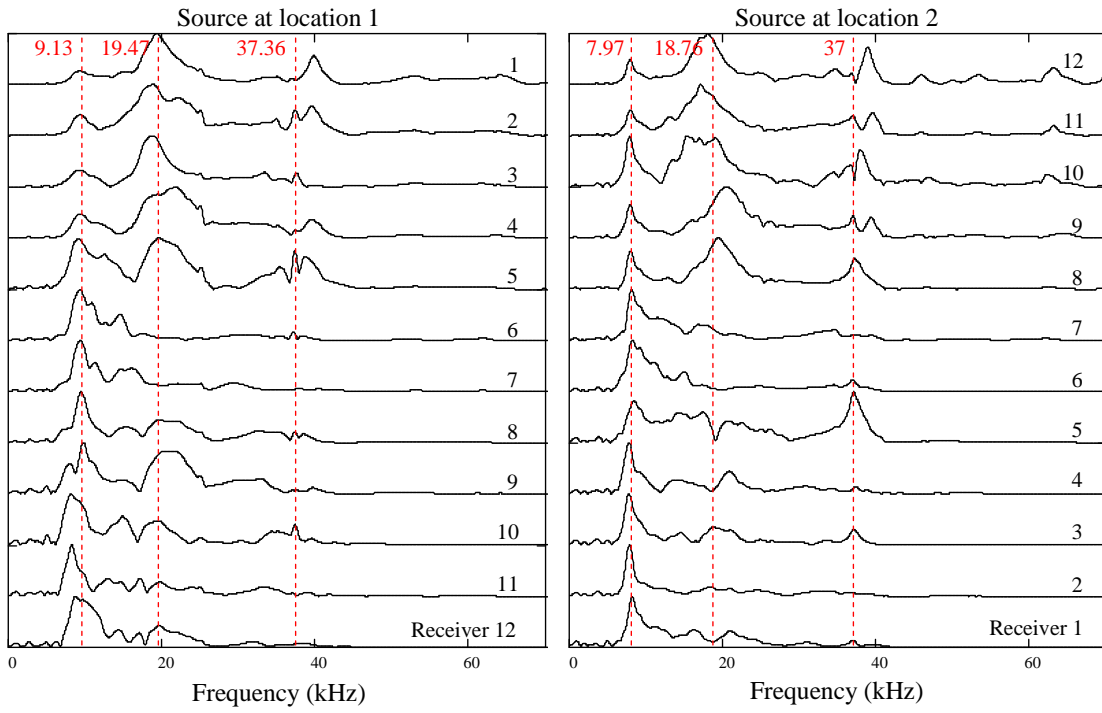Figure 7-6: FK spectrum for configuration A, source at location 2 (Slab 2)

*(A)* Dytran + Grease

*(B)* Dytran + Plates



*(C)* PCB + Plates
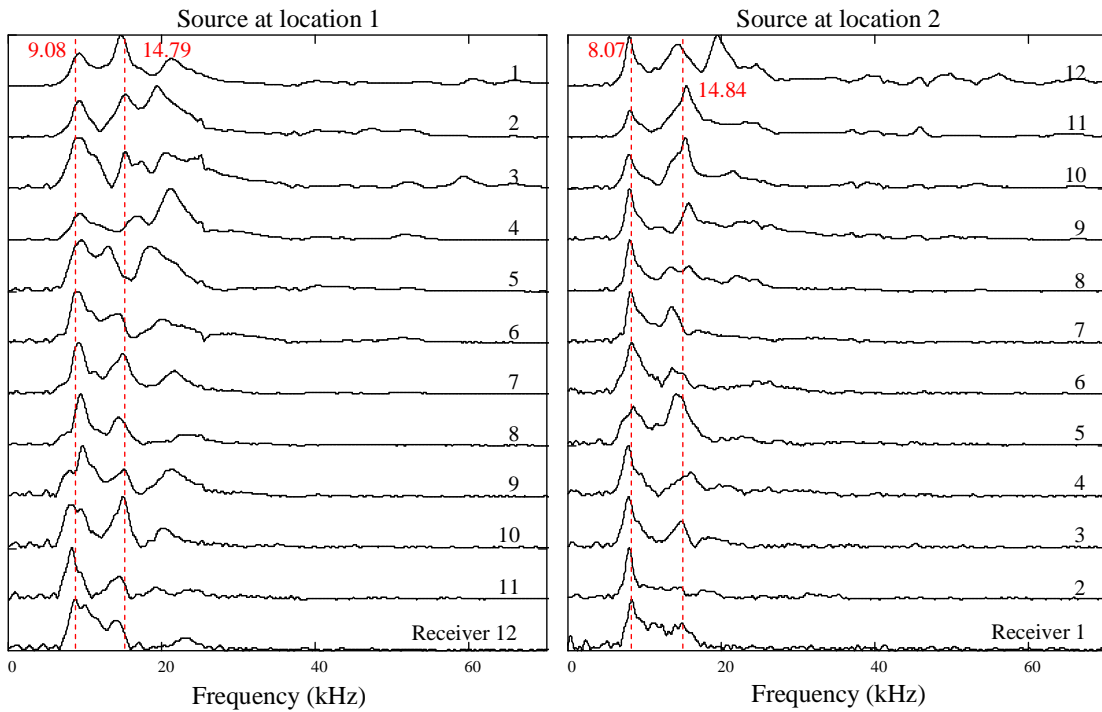


Figure 7-7: Normalized frequency spectra for configurations A, B and C (Slab 2)
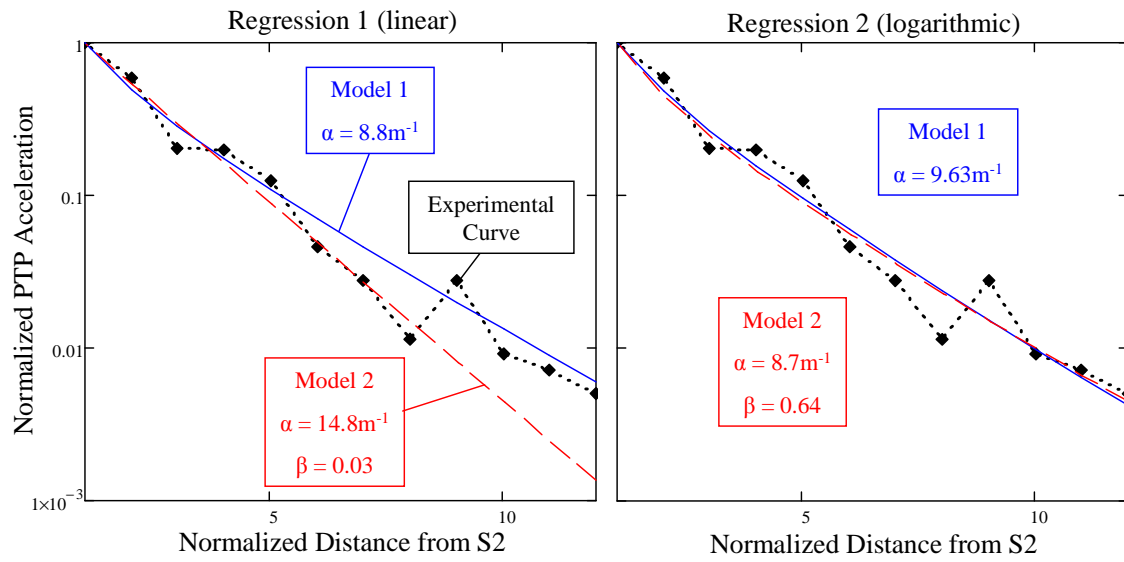
Figure 7-8: Normalized PTP acceleration for configuration A, source at location 2 (Slab 2)

(Y-axis: logarithmic scale)
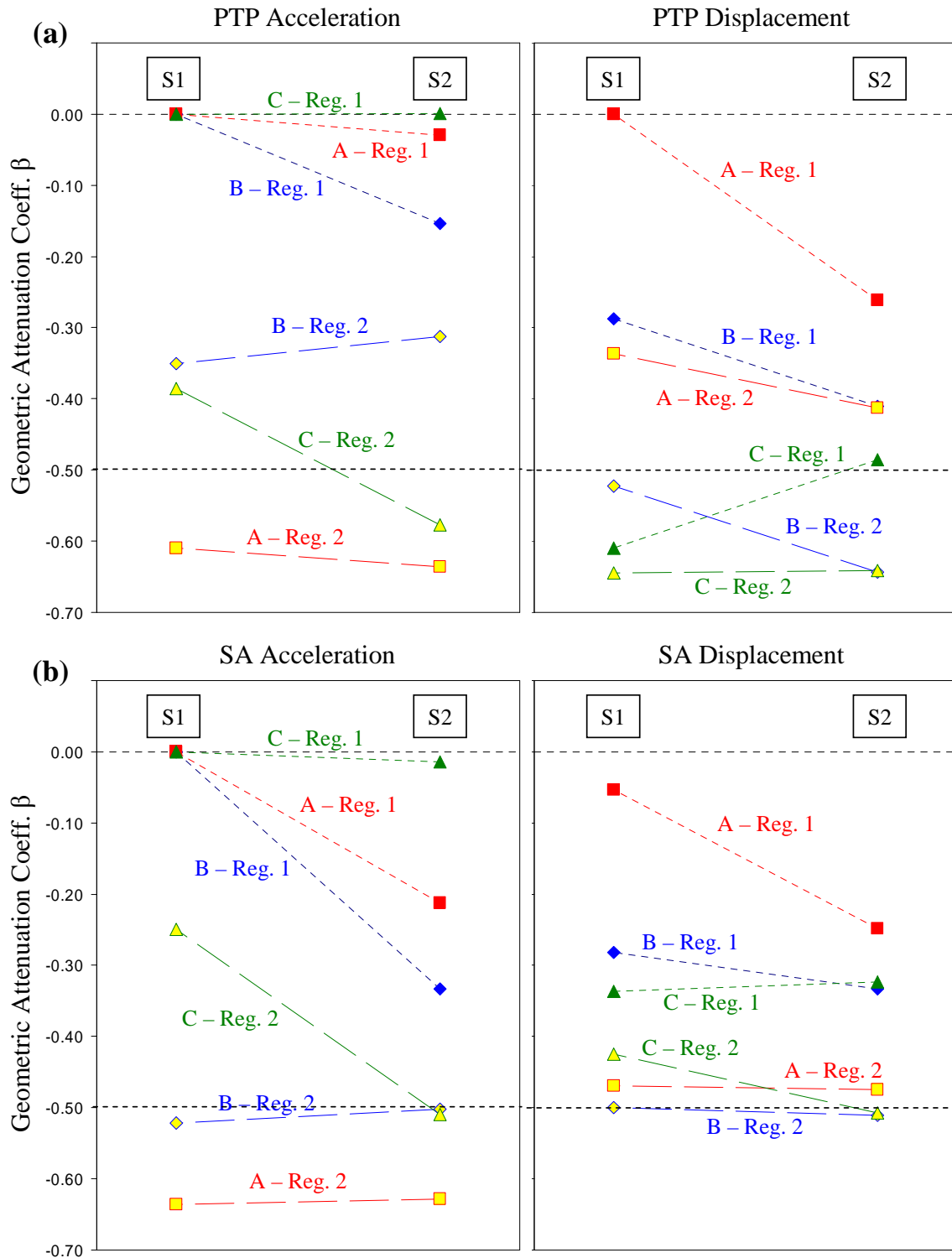
Figure 7-9: β calculated with Model 2 for (a) PTP and (b) SA (Slab 2)
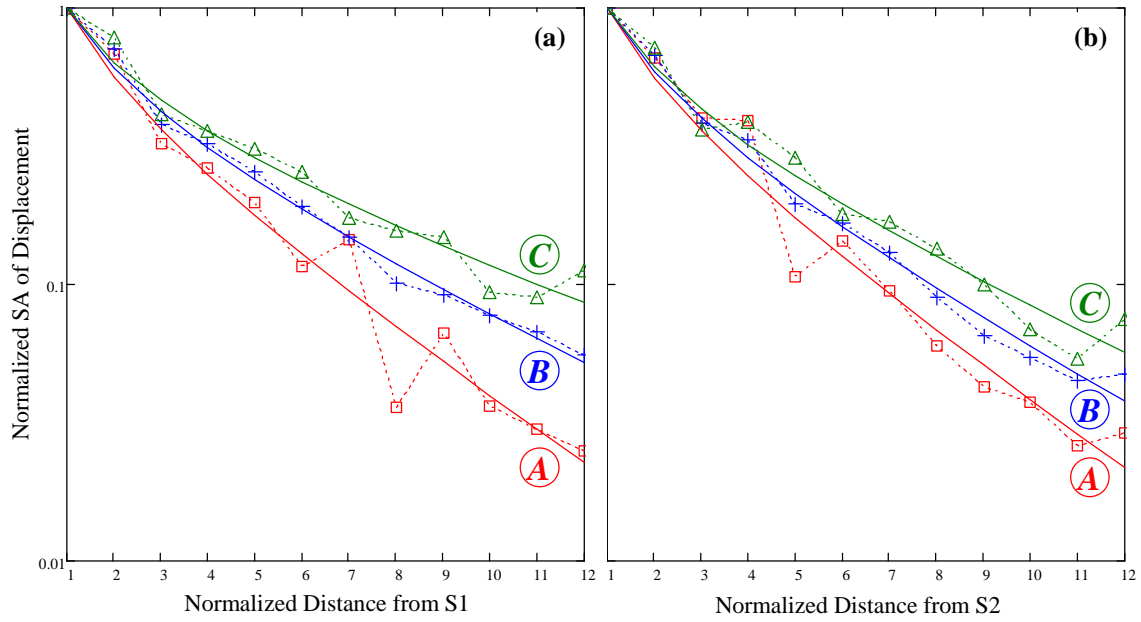
Figure 7-10: SA of displacement and regression models for configurations A, B and C with the source (a) at location 1 and (b) at location 2 (Slab 2) (Y-axis: logarithmic scale)
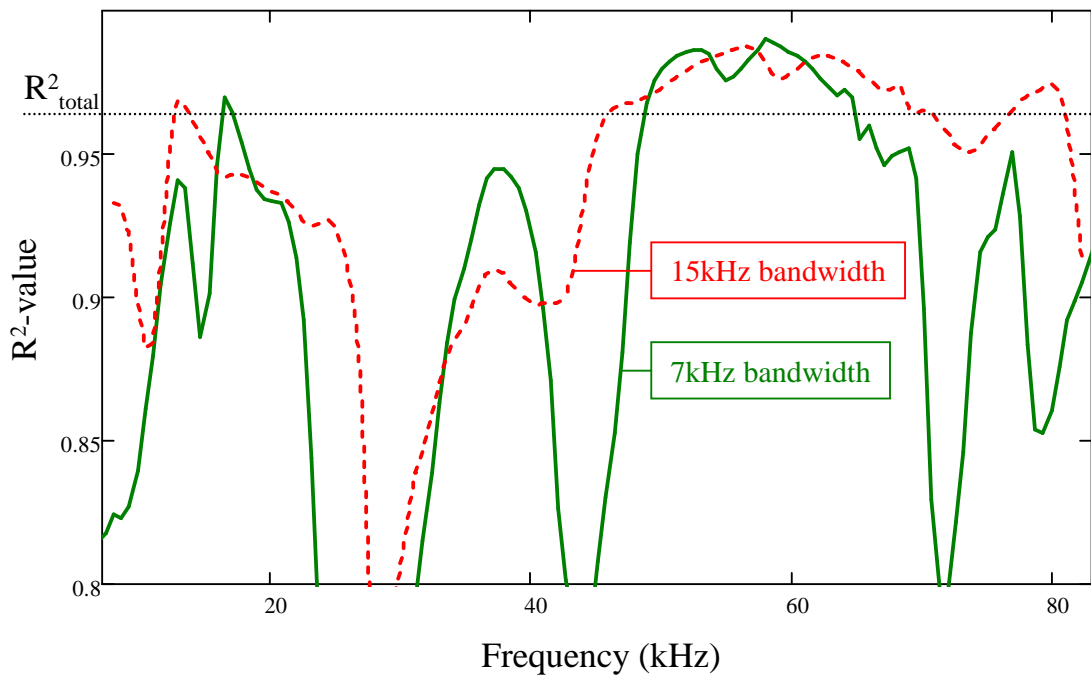


Figure 7-11: $R^2$-value vs. frequency for two bandwidths (configuration A, source 1, Slab 2)
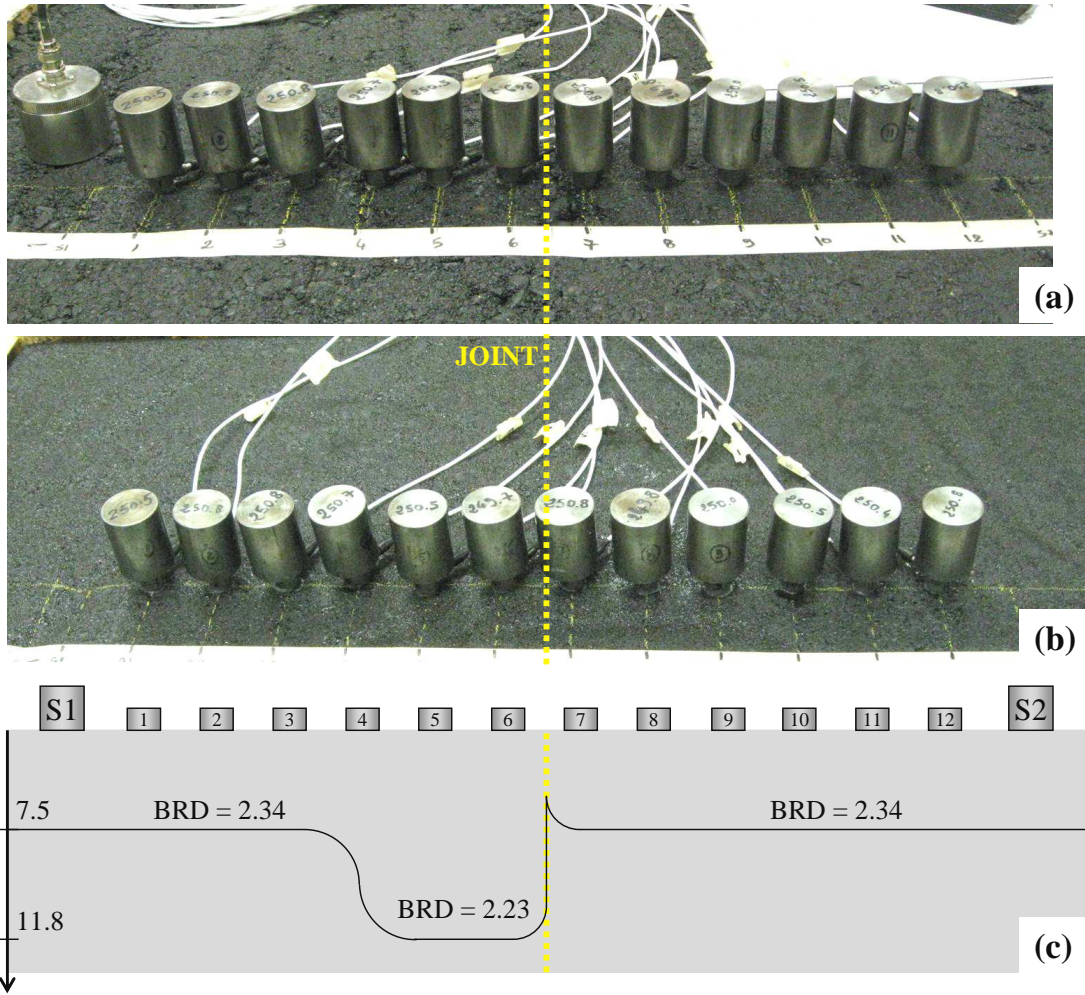
Figure 7-12: MASW testing with configuration A at (a) surface X and (b) surface Y of Slab 3; and (c) horizontal density profile of the tested section
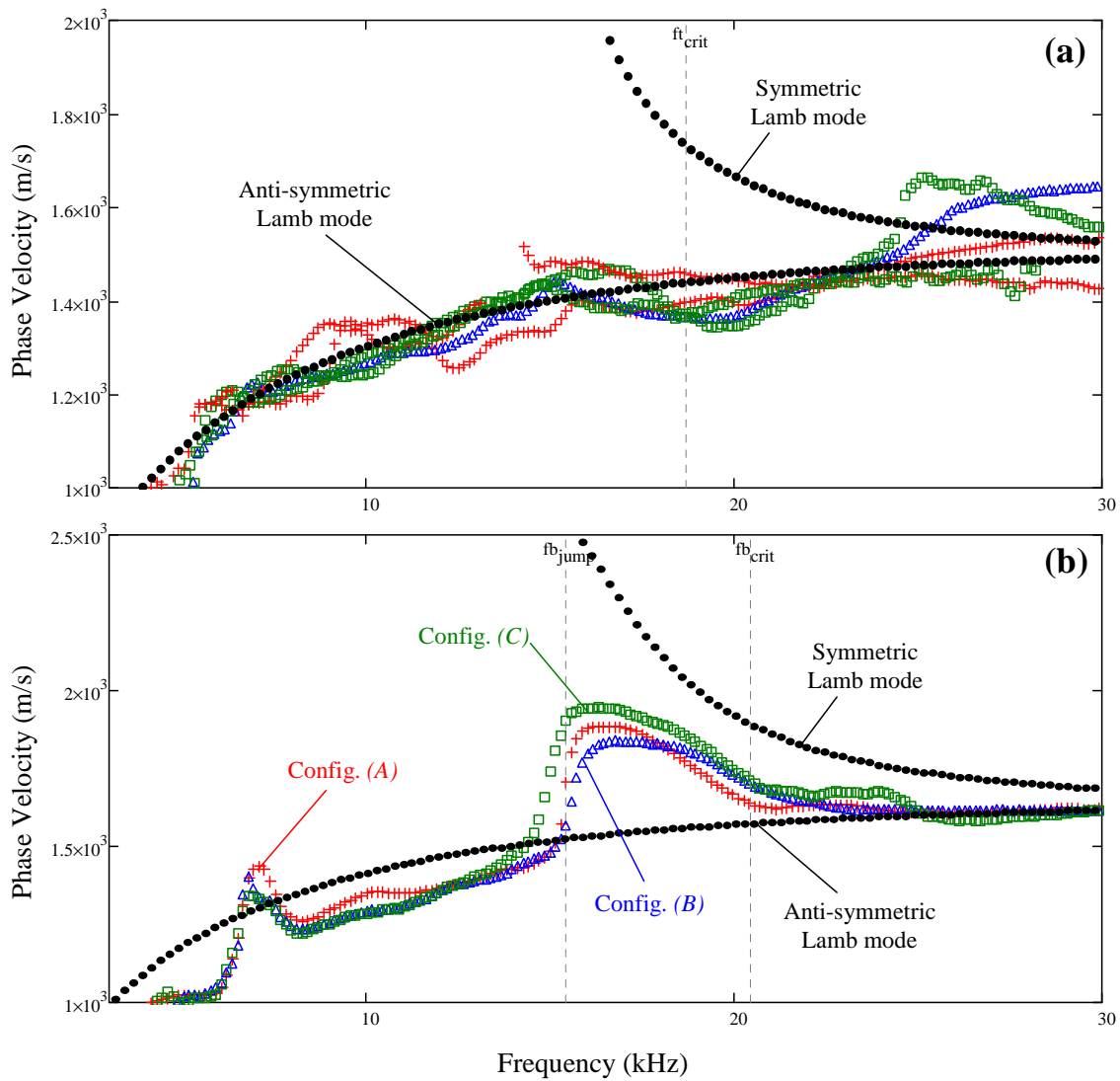
Figure 7-13: Dispersion curves measured on (a) surface X and (b) surface Y of Slab 3

(Only curves measured with the source at location 2 are showed for (b))
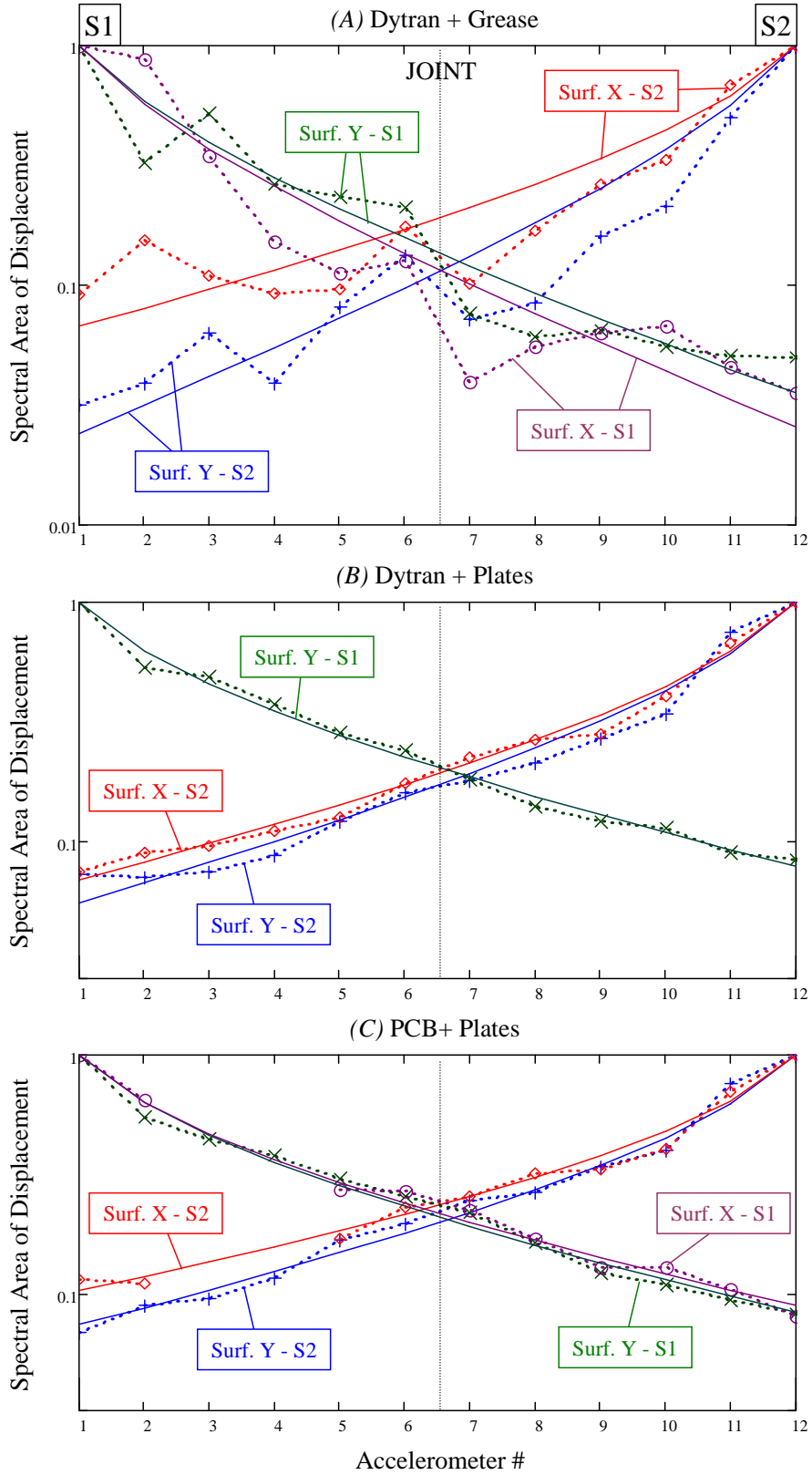
Figure 7-14: Experimental attenuation curves and regression models (testing on Slab 3)

(Y-axis: logarithmic scale)
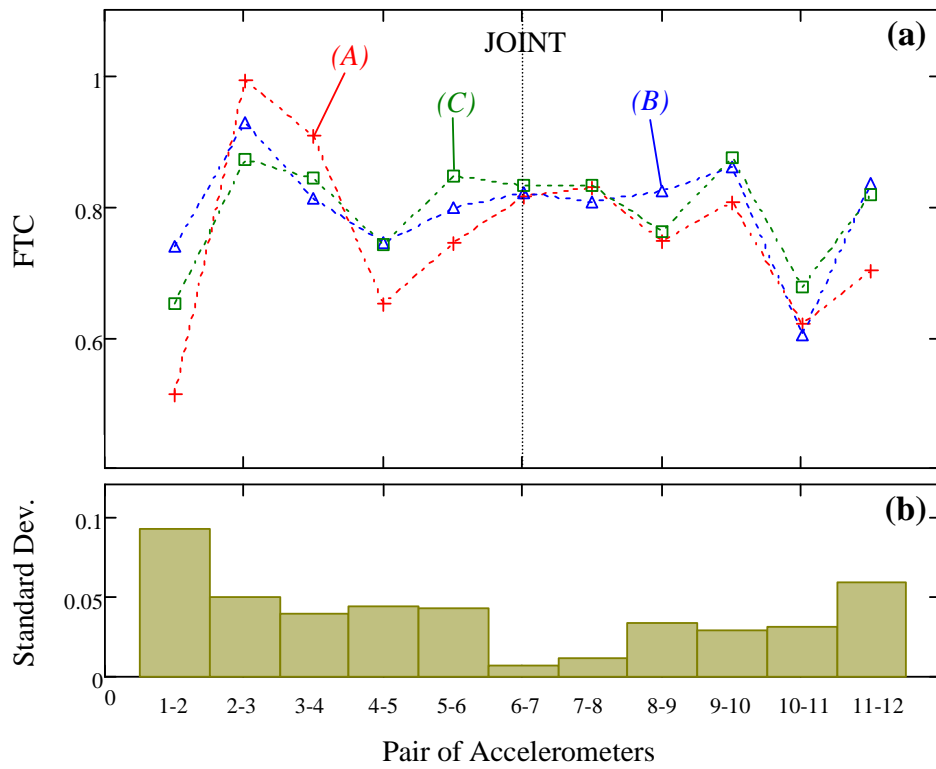
Figure 7-15: (a) FTC calculated with spectral areas of displacements and (b) standard deviation between the three configurations (surface Y of Slab 3)
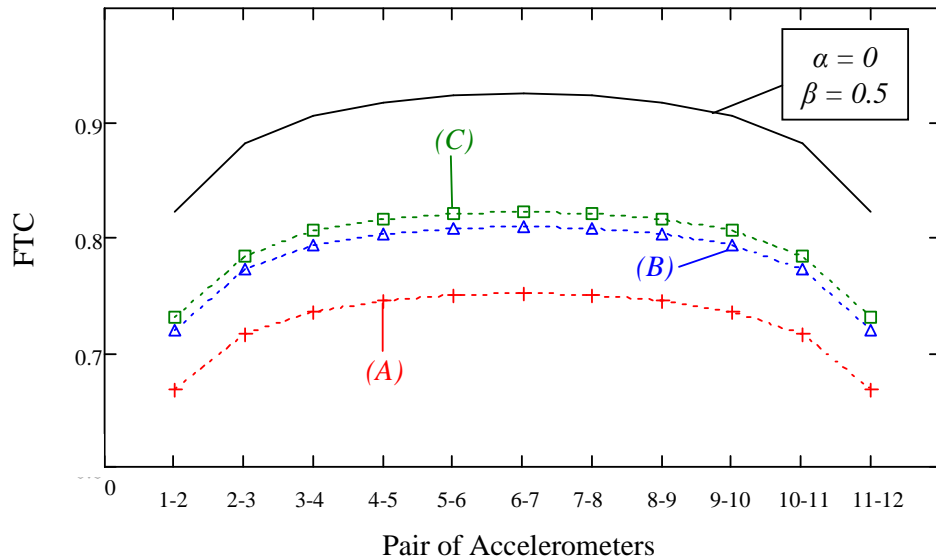


Figure 7-16: Theoretical FTC curves for the three configurations (surface Y of Slab 3)
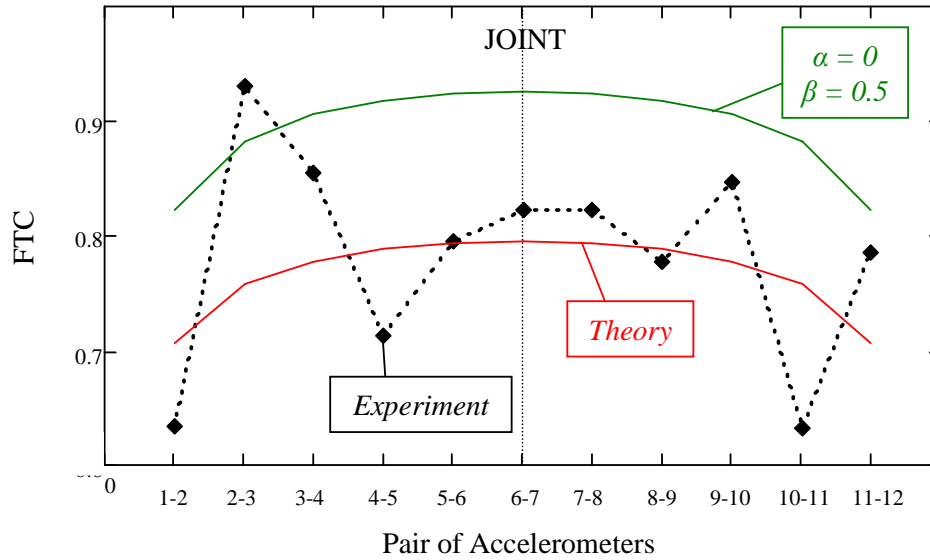
Figure 7-17: Average experimental and theoretical FTC curves (surface Y of Slab 3)
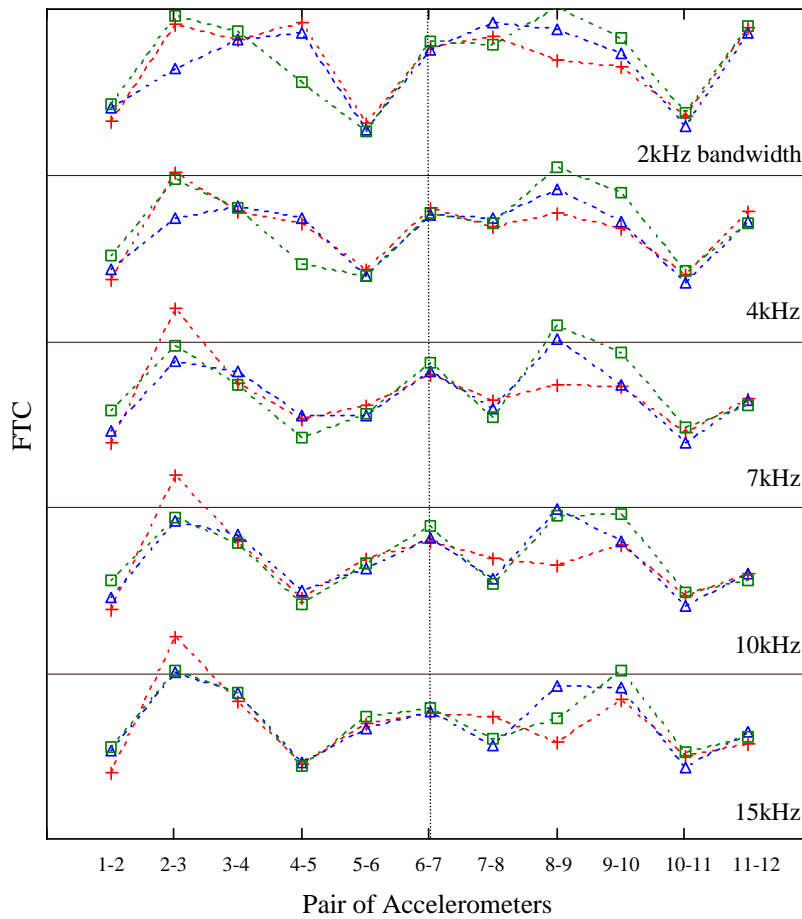


Figure 7-18: FTC calculated at 20k Hz with 5 different frequency bandwidths

(Surface Y of Slab 3)

**(a)**

709 m

567

420

283

153

Seismic Test Locations

B: 50m

A: 25m

0 m

South Lane

HL3-2    Superpave    SMA    PMA    HL3-1

North Lane

8m

425

284

**(b)**

Surface Course — 50 mm

Binder Course HL4 — 40 mm

Granular Base — 200 mm

Geotextile

Subgrade — Mainly clay and sand
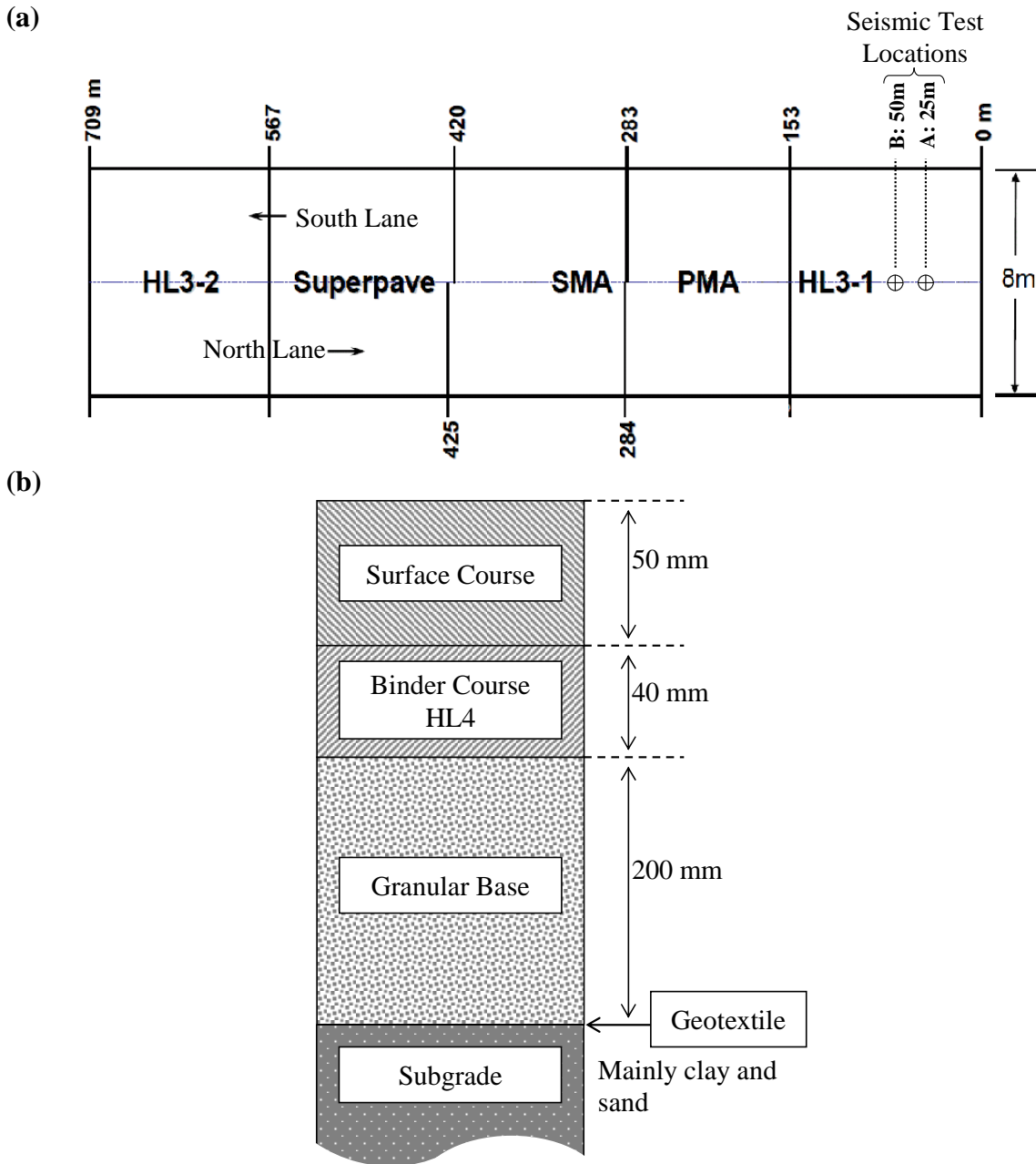
Figure 7-19: (a) Layout and (b) structure of the flexible section of the CPATT Test Track
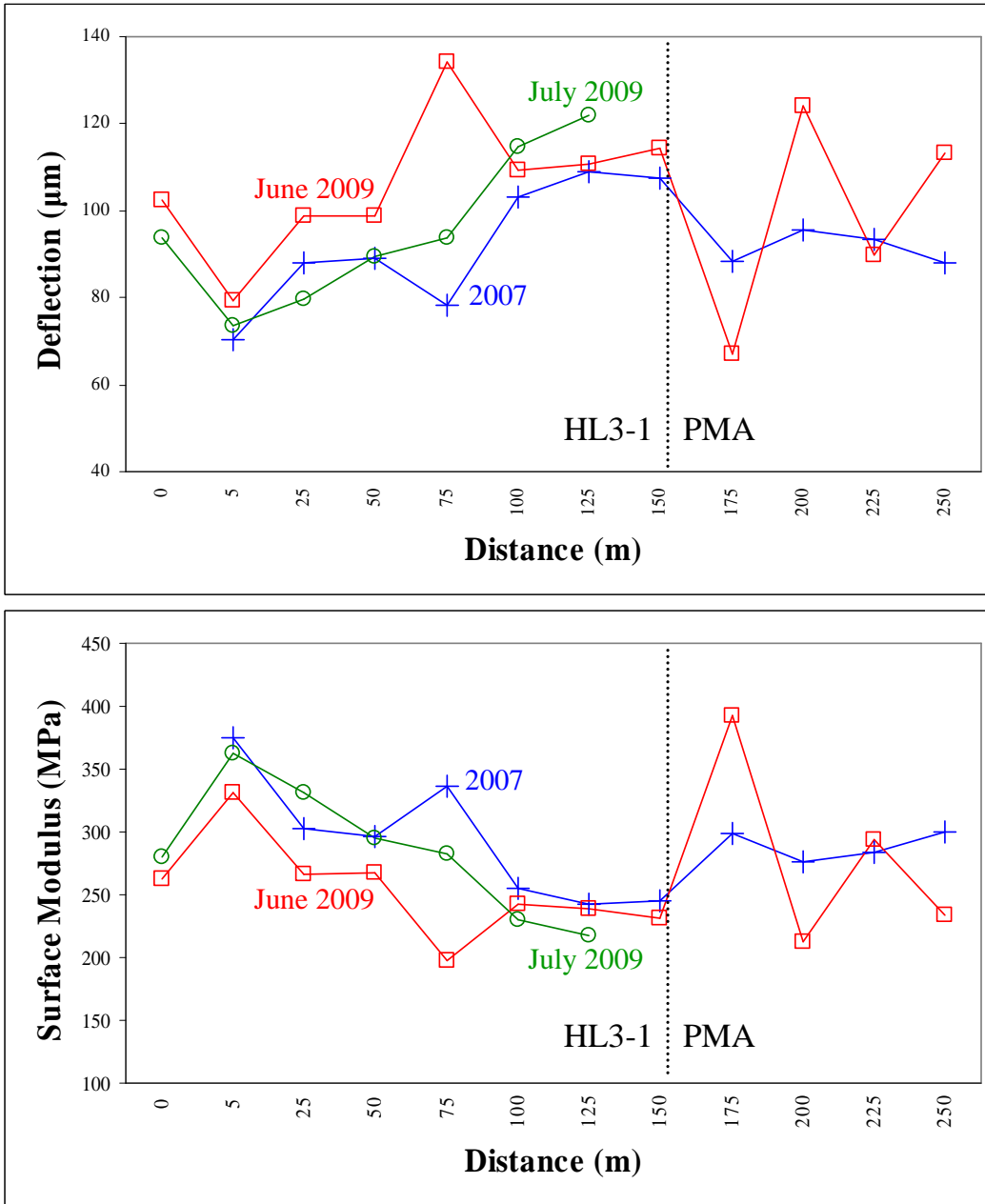
Figure 7-20: (a) Deflection and (b) surface modulus measured on the right wheel path of the
CPATT Test Track
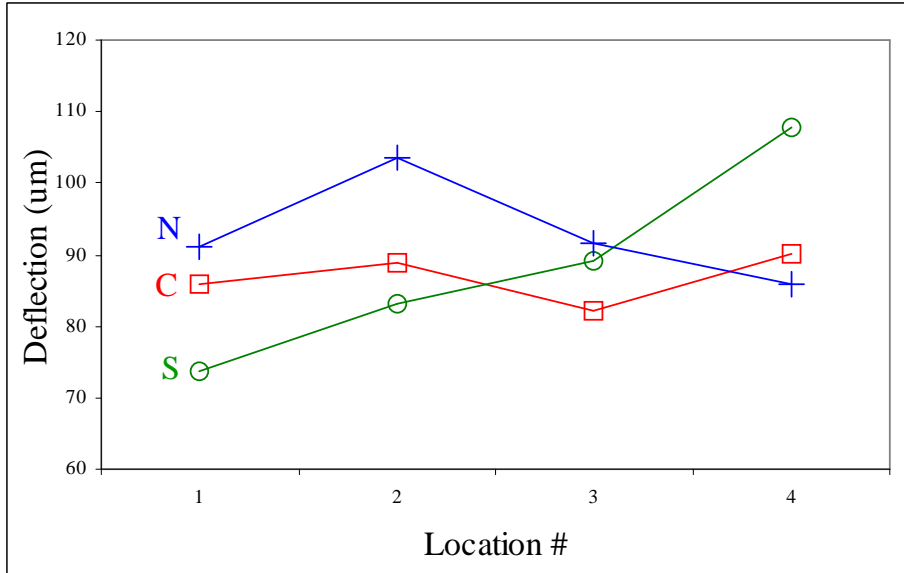
Figure 7-21: Deflection measured across the centreline of the CPATT Test Track



**(a)**                  **(b)**
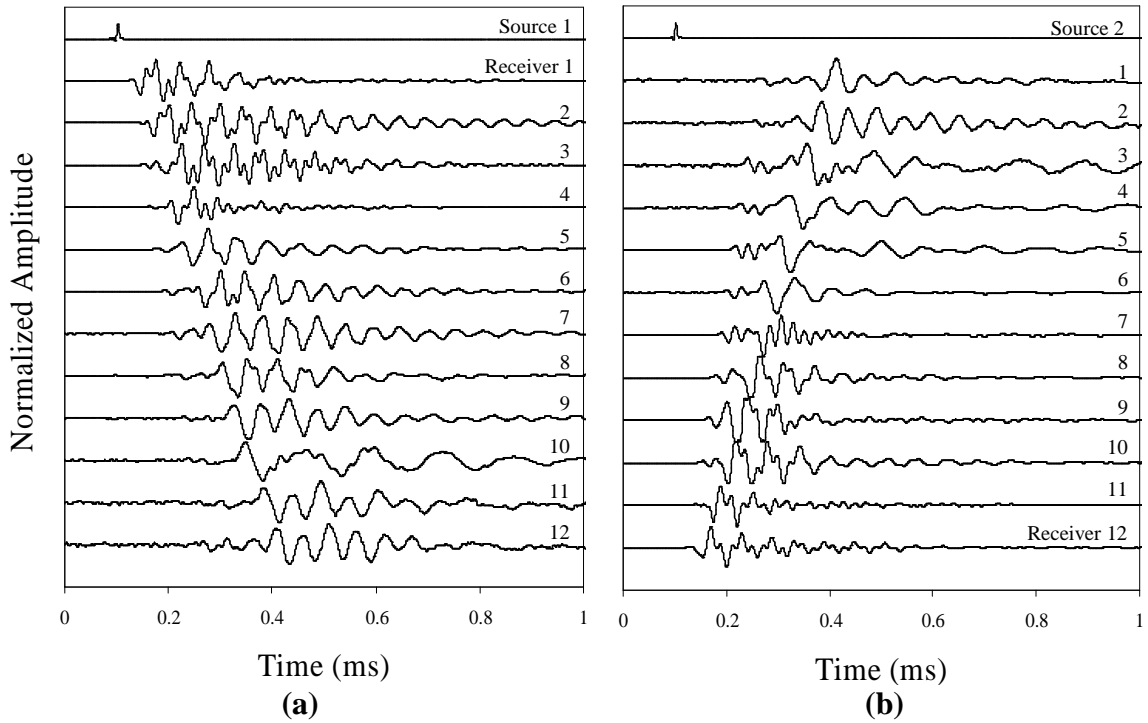
Figure 7-22: Normalized time signals for the source located (a) on the south lane and (b) on the

north lane of location A
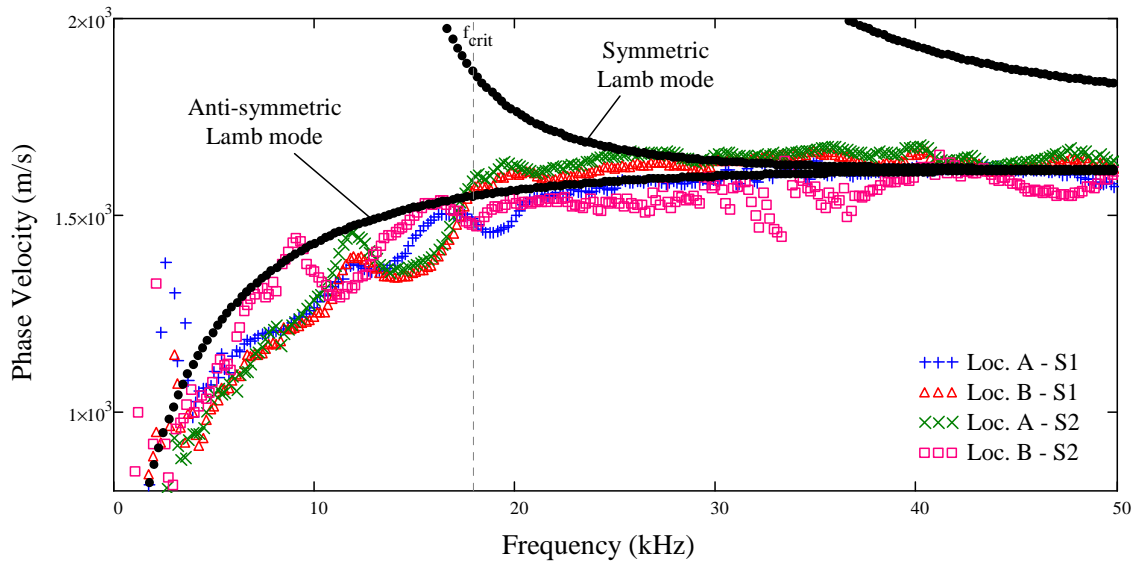
Figure 7-23: Dispersion curves computed from the data collected at the CPATT Test Track
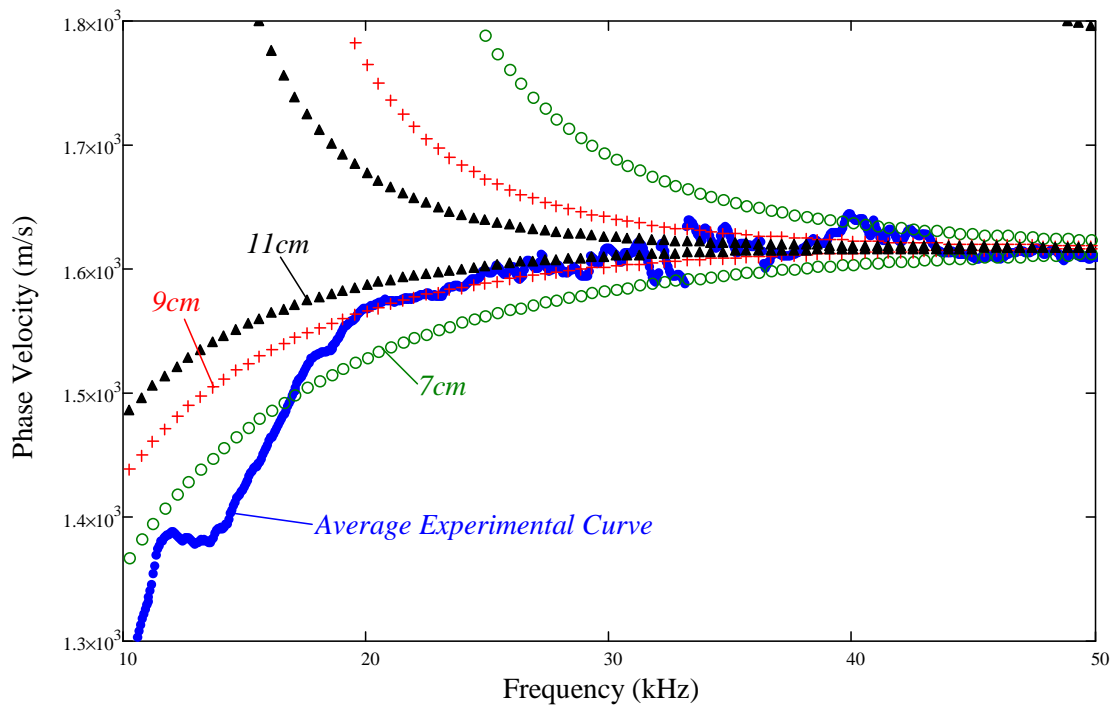


Figure 7-24: Experimental and theoretical dispersion curves for different thicknesses of the asphalt layer (7, 9 and 11 cm)
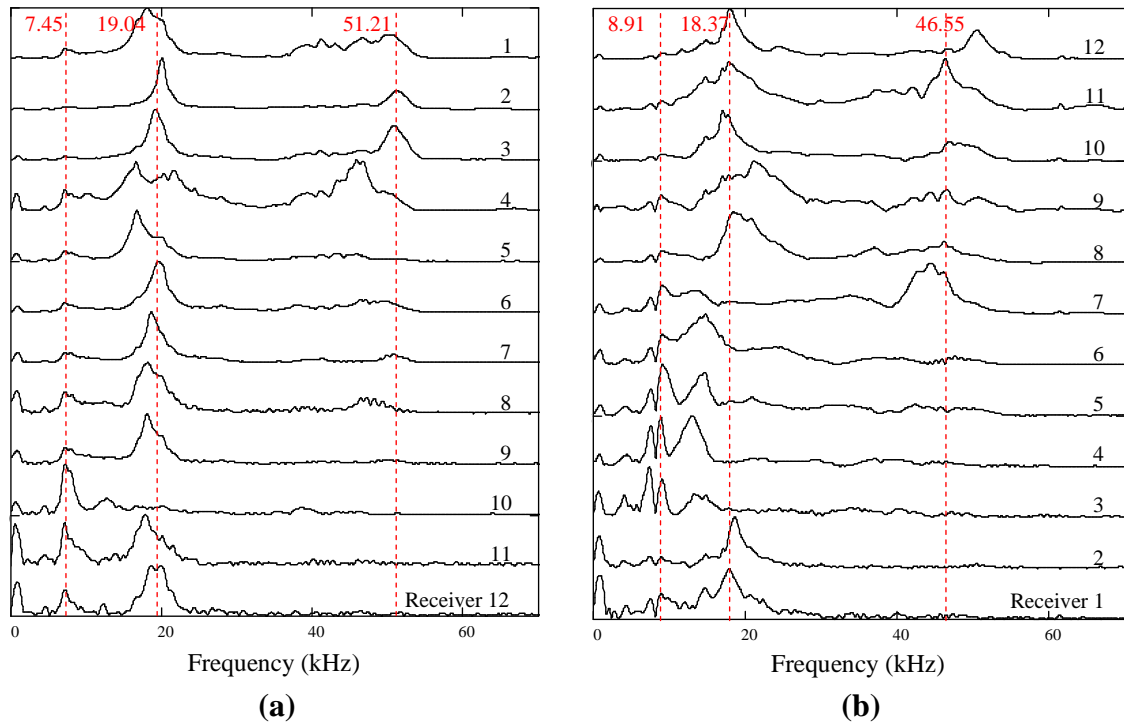
Figure 7-25: Normalized frequency spectra for the source placed (a) on the south lane and (b) on the north lane of location A
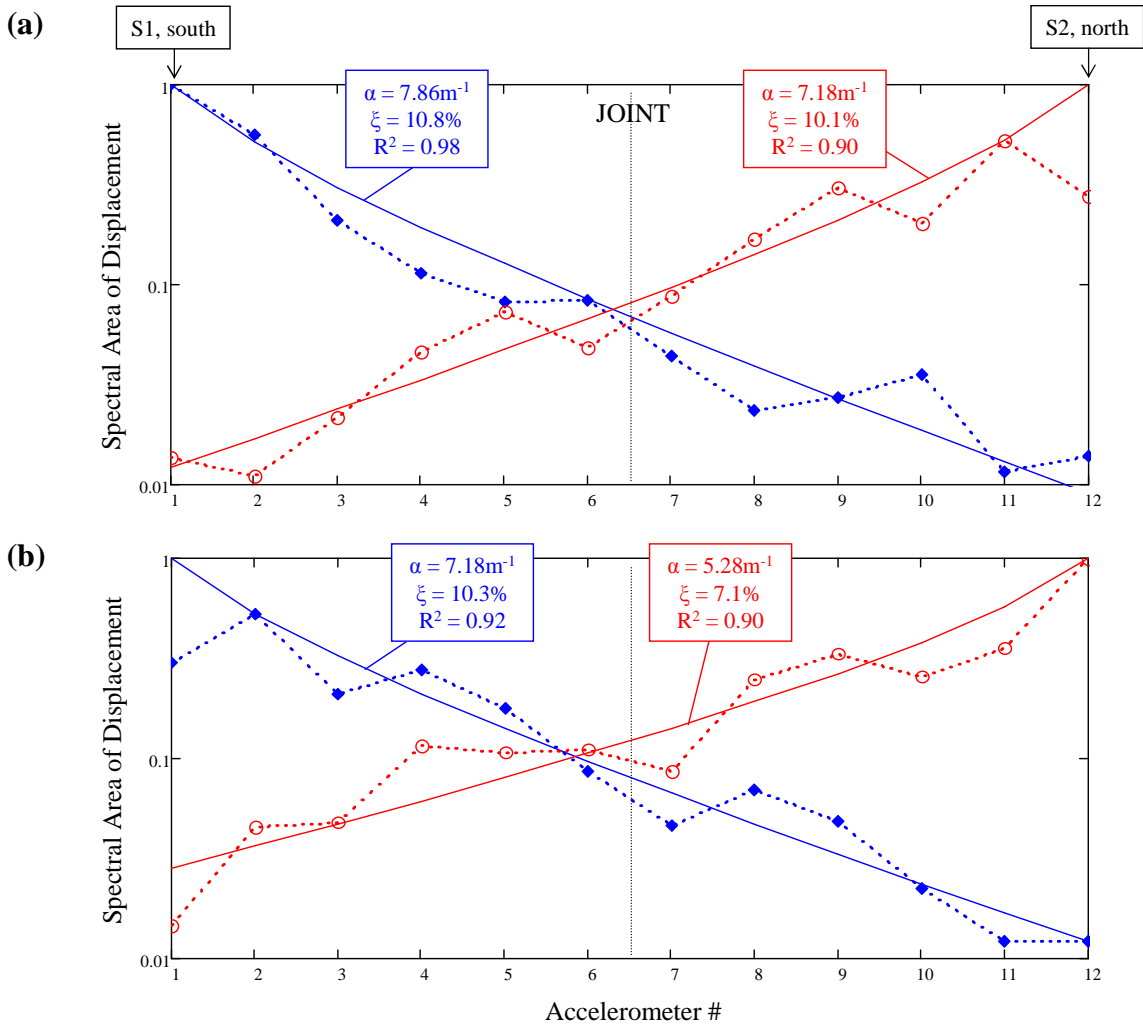
Figure 7-26: Attenuation curves and regression models measured at (a) location A and (b) location B of the CPATT Test Track
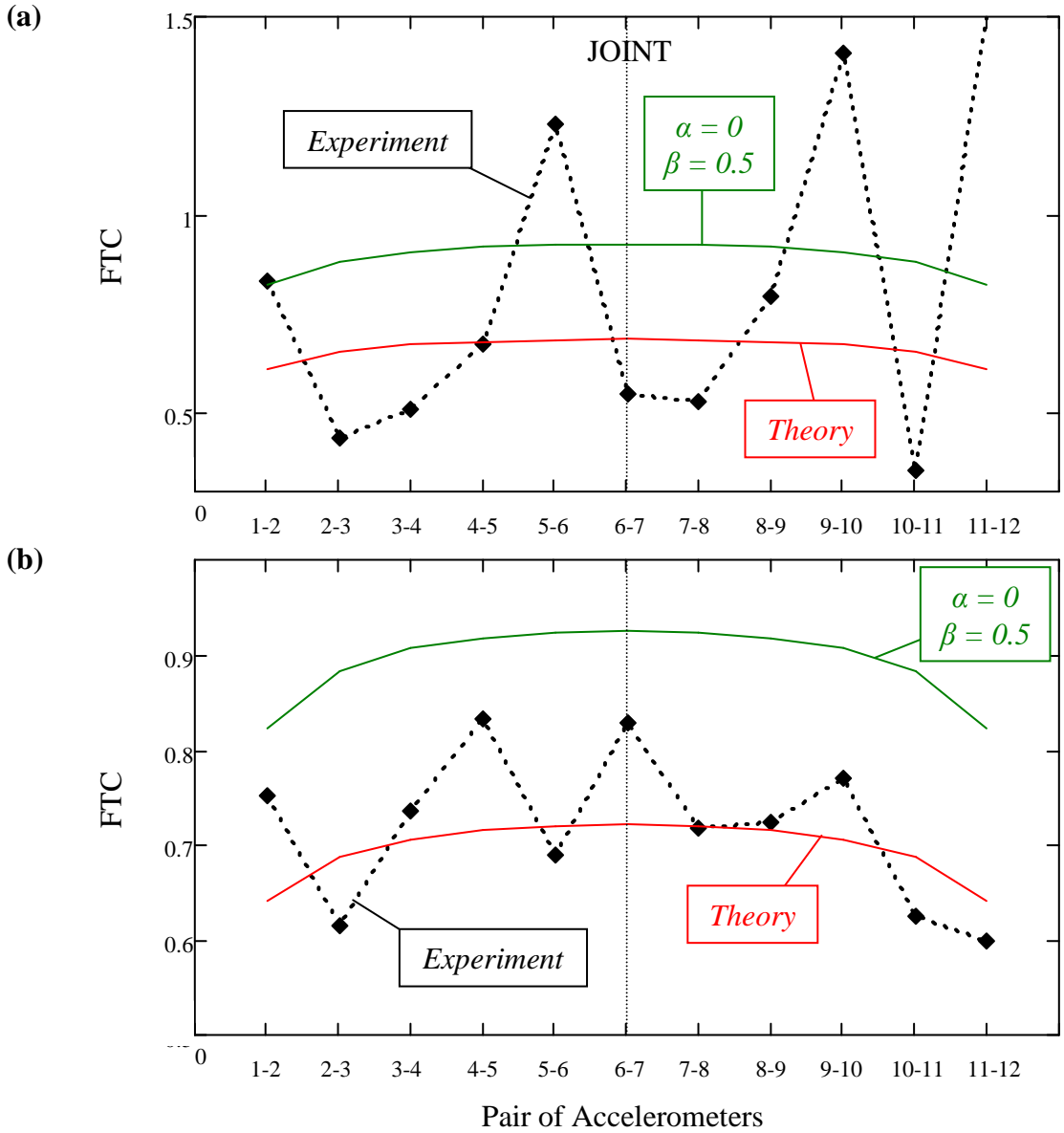
Figure 7-27: Experimental and theoretical FTC coefficients measured at (a) location A and (b) location B of the CPATT Test Track
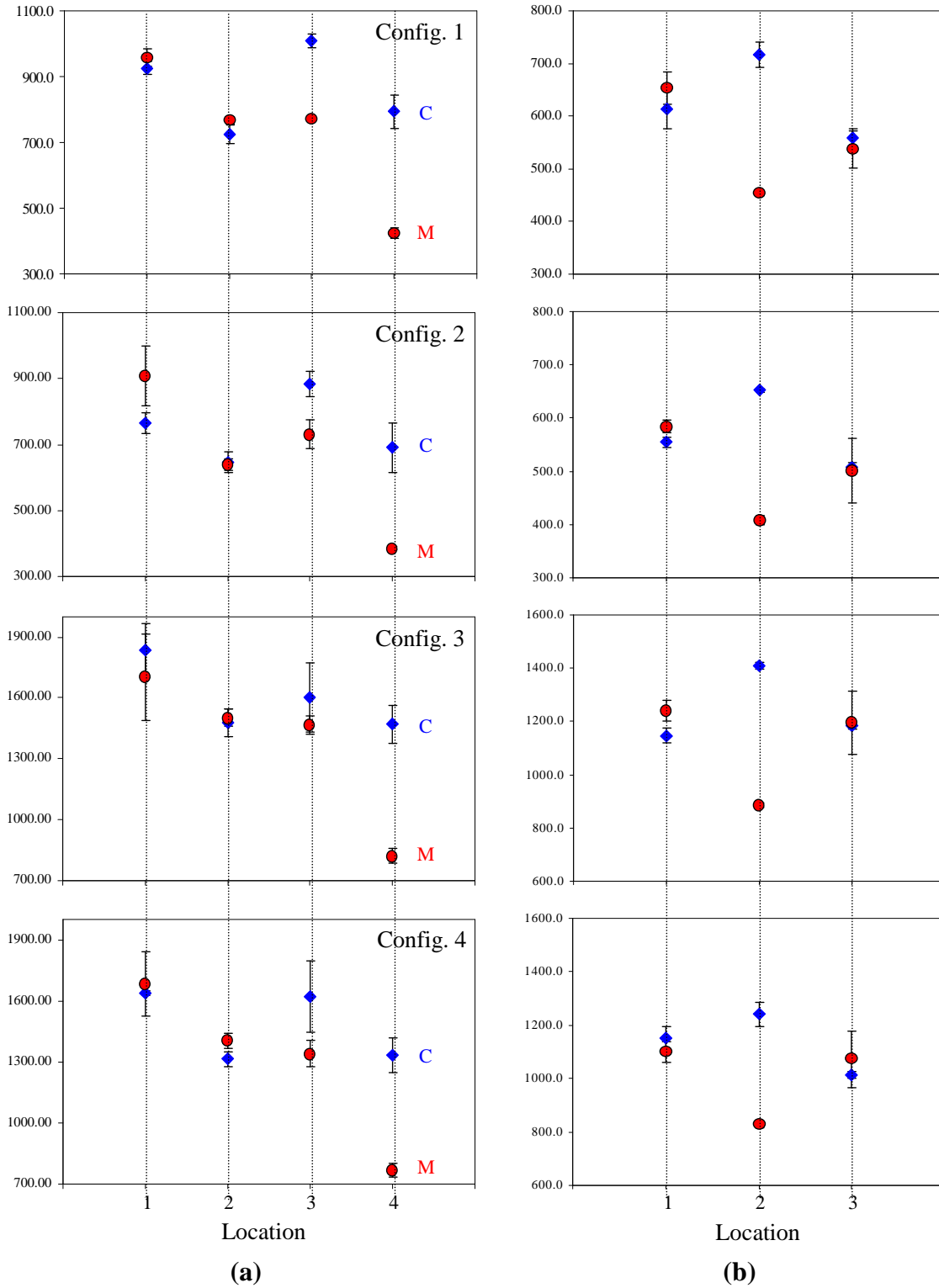
Figure 7-28: Surface modulus (MPa) measured at (a) the WMA and (b) the HMA sections

(Garth Street, city of Hamilton)
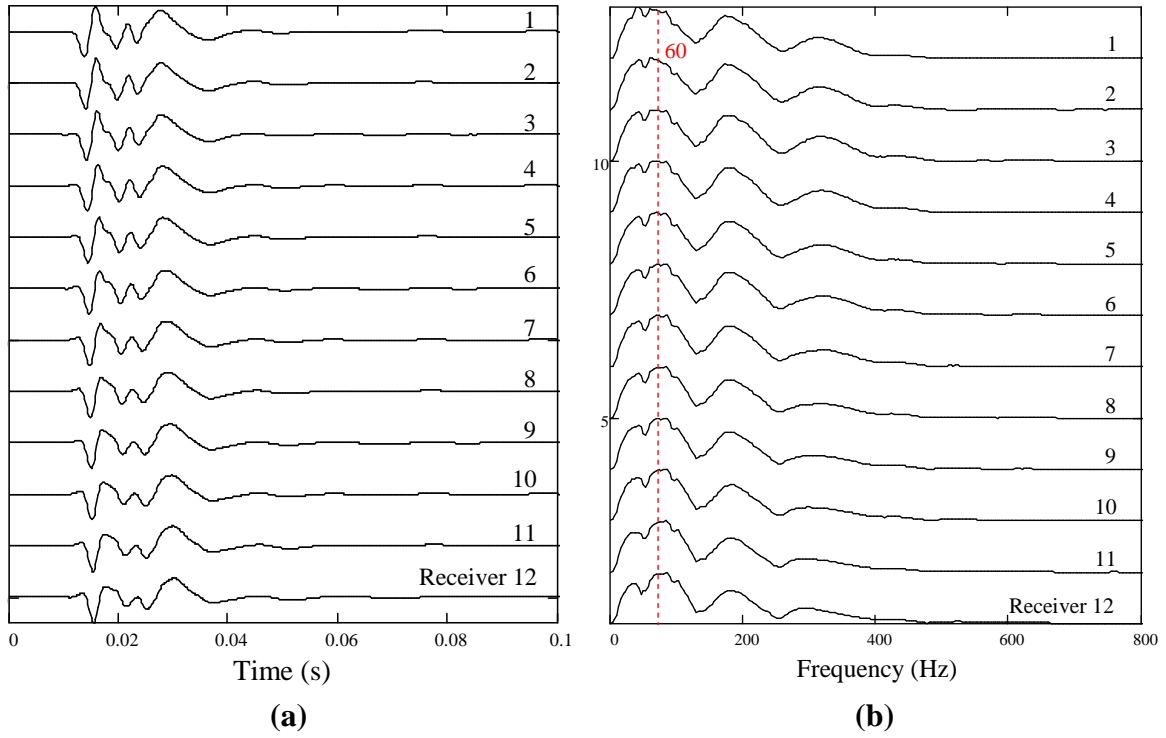
Figure 7-29: (a) Time signals and (b) frequency spectra generated by the LWD
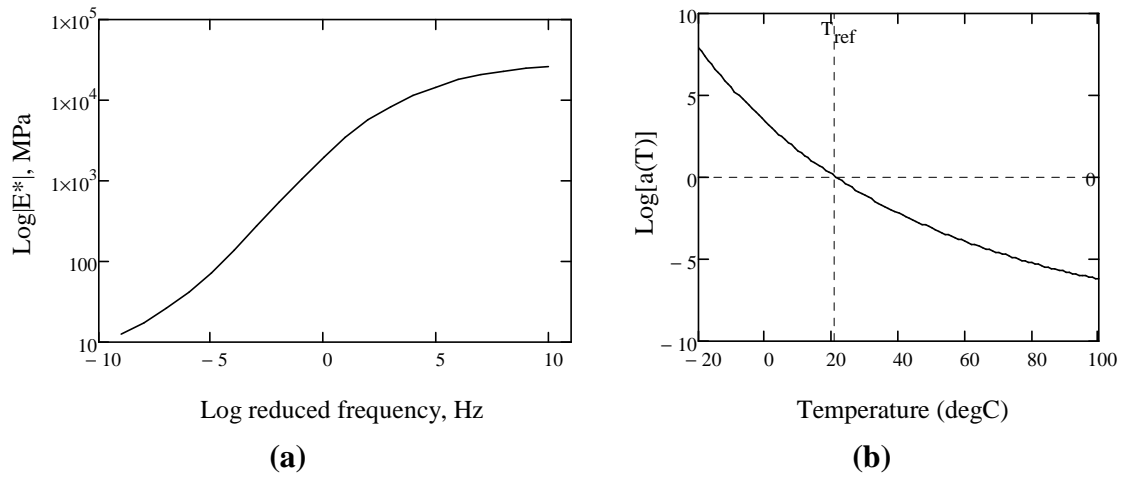


Figure 7-30: Estimated (a) master curve and (b) shift factors for the Test Track
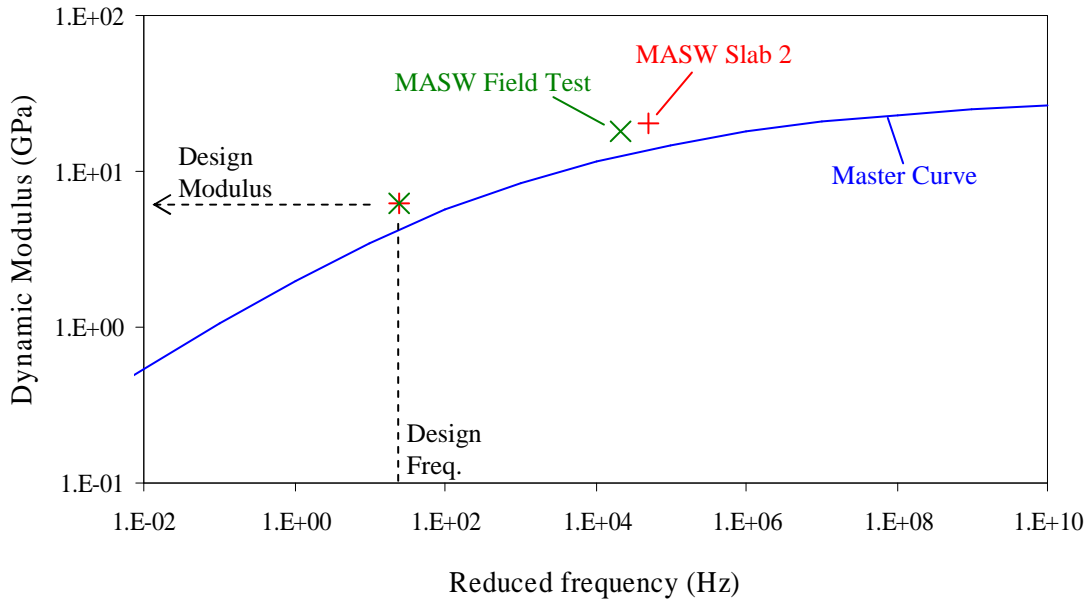
Figure 7-31: Master curve and seismic moduli for the HL 3 section of the Test Track



Figure 7-32: Seed values entered in the LWDmod software to backcalculate the modulus of the pavement layers of the CPATT Test Track
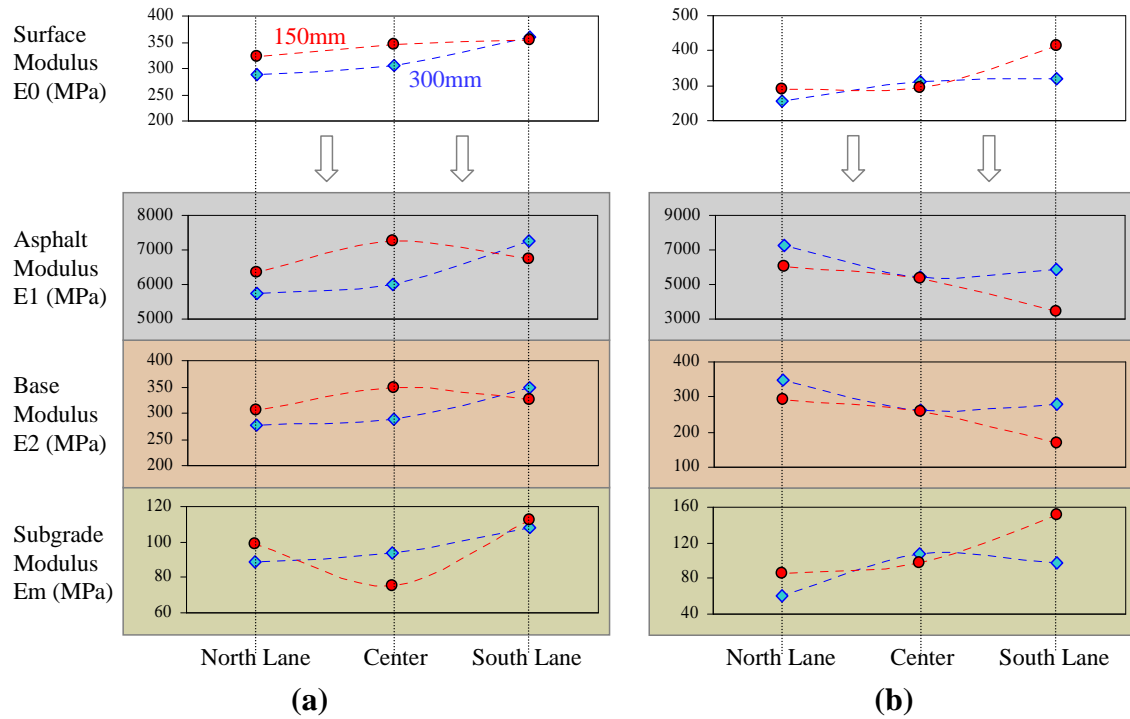
Figure 7-33: Modulus of the pavement layers determined across the centreline of (a) location A and (b) location B of the CPATT Test Track
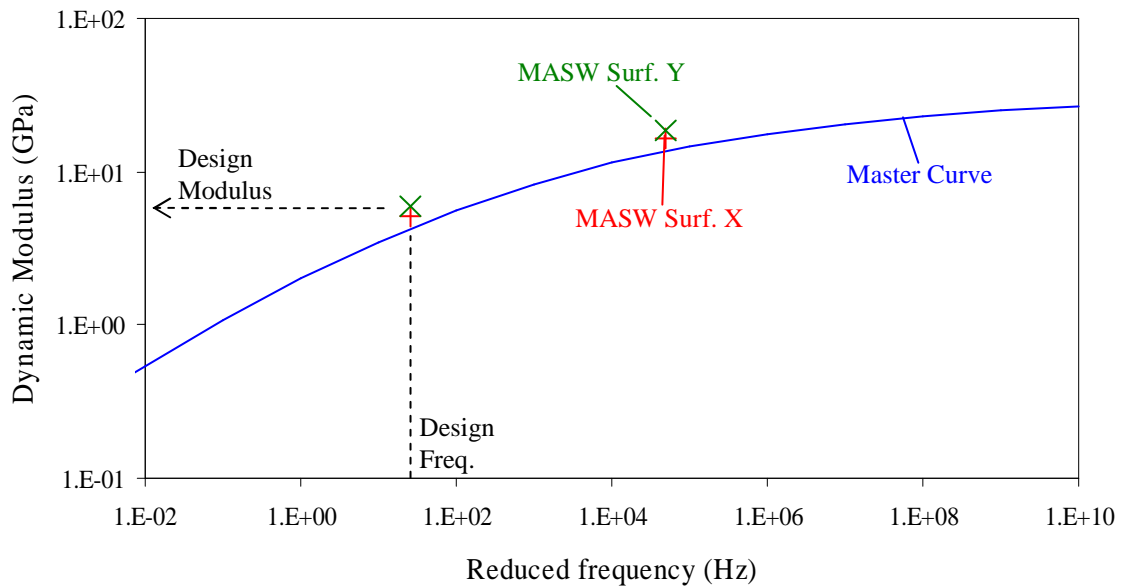


Figure 7-34: Master curve and seismic moduli determined at the surfaces X and Y of Slab 3

Table 7-1: P-wave and R-wave velocities calculated with time signals (Slab 2)

| Configuration | (A) Dytran + Grease | | | (B) Dytran + Plates | | | (C) PCB + Plates | | |
|---|---|---|---|---|---|---|---|---|---|
| Source location | S1 | S2 | Diff. (%) | S1 | S2 | Diff. (%) | S1 | S2 | Diff. (%) |
| $V_P$ (m/s) | **3444** | **3413** | **0.9** | **3466** | **3503** | **1.1** | **3288** | **3216** | **2.2** |
| $R^2$ value | 0.9984 | 0.9965 | | 0.9994 | 0.9996 | | 0.9992 | 0.9993 | |
| $V_R$ (m/s) | **1719** | **1697** | **1.3** | **1673** | **1668** | **0.3** | **1608** | **1675** | **4.0** |
| $R^2$ value | 0.9995 | 0.9995 | | 0.9993 | 0.9995 | | 0.9992 | 0.9998 | |

Table 7-2: R-wave velocities calculated with dispersion curves (Slab 2)

| Configuration | (A) Dytran + Grease | | | (B) Dytran + Plates | | | (C) PCB + Plates | | |
|---|---|---|---|---|---|---|---|---|---|
| Source location | S1 | S2 | Diff. (%) | S1 | S2 | Diff. (%) | S1 | S2 | Diff. (%) |
| $V_R$ (m/s) | **1687** | **1704** | **1.0** | **1691** | **1696** | **0.3** | **1680** | **1702** | **1.3** |

Table 7-3: Coefficient of determination for the regressions of the attenuation curves (Slab 2)

| Para-meter | Trace | Regr. Type | (A) Dytran + Grease | | (B) Dytran + Plates | | (C) PCB + Plates | | Means | | |
|---|---|---|---|---|---|---|---|---|---|---|---|
| | | | S1 | S2 | S1 | S2 | S1 | S2 | | | |
| PTP | Accel. | 1 | 0.96 | 0.98 | 0.95 | 0.96 | 0.95 | 0.95 | **0.958** | **0.956** | **0.966** |
| | | 2 | 0.95 | 0.98 | 0.93 | 0.96 | 0.95 | 0.95 | **0.953** | | |
| | Displ.. | 1 | 0.95 | 0.98 | 0.99 | 0.97 | 0.99 | 0.98 | **0.977** | **0.976** | |
| | | 2 | 0.94 | 0.98 | 0.99 | 0.97 | 0.99 | 0.98 | **0.975** | | |
| SA | Accel. | 1 | 0.97 | 0.99 | 0.97 | 0.98 | 0.94 | 0.97 | **0.970** | **0.967** | **0.973** |
| | | 2 | 0.96 | 0.99 | 0.97 | 0.98 | 0.92 | 0.96 | **0.963** | | |
| | Displ. | 1 | 0.97 | 0.98 | 0.99 | 0.99 | 0.98 | 0.97 | **0.980** | **0.979** | |
| | | 2 | 0.96 | 0.98 | 0.99 | 0.99 | 0.98 | 0.97 | **0.978** | | |
| Mean | | | **0.970** | | **0.974** | | **0.964** | | | | |

Table 7-4: Damping ratios determined with the best fitting method (Slab 2)

| Configuration | (A) Dytran + Grease | | (B) Dytran + Plates | | (C) PCB + Plates | |
|---|---|---|---|---|---|---|
| Source location | S1 | S2 | S1 | S2 | S1 | S2 |
| Main Frequency (kHz) | 19.61 | 19.68 | 19.41 | 18.74 | 14.77 | 14.83 |
| Material Attenuation Coefficient $\alpha$ (m$^{-1}$) | 5.87 | 5.78 | 4.62 | 3.88 | 3.69 | 2.75 |
| **Damping Ratio (%)** | **8.04** | **7.96** | **6.41** | **5.59** | **6.67** | **5.02** |

Table 7-5: $V_P$ and $V_R$ calculated with time signals and dispersions curves respectively (Slab 3)

***Surface X***

| Configuration | (A) Dytran + Grease | | | (B) Dytran + Plates | | | (C) PCB + Plates | | |
|---|---|---|---|---|---|---|---|---|---|
| Source location | S1 | S2 | Diff. (%) | S1 | S2 | Diff. (%) | S1 | S2 | Diff. (%) |
| **$V_P$ (m/s)** | **3115** | **3156** | **1.3** | **NA** | **3134** | **NA** | **2952** | **2920** | **1.1** |
| $R^2$ value | 0.9983 | 0.9961 | | NA | 0.9993 | | 0.9979 | 0.9987 | |
| **$V_R$ (m/s)** | **1441** | **1509** | **4.5** | **NA** | **1610** | **NA** | **1508** | **1421** | **5.8** |

***Surface Y***

| Configuration | (A) Dytran + Grease | | | (B) Dytran + Plates | | | (C) PCB + Plates | | |
|---|---|---|---|---|---|---|---|---|---|
| Source location | S1 | S2 | Diff. (%) | S1 | S2 | Diff. (%) | S1 | S2 | Diff. (%) |
| **$V_P$ (m/s)** | **3259** | **3328** | **2.1** | **3285** | **3330** | **1.4** | **3118** | **3160** | **1.3** |
| $R^2$ value | 0.9988 | 0.9992 | | 0.9992 | 0.9989 | | 0.9986 | 0.9977 | |
| **$V_R$ (m/s)** | **1632** | **1627** | **0.3** | **1610** | **1671** | **3.7** | **1624** | **1665** | **2.5** |

Table 7-6: Damping ratios determined with the best fitting method (Slab 3)

*Surface X*

| Configuration | *(A)* Dytran + Grease | | *(B)* Dytran + Plates | | *(C)* PCB + Plates | |
|---|---|---|---|---|---|---|
| Source location | S1 | S2 | S1 | S2 | S1 | S2 |
| Main Frequency (kHz) | 17.82 | 19.35 | NA | 18.31 | 14.16 | 15.63 |
| Material Attenuation Coefficient $\alpha$ (m$^{-1}$) | 5.50 | 3.30 | NA | 3.25 | 2.65 | 2.33 |
| **Damping Ratio (%)** | **7.4** | **3.5** | **NA** | **4.5** | **4.5** | **3.4** |

*Surface Y*

| Configuration | *(A)* Dytran + Grease | | *(B)* Dytran + Plates | | *(C)* PCB + Plates | |
|---|---|---|---|---|---|---|
| Source location | S1 | S2 | S1 | S2 | S1 | S2 |
| Main Frequency (kHz) | 21.85 | 22.10 | 17.58 | 18.37 | 16.97 | 18.68 |
| Material Attenuation Coefficient $\alpha$ (m$^{-1}$) | 4.77 | 5.64 | 2.95 | 3.74 | 2.81 | 3.08 |
| **Damping Ratio (%)** | **5.7** | **6.6** | **4.5** | **5.2** | **4.4** | **4.3** |

Table 7-7: Average deflection measured on the right wheel path of the CPATT Test Track

| Date | April 2007 | | June 2009 | | July 2009 |
|---|---|---|---|---|---|
| **Section** | **HL 3-1** | **PMA** | **HL 3-1** | **PMA** | **HL 3-1** |
| No. of tested locations | 7 | 4 | 8 | 4 | 7 |
| **Deflection (μm)** | **92** | **90** | **106** | **99** | **95** |
| Standard deviation | 15 | 4 | 16 | 25 | 18 |
| **Modulus (MPa)** | **293** | **294** | **255** | **283** | **286** |
| Standard deviation | 50 | 13 | 39 | 81 | 51 |

Table 7-8: Average deflection measured across the centreline of the CPATT Test Track

| Location | North | Centreline | South |
|---|---|---|---|
| **Deflection (µm)** | **93** | **87** | **89** |
| Standard deviation | 7 | 4 | 14 |
| **Modulus (MPa)** | **285** | **304** | **304** |
| Standard deviation | 22 | 13 | 47 |

Table 7-9: $V_P$ and $V_R$ determined with time signals and dispersion curves at locations A and B of the CPATT Test Track

| Location | A | | | B | | |
|---|---|---|---|---|---|---|
| Source location | S1 | S2 | Diff. (%) | S1 | S2 | Diff. (%) |
| **$V_P$ (m/s) Time signals** | **3116** | **3282** | **5.3** | **3325** | **3132** | **5.6** |
| $R^2$ value | 0.9983 | 0.9991 | | 0.9987 | 0.9946 | |
| **$V_{R1}$ (m/s) Time signals** | **1499** | **1564** | **4.3** | **1524** | **1460** | **4.2** |
| $R^2$ value | 0.9990 | 0.9976 | | 0.9968 | 0.9973 | |
| **$V_{R2}$ (m/s) Disp. curves** | **1605** | **1651** | **2.8** | **1635** | **1570** | **3.9** |
| $V_{R2}/V_{R1}$ | 1.071 | 1.056 | | 1.073 | 1.075 | |

Table 7-10: LWD test configurations used at the city of Hamilton.

| Configuration | Plate Diameter (mm) | Dropping Height (mm) | Resulting Stress (kPa) |
|---|---|---|---|
| 1 | **300** | **710** | ~ 150 |
| 2 | **300** | **410** | ~ 100 |
| 3 | **150** | **710** | ~ 600 |
| 4 | **150** | **410** | ~ 400 |

Table 7-11: Average surface modulus (MPa) measured at the WMA and HMA sections

| Configuration | WMA | HMA |
|:---:|:---:|:---:|
| 1 | 796.8 | 588.4 |
| 2 | 705.8 | 534.6 |
| 3 | 1484.4 | 1177.3 |
| 4 | 1387.5 | 1067.1 |

Table 7-12: Parameters used for the master curve of the HL 3 section of the Test Track

| Mix design parameters | |
|:---|:---:|
| Binder Type | PG 58-28 |
| Air voids, $V_a$, % | 7.0 |
| Effective Binder Content, $V_{beff}$, % | 10.02 |
| $\rho_{34}$, % | 0 |
| $\rho_{38}$, % | 19.4 |
| $P_4$, % | 45.8 |
| $P_{200}$, % | 3.1 |
| Master curve parameters | |
| A | 11.010 |
| VTS | -3.701 |
| Reference temperature, °C | 21.11 |
| $\alpha$ | 3.846184 |
| $\beta$ | -0.792671 |
| $\gamma$ | 0.313351 |
| $\delta$ | 2.814556 |
| c | 1.255882 |

Table 7-13: Seismic elastic moduli of Slab 2 and the HL 3-1 section of the CPATT Test Track

| Test location | Slab 2 | | | CPATT Test Track |
|---|---|---|---|---|
| MASW Configuration | A | B | C | A |
| Frequency (kHz) | 50 | 50 | 50 | 50 |
| Temperature (°C) | 21.11 | 21.11 | 21.11 | 24 |
| Reduced Freq. (kHz) | 50 | 50 | 50 | 20.93 |
| **Elastic Modulus (GPa) at ref. temperature** | **20.1751** | **20.214** | **19.7789** | **18.2318** |
| Design Frequency (Hz) | 25 | 25 | 25 | 25 |
| **Design Modulus (Gpa) at ref. temperature** | **6.268** | **6.28** | **6.145** | **6.221** |

Table 7-14: Parameters used for the master curve of Slab 3

| Mix design parameters | |
|---|---|
| Binder Type | PG 58-28 |
| Air voids, $V_a$, % | 7.5 |
| Effective Binder Content, $V_{beff}$, % | 10.8 |
| $\rho_{34}$, % | 0 |
| $\rho_{38}$, % | 16.8 |
| $P_4$, % | 42.3 |
| $P_{200}$, % | 4.3 |
| Master curve parameters | |
| A | 11.010 |
| VTS | -3.701 |
| Reference temperature, °C | 21.11 |
| $\alpha$ | 3.844843 |
| $\beta$ | -0.792671 |
| $\gamma$ | 0.313351 |
| $\delta$ | 2.813692 |
| c | 1.255882 |

Table 7-15: Seismic elastic moduli measured at surface X and Y of Slab 3

| Test location | Surface X | | | Surface Y | | |
|---|---|---|---|---|---|---|
| MASW Configuration | A | B | C | A | B | C |
| Frequency (kHz) | 50 | 50 | 50 | 50 | 50 | 50 |
| Temperature (°C) | 21.11 | 21.11 | 21.11 | 21.11 | 21.11 | 21.11 |
| **Elastic Modulus (GPa) at ref. temperature** | **15.575** | **18.15** | **15.145** | **18.789** | **19.032** | **18.822** |
| **Design Modulus (Gpa) at ref. temperature** | **4.841** | **5.641** | **4.707** | **5.84** | **5.915** | **5.85** |

# CHAPTER 8.   CONCLUSIONS

The different theories and methods related to the non-destructive evaluation of asphalt pavements have been reviewed in this research. The response of pavements to static plate loads was understood. The theory of wave propagation and the different signal processing techniques used for data analysis were studied. The methods used to characterize the frequency-dependence of asphalt dynamic modulus were reviewed. The different NDT techniques used for pavement evaluation were compared to explain why the LWD and MASW methods were selected for this project. The following sections present the main conclusions drawn from the experiments performed in this research.

## 8.1.  Preparation of a Jointed HMA Slab in the Laboratory

Several asphalt specimens were prepared in this project, and their density was determined using different test methods. The following conclusions were made:

- Based on the compaction of fourteen asphalt samples ($20\times20\times8$ cm$^3$) in the CPATT Pavement laboratory, an exponential regression model was determined between the air void and the compaction effort applied to the mixture with a hand hammer. A coefficient of determination of 0.994 was obtained.

- Using the calibrated procedure, an asphalt slab ($80\times60\times8$ cm$^3$) was compacted in two stages in order to create a joint in the middle. A vertical semi-hot joint of medium quality was obtained and the air void of the 10 cm wide unconfined edge was estimated to be 4.3% higher than the rest of the slab.

- Nuclear density measurements indicated that the achieved horizontal density profile agreed well with the prediction based on the regression model.

## 8.2.  LWD Test in the Field

Deflection testing was performed across longitudinal joints in the field, at the CPATT Test Track in Waterloo and at the City of Hamilton. The following conclusions were reached:

- Less than 7% change was observed between the surface modulus measured on the south lane, centreline, and north lane of the Test Track.

- Most locations tested in the City of Hamilton indicated that the modulus at the joint was slightly lower than inside the lane. However, three locations showed much higher

modulus at the joint than inside the lane, which might be due to a difference in the base or subgrade structural capacity.

- Since 300 mm and 150 mm diameter loading plates were used, the measurement depth exceeded the thickness of the asphalt surface course, and the results could not be directly related to the condition of the joint.

- Backcalculation with the LWDmod software showed that the surface modulus was mostly affected by the base and subgrade moduli, and was not a good indicator of the condition of the surface layer that contains the longitudinal joints.

- The modulus of the asphalt layer could be estimated through the backcalculation process. However, the results presented large standard deviations.


## 8.3. MASW Tests in the Laboratory and the Field

Seismic measurements were conducted in the field at the CPATT Test Track, and in the laboratory on a slab cut from the Test Track (Slab 2) and on the jointed slab prepared in the laboratory (Slab 3). Three different configurations were used for testing in the laboratory, in order to determine the effect of different coupling and receivers on the measurements. The main conclusions are:

- Good estimation of P-wave and R-wave velocities were determined from the time signals and the dispersion curves. For all tests performed in this study, measurements with the source placed at the two ends of the receiver array provided consistent velocities (less than 6% difference). This variation was significantly reduced when testing on smooth surfaces (less than 2% difference in most cases).

- Wave velocities measured in the laboratory were higher than in the field (~ 5% difference). This may be caused by the difference in pavement temperature, which was 3°C higher in the field than in the laboratory. Moreover, field tests were taken across the longitudinal joint, which was expected to have a lower density than Slab 2.

- Slab 2 presented higher wave velocities than Slab 3 (~ 7% difference), resulting in the same conclusion as the nuclear density measurements: higher densities were achieved at the Test Track than in the laboratory. Moreover, asphalt hardening that occurred in the field contributed in increasing the velocity in Slab 2.

- Measurements at the smooth surface of Slab 3 showed higher velocities than at the rough surface. This may be attributed to the difference in surface condition. The rough surface did not provide a good coupling quality between the receivers and the asphalt, yielding significant noise in the time signals that could hide the first P-wave arrivals. Another

reason for this difference in velocities may be the compaction method, which produced a higher density in the bottom layer than in the top one.

- Dispersion curves could be used to determine the thickness of the slabs or the asphalt layer in the field with a precision of ±1 cm.

- The theoretical and experimental dispersion curves indicated that Lamb waves were mainly generated in the asphalt layer. A jump from the anti-symmetric to the symmetric fundamental Lamb mode was observed in the slab, but not in the field. Mode conversion probably occurred at the edges of the slabs. The boundary condition at the bottom surface of the asphalt layer may also influence the generation of different Lamb modes.

- Among all the attenuation parameters computed in this project, spectral areas of displacements provided attenuation curves that best matched the theoretical curves (β ~ 0.5). Fitting of the attenuation curves provided $R^2$-values higher than 0.90 and 0.96 for field and laboratory measurements respectively.

- Field tests showed higher material attenuation and damping ratios than laboratory tests, which was consistent with the conclusion drawn from the analysis of wave velocities. The temperature of the pavement was higher in the field than in the laboratory, resulting in softer material.

- The effect of the joint could not be identified on the attenuation curves because of the variability introduced by the coupling condition between the receivers and the asphalt surface. The quality of the coupling had a more significant effect on the attenuation parameters than the condition of the joint.

- FTC coefficient showed consistency from one configuration to another. Hence, the calculation reduced the undesired variability due to the receivers and the coupling system; and the coefficients were representative of the HMA condition.

- Experimental and theoretical FTC curves were compared to identify weak sections in the pavement. The results suggested that the joint might be in good condition at the second location tested at the CPATT Test Track, whereas the joint might be of poor quality at the first test location. Nevertheless, some variations of the FTC coefficients could not be related to pavement condition, especially for Slab 3.

## 8.4. Master Curves and Comparison of LWD and MASW Moduli

Master curves were computed with an E* predictive equation based on information readily available from material specifications. Asphalt moduli measured with the two NDT methods were compared to the master curves, and the following conclusions were drawn:

- The high frequency moduli determined with seismic measurements were shifted to a design frequency of 25 Hz using the master curve. Although different seismic moduli were obtained for Slab 2 and the field section (9.1% difference), both measurements provided very similar design moduli (less than 0.2% difference). This confirms that the difference in wave velocity and modulus observed between laboratory and field measurements were mainly due to a difference in pavement temperature.

- A good agreement was found between the moduli measured with the LWD and the MASW method after shifting to the design frequency (~ 3% difference). However, the elastic moduli of the asphalt layer backcalculated with the LWDmod software showed a high standard deviation of 1.07 GPa (~18% of the design modulus).

- The E* predictive equation combined with NDT tests could provide a good estimation of the dynamic modulus over a range of frequency, without requiring testing on field or laboratory samples.

## 8.5. Recommendations

Based on the findings of this research, the following recommendations are made:

- Cores should be taken at different locations of Slab 3 in order to measure asphalt density with the automatic vacuum sealing method, which provides more accurate results than nuclear density gauges.

- Additional slabs with joints of different qualities should be prepared in the laboratory. Poor quality joints should be constructed by allowing the first side to cool down to room temperature before placing the second side.

- LWD tests should be performed with various dropping heights and plate sizes in order to optimize the LWDmod backcalculation and estimate the modulus of the asphalt layer that contains the joint.

- Mainly Lamb waves were generated by the ultrasonic source in the asphalt layer. The effect of vertical discontinuities on the propagation of Lamb modes must be studied for further analysis of the data.

- The generation of surface waves requires a better control of the frequency content sent by the source in the pavement. Most of the energy should be produced at frequencies higher than 30 kHz.

- An important part of this project was aimed at developing a good coupling system between the receivers and the asphalt surface that would be suitable for testing in the

field. However, further work is still required on this point to improve the ability of the technique to detect and assess the condition of longitudinal joints.

- Poorly compacted asphalt at the joint usually has a low modulus and high permeability. An effective cold joint construction technique includes using a bituminous tape which does not increase the modulus but reduces the permeability of the asphalt. The LWD cannot detect the change in permeability due to the usage of the bituminous tape because it only measures modulus. Surface waves are affected by changes in material impedance. Thus, the MASW is, in theory, able to detect changes in asphalt permeability across longitudinal joints. Future work should examine whether different permeabilities (i.e. area that use bituminous tape and those that don't) can be detected with a MASW test.

# REFERENCES

AASHTO T 166-07. 2009. *Bulk specific gravity of compacted hot mix asphalt (HMA) using saturated surface-dry specimens*. Standard Specifications for Transportation Materials and Methods of Sampling and Testing. 29th ed. Washington, D.C.

AASHTO T 331-08. 2009. *Bulk specific gravity and density of compacted hot mix asphalt (HMA) using automatic vacuum sealing method*. Standard Specifications for Transportation Materials and Methods of Sampling and Testing. 29th ed. Washington, D.C.

AASHTO TP 62-07. 2009. *Determining dynamic modulus of hot mix asphalt (HMA)*. AASHTO Provisional Standards. 29th ed. Washington, D.C.

Achenbach, J. D. 1973. *Wave propagation in elastic solids*. North-Holland series in applied mathematics and mechanics; V.1. Amsterdam: North-Holland Pub. Co.

Asphalt Research Consortium. 2008. *Quarterly technical progress report January 1 – March 31, 2008.*

ASTM Standard E 2583-07. 2007. *Standard test method for measuring deflections with a light weight deflectometer (LWD)*. Book of Standards, Volume 04.03. West Conshohocken, PA: ASTM International.

ASTM Standard E 494-05. 2005. *Standard practice for measuring ultrasonic velocity in materials*. Book of Standards, Volume 03.03. West Conshohocken, PA: ASTM International.

Bari, J., and M. W. Witczak. 2006. Development of a new revised version of the Witczak E* predictive model for hot mix asphalt mixtures. *Journal of the Association of Asphalt Paving Technologists* 75, 381-423.

Barnes, C. L., and J. F. Trottier. 2009. Evaluating high-frequency visco-elastic moduli in asphalt concrete. *Research in Nondestructive Evaluation* 20, 116-30.

Bérubé, S. 2008. *Sample size effect in ultrasonic testing of geomaterials - numerical and experimental study*. Waterloo, Ont.: University of Waterloo.

Blitz, J., and G. Simpson. 1996. *Ultrasonic methods of non-destructive testing*. Non-destructive evaluation series. 1st ed. London: Chapman & Hall.

Bonaquist, R., and D. W. Christensen. 2005. Practical procedure for developing dynamic modulus master curves for pavement structural design.

Boussinesq, J. 1885. *Application des potentiels à l'étude de l'équilibre et du mouvement des solides élastiques*. Paris: Gauthier-Villars.

Craig, R. F. 1997. *Soil mechanics*. 6th ed. London, UK, New York, US: Spon Press.

Du Tertre, A., G. Cascante, and S. L. Tighe. In Print. Combining PFWD and surface wave measurements for evaluation of longitudinal joints in asphalt pavements. *Transportation Research Record*.

Dynatest International. 2006. "Dynatest 3031 LWD Test System: Owner's Manual".

Estakhri, C. K., T. J. Freeman, and C. H. Spiegelman. 2001. *Density evaluation of the longitudinal construction joint of hot-mix asphalt pavements*. FHWA/TX-01/1757-1.

Garcia, G., and M. Thompson. 2007. *HMA dynamic modulus predictive models - A review*. FHWA-ICT-07-005.

Graff, K. F. 1975. *Wave motion in elastic solids*. (Columbus): Ohio State University Press.

Gucunski, N., and A. Maher. 2002. *Evaluation of seismic pavement analyzer for pavement condition monitoring*. FHWA-NJ-2002-012.

Haas, R. C. G., W. R. Hudson, and J. P. Zaniewski. 1994. *Modern pavement management*. Original ed. Malabar, Fla.: Krieger Pub. Co.

Heisey, J. S., A. H. Meyer, K. H. Stokoe, and W. R. Hudson. 1982a. Moduli of pavement systems from spectral analysis of surface waves. Washington, D.C.

Heisey, J. S., K. H. Stokoe, W. R. Hudson, and A. H. Meyer. 1982b. *Determination of in situ wave velocities from spectral analysis of surface waves*. Centre for Transportation Research, University of Texas at Austin, Research Report 256-2.

Humboldt. Humboldt HS-5001EZ nuclear density gauge. 2010 [cited August 8 2010]. Available from http://www.humboldtmfg.com/.

Jiang, Z., J. Ponniah, and G. Cascante. 2010. In Print. Nondestructive test methodology for condition assessment of hot mix asphalt mixtures. *Canadian Geotechnical Journal*.

Jiang, Z., J. Ponniah, and G. Cascante. 2008. Field condition assessment of longitudinal joints in asphalt pavements using seismic wave technology. Paper presented at Introducing Innovation into Pavement Design and Rehabilitation Session of the 2008 Annual Conference of the Transportation Association of Canada, Toronto, ON.

Jiang, Z. 2007. *Innovative nondestructive testing (NDT) for condition assessment of longitudinal joints in asphalt pavement*. Waterloo, Ont.: University of Waterloo.

Kandhal, Prithvi S., and Rajib B. Mallick. 1996. Study of longitudinal-joint construction techniques in hot-mix asphalt pavements. *Transportation Research Record* (1543): 106-12.

Karray, M., and G. Lefebvre. 2009. Detection of cavities beneath pavements by modal analysis of surface waves (Rayleigh waves) (MASW). *Canadian Geotechnical Journal* 46, (4): 424-37.

Lamb, H. 1917. On waves in an elastic plate. *Proceedings of the Royal Society of London. Series A, Containing Papers of a Mathematical and Physical Character* 93, (648) (Mar. 1): 114-28.

Love, A. E. H. 1911. *Some problems of geodynamics*. Cambridge, U.K.: Cambridge, University Press.

Marks, P., C. Cautillo, K. K. Tam, and S. McInnis. 2009. Enhancing longitudinal joint performance in flexible pavements. Paper presented at the Fifty-Fourth Annual Conference of the Canadian Technical Asphalt Association, Moncton, New Brunswick.

Medani, T. O., M. Huurman, and A. A. A. Molenaar. 2004. On the computation of master curves for bituminous mixes. Paper presented at the 3rd Euroasphalt and Eurobitume Congress, Vienna, Austria.

Miller, G. F., and H. Pursey. 1955. On the partition of energy between elastic waves in a semi-infinite solid. *Proceedings of the Royal Society of London. Series A, Mathematical and Physical Sciences* 233, (1192) (Dec. 6): 55-69.

Miller, G. F., and H. Pursey. 1954. The field and radiation impedance of mechanical radiators on the free surface of a semi-infinite isotropic solid. *Proceedings of the Royal Society of London. Series A, Mathematical and Physical Sciences* 223, (1155) (May 20): 521-41.

Mooney, M. A., and P. K. Miller. 2009. Analysis of lightweight deflectometer test based on in situ stress and strain response. *Journal of Geotechnical and Geoenvironmental Engineering* 135, (2) (February): 199-208.

Nasseri-Moghaddam, A. 2006. *Study of the effect of lateral inhomogeneities on the propagation of Rayleigh waves in an elastic medium*. Waterloo, Ont.: University of Waterloo.

Nazarian, S., M. R. Baker, and K. Crain. 1993. *Development and testing of a seismic pavement analyzer*. The University of Texas at El Paso: Centre for Geotechnical and Highway Materials Research, SHRP-H-375.

Nazarian, S., D. Yuan, V. Tandon, and M. Arellano. 2002. *Quality management of flexible pavement layers with seismic methods*. FHWA/TX-03/0-1735-3.

Nazarian, S., and K. H. Stokoe. 1986. Use of surface waves in pavement evaluation. *Transportation Research Record* (19860101): 132-44.

Nazarian, S., K H. Stokoe, and W. R. Hudson. 1983. Use of spectral analysis of surface waves method for determination of moduli and thicknesses of pavement systems. *Transportation Research Record* (19830101): 38-45.

NCHRP 1-37A. 2004. *Guide for mechanistic-empirical design of new and rehabilitated pavement structures*. National Cooperative Highways Research Program, Project 1-37AARA, Inc. and ERES Consultants Division.

NDT Resource Centre. Modes of sound wave propagation. 2010 [cited August 8 2010]. Available from http://www.ndt-ed.org/index_flash.htm.

Park, C. B., R. D. Miller, and J. Xia. 1999. Multimodal analysis of high frequency surface waves. Paper presented at the Symposium on the Application of Geophysics to Engineering and Environmental Problems (SAGEEP 99), Oakland, CA.

Popovics, J. S., W-J Song, and J. D. Achenbach. 1998. A study of surface wave attenuation measurement for application to pavement characterization. Paper presented at Structural Materials Technology III, start date 19980331-end date 19980403.

Popovics, J. S., W-J Song, and M. Ghandehari. 2000. Application of surface wave transmission measurements for crack depth determination in concrete. *ACI Materials Journal* 97, (2) (March/April): 127-35.

Rayleigh, L. 1885. On waves propagated along the plane surface of an elastic solid. *Proceedings of the London Mathematical Society* s1-17, (1) (November 1): 4-11.

Rix, G. J. 2000. Site characterization using surface waves. Paper presented at Symposium on the Application of Geophysics to Environmental and Engineering Problems (SAGEEP) 2000, Arlington, VA.

Roberts, F. L., L. N. Mohammad, and L. B. Wang. 2003. History of hot mix asphalt mixture design in the United States. Paper presented at Perspectives in Civil Engineering: Commemorating the 150th Anniversary of the American Society of Civil Engineers.

Russo, M. 2006. "SWAN (Surface Waves Analysis)", http://www.geoastier.com.

Ryden, N., and M. A. Mooney. 2009. Analysis of surface waves from the light weight deflectometer. *Soil Dynamics and Earthquake Engineering* 29 (7) (Jul): 1134-42.

Sansalone, M., and N. J. Carino. 1989. Detecting delaminations in concrete slabs with and without overlays using the impact-echo method. *ACI Materials Journal* 86.

Sansalone, M., and N. J. Carino. 1986. *Impact-echo: A method for flaw detection in concrete using transient stress waves.* Washington, D.C.: National Bureau of Standards, NBSIR 86-3452.

Schepers, W., S. Savidis, and E. Kausel. 2009. Dynamic stresses in an elastic half-space. *Soil Dynamics and Earthquake Engineering*.

Steinert, B. C., D. N. Humphrey, and M. A. Kestler. 2005. *Portable falling weight deflectometer study.* NETCR52.

Steyn, W. J. vdM, and E. Sadzik. 2007. Application of the portable pavement seismic analyser (PSPA) for pavement analysis. Paper presented at the 26th Southern African Transport Conference (SATC 2007), Pretoria, South Africa.

Tallavó, F., G. Cascante, and M. D. Pandey. 2009. New methodology for source characterization in pulse velocity testing.

Tallavó, F. J. 2009. *New methodology for the assessment of decayed utility wood poles*. Waterloo, Ont.: University of Waterloo.

Test Method LS-261. 2001. *Method of test for preparation of Marshall specimens*. MTO Laboratory Testing Manual, Ministry of Transportation, Ontario.

Test Method LS-264. 2001. *Method of test for theoretical maximum relative density of bituminous paving mixture*. MTO Laboratory Testing Manual, Ministry of Transportation, Ontario.

Tighe, S. L., and others. 2008 "Evaluating Warm Asphalt Technology as a Possible Tool for Resolving Longitudinal Joint Problem". Report #3 prepared for the City of Hamilton.

Tighe, S. L., Lynne Cowe Falls, and Guy Doré. 2007. Pavement performance evaluation of three Canadian low-volume test roads. *Transportation Research Record* 2, (1989) (20070101): 211-8.

Ullidtz, P. 1987. *Pavement analysis*. Developments in civil engineering; v. 1. Amsterdam: Elsevier.

Uzarowski, L., G. Moore, M. Halloran, and S. Tighe. 2009. Innovative approach to construction of durable longitudinal joints. Paper presented at the Fifty-Fourth Annual Conference of the Canadian Technical Asphalt Association, Moncton, New Brunswick.

Washington State DOT. WSDOT pavement guide. 2010 [cited June 10 2010]. Available from http://training.ce.washington.edu/wsdot/.

Wasley, R. J. 1973. *Stress wave propagation in solids; an introduction*. Monographs and textbooks in material science. New York: M. Dekker.

Williams, S. G., A. Pervis, L. S. Bhupathiraju, and A. Porter. 2009. Methods for evaluating longitudinal joint quality in asphalt pavements. *Transportation Research Record* 2098, 113-23.

Williams, M. L., R. F. Landel, and J. D. Ferry. 1955. The temperature dependence of relaxation mechanisms in amorphous polymers and other glass-forming liquids. *Journal of the American Chemical Society* 77 (14), 3701-7.

M. W. Witczak and J. Bari. 2004. "Development of a E* Master Curve Database for Lime Modified Asphaltic Mixtures" Arizona State University Research Project.

Yang, Y. 2009. *Nondestructive evaluation of the depth of cracks in concrete plates using surface waves*. Waterloo, Ont.: University of Waterloo.

# APPENDIX A: Marshall Mix Design Report for the HL 3-R15 Mix Used for Preparation of the Asphalt Slab

## TABLE 1: MARSHALL MIX DESIGN REPORT
MTOMIX Ver. 6.1 - HMA Mix Design Software (OPSS 1150 - November 2002 Edition)

| Contractor: | Steed and Evans | | Job Number: | brge00280356a |
|---|---|---|---|---|

| Contract Number: | Various | Hot Mix Type: | HL3-R15 Mix Design | Item Number: | --- |
|---|---|---|---|---|---|
| Highway: Various | | Location: | --- Heidelberg | | |
| Date Samples Received: | January 15, 2009 | | Date Mix Completed: | March 10, 2009 | |

Test Results Supplied By:
Farid A. Khan, P.Eng.
Salman Bhutta, Ph.D., P.Eng.
Trow Associates Inc.

### JOB MIX FORMULA - GRADATION PERCENT PASSING[1,2]

| PGAC (%)[3] | 26.5 mm | 19 mm | 16 mm | 13.2 mm | 9.5 mm | 4.75 mm | 2.36 mm | 1.18 mm | 600µm | 300µm | 160µm | 75µm |
|---|---|---|---|---|---|---|---|---|---|---|---|---|
| 5.00% | | | 100.0 | 99.1 | 83.2 | 57.7 | 45.2 | 31.2 | 20.7 | 11.5 | 6.7 | 4.3 |

| Marshall Data | | Specification | Selected | | | | |
|---|---|---|---|---|---|---|---|
| Percent Air Voids | min | 3.5% | 4.1% | | CA. No. 1 | 37.0% |
| | max | 4.5% | | | FA. No. 1 | 8.0% |
| Flow (0.25 mm) | min | 8.0 | 10.0 | | FA. No. 2 | 40.0% |
| Stability (N) | min | 8900 | 12241 | | RAP | 15.0% |
| % VMA | min | 15.3% | 15.3% | | $G_b$ | 2.690 |

| | |
|---|---|
| Percent RAP | 15.0% |
| RAP Percent PGAC | 4.00 |
| RAP Penetration | 25.00 |
| BRD | 2.399 |
| MRD | 2.503 |
| MRD (SSD) | |

| PGAC[4,5] | | | Additive | | |
|---|---|---|---|---|---|
| Supplier | Grade | | Supplier | Name/Type | Percent of PGAC |
| McAsphalt | PG 58-28 | | --- | --- | --- |

| Material | Description - Source | Inventory Number | Bulk Relative Density | Apparent Bulk Relative Density | Percent Absorption |
|---|---|---|---|---|---|
| CA. No. 1 | HL3 Stone (Heidelberg) | --- | 2.710 | 2.799 | 1.325 |
| FA. No. 1 | Screenings (Heidelberg) | --- | 2.689 | 2.805 | 1.558 |
| FA. No. 2 | Asphalt Sand (Heidelberg) | --- | 2.676 | 2.735 | 0.801 |
| RAP | 16mm RAP | --- | 2.681 | 2.760 | 1.061 |

### Aggregate Gradation - Percent Passing

| Material | 26.5 mm | 19 mm | 16 mm | 13.2 mm | 9.5 mm | 4.75 mm | 2.36 mm | 1.18 mm | 600µm | 300µm | 160µm | 75µm |
|---|---|---|---|---|---|---|---|---|---|---|---|---|
| CA. No. 1 | | | 100.0 | 95.8 | 59.0 | 1.6 | 1.5 | 1.4 | 1.2 | 1.0 | 0.9 | 0.8 |
| FA. No. 1 | | | | | 100.0 | 84.2 | 63.1 | 48.0 | 35.6 | 24.6 | 19.2 | 14.7 |
| FA. No. 2 | | | | | 100.0 | 99.5 | 77.4 | 49.4 | 29.8 | 13.2 | 5.1 | 1.8 |
| RAP | | | 100.0 | 97.4 | 88.3 | 67.6 | 54.1 | 42.6 | 31.5 | 19.9 | 12.1 | 8.0 |

[1] FINES RETURNED TO MIX ARE 1.0%
[2] PERCENT TOTAL ASPHALT CONTENT 5.00%
[3] TOTAL PGAC INCLUDES VIRGIN PGAC and RAP AS APPLICABLE FOR THIS MIX
[4] RECOMMENDED MIXING TEMPERATURE IS 150°C
RECOMMENDED COMPACTION TEMPERATURE IS 138°C
RECOMMENDED RECOMPACTION TEMPERATURE IS 138°C
NUMBER OF BLOWS USED 75 HAND BLOWS EACH SIDE
[5] THEORATICAL ASPHALT FILM THICKNESS IS 9.6 microns
DUST TO ASPHALT RATIO IS 0.87
FINE AGGREGATE PROPORTION BY VOLUME AT 4.75-mm SIEVE IS 57.5%
WEIGHT REQUIRED FOR BRIQUETTES TO BE 63.5 ± 1.5 mm IN HEIGHT IS 1,275.8 g
PLANT TYPE IS DRY COLLECTOR

REMARKS

VIRGIN ASPHALT CEMENT TO BE ADDED TO THE MIX IS 4.41%
GRADATIONS FROM SAMPLES (CHECKED AGAINST PROCESS CONTROL).
ASPHALT INSTITUTE MS-2 PROCEDURES FOLLOWED.
THIS MIX DESIGN IS SUBJECT TO MARSHALL COMPLIANCE CHECKS AND POSSIBLE JOB MIX ADJUSTMENT.
NO AIR VOIDS CORRECTION REQUIRED.
AGGREGATE COMPONENT OF JMF ADJUSTED.

# APPENDIX B:   Nuclear Densities Measured on Slab 3

| Location | 1 | 2 | 3 | 4 | 5 | 6 |
|---|---|---|---|---|---|---|
| Line 1 | | | | | | |
| | 2298 | 2282 | 2188 | 2227 | 2199 | 2244 |
| | 2320 | 2265 | 2144 | 2169 | 2252 | 2261 |
| | 2334 | 2265 | 2132 | 2162 | 2249 | 2268 |
| | 2344 | 2274 | 2154 | 2191 | 2234 | 2267 |
| | 2349 | 2267 | 2191 | 2181 | 2220 | 2241 |
| Average | **2329.0** | **2270.6** | **2161.8** | **2186.0** | **2230.8** | **2256.2** |
| Stdev | 20.6 | 7.4 | 26.5 | 25.5 | 21.9 | 12.8 |
| Line 1 Reversed | | | | | | |
| Location | 1 | 2 | 3 | 4 | 5 | 6 |
| | 2267 | 2300 | 2232 | 2252 | 2284 | 2396 |
| | 2293 | 2246 | 2177 | 2242 | 2305 | 2412 |
| | 2280 | 2246 | 2222 | 2224 | 2316 | 2368 |
| | 2300 | 2316 | 2230 | 2242 | 2238 | 2363 |
| | 2291 | 2273 | 2175 | 2269 | 2255 | 2394 |
| Average | **2286.2** | **2276.2** | **2207.2** | **2245.8** | **2279.6** | **2386.6** |
| Stdev | 12.9 | 31.6 | 28.7 | 16.4 | 32.9 | 20.6 |
| Line 2 | | | | | | |
| Location | 1 | 2 | 3 | 4 | 5 | 6 |
| | 2203 | 2278 | 2246 | 2304 | 2270 | 2222 |
| | 2223 | 2297 | 2255 | 2273 | 2238 | 2283 |
| | 2212 | 2289 | 2244 | 2241 | 2295 | 2228 |
| | 2247 | 2285 | 2240 | 2276 | 2284 | 2273 |
| | 2255 | 2276 | 2232 | 2261 | 2257 | 2261 |
| Average | **2228.0** | **2285.0** | **2243.4** | **2271.0** | **2268.8** | **2253.4** |
| Stdev | 22.3 | 8.5 | 8.4 | 23.0 | 22.4 | 27.2 |
| Line 2 Reversed | | | | | | |
| Location | 1 | 2 | 3 | 4 | 5 | 6 |
| | 2226 | 2202 | 2172 | 2224 | 2256 | 2228 |
| | 2177 | 2249 | 2230 | 2218 | 2257 | 2238 |
| | 2230 | 2189 | 2213 | 2295 | 2242 | 2210 |
| | 2203 | 2187 | 2220 | 2216 | 2316 | 2246 |
| | 2167 | 2186 | 2222 | 2248 | 2244 | 2234 |
| Average | **2200.6** | **2202.6** | **2211.4** | **2240.2** | **2263.0** | **2231.2** |
| Stdev | 28.3 | 26.7 | 22.8 | 33.2 | 30.4 | 13.5 |

# APPENDIX C: Marshall Mix Design Report for the HL 3 Section of the CPATT Test Track

| Materials | HL4 | HL3 |
|---|---|---|
| Coarse Aggregate | 36.53% | 43.70% |
| Fine Aggregate 1 | 40.17% | 38.00% |
| Fine Aggregate 2 | - | 13.30% |
| RAP | 19.17% | - |
| Filler | - | - |
| Virgin Asphalt Cement | 4.13% | 5.00% |
| PG-AC Grade | PG 58-28 | PG 58-28 |
| **Gradation % Passing** | | |
| 26.5 mm | | |
| 19 mm | 100.0 | |
| 16 mm | 99.3 | 100.0 |
| 13.2 mm | 92.7 | 98.0 |
| 9.5 mm | 76.9 | 80.6 |
| 4.75 mm | 55.1 | 54.2 |
| 2.36 mm | 46.9 | 44.5 |
| 1.18 mm | 34.6 | 31.9 |
| 600 $\mu$m | 21.8 | 19.8 |
| 300 $\mu$m | 10.5 | 10.3 |
| 150 $\mu$m | 4.4 | 5.2 |
| 75 $\mu$m | 2.0 | 3.1 |
| **Properties** | **HL4** | **HL3** |
| $N_{design}$ | NA | NA |
| % $G_{mm}$ @ $N_{initial}$ | NA | NA |
| % $G_{mm}$ @ $N_{max}$ | NA | NA |
| Air Voids (%) | 4.62% | 4.62% |
| VMA (%) | 16.40% | 14.90% |
| VFA (%) | 71.83% | 71.41% |
| Flow (0.25 mm) | 9.6 | 9.2 |
| Stability (N) | 9500 | 8915 |
| Tensile Strength Ratio (%) | NA | NA |
| $G_{mb}$ - Blend | 2.359 | 2.403 |
| $G_{mm}$ - Blend | 2.474 | 2.510 |

NA=Not Available

# APPENDIX D:  Testing at the City of Hamilton Using the WTC

## Method (Nov. 2008)

**Test Configuration**

This test was developed by Zhiyong Jiang during his Master of Science at the University of Waterloo (Jiang 2007). The WTC method, described in Chapter 4 and illustrated in Figure D-1, is used to perform this test. Two accelerometers R1 and R2 are receiving a signal from a source which is placed in A or B. For both locations of the source, one receiver records the response of the joint free surface while the second one records the response of the joint surface. The comparison of these signals shows the impact of a joint on the propagation of surface waves.

Two tests using different sources have been performed. The first test, which uses an ultrasonic source generating high frequencies (~50 kHz), thus small wavelengths, provides an insight of the condition of the near-joint asphalt. For the second test, a hammer source generating bigger wavelengths is used to look at the asphalt further from the joint.

The instrumentation used for the ultrasonic tests is showed in Figure D-2. The source is driven by a pulser/receiver. The signals measured by the accelerometers are amplified by a power amplifier. A data acquisition system is used to gather the data which is then displayed and recorded on a computer for further analysis.

**Results**

Transmission coefficients are used to quantify the condition of the joint. The Coefficient selected as the best indicator for the condition assessment of the joints is the WTC:

$$\text{WTC} = \sqrt{\frac{W_{AR1} \times W_{BR2}}{W_{AR2} \times W_{BR1}}} \tag{8-1}$$

where $W_{AR1}$ ($W_{AR2}$) is the wavelet transform using a Morlet function of the signal transmitted by source A and recorded by receiver R1 (R2 respectively), and $W_{BR1}$ ($W_{BR2}$) is the wavelet transform of the signal transmitted by source B and recorded by receiver R1 (R2 respectively).

The selection of the centre frequency is a very important step in the calculation of the WTC. A logical choice would be to select the frequency associated to the maximum magnitude. On one

hand, the ultrasonic source used for the test has a resonant frequency around 50 kHz. On the other hand, the signals recorded by the accelerometers present an important amount of energy at frequencies around 30 kHz, which is caused by the resonance of the accelerometers. The selection of only one centre frequency would emphasis too much the impact on the results of one of the two phenomena described previously. Therefore, the WTC was calculated for centre frequencies ranging from 10 kHz to 60 kHz, by 5 kHz increments. For the Hammer test, as the main frequency recorded by the transducer was about 3 kHz, the WTC was calculated for centre frequencies ranging from 1 to 10 kHz, by 1 kHz increments.

Tests have been performed in three sections for both Warm Mix Asphalt (WMA) and Hot Mix Asphalt (HMA) pavements. On each section, both tests using the ultrasonic and the hammer sources are conducted. Figure D-3 presents the evolution of the WTC coefficients with respect to frequency. The condition of the joints at different sections can be compared. For example, the WTC plots for WMA with both sources indicate that the joints at sections 1 and 2 are in better condition than the joint at section 3.

For each pavement (WMA or HMA) and each type of source (ultrasonic or Hammer) a mean of the WTC of all 3 sections is calculated to get an idea of the joint condition over the whole pavement. In all situations, the WTC have values below one for most of the frequencies which indicates that there is attenuation due to the joints. In Figure D-4, the WTC from WMA and HMA testing are plotted on the same graph for comparison. A mean of the WTC values at different frequencies is calculated to quantify the condition of the joint for each pavement. This mean is slightly higher for testing of the WMA pavement with both ultrasonic and hammer sources. Therefore, the WMA section present a better quality joint than the HMA pavement.

The accuracy and reliability of these results are affected by the following factors, which have to be taken into consideration for further testing:

· The spacing between the transducers has to be improved in the test with the hammer source. In the time domain, we can notice that the signals recorded by the receiver overlap the trigger signal. Thus, the spacing is too small and near-field effects appear.

· In the tests with the ultrasonic source, the resonance of the transducers is observed. Most of the energy of the signal recorded by the transducers is located at frequencies around the resonant frequency, which can badly affect the results.
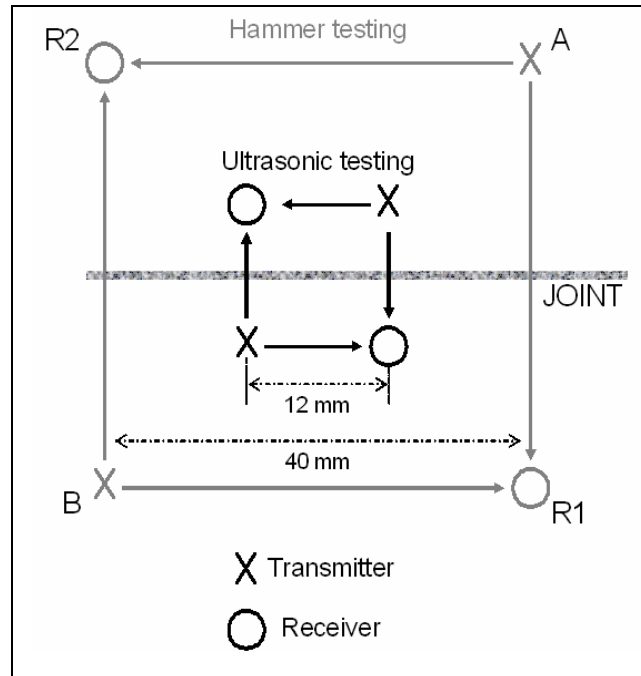
Figure D-1: Testing configuration
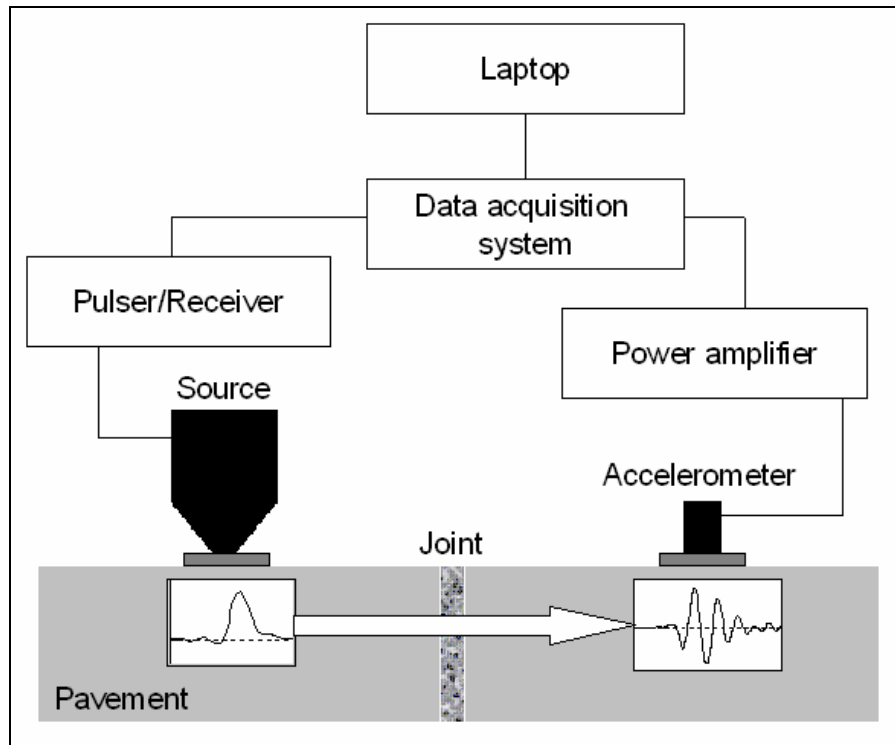


Figure D-2: Ultrasonic experimental setup
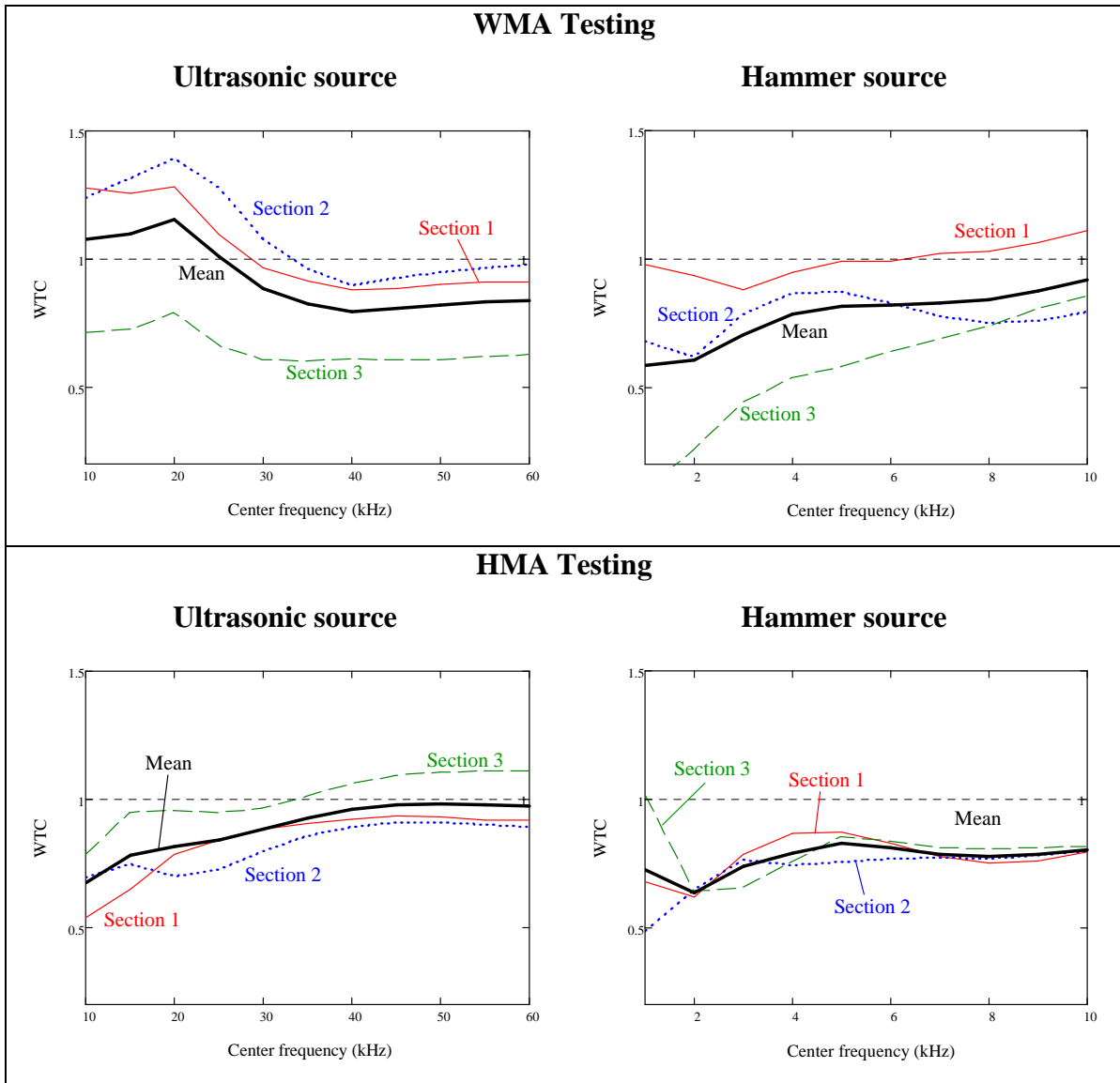
Figure D-3: WTC coefficients vs. frequency

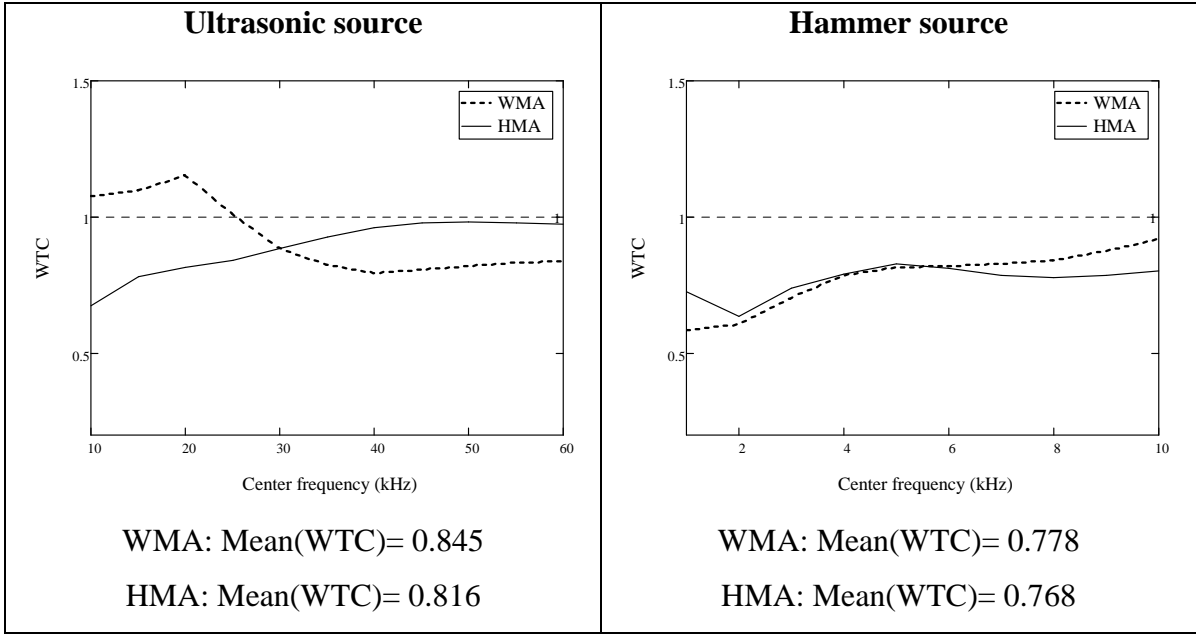| Ultrasonic source | Hammer source |
|---|---|
| WMA: Mean(WTC)= 0.845 | WMA: Mean(WTC)= 0.778 |
| HMA: Mean(WTC)= 0.816 | HMA: Mean(WTC)= 0.768 |

Figure D-4: Comparison of WTC obtained at the HMA and WMA sections

# APPENDIX E:  MathCAD Files

This Appendix is available in the CD. It consists of all the MathCAD files developed in this research to process the MASW data collected in the laboratory and the field.

The MathCAD files include:

- Time signals
- $V_P$ and $V_R$ calculation by detection of arrival times
- Frequency Spectra
- Attenuation in time domain: Peak-to-Peak amplitude
- Attenuation in frequency domain: Spectral Area
- Fourier Transmission Coefficients
- Dispersion curves

Associated data files are also provided in the CD.

The following section shows a typical MathCAD file, which was used to analyse the data recorded on the smooth surface (bottom surface Y) of laboratory Slab 3. The calculations are presented for the source on the right side of the receiver array (location S2). Similar calculations were made for the source on the left side (S1).

# File: "Time Signals, Velocities, Dispersion Curves"

▼ ACCELERATION DATA

ORIGIN ≡ 1

data21 := READPRN("SlabA-061.txt" )     data31 := READPRN("SlabA-071.txt" )

data22 := READPRN("SlabA-062.txt" )     data32 := READPRN("SlabA-072.txt" )

data23 := READPRN("SlabA-063.txt" )     data33 := READPRN("SlabA-073.txt" )

data24 := READPRN("SlabA-064.txt" )     data34 := READPRN("SlabA-074.txt" )

data25 := READPRN("SlabA-065.txt" )     data35 := READPRN("SlabA-075.txt" )

data26 := READPRN("SlabA-066.txt" )     data36 := READPRN("SlabA-076.txt" )

data27 := READPRN("SlabA-067.txt" )     data37 := READPRN("SlabA-077.txt" )

data28 := READPRN("SlabA-068.txt" )     data38 := READPRN("SlabA-078.txt" )

data29 := READPRN("SlabA-069.txt" )     data39 := READPRN("SlabA-079.txt" )

data30 := READPRN("SlabA-070.txt" )     data40 := READPRN("SlabA-080.txt" )

$N$ := rows(data21)      $N = 2 \times 10^3$      $i := 1 .. N$

$Nx := cols(data21)$      $Nx = 13$      $j := 1 .. Nx$

### Source on S2 (right):

$S2_{i,j} := mean\left(data21_{i,j}, data22_{i,j}, data23_{i,j}, data24_{i,j}, data25_{i,j}, data26_{i,j}, data27_{i,j}, data28_{i,j}, data29_{i,j}, da\right.$

$S2_{i,10} := mean\left(data31_{i,11}, data32_{i,11}, data33_{i,11}, data34_{i,11}, data35_{i,11}, data36_{i,11}, data37_{i,11}, data38_{i,11}\right.$

▲ ACCELERATION DATA

## TIME SIGNALS

▼ ACCELERATION

**Source**      $SourceR := S2^{\langle 13 \rangle}$

### Sensitivity of the accelerometers:

$k := 1 .. 12$

$$\text{mV/g}: \quad \Sigma := \begin{pmatrix} 511.8 \\ 497.2 \\ 504.1 \\ 496.2 \\ 495.7 \\ 496.9 \\ 500.4 \\ 497.1 \\ 497.2 \\ 508.5 \\ 498.6 \\ 493.1 \end{pmatrix} \qquad \text{g/V}: \quad K_k := \frac{1000}{\Sigma_k}$$

### Receivers

$$k1 := 1..4 \quad RR_{i,k1} := \frac{S2_{i,k1}}{100} \cdot K_{k1} \qquad k2 := 5..10 \quad RR_{i,k2} := \frac{S2_{i,k2}}{10} \cdot K_{k2}$$

$$k3 := 11..12 \quad RR_{i,k3} := S2_{i,k3} \cdot K_{k3}$$

**Offset suppression** $\qquad RRO_{i,k} := RR_{i,k} - \text{mean}\left(RR^{\langle k \rangle}\right)$

**Normalization** $\qquad \text{MaxRRO}_k := \max\left(\overrightarrow{\left|RRO^{\langle k \rangle}\right|}\right) \qquad RRN_{i,k} := \frac{RRO_{i,k}}{\text{MaxRRO}_k}$

**Distance from S1** $\qquad \Delta X := 0.04\,\text{m} \qquad X_k := k \cdot \Delta X \qquad D := 13 \cdot \Delta X$

**Time** $\qquad \Delta t := 10^{-6}\,\text{s} \qquad t_i := (i-1)\Delta t \qquad t_N = 1.999 \times 10^{-3}\,\text{s}$

$$\alpha 0 := 2 \quad x(k) := RRN^{\langle k \rangle} - k \cdot \alpha 0$$

## Normalized Time Signals



Normalized Amplitude vs Time (s)

---
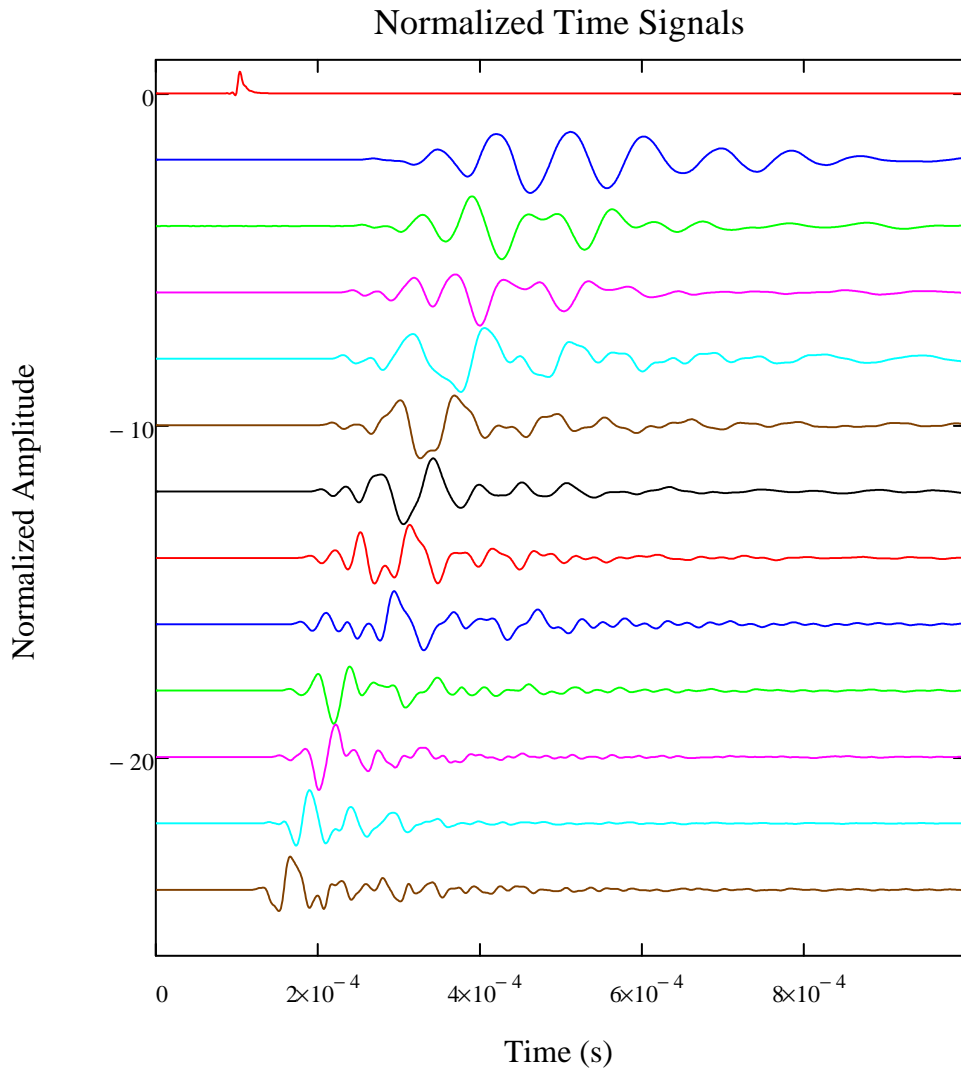
**Displacement**  $\quad DR := READPRN("RRO\text{-}SlabAbot\text{-}DYTglue\_a\_W\_v\_a\_W\_d.txt")$

**Offset suppression**  $\quad DRO_{i,k} := DR_{i,k} - mean\left(DR^{\langle k \rangle}\right)$

**Normalization**  $\quad MaxDRO_k := max\left(\overrightarrow{\left|DRO^{\langle k \rangle}\right|}\right) \qquad DRN_{i,k} := \dfrac{DRO_{i,k}}{MaxDRO_k}$

$\alpha 0 := 2 \quad x(k) := DRN^{\langle k \rangle} - k \cdot \alpha 0$

## Normalized Time Signals
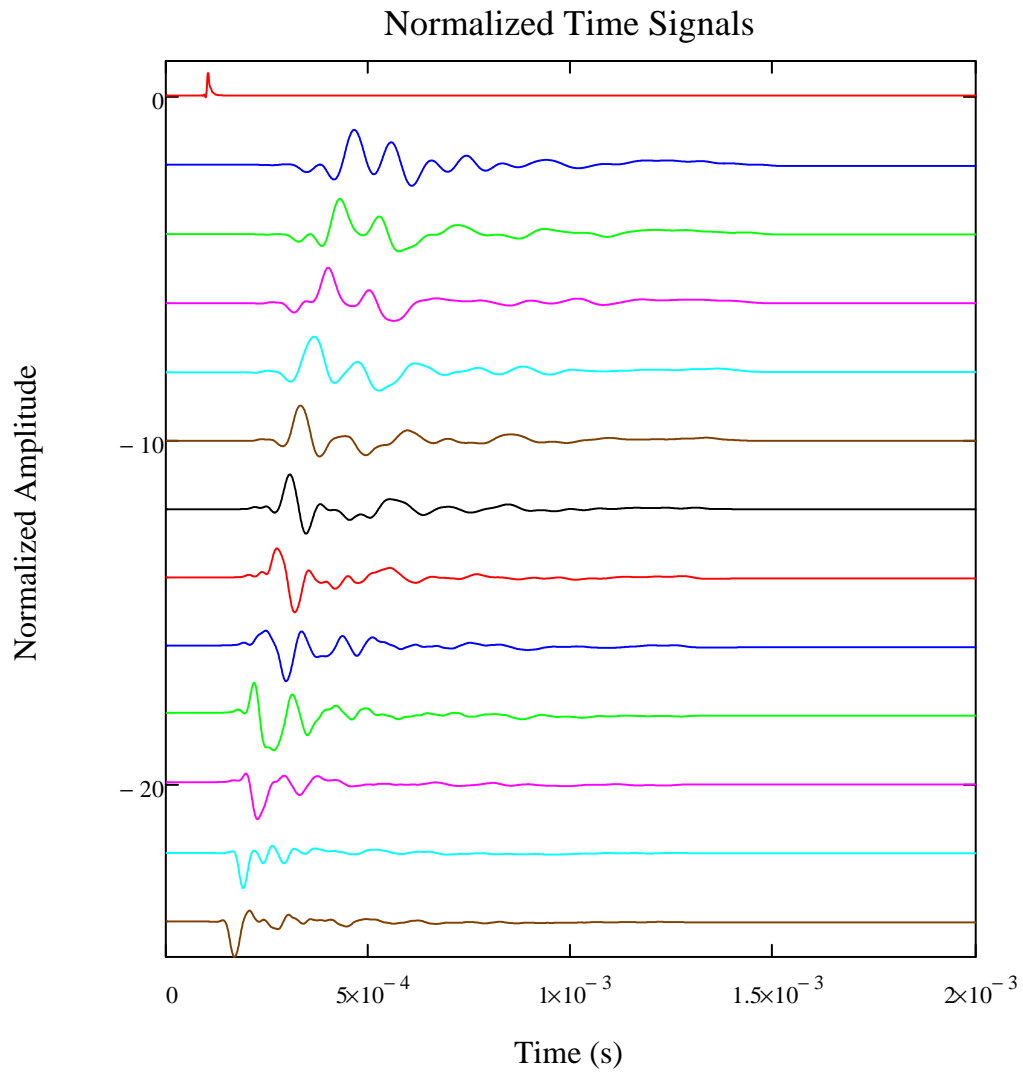


**Derivation: velocity**     $iv := 1 .. N - 1$

$$VR_{iv, k} := \frac{DR_{iv+1, k} - DR_{iv, k}}{\Delta t}$$

**Derivation: acceleration**     $ia := 2 .. N - 1$

$$AR_{ia, k} := \frac{VR_{ia, k} - VR_{ia-1, k}}{\Delta t}$$

$h := 1$

$TRp_{11} := 0.131ms$

$TRp_{10} := 0.142ms$
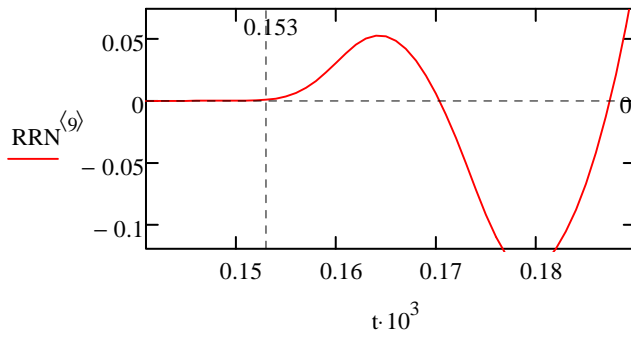
$TRp_9 := 0.153ms$
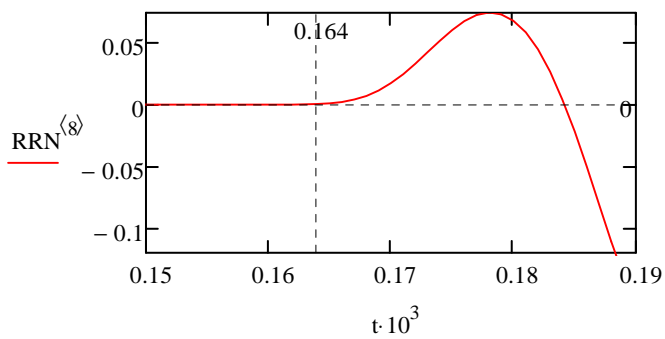
$TRp_8 := 0.164ms$
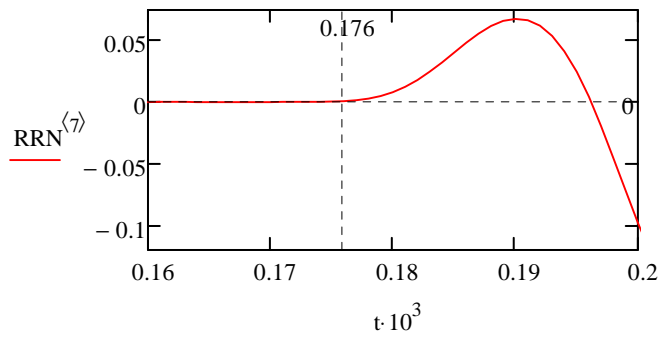
$$TRp_7 := 0.176ms$$
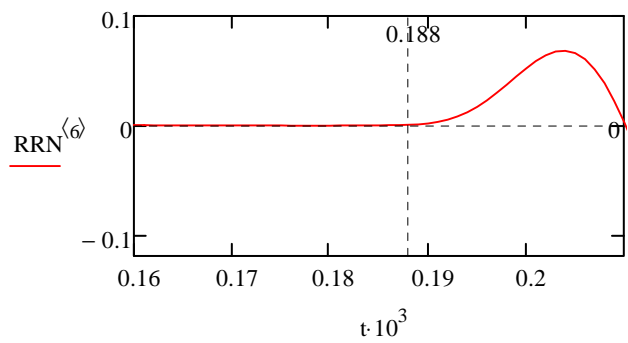


$$TRp_6 := 0.188ms$$
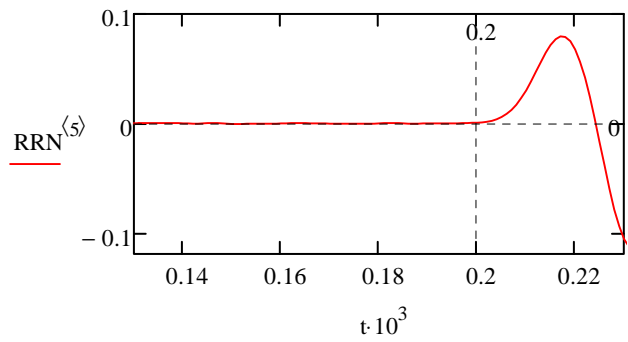


$$TRp_5 := 0.2ms$$



$$TRp_4 := 0.215ms$$

196
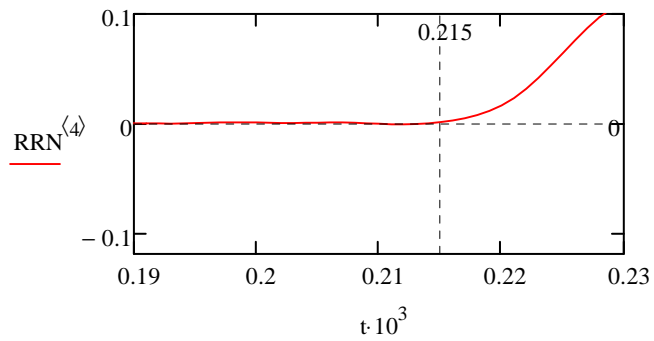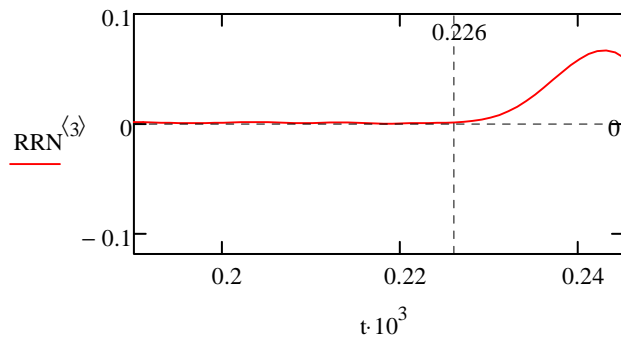
$TRp_3 := 0.226ms$
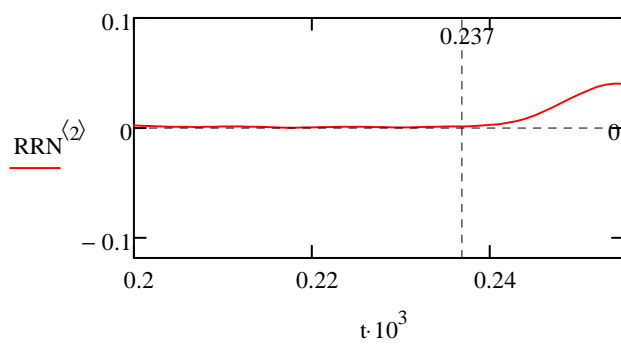


$TRp_2 := 0.237ms$
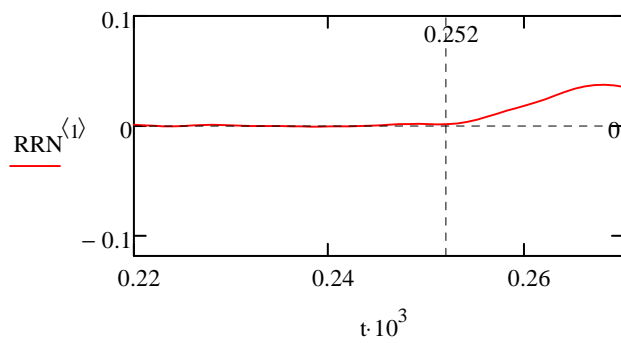


$TRp_1 := 0.252ms$

## *P-wave velocity*

$$VRp1 := \frac{1}{slope(D - X, TRp - t_0)} = 3.33 \times 10^3 \frac{m}{s}$$

$$bR1 := intercept(D - X, TRp - t_0) = 7.515 \times 10^{-6} s$$

**_Total SofS_**  $\quad SST1_R := \displaystyle\sum_{k=1}^{12} \left(TRp_k - mean(TRp)\right)^2 = 2.065 \times 10^{-8}\,s^2$

**_Regression SofS_**  $\quad SSR1_R := \displaystyle\sum_{k=1}^{12} \left[\left(\dfrac{D - X_k}{VRp1} + bR1\right) - mean\left(TRp - t_0\right)\right]^2 = 2.063 \times 10^{-8}\,s^2$

**_Coef of Determination_**  $\quad Rsq1_R := \dfrac{SSR1_R}{SST1_R} = 0.99889$

---

**_Arrival times determined AUTOMATICALLY, from Acceleration_**

---

**_Window width (Nb points)_**  $\quad width := 10$

$$u := 1 + width .. N \qquad v := 1 + width .. N - 1$$

**_RMS (acceleration)_**  $\quad RMSR_{u,k} := \sqrt{\dfrac{1}{10} \cdot \displaystyle\sum_{i=u-width}^{u} \left(RRN_{i,k}\right)^2}$

$$diffR_{v,k} := \left| RMSR_{v+1,k} - RMSR_{v,k} \right|$$

198

$h := 8$



Index

**Max RMS difference**     $\text{MaxdiffR}_k := \max\left(\text{diffR}^{\langle k \rangle}\right)$

**Arrival Time from Acceleration**

$\text{Cst} := 0.001 \quad q := 1 .. 100 \quad \%_q := \text{Cst} \cdot q$

$\text{aRR}(k,q) := \begin{vmatrix} n \leftarrow 1 \\ \text{while} \ \left| \text{diffR}_{n,k} \right| < \text{MaxdiffR}_k \cdot \%_q \\ \quad n \leftarrow n + 1 \\ (n) \end{vmatrix} \qquad \text{atRR}_{k,q} := t_{\text{aRR}(k,q)}$

**P - Wave velocities from Acceleration**     $\text{VRp2}_q := \dfrac{1}{\text{slope}\left(D - X, \text{atRR}^{\langle q \rangle} - t_0\right)}$

$\text{bR2}_q := \text{intercept}\left(D - X, \text{atRR}^{\langle q \rangle} - t_0\right)$

**% Difference between Vp1 and Vp2**     $\text{DiffVRp2}_q := \left| \dfrac{\text{VRp2}_q - \text{VRp1}}{\text{VRp1}} \right| \cdot 100$

199

*% Difference between Vp1 and Vp2 inferior to 2% for both right and left if: 8 < q < 12*

$q0 := 10 \qquad \%_{q0} = 0.01 \qquad atRR := atRR^{\langle q0 \rangle}$

$$VRp2 := VRp2_{q0} = 3.28 \times 10^3 \frac{m}{s}$$

$$bR2 := bR2_{q0}$$



**Total SofS** $\qquad SST2_R := \sum_{k=1}^{12} \left( atRR_k - mean(atRR) \right)^2 = 2.128 \times 10^{-8} s^2$

**Regression SofS** $\qquad SSR2_R := \sum_{k=1}^{12} \left[ \left( \frac{D - X_k}{VRp2} + bR2 \right) - mean(atRR - t_0) \right]^2 = 2.127 \times 10^{-8} s^2$

**Coef of Determination** $\qquad Rsq2_R := \dfrac{SSR2_R}{SST2_R} = 0.99951$

▲ P-WAVES

▼ R-WAVES

$RRN^{\langle 12 \rangle}$

0.152

$TRr_{12} := 0.152ms$

$t \cdot 10^3$



$RRN^{\langle 11 \rangle}$

0.173

$TRr_{11} := 0.173ms$

$t \cdot 10^3$



$RRN^{\langle 10 \rangle}$

0.201

$TRr_{10} := 0.201ms$

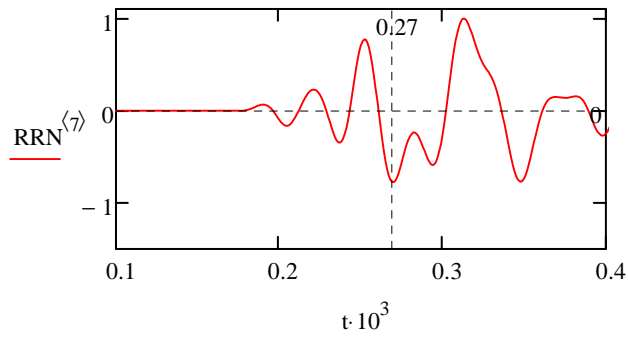$t \cdot 10^3$

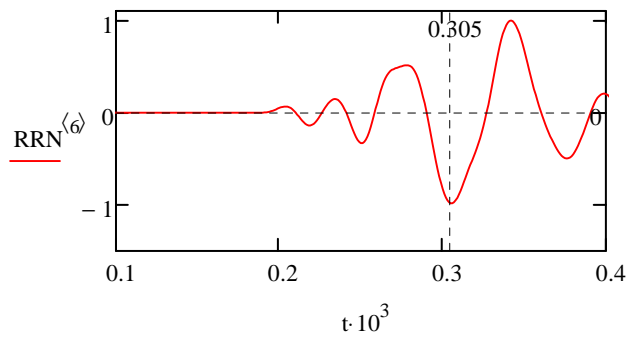

$RRN^{\langle 9 \rangle}$

0.219

$TRr_9 := 0.219ms$

$t \cdot 10^3$

*Very hard to determine which peak corresponds to R-waves at this distance from the source...*
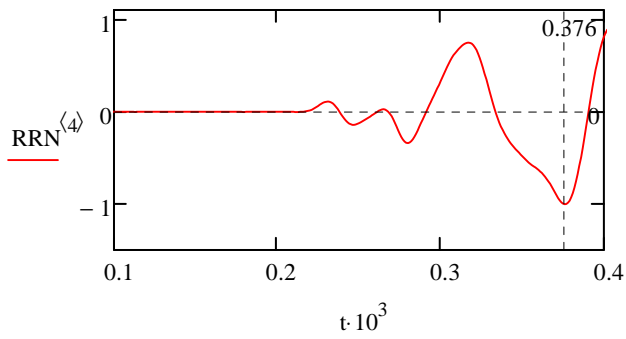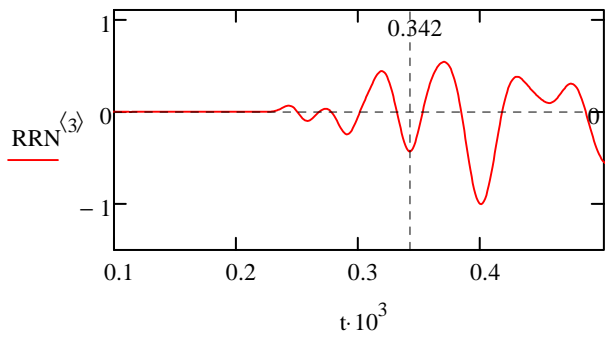
201
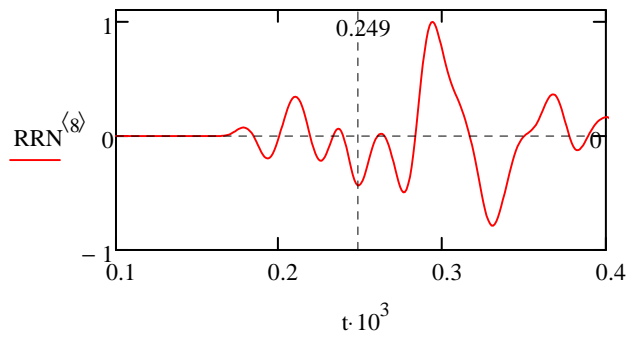
$TRr_8 := 0.249ms$



$TRr_7 := 0.27ms$



$TRr_6 := 0.305ms$



$TRr_5 := 0.317ms$

202
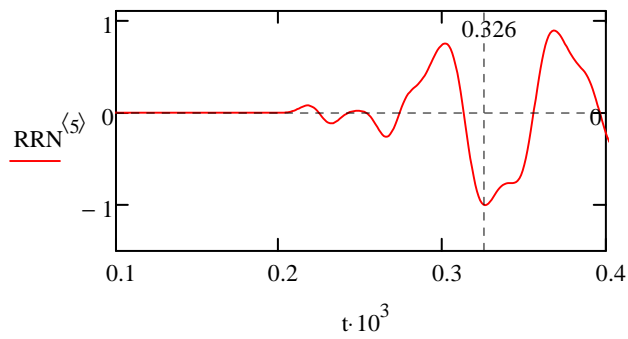
$$TRr_4 := 0.376ms$$



$$TRr_3 := 0.342ms$$

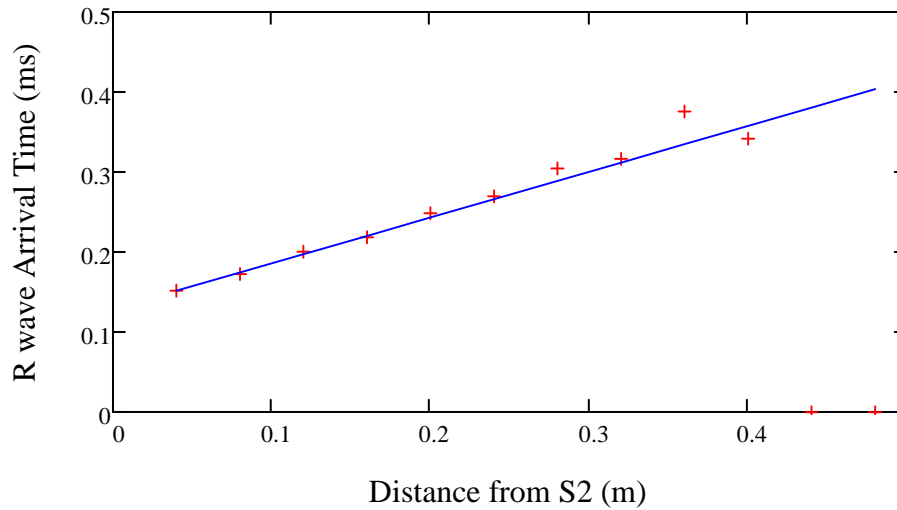## *R-wave velocity*

*Points selected for regression*

$$ArrivalR := \begin{pmatrix} TRr_9 \\ TRr_{10} \\ TRr_{11} \\ TRr_{12} \end{pmatrix} \qquad DistanceR := \begin{pmatrix} D - X_9 \\ D - X_{10} \\ D - X_{11} \\ D - X_{12} \end{pmatrix}$$

$$VRr1 := \frac{1}{slope(DistanceR, ArrivalR)} = 1.747 \times 10^3 \frac{m}{s}$$

$$cR := intercept(DistanceR, ArrivalR) = 1.29 \times 10^{-4} s$$

Figure with y-axis "R wave Arrival Time (ms)" and x-axis "Distance from S2 (m)".

**Total SofS**    $kR := 4$    $SST3_R := \displaystyle\sum_{k=1}^{kR} \left( ArrivalR_k - mean(ArrivalR) \right)^2 = 2.639 \times 10^{-9}\, s^2$

**Regression SofS**    $SSR3_R := \displaystyle\sum_{k=1}^{kR} \left[ \left( \dfrac{DistanceR_k}{VRr1} + cR \right) - mean(ArrivalR) \right]^2 = 2.622 \times 10^{-9}\, s^2$

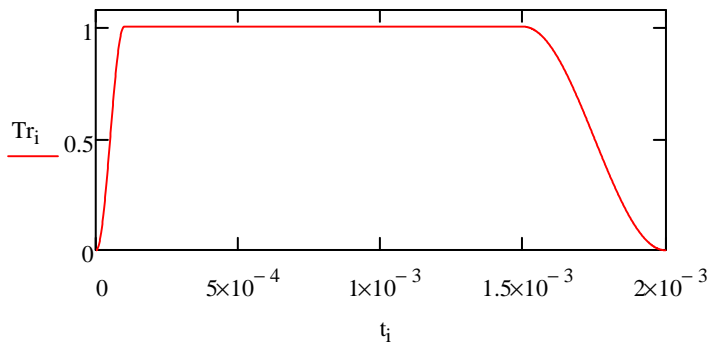**Coef of Determination**    $Rsq3_R := \dfrac{SSR3_R}{SST3_R} = 0.99367$

▲ R-WAVES

## FREQUENCY SPECTRA

▼ ACCELERATION

*Windowing:*

$$Tr_i := \begin{cases} 0.5 \cdot \left[ 1 - \cos\left[ \dfrac{\pi \cdot (i-1)}{floor\left( \dfrac{N-2}{20} \right)} \right] \right] & \text{if } 1 \le i \le floor\left( \dfrac{N-2}{20} \right) + 1 \\[4ex] 0.5 \cdot \left[ 1 - \cos\left[ \dfrac{\pi \cdot (i)}{floor\left( \dfrac{N-2}{4} \right) + 1} \right] \right] & \text{if } N - floor\left( \dfrac{N-2}{4} \right) - 1 \le i \le N \\[4ex] 1 & \text{otherwise} \end{cases}$$
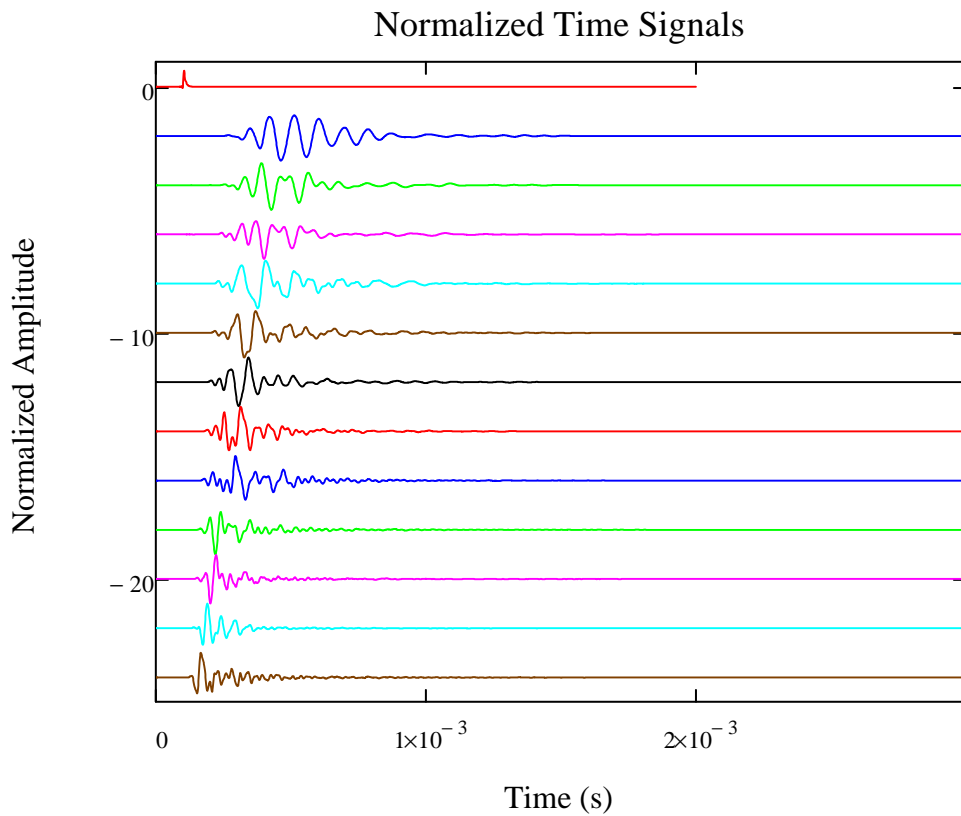
$$Tr_1 = 0$$

$$Tr_N = 0$$

$$RRW_{i,k} := RRO_{i,k} \cdot Tr_i$$

### *Zero-padding:*

$$N = 2 \times 10^3 \qquad N2 := 2^{14} = 1.638 \times 10^4 \qquad i2 := 1 .. N2 \qquad t_{i2} := (i2 - 1)\Delta t \qquad t_{N2} = 0.016\,s$$

$$RRZ_{i2,k} := \begin{vmatrix} RRW_{i2,k} & \text{if } i2 \le N \\ 0 & \text{otherwise} \end{vmatrix} \qquad\qquad RRZN_{i2,k} := \frac{RRZ_{i2,k}}{MaxRRO_k}$$

$$\alpha0 := 2 \qquad x(k) := RRZN^{\langle k \rangle} - k \cdot \alpha0$$

## Normalized Time Signals



Normalized Amplitude

Time (s)

**Fourier Transform - Receivers**     $FTR^{\langle k \rangle} := FFT\left(RRZ^{\langle k \rangle}\right)$     $MagR^{\langle k \rangle} := \left|\overrightarrow{FTR^{\langle k \rangle}}\right|$

**Normalization**     $MaxMagR_k := \max\left(MagR^{\langle k \rangle}\right)$     $MagRN^{\langle k \rangle} := \dfrac{MagR^{\langle k \rangle}}{MaxMagR_k}$

**Frequency**     $N3 := 2^{14-1} + 1 = 8.193 \times 10^3$     $i3 := 1 .. N3$     $\Delta f := \dfrac{1}{t_{N2}}$     $\Delta f = 61.039\,\dfrac{1}{s}$

$f_{i3} := (i3 - 1)\cdot \Delta f$     $f_{N3} = 5 \times 10^5\,\dfrac{1}{s}$

$\alpha 0 := 1$     $x(k) := MagRN^{\langle k \rangle} - k\cdot\alpha 0$

## Normalized Fourier Spectra
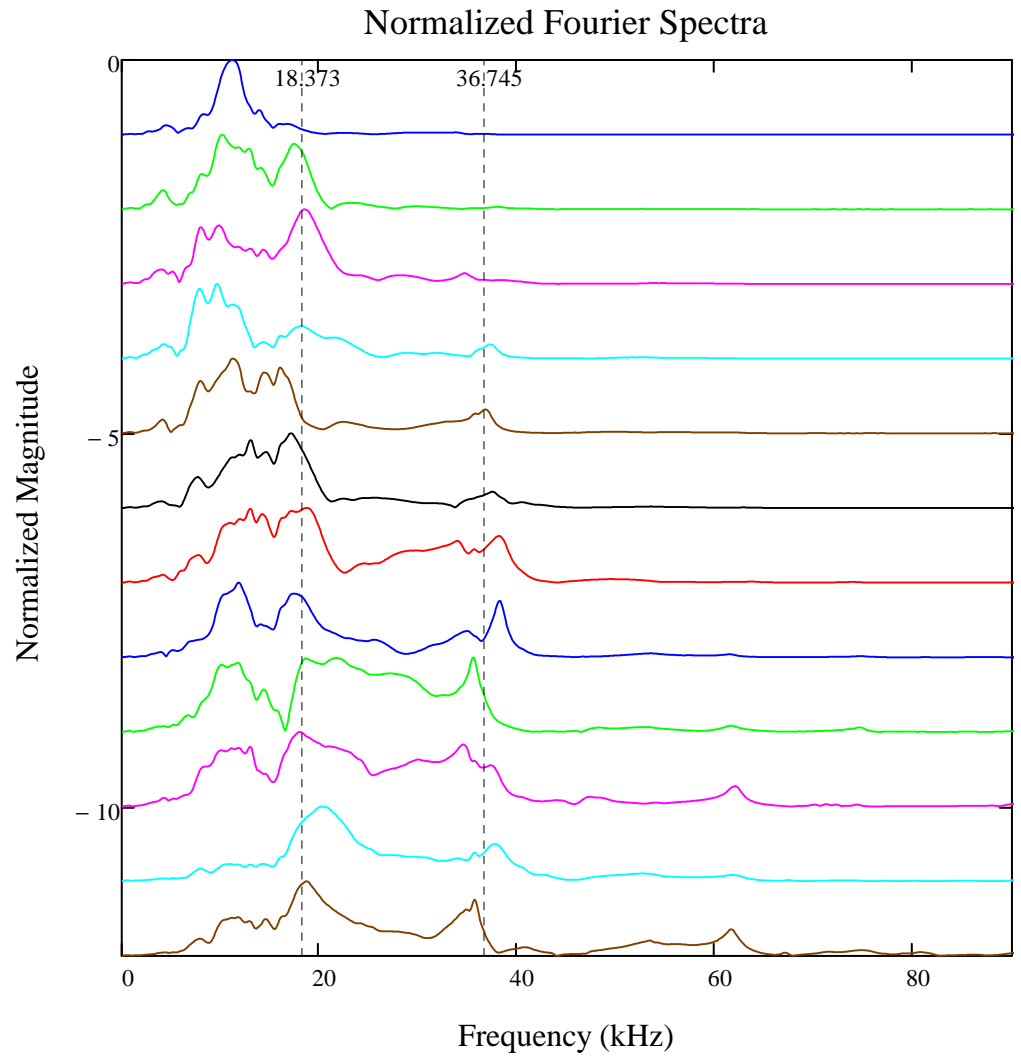


**Main frequencies**

$f_{R1} := 11.17\text{kHz}$     $f_{R2} := 18.373\text{kHz}$     $f_{R3} := 36.745\text{kHz}$

$c_{i3} := i3$    $iR1 := floor\left(linterp\left(f, c, f_{R1}\right)\right)$    $iR2 := floor\left(linterp\left(f, c, f_{R2}\right)\right)$    $iR3 := floor\left(linterp\left(f, c, f_{R3}\right)\right)$

$$f_{iR1} = 1.111 \times 10^4 \frac{1}{s} \qquad f_{iR2} = 1.837 \times 10^4 \frac{1}{s} \qquad f_{iR3} = 3.668 \times 10^4 \frac{1}{s}$$

**Penetration depth of surface waves**

$i\lambda := 2 .. N3$    $\lambda R_{i\lambda} := \dfrac{VRr1}{f_{i\lambda}}$    $\lambda R_{iR1} = 0.157\,m$    $\lambda R_{iR2} = 0.095\,m$
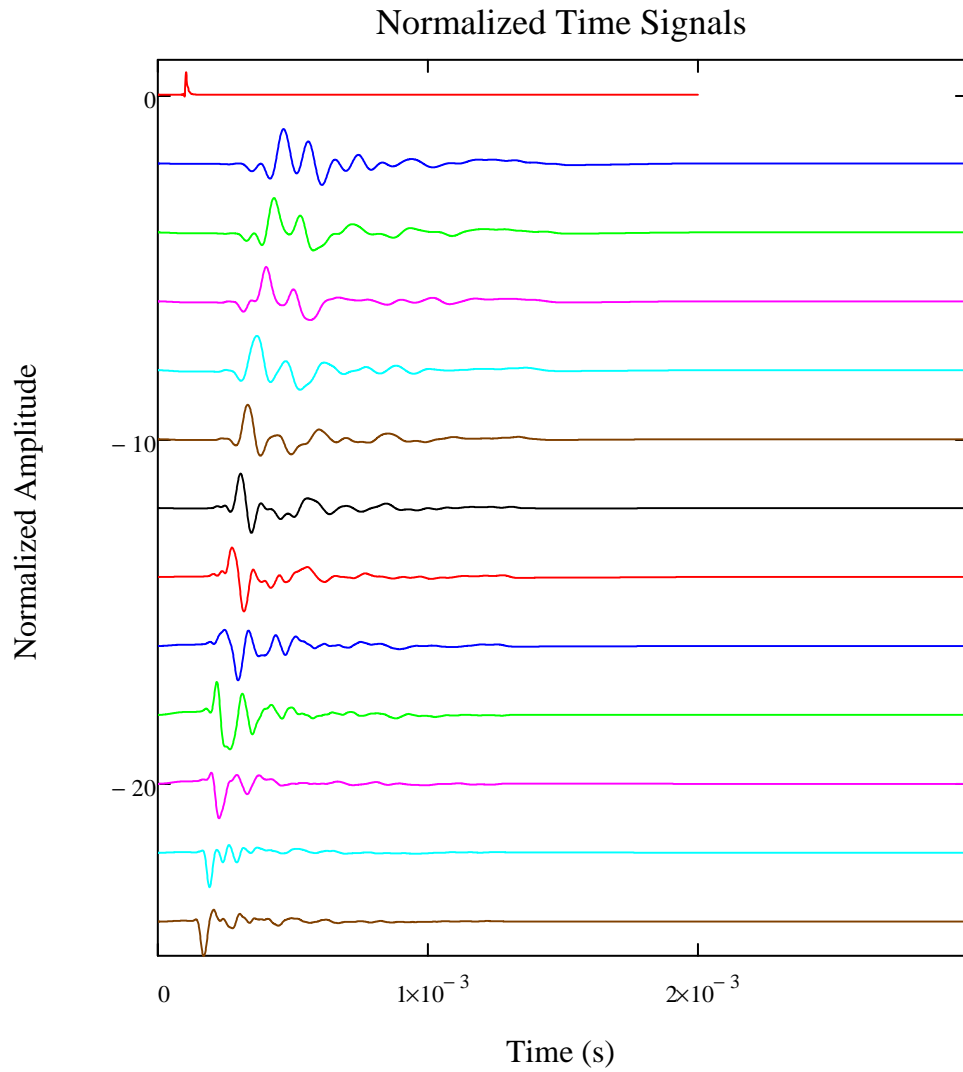
🔺 ACCELERATION

🔻 DISPLACEMENT

$DRW_{i,k} := DRO_{i,k} \cdot Tr_i$

**Zero-padding:**

$DRZ_{i2,k} := \begin{vmatrix} DRW_{i2,k} & \text{if } i2 \le N \\ 0 & \text{otherwise} \end{vmatrix}$    $DRZN_{i2,k} := \dfrac{DRZ_{i2,k}}{MaxDRO_k}$

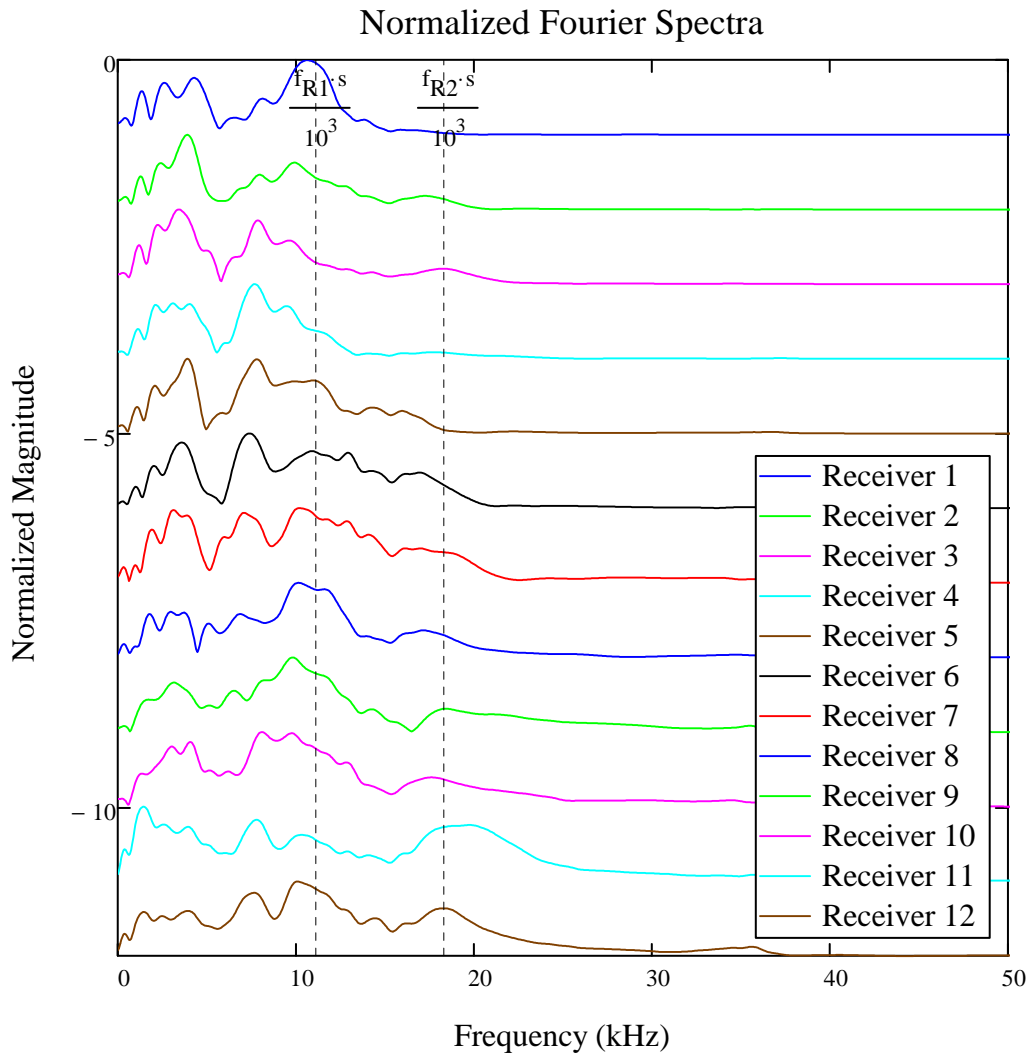$\alpha0 := 2$    $x(k) := DRZN^{\langle k \rangle} - k \cdot \alpha0$

207

## Normalized Time Signals

*Fourier Transform - Receivers* $\qquad \text{FTDR}^{\langle k \rangle} := \text{FFT}\left(\text{DRZ}^{\langle k \rangle}\right) \qquad \text{MagDR}^{\langle k \rangle} := \overrightarrow{\left|\text{FTDR}^{\langle k \rangle}\right|}$

*Normalization* $\qquad \text{MaxMagDR}_k := \max\left(\text{MagDR}^{\langle k \rangle}\right) \qquad \text{MagDRN}^{\langle k \rangle} := \dfrac{\text{MagDR}^{\langle k \rangle}}{\text{MaxMagDR}_k}$

$\alpha 0 := 1 \qquad x(k) := \text{MagDRN}^{\langle k \rangle} - k \cdot \alpha 0$

## Normalized Fourier Spectra



DISPLACEMENT

## DISPERSION CURVES

Measured Disp Curve (SWAN)

DC_Right := READPRN("SlabAbot-DYTglue-R-DC.txt")

N4 := rows(DC_Right) = 747        i4 := 1 .. N4

**Phase velocity**        $VphR := DC\_Right^{\langle 2 \rangle} \cdot \frac{m}{s}$

**Frequency**        $fR_{i4} := DC\_Right_{i4, 1} \cdot Hz$

$f_{low} := 24kHz$ $\qquad\qquad\qquad$ $f_{high} := 34kHz$

$p_{i4} := i4$ $\qquad$ $i4_{low} := floor\left(linterp\left(fR, p, f_{low}\right)\right)$ $\qquad$ $i4_{high} := floor\left(linterp\left(fR, p, f_{high}\right)\right)$

$\qquad\qquad fR_{i4_{low}} = 2.397 \times 10^4 \dfrac{1}{s}$ $\qquad\qquad\qquad$ $fR_{i4_{high}} = 3.398 \times 10^4 \dfrac{1}{s}$
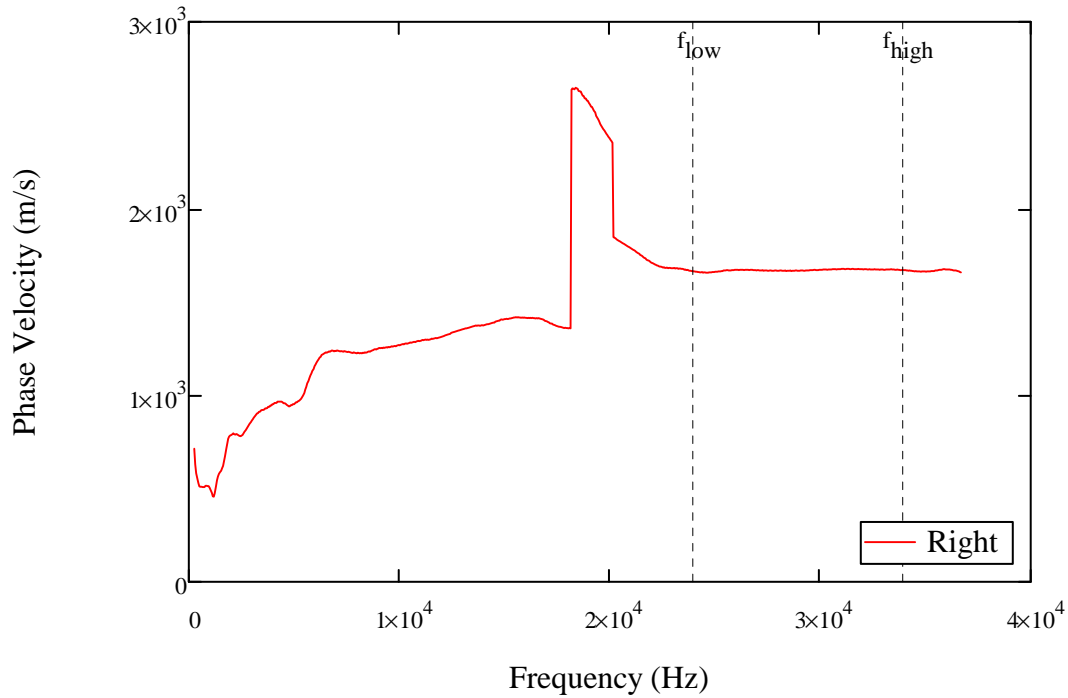


**R waves velocity** $\qquad$ $VRr2 := \displaystyle\sum_{i4 = i4_{low}}^{i4_{high}} \dfrac{VphR_{i4}}{i4_{high} - i4_{low} + 1}$ $\qquad$ $VRr2 = 1.671 \times 10^3 \dfrac{m}{s}$

$\qquad\qquad\qquad\qquad\qquad\qquad\qquad$ *From TD* $\qquad$ $VRr1 = 1.747 \times 10^3 \dfrac{m}{s}$

$\qquad\qquad\qquad\qquad\qquad\qquad\qquad$ *Difference %* $\qquad$ $\left| \dfrac{VRr2 - VRr1}{VRr1} \right| \cdot 100 = 4.33$

▲ Measured Disp Curve (SWAN)

THEORETICAL DISPERSION CURVE (YANG)

▼ Elastic constants

$zero := 10^{-300}$

**P-wave and R-wave velocity:** $\quad VP_R := VRp1 \cdot \dfrac{s}{m} = 3.33 \times 10^3 \quad VR_R := VRr2 \cdot \dfrac{s}{m} = 1.671 \times 10^3$

**Half the thickness of a plate:** $\quad h := \dfrac{0.08}{2} \qquad h = 0.04$

**Poisson ratio:** $\quad fun_R(x) := \dfrac{VR_R}{VP_R} - \left( \dfrac{0.862 + 1.14 \cdot x}{1 + x} \right) \sqrt{\dfrac{1 - 2 \cdot x}{2 \cdot (1 - x)}} \quad \nu_R := root\left( fun_R(x), x, 0.1, 0.5 \right)$

$\qquad\qquad\qquad\qquad\qquad\qquad\qquad\qquad\qquad\qquad\qquad\qquad\qquad\qquad\qquad\quad \nu_R = 0.291$

**S-wave velocity:** $\quad VS_R := \dfrac{1 + \nu_R}{0.862 + 1.14 \cdot \nu_R} \cdot VR_R \quad VS_R = 1.807 \times 10^3$

**Mass density:** $\quad \rho := 2350$

**Shear modulus:** $\quad G_R := VS_R{}^2 \cdot \rho \quad G_R = 7.675 \times 10^9$

**Young's modulus:** $\quad E_R := G_R \cdot 2 \left( 1 + \nu_R \right) \quad E_R = 1.982 \times 10^{10}$

**Constraint modulus:** $\quad M_R := \dfrac{1 - \nu_R}{\left( 1 + \nu_R \right) \cdot \left( 1 - 2 \cdot \nu_R \right)} \cdot E_R \qquad M_R = 2.606 \times 10^{10}$

**Bulk modulus:** $\quad K_R := \dfrac{E_R}{3 \cdot \left( 1 - 2 \cdot \nu_R \right)} \qquad K_R = 1.583 \times 10^{10}$

🔼 Elastic constants
___

🔽 Rayleigh - Lamb - Frequency  Equations
___

$$p_R(\omega, k) := \sqrt{\left( \dfrac{\omega}{VP_R} \right)^2 - k^2} \qquad\qquad q_R(\omega, k) := \sqrt{\left( \dfrac{\omega}{VS_R} \right)^2 - k^2}$$

**For symmetric Lamb modes:**

$$F_{symR}(\omega, k) := \infty \text{ on error } \dfrac{\tan\left( q_R(\omega, k) \cdot h \right)}{q_R(\omega, k)} + \dfrac{4 \cdot k^2 \cdot p_R(\omega, k) \cdot \tan\left( p_R(\omega, k) \cdot h \right)}{\left( q_R(\omega, k)^2 - k^2 \right)^2}$$

**For anti-symmetric Lamb modes:**

$$F_{antiR}(\omega, k) := \infty \text{ on error } q_R(\omega, k) \cdot \tan\left( q_R(\omega, k) \cdot h \right) + \dfrac{\left( q_R(\omega, k)^2 - k^2 \right)^2 \cdot \tan\left( p_R(\omega, k) \cdot h \right)}{4 \cdot k^2 \cdot p_R(\omega, k)}$$

🔼 Rayleigh - Lamb - Frequency  Equations
___

**Numerical time increment:**   $delta\_t := 4 \cdot 10^{-7}$

$$f\_inc := \frac{1}{256 \cdot 10 \cdot 4 delta\_t}$$   $f\_max := 70 \cdot 10^3$   $f\_inc = 244.141$

**Point number in frequency:**   $Nf := ceil\left(\dfrac{f\_max}{f\_inc}\right)$   $Nf = 287$

**Frequency range:**

   **Increment:** $\omega\_inc := 2 \cdot \pi \cdot f\_inc$   **Start:** $\omega 0 := 2 \cdot \pi \cdot f\_inc$   **End:** $\omega\_max := 2 \cdot \pi \cdot f\_max$

**Phase velocity range:**

   **Increment:** $v\_inc := 1.0$   **Start:** $v0 := 10$   **End:** $v\_max := 10000$

▲ Range for frequency and phase velocity
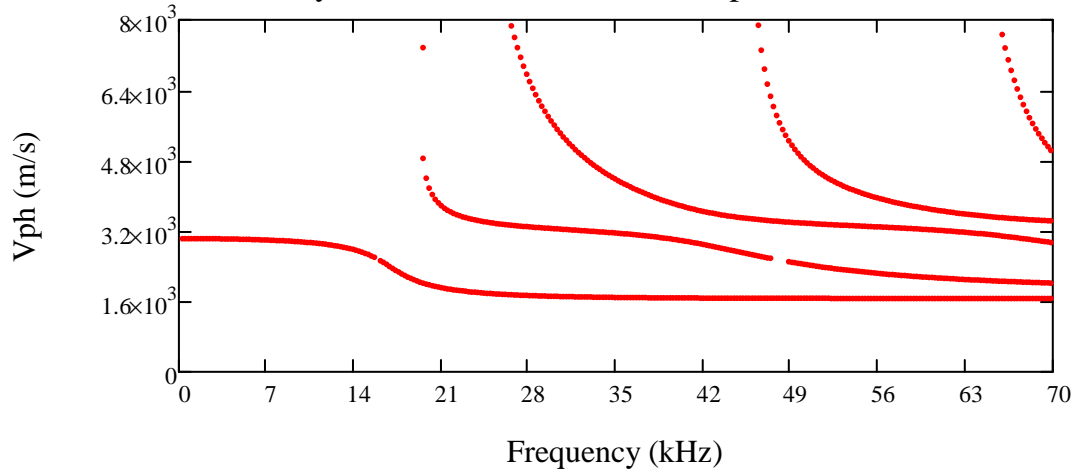
▼ Symmetric Lamb modes

**Frequency and Phase Velocity:**

**MX1,1: f**
**MX1,2: Vph**

$\text{MX1}_R :=$ 
$\quad$ row ← 1
$\quad$ ω ← ω0
$\quad$ while ω ≤ ω_max
$\quad\quad$ v ← v0
$\quad\quad$ val ← $F_{symR}\left(\omega, \dfrac{\omega}{v}\right)$
$\quad\quad$ sgn ← sign(val)
$\quad\quad$ v2 ← v + v_inc
$\quad\quad$ val2 ← $F_{symR}\left(\omega, \dfrac{\omega}{v2}\right)$
$\quad\quad$ sgn2 ← sign(val2)
$\quad\quad$ while v2 < v_max
$\quad\quad\quad$ while v2 < v_max ∧ sgn·sgn2 ≥ 0
$\quad\quad\quad\quad$ v2 ← v2 + v_inc
$\quad\quad\quad\quad$ val2 ← $F_{symR}\left(\omega, \dfrac{\omega}{v2}\right)$
$\quad\quad\quad\quad$ sgn2 ← sign(val2)
$\quad\quad\quad$ if v2 < v_max ∧ sgn·sgn2 < 0
$\quad\quad\quad\quad$ cond ← 1
$\quad\quad\quad\quad$ cond ← 0  on error $\text{root}\left(F_{symR}(\omega, k), k, \dfrac{\omega}{v2}, \dfrac{\omega}{v}\right)$
$\quad\quad\quad\quad$ if cond = 1
$\quad\quad\quad\quad\quad$ $M_{row, 1} \leftarrow \dfrac{\omega}{2 \cdot \pi}$
$\quad\quad\quad\quad\quad$ $M_{row, 2} \leftarrow \dfrac{\omega}{\text{root}\left(F_{symR}(\omega, k), k, \dfrac{\omega}{v2}, \dfrac{\omega}{v}\right)}$
$\quad\quad\quad\quad\quad$ row ← row + 1
$\quad\quad\quad$ v ← v2
$\quad\quad\quad$ val ← val2
$\quad\quad\quad$ sgn ← sign(val2)
$\quad\quad\quad$ v2 ← v + v_inc
$\quad\quad\quad$ val2 ← $F_{symR}\left(\omega, \dfrac{\omega}{v2}\right)$
$\quad\quad\quad$ sgn2 ← sign(val2)
$\quad\quad$ ω ← ω + ω_inc
$\quad$ M

## Symmetric Lamb modes - Dispersion Curve



**Frequency and Wave Number:**

**MK1,1: f**
**MK1,2: k/2π**

$$MK1_R := \begin{vmatrix} \text{for } i \in 1 .. \text{rows}(MX1_R) \\ \quad \begin{vmatrix} M_{i,1} \leftarrow MX1_{R_{i,1}} \\ \\ M_{i,2} \leftarrow \dfrac{MX1_{R_{i,1}}}{MX1_{R_{i,2}}} \end{vmatrix} \\ M \end{vmatrix}$$

## Symmetric Lamb modes - FK spectrum
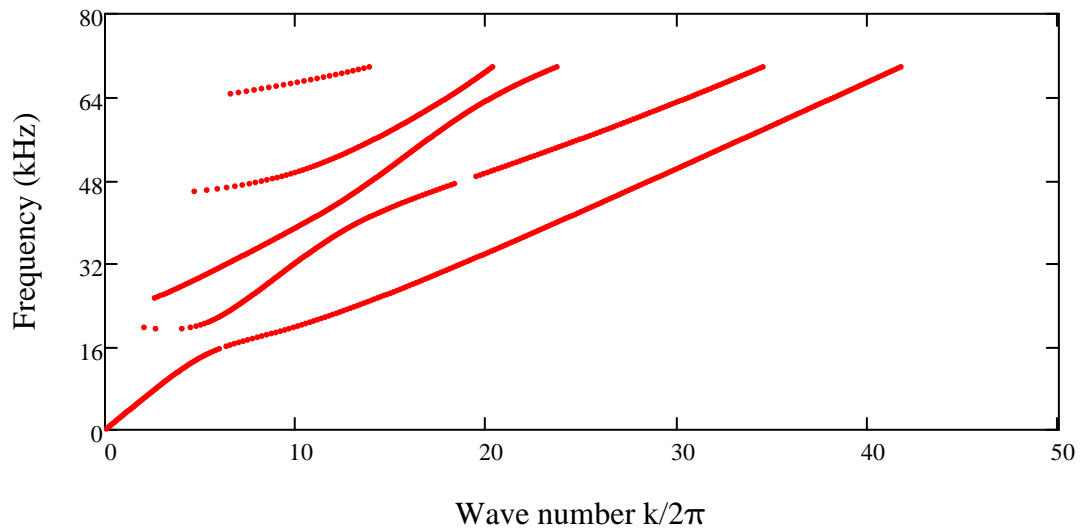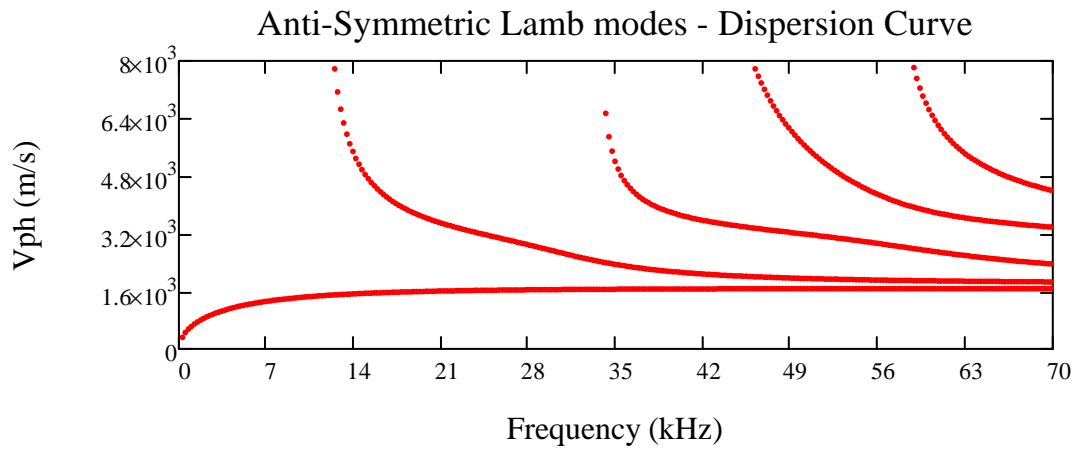


🔺 Symmetric Lamb modes

🔻 Anti-symmetric Lamb modes

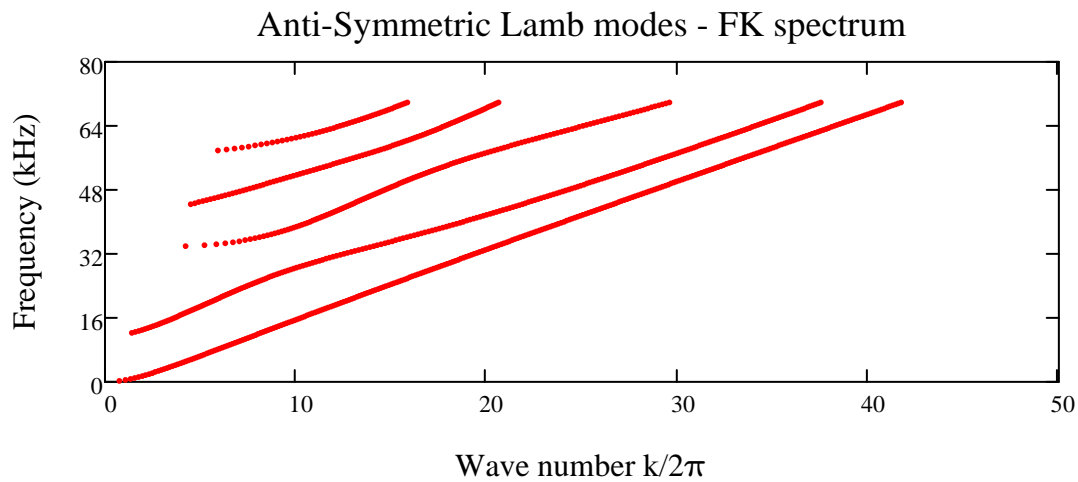**Frequency and Phase Velocity:**

**MX2,1: f**
**MX2,2: Vph**

$MX2_R :=$

$row \leftarrow 1$

$\omega \leftarrow \omega0$

while $\omega \leq \omega\_max$

$\quad v \leftarrow v0$

$\quad val \leftarrow F_{antiR}\left(\omega, \dfrac{\omega}{v}\right)$

$\quad sgn \leftarrow sign(val)$

$\quad v2 \leftarrow v + v\_inc$

$\quad val2 \leftarrow F_{antiR}\left(\omega, \dfrac{\omega}{v2}\right)$

$\quad sgn2 \leftarrow sign(val2)$

$\quad$ while $v2 < v\_max$

$\quad\quad$ while $v2 < v\_max \wedge sgn\cdot sgn2 \geq 0$

$\quad\quad\quad v2 \leftarrow v2 + v\_inc$

$\quad\quad\quad val2 \leftarrow F_{antiR}\left(\omega, \dfrac{\omega}{v2}\right)$

$\quad\quad\quad sgn2 \leftarrow sign(val2)$

$\quad\quad$ if $v2 < v\_max \wedge sgn\cdot sgn2 < 0$

$\quad\quad\quad cond \leftarrow 1$

$\quad\quad\quad cond \leftarrow 0$ on error $root\left(F_{antiR}(\omega, k), k, \dfrac{\omega}{v2}, \dfrac{\omega}{v}\right)$

$\quad\quad\quad$ if $cond = 1$

$\quad\quad\quad\quad M_{row,1} \leftarrow \dfrac{\omega}{2\cdot\pi}$

$\quad\quad\quad\quad M_{row,2} \leftarrow \dfrac{\omega}{root\left(F_{antiR}(\omega, k), k, \dfrac{\omega}{v2}, \dfrac{\omega}{v}\right)}$

$\quad\quad\quad\quad row \leftarrow row + 1$

$\quad\quad v \leftarrow v2$

$\quad\quad val \leftarrow val2$

$\quad\quad sgn \leftarrow sign(val2)$

$\quad\quad v2 \leftarrow v + v\_inc$

$\quad\quad val2 \leftarrow F_{antiR}\left(\omega, \dfrac{\omega}{v2}\right)$

$\quad\quad sgn2 \leftarrow sign(val2)$

$\quad \omega \leftarrow \omega + \omega\_inc$

$M$

215

## Anti-Symmetric Lamb modes - Dispersion Curve



**Frequency and Wave Number:**

**MK1,1: f**
**MK1,2: k/2π**

$$MK2_R := \begin{vmatrix} \text{for } i \in 1 .. \text{rows}(MX2_R) \\ \quad \begin{vmatrix} M_{i,1} \leftarrow MX2_{R_{i,1}} \\ \\ M_{i,2} \leftarrow \dfrac{MX2_{R_{i,1}}}{MX2_{R_{i,2}}} \end{vmatrix} \\ M \end{vmatrix}$$

## Anti-Symmetric Lamb modes - FK spectrum



▲ Anti-symmetric Lamb modes

▼ Comparison Measured and Theoretical Disp Curves

***Frequency of Jump Antisymetric --> Symetric***    $fR_{jp1} := 18164 Hz$    $fR_{jp2} := 20166 Hz$
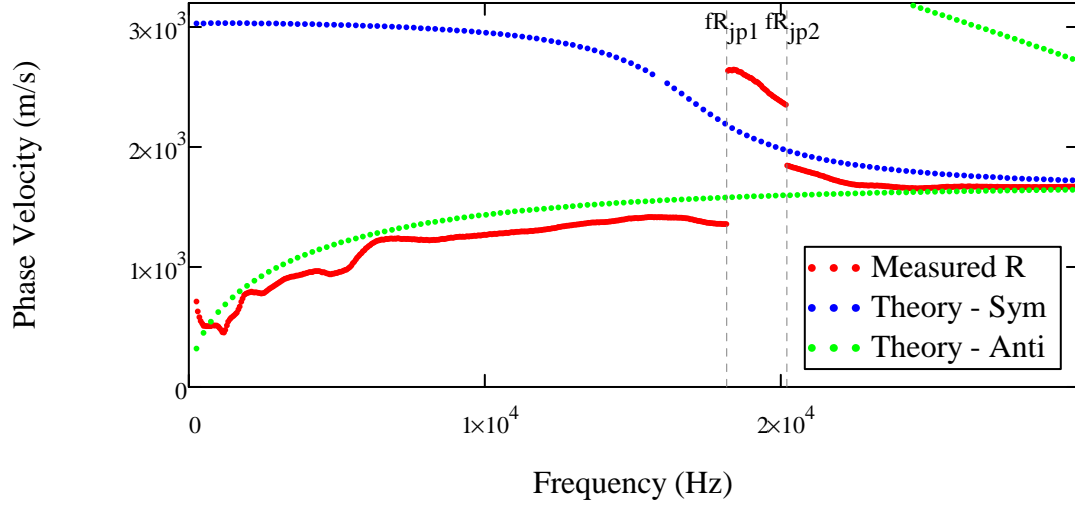
**Wavelength of Jump Antisymetric --> Symetric**

*Antisymetric Mode*     $\lambda R_{jpa} := 0.07502 m$     $\dfrac{\lambda R_{jpa}}{H \cdot m} = 0.075 \dfrac{1}{H}$

*Symetric Mode*     $\lambda R_{jps} := 0.14525 m$     $\dfrac{\lambda R_{jps}}{H \cdot m} = 0.145 \dfrac{1}{H}$
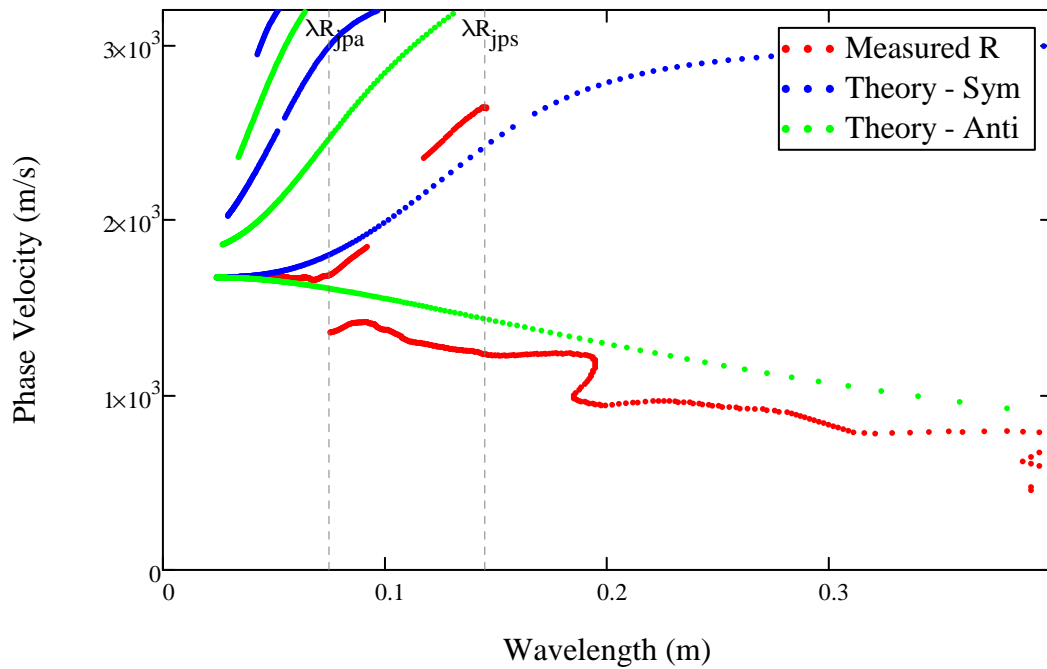


🔺 Comparison Measured and Theoretical Disp Curves

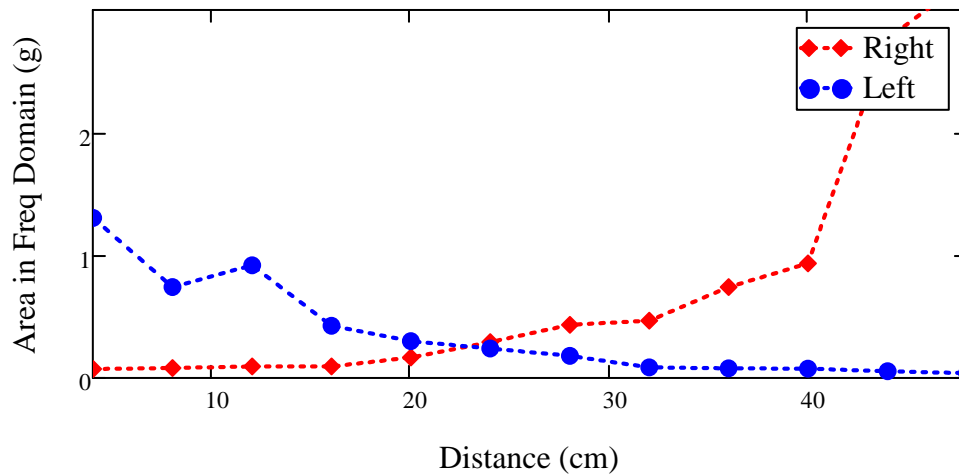# File: "Attenuation in Frequency Domain"

**Measured Attenuation**

**Total area**

$$\text{AreaR}_k := \sum_{i3 = 1}^{\frac{N}{2}} \text{MagR}_{i3, k}$$

**Maximum Area**

$$\text{MaxAreaR} := \max(\text{AreaR}) = 3.248$$

**Normalized Area**

$$\text{AreaRN}_k := \frac{\text{AreaR}_k}{\text{MaxAreaR}}$$

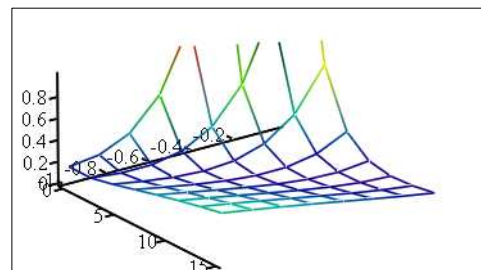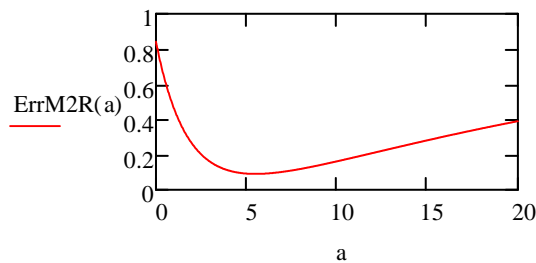## Area in Freq Domain vs. Distance from the Source



$$XR := \text{AreaRN}$$

***Call refecrence file: "Attenuation"***

**Fitting - LINEAR scale**

***Error between Theoretical model and Measured attenuation***
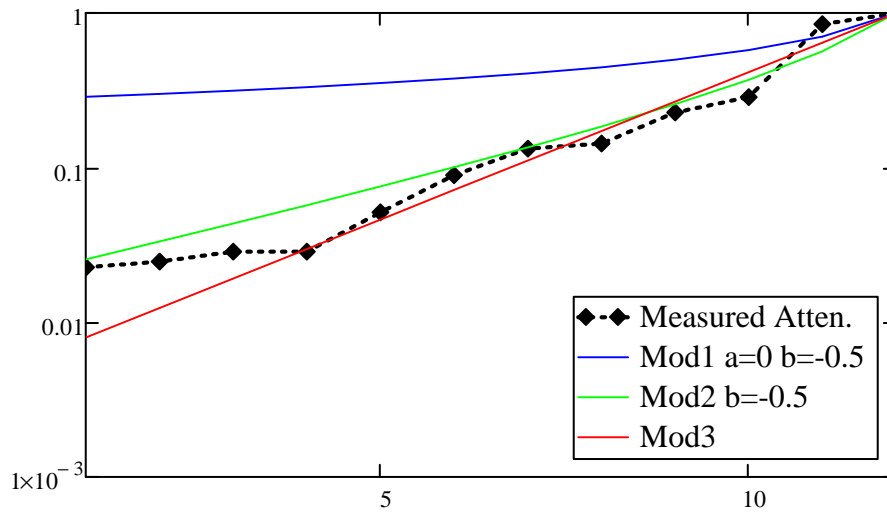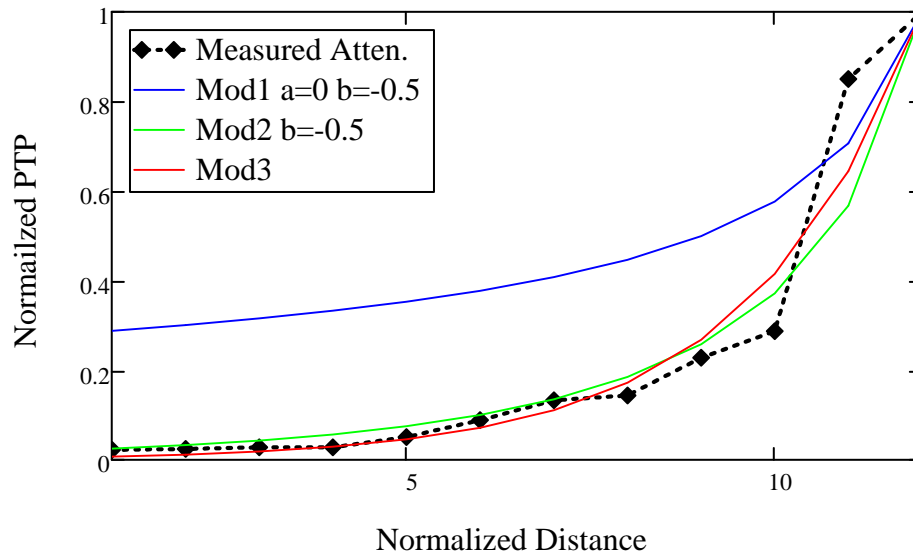


ErrM3R

## Minimize the Error

$E2AR := E2R = 5.498$          $ErrM2R(E2R) = 0.092$

$$E3AR := E3R = \begin{pmatrix} 10.966 \\ 0 \end{pmatrix} \qquad ErrM3R\left(E3R_1, E3R_2\right) = 0.063$$
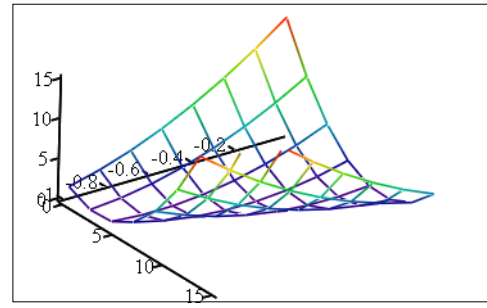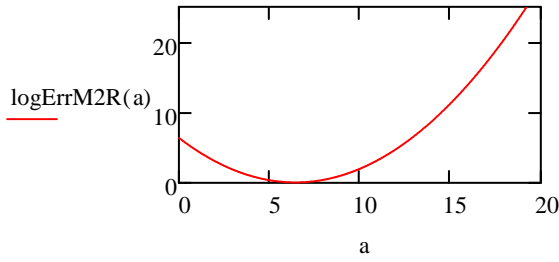




## Coef of Determination R2 = (SST-SSE)/SST

$Rsq_{2AR} := Rsq_{2R} = 0.924$

$Rsq_{3AR} := Rsq_{3R} = 0.948$

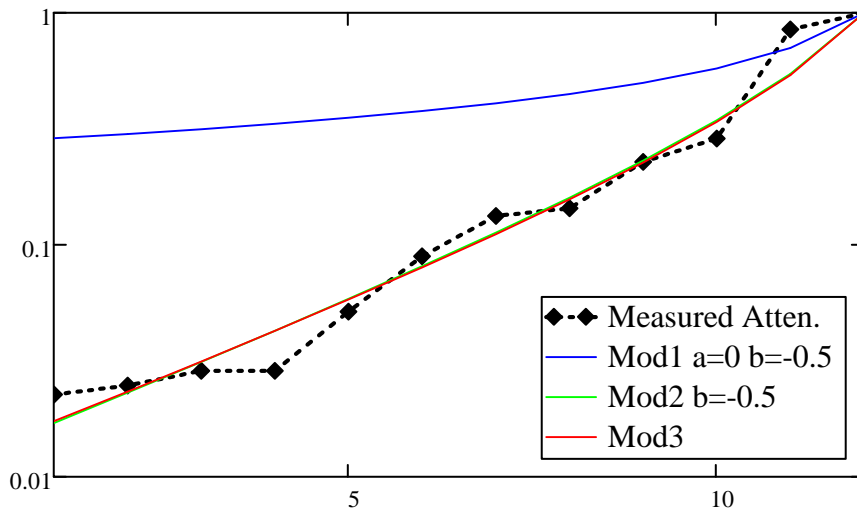**Fitting - LOG scale**

logErrM3R

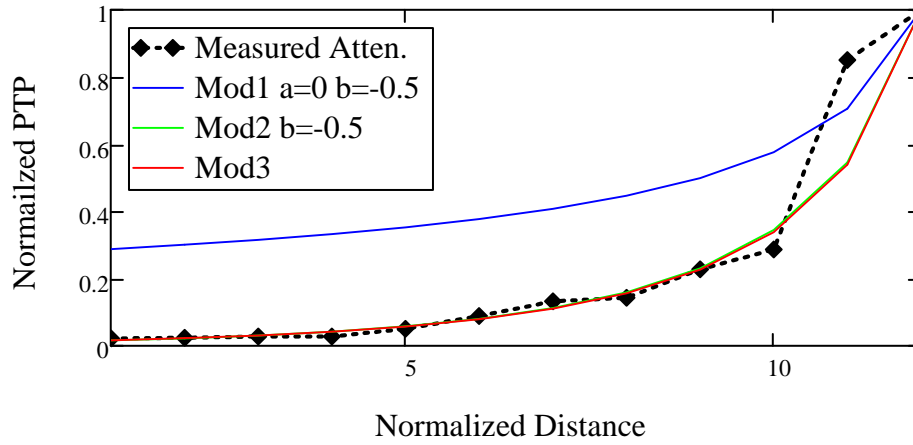## Minimize the Error

$logE2AR := logE2R = 6.42$          $logErrM2R(logE2R) = 0.103$

$logE3AR := logE3R = \begin{pmatrix} 6.199 \\ -0.532 \end{pmatrix}$          $logErrM3R\left(logE3R_1, logE3R_2\right) = 0.102$

*Coef of Determination R2 = (SST-SSE)/SST*

$logRsq_{2AR} := logRsq_{2R} = 0.92$

$logRsq_{3AR} := logRsq_{3R} = 0.917$

▲ ATTENUATION: TOTAL AREA ACCELERATION

▼ ATTENUATION: TOTAL AREA DISPLACEMENT

| ***Measured Attenuation*** |
|---|

**Total area**    $AreaDR_k := \sum_{i3=1}^{\frac{N}{2}} MagDR_{i3,k}$

**Maximum Area**    $MaxAreaDR := max(AreaDR) = 3.086 \times 10^{-10}$

**Normalized Area**    $AreaDRN_k := \dfrac{AreaDR_k}{MaxAreaDR}$



Area in Freq Domain vs. Distance from the Source
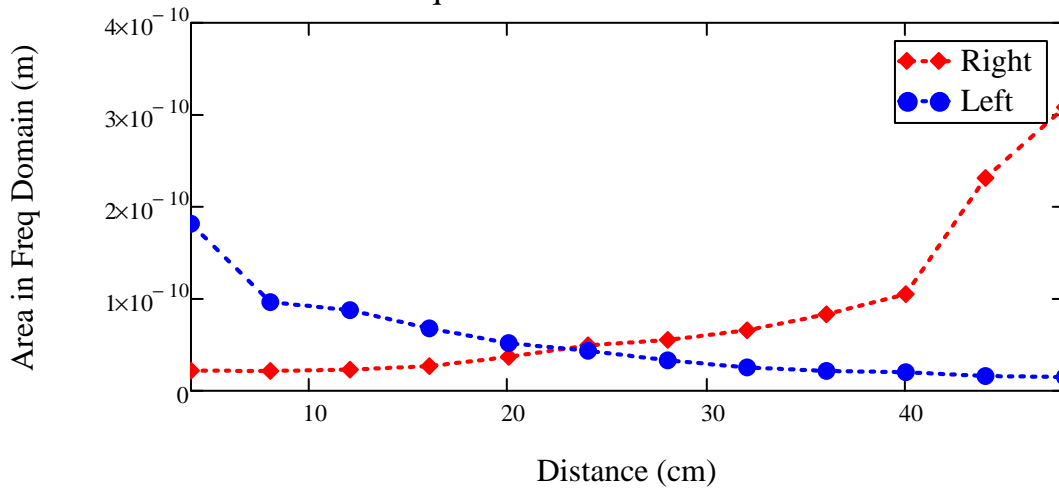
$XR := AreaDRN$

***Call refecrence file: "Attenuation"***

| ***Fitting - LINEAR scale*** |
|---|

***Error between Theoretical model and Measured attenuation***
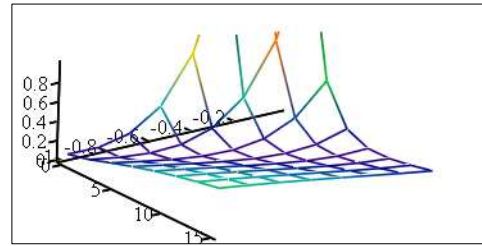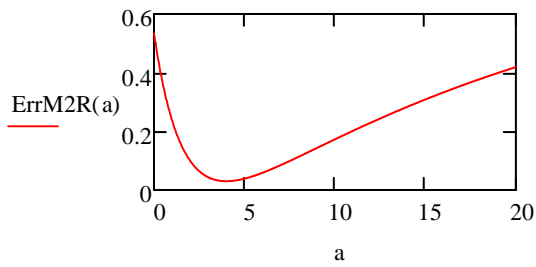
ErrM2R(a)



ErrM3R

## *Minimize the Error*

$\text{E2DR} := \text{E2R} = 4.005$ $\qquad \text{ErrM2R}(\text{E2R}) = 0.031$

$\text{E3DR} := \text{E3R} = \begin{pmatrix} 5.22 \\ -0.378 \end{pmatrix}$ $\qquad \text{ErrM3R}\left(\text{E3R}_1, \text{E3R}_2\right) = 0.03$
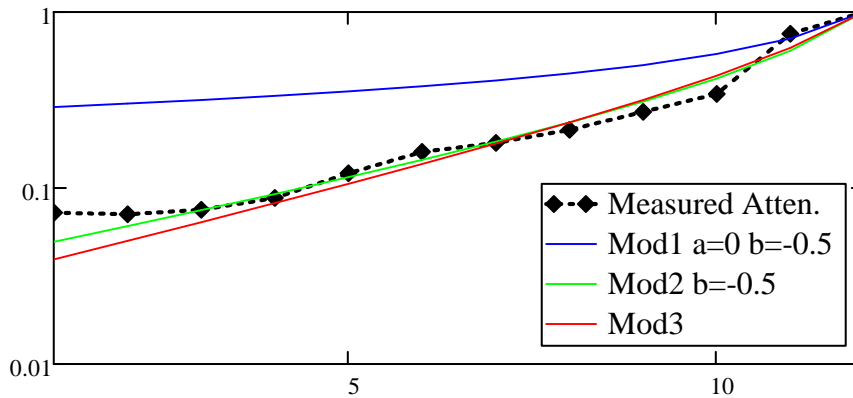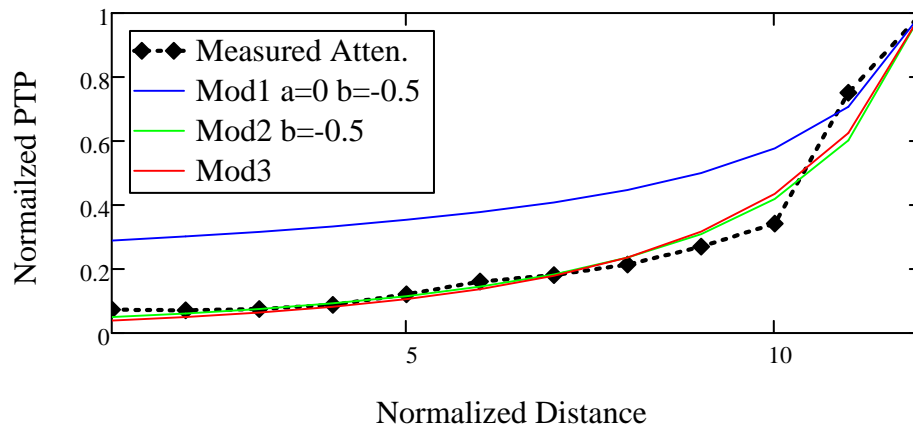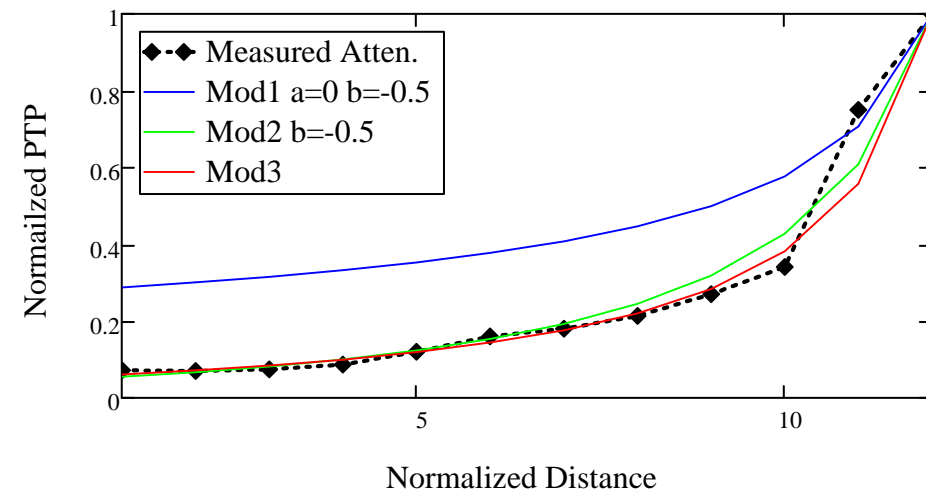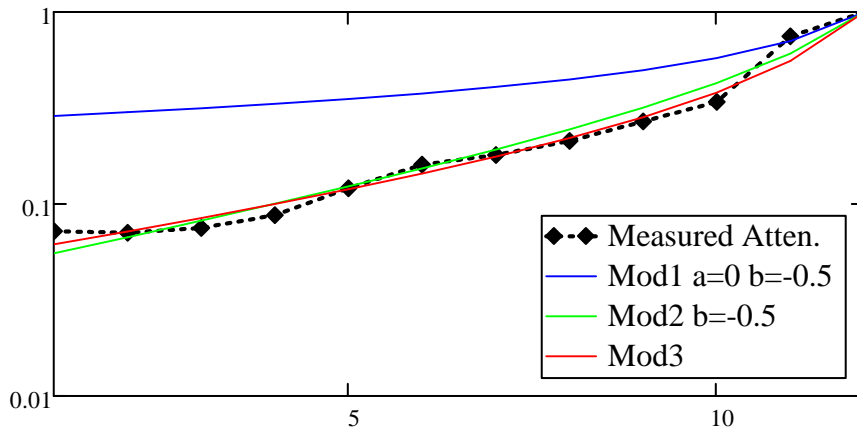




## *Coef of Determination R2 = (SST-SSE)/SST*

$\text{Rsq}_{2\text{DR}} := \text{Rsq}_{2\text{R}} = 0.968$

$\text{Rsq}_{3\text{DR}} := \text{Rsq}_{3\text{R}} = 0.969$

## Minimize the error: right and left simultaneously

E2D := E2 = 3.452　　　　　　ErrM2(E2) = 0.025

$E3D := E3 = \begin{pmatrix} 3.32 \\ -0.514 \end{pmatrix}$　　　　$ErrM3(E3_1, E3_2) = 0.025$

## Coef of Determination R2 = (SST-SSE)/SST

$Rsqsim_{2DR} := Rsqsim_{2R} = 0.964$

$Rsqsim_{3DR} := Rsqsim_{3R} = 0.964$

---

### Fitting - LOG scale



logErrM3R

## Minimize the Error

$logE2DR := logE2R = 3.743$　　　　$logErrM2R(logE2R) = 0.047$

$logE3DR := logE3R = \begin{pmatrix} 2.344 \\ -0.705 \end{pmatrix}$　　$logErrM3R(logE3R_1, logE3R_2) = 0.033$

### Coef of Determination R2 = (SST-SSE)/SST

$logRsq_{2DR} := logRsq_{2R} = 0.967$

$logRsq_{3DR} := logRsq_{3R} = 0.959$

---

🔺 ATTENUATION: TOTAL AREA DISPLACEMENT

🔽 FTC

$n := 1 .. 11$          $FTC_n := \sqrt{\dfrac{AreaDL_{n+1} \cdot AreaDR_n}{AreaDL_n \cdot AreaDR_{n+1}}}$
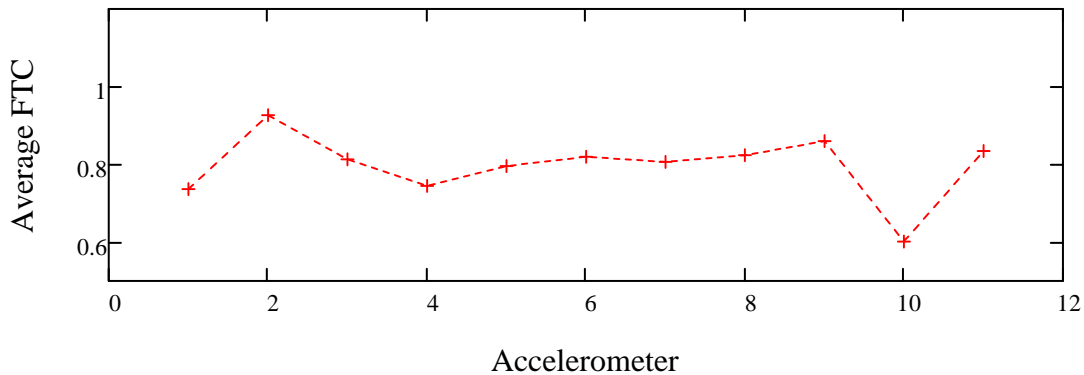


$i3_{min} := floor(linterp(f, c, 45kHz)) = 738$          $f_{i3_{min}} = 4.499 \times 10^4 \frac{1}{s}$

$i3_{max} := floor(linterp(f, c, 150kHz)) = 2.458 \times 10^3$          $f_{i3_{max}} = 1.5 \times 10^5 \frac{1}{s}$

***FTC with theoretical attenaution curves*** $FTCth_n := \sqrt{\dfrac{Mod2L(logE2DL, n+1) \cdot Mod2R(logE2DR, n)}{Mod2L(logE2DL, n) \cdot Mod2R(logE2DR, n+1)}}$

$$FTCth0_n := \sqrt{\frac{Mod2L(0,n+1) \cdot Mod2R(0,n)}{Mod2L(0,n) \cdot Mod2R(0,n+1)}}$$
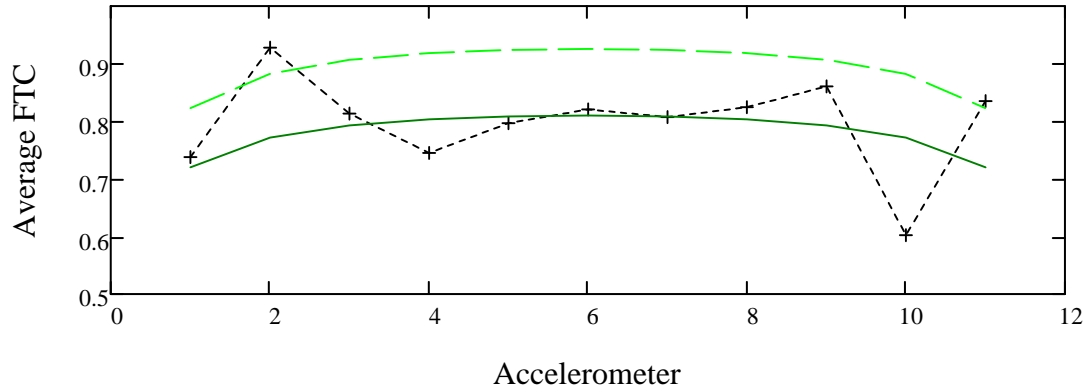


**Symmetric configuration:** $\quad q := 1..6$

$$FTCsym_q := \sqrt{\frac{AreaDL_{13-q} \cdot AreaDR_q}{AreaDL_q \cdot AreaDR_{13-q}}} \qquad FTCsymth_q := \sqrt{\frac{Mod2L(logE2DL, 13-q) \cdot Mod2R(logE2DR, q)}{Mod2L(logE2DL, q) \cdot Mod2R(logE2DR, 13-q)}}$$

$$FTCsymth0_q := \sqrt{\frac{Mod2L(0, 13-q) \cdot Mod2R(0, q)}{Mod2L(0, q) \cdot Mod2R(0, 13-q)}}$$
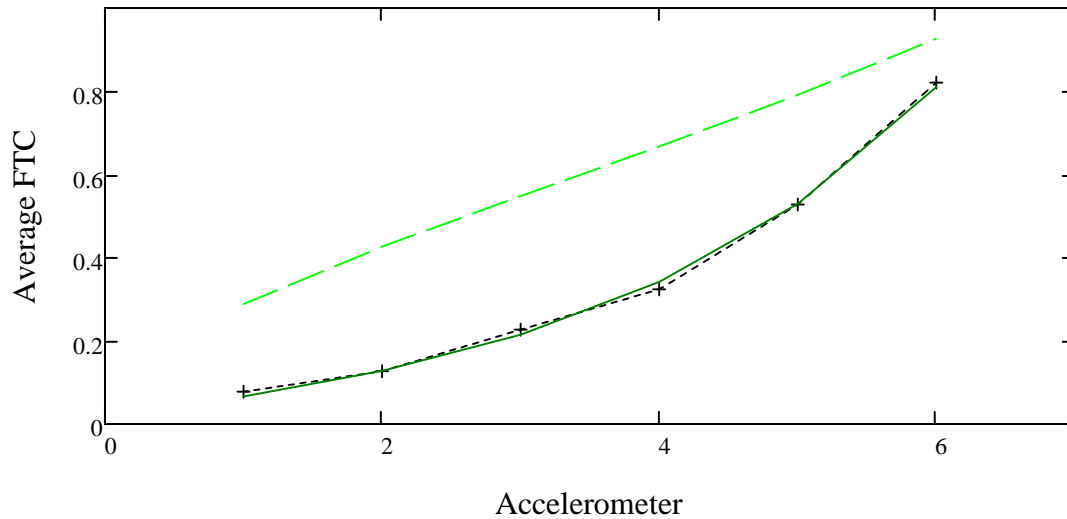


▲ FTC

▼ Total Area Displacement: $\alpha$ and Rsq vs. Distance

**Error Mod 2 LIN**   $\text{errM2R}(\alpha, k) := \left[ \sum\limits_{u = k}^{12} \left( \text{Mod2R}(\alpha, u) - XR_u \right)^2 \right]$

$\alpha := 10$   Given   $0 \leq \alpha \leq 100$   $\alpha_R(k) := \text{Minimize}(\text{errM2R}, \alpha)$

**Error Mod 2 LOG**   $\text{logerrM2R}(\alpha, k) := \left[ \sum\limits_{u = k}^{12} \left( \log(\text{Mod2R}(\alpha, u)) - \log\left(XR_u\right) \right)^2 \right]$

$\alpha := 10$   Given   $0 \leq \alpha \leq 100$   $\log\alpha_R(k) := \text{Minimize}(\text{logerrM2R}, \alpha)$
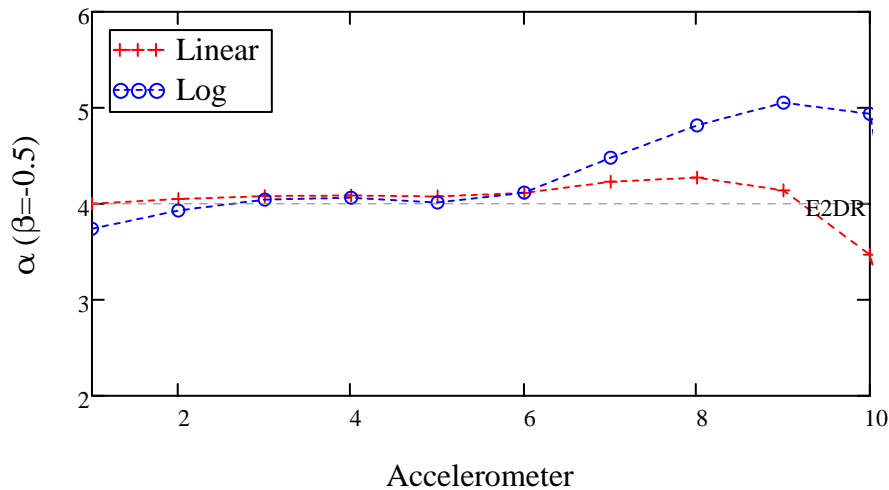


*Coef of Determination R2 = (SST-SSE)/SST*

*Mean*   $\text{Mean}_R(k) := \sum\limits_{u = k}^{12} \dfrac{XR_u}{12 - k + 1}$

*Total SofS*   $\text{sst}_R(k) := \sum\limits_{u = k}^{12} \left( XR_u - \text{Mean}_R(k) \right)^2$

*LIN - Residual SofS*   $\text{sse}_R(k) := \sum\limits_{u = k}^{12} \left( \text{Mod2R}\left(\alpha_R(k), u\right) - XR_u \right)^2$

*R-square value*   $\text{Rsqr}_R(k) := \dfrac{\text{sst}_R(k) - \text{sse}_R(k)}{\text{sst}_R(k)}$

*LOG - Residual SofS*

$$\text{logsse}_R(k) := \sum_{u=k}^{12} \left( \text{Mod2R}\left(\log\alpha_R(k), u\right) - XR_u \right)^2$$

*R-square values*

$$\text{logRsqr}_R(k) := \frac{\text{sst}_R(k) - \text{logsse}_R(k)}{\text{sst}_R(k)}$$



Total Area Displacement: α and Rsq vs. Distance

DAMPING RATIO

**Acceleration**

*LINEAR fitting*

$f_{iR1} = 1.111 \times 10^4 \, \frac{1}{s}$      $f_{iR2} = 1.837 \times 10^4 \, \frac{1}{s}$

**Model 2**    $\xi_{2AR} := \left(\frac{\lambda R}{2\pi}\right) \cdot \frac{E2AR}{m}$    $\xi_{2AR_{iR1}} = 0.138$    $\xi_{2AR_{iR2}} = 0.083$

**Model 3**    $\xi_{3AR} := \left(\frac{\lambda R}{2\pi}\right) \cdot \frac{E3AR_1}{m}$    $\xi_{3AR_{iR1}} = 0.274$    $\xi_{3AR_{iR2}} = 0.166$

*LOG fitting*

**Model 2**    $\log\xi_{2AR} := \left(\frac{\lambda R}{2\pi}\right) \cdot \frac{\log E2AR}{m}$    $\log\xi_{2AR_{iR1}} = 0.161$    $\log\xi_{2AR_{iR2}} = 0.097$

**Model 3**    $\log\xi_{3AR} := \left(\frac{\lambda R}{2\pi}\right) \cdot \frac{\log E3AR_1}{m}$    $\log\xi_{3AR_{iR1}} = 0.155$    $\log\xi_{3AR_{iR2}} = 0.094$

**Displacement**

$$f_{iR1} = 1.111 \times 10^4 \frac{1}{s} \qquad f_{iR2} = 1.837 \times 10^4 \frac{1}{s}$$

*Model 2*
$$\xi_{2DR} := \left(\frac{\lambda R}{2\pi}\right) \cdot \frac{E2DR}{m}$$
$$\xi_{2DR_{iR1}} = 0.1 \qquad \xi_{2DR_{iR2}} = 0.061$$

*Model 3*
$$\xi_{3DR} := \left(\frac{\lambda R}{2\pi}\right) \cdot \frac{E3DR_1}{m}$$
$$\xi_{3DR_{iR1}} = 0.131 \qquad \xi_{3DR_{iR2}} = 0.079$$

*LOG fitting*

*Model 2*
$$\log\xi_{2DR} := \left(\frac{\lambda R}{2\pi}\right) \cdot \frac{\log E2DR}{m}$$
$$\log\xi_{2DR_{iR1}} = 0.094 \qquad \log\xi_{2DR_{iR2}} = 0.057$$

*Model 3*
$$\log\xi_{3DR} := \left(\frac{\lambda R}{2\pi}\right) \cdot \frac{\log E3DR_1}{m}$$
$$\log\xi_{3DR_{iR1}} = 0.059 \qquad \log\xi_{3DR_{iR2}} = 0.035$$

---

🔺 DAMPING RATIO

🔻 AREA OF WINDOWED SPECTRA: ACCELERATION

*Start frequency*   $fi := 0Hz$
*End frequency*   $ff := 90000Hz$

*Window widths*
$$WW := \begin{pmatrix} 2000 \\ 4000 \\ 7000 \\ 10000 \\ 15000 \end{pmatrix} \cdot Hz \qquad w := 1 .. \text{length}(WW) \qquad iw := \text{floor}\left(\frac{WW}{2 \cdot \Delta f}\right)$$

$$c_{i3} := i3$$

$$fmin_w := fi + \frac{WW_w}{2} \qquad imin := \text{floor}(\text{linterp}(f, c, fmin))$$

$$fmax_w := ff - \frac{WW_w}{2} \qquad imax := \text{floor}(\text{linterp}(f, c, fmax))$$

*Resolution*   $res := 10$   $\underset{\sim\sim\sim\sim}{imin} := \left(\text{floor}\left(\frac{imin}{res}\right) + 1\right) \cdot res$   $\underset{\sim\sim\sim\sim}{imax} := \text{floor}\left(\frac{imax}{res}\right) \cdot res$

*Indices for the different window widths*

$$c1 := imin_1, imin_1 + res .. imax_1 \qquad imin_1 = 20$$

$$c2 := imin_2, imin_2 + res .. imax_2 \qquad imin_2 = 40$$

$$c3 := imin_3, imin_3 + res .. imax_3 \qquad imin_3 = 60$$

$$c4 := imin_4, imin_4 + res .. imax_4 \qquad imin_4 = 90$$

$$c5 := imin_5, imin_5 + res .. imax_5 \qquad imin_5 = 130$$

## Area of windowed spectrum

$$\text{WAreaR}(c, \text{wid}, k) := \sum_{n = c-\text{wid}}^{c+\text{wid}} \left[ \frac{\left(\text{MagR}_{n, k} + \text{MagR}_{n+1, k}\right)}{2} \cdot \Delta f \right]$$

$$\text{WAR1}_{c1, k} := \text{WAreaR}\left(c1, iw_1, k\right) \qquad \text{WAR2}_{c2, k} := \text{WAreaR}\left(c2, iw_2, k\right)$$

$$\text{WAR3}_{c3, k} := \text{WAreaR}\left(c3, iw_3, k\right) \qquad \text{WAR4}_{c4, k} := \text{WAreaR}\left(c4, iw_4, k\right)$$

$$\text{WAR5}_{c5, k} := \text{WAreaR}\left(c5, iw_5, k\right)$$

$$h := 1$$
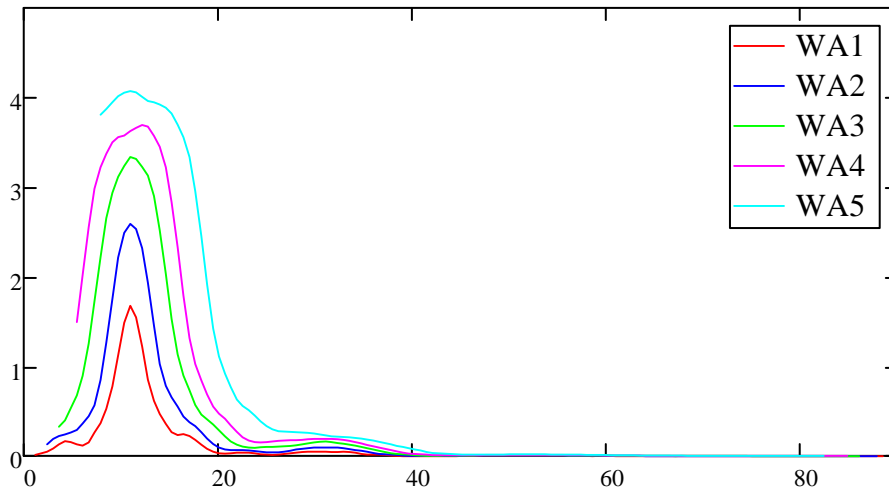


## Measured attenuation

$$\text{AttR1}_{c1, k} := \frac{\text{WAR1}_{c1, k}}{\text{WAR1}_{c1, 12}} \qquad \text{XR1} := \text{AttR1}$$

$$\text{AttR2}_{c2, k} := \frac{\text{WAR2}_{c2, k}}{\text{WAR2}_{c2, 12}} \qquad \text{XR2} := \text{AttR2}$$

$$\text{AttR3}_{c3, k} := \frac{\text{WAR3}_{c3, k}}{\text{WAR3}_{c3, 12}} \qquad \text{XR3} := \text{AttR3}$$

$$\text{AttR4}_{c4, k} := \frac{\text{WAR4}_{c4, k}}{\text{WAR4}_{c4, 12}} \qquad \text{XR4} := \text{AttR4}$$

$$\text{AttR5}_{c5, k} := \frac{\text{WAR5}_{c5, k}}{\text{WAR5}_{c5, 12}} \qquad \text{XR5} := \text{AttR5}$$

**Call refecrence file: "Attenuation - Area of Window - Linear"**

**Attenuation Coefficients and Minimized Error**

**Model 2**          **Model 3**

$\alpha AR2_1 := \alpha R2_1$          $\alpha AR3_1 := \alpha R3_1$          $\beta AR_1 := \beta R_1$

$\alpha AR2_2 := \alpha R2_2$          $\alpha AR3_2 := \alpha R3_2$          $\beta AR_2 := \beta R_2$

$\alpha AR2_3 := \alpha R2_3$          $\alpha AR3_3 := \alpha R3_3$          $\beta AR_3 := \beta R_3$

$\alpha AR2_4 := \alpha R2_4$          $\alpha AR3_4 := \alpha R3_4$          $\beta AR_4 := \beta R_4$

$\alpha AR2_5 := \alpha R2_5$          $\alpha AR3_5 := \alpha R3_5$          $\beta AR_5 := \beta R_5$

Fitting model 2 - $\alpha$ values - Right



Frequency (kHz)
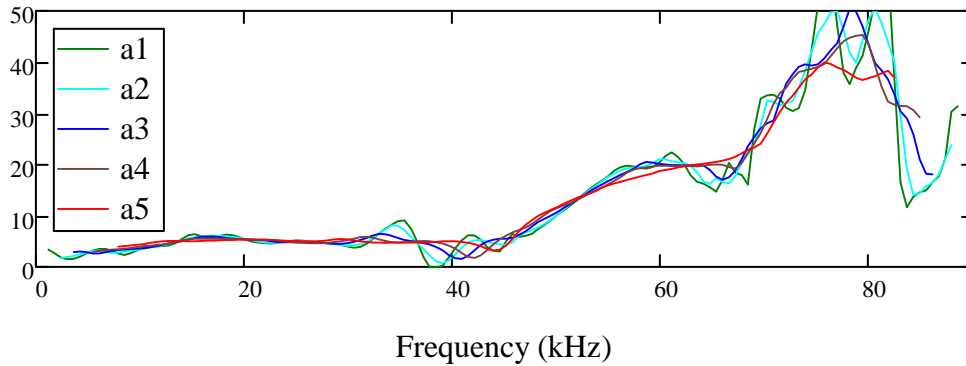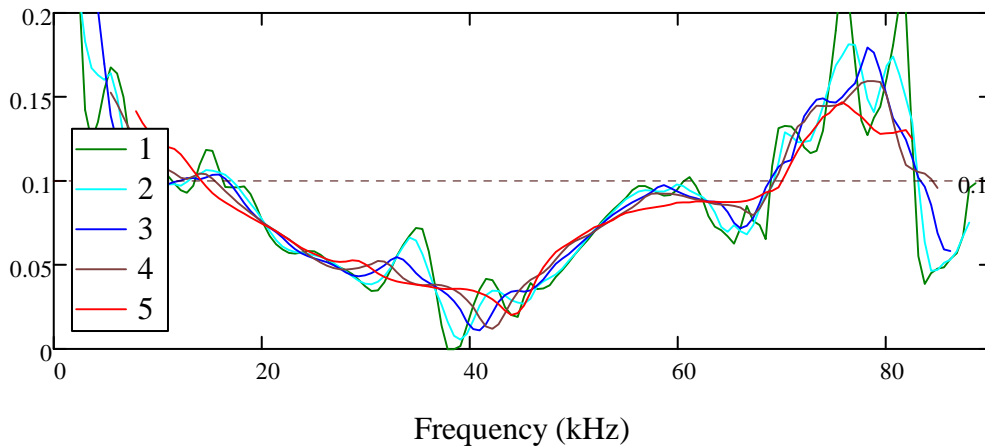
Fitting model 3 - $\alpha$ values - Right



Frequency (kHz)

## Fitting model 3 - β values - Right



**Damping Ratio (Assuming Vph = Vr)**

**Model 2**

$$\xi RA2_1 := \xi R2_1$$

$$\xi RA2_2 := \xi R2_2$$

$$\xi RA2_3 := \xi R2_3$$

$$\xi RA2_4 := \xi R2_4$$

$$\xi RA2_5 := \xi R2_5$$

**Model 3**

$$\xi RA3_1 := \xi R3_1$$

$$\xi RA3_2 := \xi R3_2$$

$$\xi RA3_3 := \xi R3_3$$

$$\xi RA3_4 := \xi R3_4$$

$$\xi RA3_5 := \xi R3_5$$

## Fitting model 2 - ξ values - Right

## Fitting model 3 - ξ values - Right



Frequency (kHz)
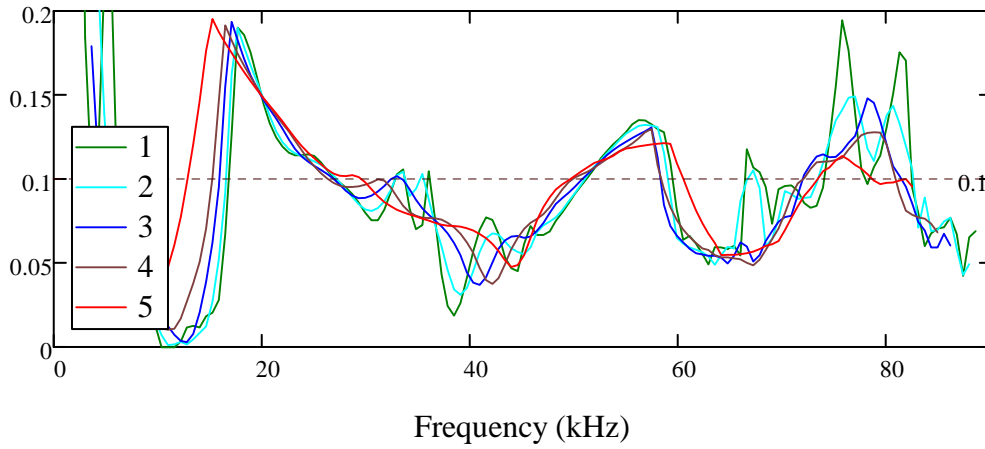
**Maximum Error**

$$\text{MaxErr2} := \max\left(\text{errR2}_1, \text{errR2}_2, \text{errR2}_3, \text{errR2}_4, \text{errR2}_5, \text{errL2}_1, \text{errL2}_2, \text{errL2}_3, \text{errL2}_4, \text{errL2}_5\right) = 27.455$$

$$\text{MaxErr3} := \max\left(\text{errR3}_1, \text{errR3}_2, \text{errR3}_3, \text{errR3}_4, \text{errR3}_5, \text{errL3}_1, \text{errL3}_2, \text{errL3}_3, \text{errL3}_4, \text{errL3}_5\right) = 25.258$$

**Error Normalized to MaxErrR**

## Norm. Error for Model 2 - Right



Frequency (kHz)
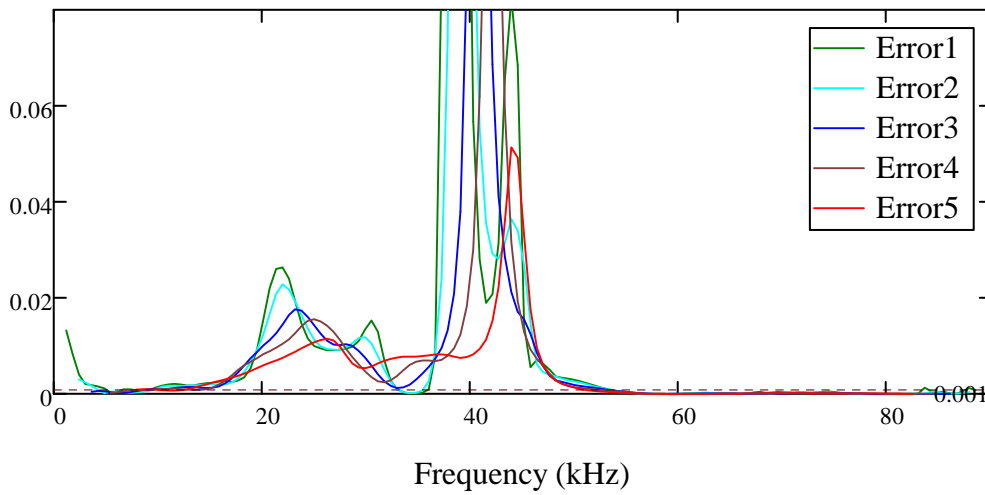
## Norm. Error for Model 3 - Right
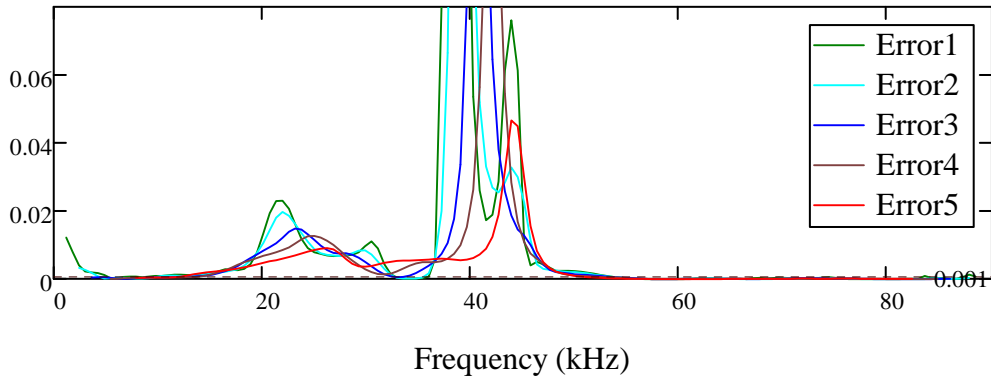
*Model 2*

$$RsqAR2_1 := RsqR2_1 \qquad RsqAR2_2 := RsqR2_2$$

$$RsqAR2_3 := RsqR2_3 \qquad RsqAR2_4 := RsqR2_4$$

$$RsqAR2_5 := RsqR2_5$$

*Model 3*

$$RsqAR3_1 := RsqR3_1 \qquad RsqAR3_2 := RsqR3_2$$

$$RsqAR3_3 := RsqR3_3 \qquad RsqAR3_4 := RsqR3_4$$

$$RsqAR3_5 := RsqR3_5$$

## R-square for Model 2 - Right
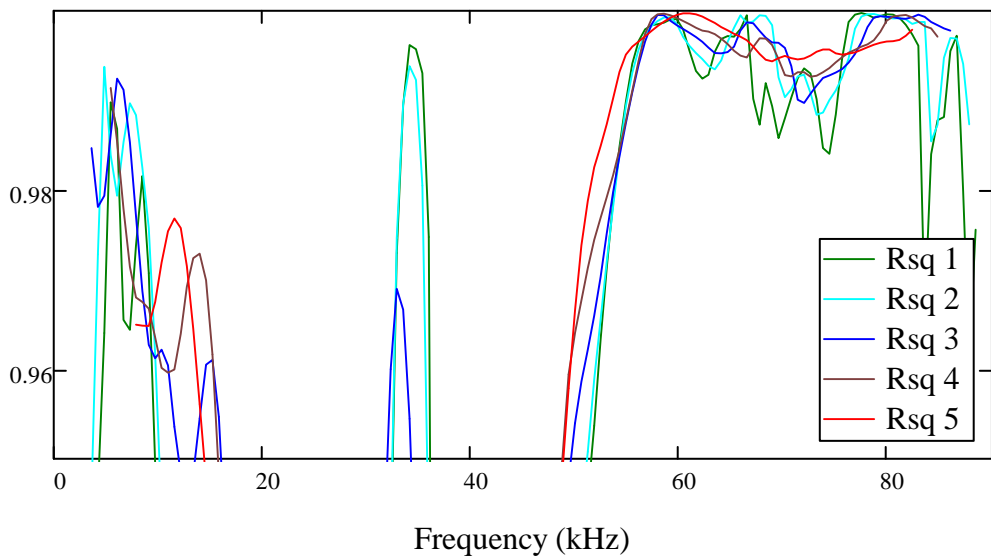
## R-square for Model 3 - Right



Frequency (kHz)

---
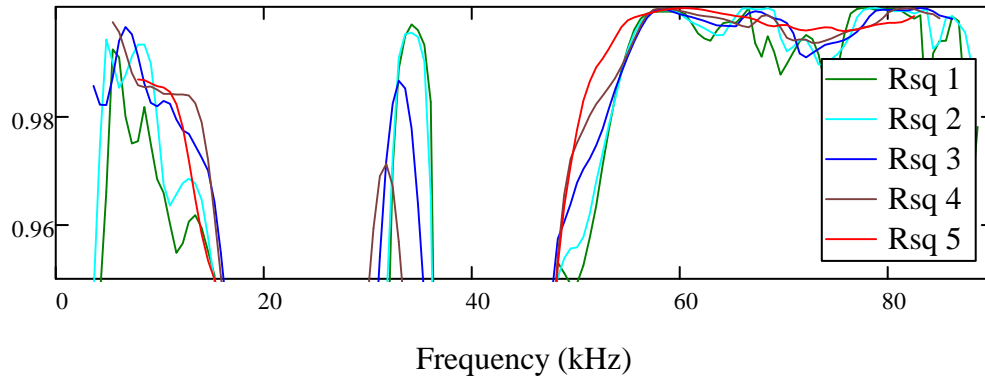
***Call refecrence file: "Attenuation - Area of Window - Log"***    --> similar to previous section

▲ AREA OF WINDOWED SPECTRA: ACCELERATION

▶ AREA OF WINDOWED SPECTRA: DISPLACEMENT

--> similar to acceleration

# Reference File: "Attenuation"

---
***Theoretical Attenuation***
---

$1/\ \alpha = 0,\ \beta = -0.5$    $\mathrm{Mod1R}(k) := \left( \dfrac{D - X_k}{\Delta X} \right)^{-0.5}$

$2/\ \alpha = ?,\ \beta = -0.5$    $\mathrm{Mod2R}(\alpha, k) := \left( \dfrac{D - X_k}{\Delta X} \right)^{-0.5} \cdot e^{\frac{-\alpha}{m} \cdot (D - X_k - \Delta X)}$

$3/\ \alpha = ?,\ \beta = ?$    $\mathrm{Mod3R}(\alpha, \beta, k) := \left( \dfrac{D - X_k}{\Delta X} \right)^{\beta} \cdot e^{\frac{-\alpha}{m} \cdot (D - X_k - \Delta X)}$

---
***Fitting - LINEAR scale***
---

### *Error between Theoretical model and Measured attenuation*

$\mathrm{ErrM1R} := \left[ \displaystyle\sum_{k=1}^{12} \left( \mathrm{Mod1R}(k) - XR_k \right)^2 \right] = \blacksquare$

$\mathrm{ErrM2R}(\alpha) := \left[ \displaystyle\sum_{k=1}^{12} \left( \mathrm{Mod2R}(\alpha, k) - XR_k \right)^2 \right]$

$\mathrm{ErrM3R}(\alpha, \beta) := \left[ \displaystyle\sum_{k=1}^{12} \left( \mathrm{Mod3R}(\alpha, \beta, k) - XR_k \right)^2 \right]$

### *Minimize the Error*

$\alpha := 10 \qquad \beta := -0.5$

Given $\qquad 0 \le \alpha \le 100 \qquad -1 \le \beta \le 0$

$\mathrm{E2R} := \mathrm{Minimize}(\mathrm{ErrM2R}, \alpha) \qquad \mathrm{E2R} = \blacksquare \qquad\qquad \mathrm{ErrM2R}(\mathrm{E2R}) = \blacksquare$

Given $\qquad 0 \le \alpha \le 100 \qquad -1 \le \beta \le 0$

$\mathrm{E3R} := \mathrm{Minimize}(\mathrm{ErrM3R}, \alpha, \beta) \qquad \mathrm{E3R} = \blacksquare \qquad\qquad \mathrm{ErrM3R}\left( \mathrm{E3R}_1, \mathrm{E3R}_2 \right) = \blacksquare$

### *Coef of Determination R2 = (SST-SSE)/SST*

*Total SofS* $\qquad$ $\mathrm{SST_R} := \displaystyle\sum_{k=1}^{12} \left(\mathrm{XR_k} - \mathrm{mean(XR)}\right)^2 =$ ∎

*Regression SofS* $\qquad$ *Model 2* $\quad$ $\mathrm{SSR_{2R}} := \displaystyle\sum_{k=1}^{12} \left(\mathrm{Mod2R(E2R,k)} - \mathrm{mean(XR)}\right)^2 =$ ∎

$\qquad\qquad\qquad$ *Model 3* $\quad$ $\mathrm{SSR_{3R}} := \displaystyle\sum_{k=1}^{12} \left(\mathrm{Mod3R}\!\left(\mathrm{E3R_1}, \mathrm{E3R_2}, k\right) - \mathrm{mean(XR)}\right)^2 =$ ∎

*Residual SofS* $\qquad$ *Model 2* $\quad$ $\mathrm{SSE_{2R}} := \displaystyle\sum_{k=1}^{12} \left(\mathrm{Mod2R(E2R,k)} - \mathrm{XR_k}\right)^2 =$ ∎

$\qquad\qquad\qquad$ *Model 3* $\quad$ $\mathrm{SSE_{3R}} := \displaystyle\sum_{k=1}^{12} \left(\mathrm{Mod3R}\!\left(\mathrm{E3R_1}, \mathrm{E3R_2}, k\right) - \mathrm{XR_k}\right)^2 =$ ∎

*R-square values* $\qquad$ *Model 2* $\quad$ $\mathrm{Rsq_{2R}} := \dfrac{\mathrm{SST_R} - \mathrm{SSE_{2R}}}{\mathrm{SST_R}} =$ ∎

$\qquad\qquad\qquad$ *Model 3* $\quad$ $\mathrm{Rsq_{3R}} := \dfrac{\mathrm{SST_R} - \mathrm{SSE_{3R}}}{\mathrm{SST_R}} =$ ∎

$$\boxed{\textbf{\textit{Fitting - LOG scale}}}$$

### *Error between Theoretical model and Measured attenuation*

$\mathrm{logErrM1R} := \left[ \displaystyle\sum_{k=1}^{12} \left(\log(\mathrm{Mod1R}(k)) - \log\!\left(\mathrm{XR_k}\right)\right)^2 \right] =$ ∎

$\mathrm{logErrM2R}(\alpha) := \left[ \displaystyle\sum_{k=1}^{12} \left(\log(\mathrm{Mod2R}(\alpha,k)) - \log\!\left(\mathrm{XR_k}\right)\right)^2 \right]$

$\mathrm{logErrM3R}(\alpha, \beta) := \left[ \displaystyle\sum_{k=1}^{12} \left(\log(\mathrm{Mod3R}(\alpha, \beta, k)) - \log\!\left(\mathrm{XR_k}\right)\right)^2 \right]$

### *Minimize the Error*

Given $\qquad$ $0 \le \alpha \le 100$

$\mathrm{logE2R} := \mathrm{Minimize}(\mathrm{logErrM2R}, \alpha)$ $\qquad$ $\mathrm{logE2R} =$ ∎ $\qquad\qquad$ $\mathrm{logErrM2R}(\mathrm{logE2R}) =$ ∎

Given $\quad 0 \leq \alpha \leq 100 \qquad -1 \leq \beta \leq 0$

$logE3R := \text{Minimize}(logErrM3R, \alpha, \beta) \quad logE3R = \blacksquare \qquad\qquad logErrM3R\left(logE3R_1, logE3R_2\right) = \blacksquare$

## **Coef of Determination R2 = (SST-SSE)/SST**

*Residual SofS* $\qquad$ *Model 2* $\qquad logSSE_{2R} := \displaystyle\sum_{k=1}^{12} \left(Mod2R(logE2R, k) - XR_k\right)^2 = \blacksquare$

$\qquad\qquad\qquad$ *Model 3* $\qquad logSSE_{3R} := \displaystyle\sum_{k=1}^{12} \left(Mod3R\left(logE3R_1, logE3R_2, k\right) - XR_k\right)^2 = \blacksquare$

*R-square values* $\qquad$ *Model 2* $\qquad logRsq_{2R} := \dfrac{SST_R - logSSE_{2R}}{SST_R} = \blacksquare$

$\qquad\qquad\qquad\qquad\qquad\qquad logRsq_{3R} := \dfrac{SST_R - logSSE_{3R}}{SST_R} = \blacksquare$

# Reference File: "Attenuation - Area of Window - Linear"

*Error between Theoretical model and Measured attenuation*

*Model 2*   $\displaystyle \mathrm{ErrR2}_1(\alpha, c1) := \left[\sum_{k\,=\,1}^{12} \left(\mathbf{Mod2R}(\alpha, k) - \mathrm{XR1}_{c1,\,k}\right)^2\right]$

$\displaystyle \mathrm{ErrR2}_2(\alpha, c2) := \left[\sum_{k\,=\,1}^{12} \left(\mathbf{Mod2R}(\alpha, k) - \mathrm{XR2}_{c2,\,k}\right)^2\right]$

$\displaystyle \mathrm{ErrR2}_3(\alpha, c3) := \left[\sum_{k\,=\,1}^{12} \left(\mathbf{Mod2R}(\alpha, k) - \mathrm{XR3}_{c3,\,k}\right)^2\right]$

$\displaystyle \mathrm{ErrR2}_4(\alpha, c4) := \left[\sum_{k\,=\,1}^{12} \left(\mathbf{Mod2R}(\alpha, k) - \mathrm{XR4}_{c4,\,k}\right)^2\right]$

$\displaystyle \mathrm{ErrR2}_5(\alpha, c5) := \left[\sum_{k\,=\,1}^{12} \left(\mathbf{Mod2R}(\alpha, k) - \mathrm{XR5}_{c5,\,k}\right)^2\right]$

*Model 3*   $\displaystyle \mathrm{ErrR3}_1(\alpha, \beta, c1) := \left[\sum_{k\,=\,1}^{12} \left(\mathbf{Mod3R}(\alpha, \beta, k) - \mathrm{XR1}_{c1,\,k}\right)^2\right]$

$\displaystyle \mathrm{ErrR3}_2(\alpha, \beta, c2) := \left[\sum_{k\,=\,1}^{12} \left(\mathbf{Mod3R}(\alpha, \beta, k) - \mathrm{XR2}_{c2,\,k}\right)^2\right]$

$\displaystyle \mathrm{ErrR3}_3(\alpha, \beta, c3) := \left[\sum_{k\,=\,1}^{12} \left(\mathbf{Mod3R}(\alpha, \beta, k) - \mathrm{XR3}_{c3,\,k}\right)^2\right]$

$\displaystyle \mathrm{ErrR3}_4(\alpha, \beta, c4) := \left[\sum_{k\,=\,1}^{12} \left(\mathbf{Mod3R}(\alpha, \beta, k) - \mathrm{XR4}_{c4,\,k}\right)^2\right]$

$\displaystyle \mathrm{ErrR3}_5(\alpha, \beta, c5) := \left[\sum_{k\,=\,1}^{12} \left(\mathbf{Mod3R}(\alpha, \beta, k) - \mathrm{XR5}_{c5,\,k}\right)^2\right]$

*Minimizing the Error*

$\alpha := 10 \qquad \beta := -0.5$

*Model 2*      Given      $0 \le \alpha \le 100$      $-1 \le \beta \le 0$      $\mathbf{meR2}_1(c1) := \mathrm{Minimize}\left(\mathrm{ErrR2}_1, \alpha\right)$

$$\text{Given} \quad 0 \leq \alpha \leq 100 \quad -1 \leq \beta \leq 0 \quad \text{meR2}_2(c2) := \text{Minimize}\left(\text{ErrR2}_2, \alpha\right)$$

$$\text{Given} \quad 0 \leq \alpha \leq 100 \quad -1 \leq \beta \leq 0 \quad \text{meR2}_3(c3) := \text{Minimize}\left(\text{ErrR2}_3, \alpha\right)$$

$$\text{Given} \quad 0 \leq \alpha \leq 100 \quad -1 \leq \beta \leq 0 \quad \text{meR2}_4(c4) := \text{Minimize}\left(\text{ErrR2}_4, \alpha\right)$$

$$\text{Given} \quad 0 \leq \alpha \leq 100 \quad -1 \leq \beta \leq 0 \quad \text{meR2}_5(c5) := \text{Minimize}\left(\text{ErrR2}_5, \alpha\right)$$

*Model 3*

$$\text{Given} \quad 0 \leq \alpha \leq 100 \quad -1 \leq \beta \leq 0 \quad \text{meR3}_1(c1) := \text{Minimize}\left(\text{ErrR3}_1, \alpha, \beta\right)$$

$$\text{Given} \quad 0 \leq \alpha \leq 100 \quad -1 \leq \beta \leq 0 \quad \text{meR3}_2(c2) := \text{Minimize}\left(\text{ErrR3}_2, \alpha, \beta\right)$$

$$\text{Given} \quad 0 \leq \alpha \leq 100 \quad -1 \leq \beta \leq 0 \quad \text{meR3}_3(c3) := \text{Minimize}\left(\text{ErrR3}_3, \alpha, \beta\right)$$

$$\text{Given} \quad 0 \leq \alpha \leq 100 \quad -1 \leq \beta \leq 0 \quad \text{meR3}_4(c4) := \text{Minimize}\left(\text{ErrR3}_4, \alpha, \beta\right)$$

$$\text{Given} \quad 0 \leq \alpha \leq 100 \quad -1 \leq \beta \leq 0 \quad \text{meR3}_5(c5) := \text{Minimize}\left(\text{ErrR3}_5, \alpha, \beta\right)$$

### Attenuation Coefficients and Minimized Error

*Model 2*

$$\alpha R2_{1_{c1}} := \text{meR2}_1(c1) \quad \text{errR2}_{1_{c1}} := \text{ErrR2}_1\left(\alpha R2_{1_{c1}}, c1\right)$$

$$\alpha R2_{2_{c2}} := \text{meR2}_2(c2) \quad \text{errR2}_{2_{c2}} := \text{ErrR2}_2\left(\alpha R2_{2_{c2}}, c2\right)$$

$$\alpha R2_{3_{c3}} := \text{meR2}_3(c3) \quad \text{errR2}_{3_{c3}} := \text{ErrR2}_3\left(\alpha R2_{3_{c3}}, c3\right)$$

$$\alpha R2_{4_{c4}} := \text{meR2}_4(c4) \quad \text{errR2}_{4_{c4}} := \text{ErrR2}_4\left(\alpha R2_{4_{c4}}, c4\right)$$

$$\alpha R2_{5_{c5}} := \text{meR2}_5(c5) \quad \text{errR2}_{5_{c5}} := \text{ErrR2}_5\left(\alpha R2_{5_{c5}}, c5\right)$$

### Model 3

$$\alpha R3_{1_{c1}} := \text{meR3}_1(c1)_1 \quad \beta R_{1_{c1}} := \text{meR3}_1(c1)_2 \quad \text{errR3}_{1_{c1}} := \text{ErrR3}_1\left(\alpha R3_{1_{c1}}, \beta R_{1_{c1}}, c1\right)$$

$$\alpha R3_{2_{c2}} := \text{meR3}_2(c2)_1 \quad \beta R_{2_{c2}} := \text{meR3}_2(c2)_2 \quad \text{errR3}_{2_{c2}} := \text{ErrR3}_2\left(\alpha R3_{2_{c2}}, \beta R_{2_{c2}}, c2\right)$$

$$\alpha R3_{3_{c3}} := \text{meR3}_3(c3)_1 \quad \beta R_{3_{c3}} := \text{meR3}_3(c3)_2 \quad \text{errR3}_{3_{c3}} := \text{ErrR3}_3\left(\alpha R3_{3_{c3}}, \beta R_{3_{c3}}, c3\right)$$

$$\alpha R3_{4_{c4}} := \text{meR3}_4(c4)_1 \quad \beta R_{4_{c4}} := \text{meR3}_4(c4)_2 \quad \text{errR3}_{4_{c4}} := \text{ErrR3}_4\left(\alpha R3_{4_{c4}}, \beta R_{4_{c4}}, c4\right)$$

$$\alpha R3_{5_{c5}} := \text{meR3}_5(c5)_1 \quad \beta R_{5_{c5}} := \text{meR3}_5(c5)_2 \quad \text{errR3}_{5_{c5}} := \text{ErrR3}_5\left(\alpha R3_{5_{c5}}, \beta R_{5_{c5}}, c5\right)$$

### Damping Ratio

*Model 2* 　　　　　　　　　　　*Model 3*

$$\xi R2_{1_{c1}} := \left(\frac{\lambda R_{c1}}{2\pi}\right) \cdot \frac{\alpha R2_{1_{c1}}}{m} \qquad \xi R3_{1_{c1}} := \left(\frac{\lambda R_{c1}}{2\pi}\right) \cdot \frac{\alpha R3_{1_{c1}}}{m}$$

$$\xi R2_{2_{c2}} := \left(\frac{\lambda R_{c2}}{2\pi}\right) \cdot \frac{\alpha R2_{2_{c2}}}{m} \qquad \xi R3_{2_{c2}} := \left(\frac{\lambda R_{c2}}{2\pi}\right) \cdot \frac{\alpha R3_{2_{c2}}}{m}$$

$$\xi R2_{3_{c3}} := \left(\frac{\lambda R_{c3}}{2\pi}\right) \cdot \frac{\alpha R2_{3_{c3}}}{m} \qquad \xi R3_{3_{c3}} := \left(\frac{\lambda R_{c3}}{2\pi}\right) \cdot \frac{\alpha R3_{3_{c3}}}{m}$$

$$\xi R2_{4_{c4}} := \left(\frac{\lambda R_{c4}}{2\pi}\right) \cdot \frac{\alpha R2_{4_{c4}}}{m} \qquad \xi R3_{4_{c4}} := \left(\frac{\lambda R_{c4}}{2\pi}\right) \cdot \frac{\alpha R3_{4_{c4}}}{m}$$

$$\xi R2_{5_{c5}} := \left(\frac{\lambda R_{c5}}{2\pi}\right) \cdot \frac{\alpha R2_{5_{c5}}}{m} \qquad \xi R3_{5_{c5}} := \left(\frac{\lambda R_{c5}}{2\pi}\right) \cdot \frac{\alpha R3_{5_{c5}}}{m}$$

## Coefficient of Determination at each frequency

**Means**
$$avXR1_{c1} := \sum_{k=1}^{12} \left(\frac{1}{12} XR1_{c1,k}\right) \qquad avXR4_{c4} := \sum_{k=1}^{12} \left(\frac{1}{12} XR4_{c4,k}\right)$$

$$avXR2_{c2} := \sum_{k=1}^{12} \left(\frac{1}{12} XR2_{c2,k}\right) \qquad avXR5_{c5} := \sum_{k=1}^{12} \left(\frac{1}{12} XR5_{c5,k}\right)$$

$$avXR3_{c3} := \sum_{k=1}^{12} \left(\frac{1}{12} XR3_{c3,k}\right)$$

**Total SofS**
$$SSTR1_{c1} := \sum_{k=1}^{12} \left(XR1_{c1,k} - avXR1_{c1}\right)^2$$

$$SSTR2_{c2} := \sum_{k=1}^{12} \left(XR2_{c2,k} - avXR2_{c2}\right)^2$$

$$SSTR3_{c3} := \sum_{k=1}^{12} \left(XR3_{c3,k} - avXR3_{c3}\right)^2$$

$$SSTR4_{c4} := \sum_{k=1}^{12} \left(XR4_{c4,k} - avXR4_{c4}\right)^2$$

$$SSTR5_{c5} := \sum_{k=1}^{12} \left(XR5_{c5,k} - avXR5_{c5}\right)^2$$

**Regression SofS**

*Model 2*

$$SSRR2_{1_{c1}} := \sum_{k=1}^{12} \left( Mod2R\left( \alpha R2_{1_{c1}}, k \right) - avXR1_{c1} \right)^2$$

$$SSRR2_{2_{c2}} := \sum_{k=1}^{12} \left( Mod2R\left( \alpha R2_{2_{c2}}, k \right) - avXR2_{c2} \right)^2$$

$$SSRR2_{3_{c3}} := \sum_{k=1}^{12} \left( Mod2R\left( \alpha R2_{3_{c3}}, k \right) - avXR3_{c3} \right)^2$$

$$SSRR2_{4_{c4}} := \sum_{k=1}^{12} \left( Mod2R\left( \alpha R2_{4_{c4}}, k \right) - avXR4_{c4} \right)^2$$

$$SSRR2_{5_{c5}} := \sum_{k=1}^{12} \left( Mod2R\left( \alpha R2_{5_{c5}}, k \right) - avXR5_{c5} \right)^2$$

*Model 3*

$$SSRR3_{1_{c1}} := \sum_{k=1}^{12} \left( Mod3R\left( \alpha R3_{1_{c1}}, \beta R1_{c1}, k \right) - avXR1_{c1} \right)^2$$

$$SSRR3_{2_{c2}} := \sum_{k=1}^{12} \left( Mod3R\left( \alpha R3_{2_{c2}}, \beta R2_{c2}, k \right) - avXR2_{c2} \right)^2$$

$$SSRR3_{3_{c3}} := \sum_{k=1}^{12} \left( Mod3R\left( \alpha R3_{3_{c3}}, \beta R3_{c3}, k \right) - avXR3_{c3} \right)^2$$

$$SSRR3_{4_{c4}} := \sum_{k=1}^{12} \left( Mod3R\left( \alpha R3_{4_{c4}}, \beta R4_{c4}, k \right) - avXR4_{c4} \right)^2$$

$$SSRR3_{5_{c5}} := \sum_{k=1}^{12} \left( Mod3R\left( \alpha R3_{5_{c5}}, \beta R5_{c5}, k \right) - avXR5_{c5} \right)^2$$

**Residual SofS**

*Model 2*

$$SSER2_{1_{c1}} := \sum_{k=1}^{12} \left( Mod2R\left( \alpha R2_{1_{c1}}, k \right) - XR1_{c1, k} \right)^2$$

$$SSER2_{2_{c2}} := \sum_{k=1}^{12} \left( Mod2R\left( \alpha R2_{2_{c2}}, k \right) - XR2_{c2, k} \right)^2$$

$$SSER2_{3_{c3}} := \sum_{k=1}^{12} \left( Mod2R\left( \alpha R2_{3_{c3}}, k \right) - XR3_{c3, k} \right)^2$$

$$SSER2_{4_{c4}} := \sum_{k=1}^{12} \left( Mod2R\left( \alpha R2_{4_{c4}}, k \right) - XR4_{c4, k} \right)^2$$

241

$$\text{SSER2}_{5_{c5}} := \sum_{k=1}^{12} \left( \text{Mod2R}\left(\alpha\text{R2}_{5_{c5}}, k\right) - \text{XR5}_{c5,k} \right)^2$$

*Model 3*
$$\text{SSER3}_{1_{c1}} := \sum_{k=1}^{12} \left( \text{Mod3R}\left(\alpha\text{R3}_{1_{c1}}, \beta\text{R1}_{c1}, k\right) - \text{XR1}_{c1,k} \right)^2$$

$$\text{SSER3}_{2_{c2}} := \sum_{k=1}^{12} \left( \text{Mod3R}\left(\alpha\text{R3}_{2_{c2}}, \beta\text{R2}_{c2}, k\right) - \text{XR2}_{c2,k} \right)^2$$

$$\text{SSER3}_{3_{c3}} := \sum_{k=1}^{12} \left( \text{Mod3R}\left(\alpha\text{R3}_{3_{c3}}, \beta\text{R3}_{c3}, k\right) - \text{XR3}_{c3,k} \right)^2$$

$$\text{SSER3}_{4_{c4}} := \sum_{k=1}^{12} \left( \text{Mod3R}\left(\alpha\text{R3}_{4_{c4}}, \beta\text{R4}_{c4}, k\right) - \text{XR4}_{c4,k} \right)^2$$

$$\text{SSER3}_{5_{c5}} := \sum_{k=1}^{12} \left( \text{Mod3R}\left(\alpha\text{R3}_{5_{c5}}, \beta\text{R5}_{c5}, k\right) - \text{XR5}_{c5,k} \right)^2$$

## Coef of Determination R2 = (SST-SSE)/SST

*Model 2*
$$\text{RsqR2}_{1_{c1}} := \frac{\text{SSTR}_{1_{c1}} - \text{SSER2}_{1_{c1}}}{\text{SSTR}_{1_{c1}}} \qquad \text{RsqR2}_{2_{c2}} := \frac{\text{SSTR}_{2_{c2}} - \text{SSER2}_{2_{c2}}}{\text{SSTR}_{2_{c2}}}$$

$$\text{RsqR2}_{3_{c3}} := \frac{\text{SSTR}_{3_{c3}} - \text{SSER2}_{3_{c3}}}{\text{SSTR}_{3_{c3}}} \qquad \text{RsqR2}_{4_{c4}} := \frac{\text{SSTR}_{4_{c4}} - \text{SSER2}_{4_{c4}}}{\text{SSTR}_{4_{c4}}}$$

$$\text{RsqR2}_{5_{c5}} := \frac{\text{SSTR}_{5_{c5}} - \text{SSER2}_{5_{c5}}}{\text{SSTR}_{5_{c5}}}$$

*Model 3*
$$\text{RsqR3}_{1_{c1}} := \frac{\text{SSTR}_{1_{c1}} - \text{SSER3}_{1_{c1}}}{\text{SSTR}_{1_{c1}}} \qquad \text{RsqR3}_{2_{c2}} := \frac{\text{SSTR}_{2_{c2}} - \text{SSER3}_{2_{c2}}}{\text{SSTR}_{2_{c2}}}$$

$$\text{RsqR3}_{3_{c3}} := \frac{\text{SSTR}_{3_{c3}} - \text{SSER3}_{3_{c3}}}{\text{SSTR}_{3_{c3}}} \qquad \text{RsqR3}_{4_{c4}} := \frac{\text{SSTR}_{4_{c4}} - \text{SSER3}_{4_{c4}}}{\text{SSTR}_{4_{c4}}}$$

$$\text{RsqR3}_{5_{c5}} := \frac{\text{SSTR}_{5_{c5}} - \text{SSER3}_{5_{c5}}}{\text{SSTR}_{5_{c5}}}$$